

UC San Diego

Scripps Institution of Oceanography Technical Report

Title

Stress in the lithosphere from non-tectonic loads with implications for plate boundary processes

Permalink

<https://escholarship.org/uc/item/5851d178>

Author

Luttrell, Karen M

Publication Date

2010-11-19

Peer reviewed

UNIVERSITY OF CALIFORNIA, SAN DIEGO

Stress in the Lithosphere from Non-Tectonic Loads
with Implications for Plate Boundary Processes

A dissertation submitted in partial satisfaction of the
requirements for the degree Doctor of Philosophy

in

Earth Sciences

by

Karen Marie Luttrell

Committee in charge:

David Sandwell, Chair
Bruce Bills
Donna Blackman
Steve Cande
Yuri Fialko
Xanthippi Markenscoff

2010

© 2010

Karen Marie Luttrell

All rights reserved

The Dissertation of Karen Marie Luttrell is approved, and it is acceptable
in quality and form for publication on microfilm and electronically:

Chair

University of California, San Diego

2010

DEDICATION

To Chad and Oliver,
with all my love

EPIGRAPH

Before the hills in order stood
or earth received her frame
from everlasting, thou art God
to endless years the same

Isaac Watts, 1719

TABLE OF CONTENTS

Signature Page	iii
Dedication	iv
Epigraph	v
Table of Contents	vi
List of Figures	ix
List of Tables	xi
Acknowledgements	xii
Vita	xv
Abstract of the Dissertation	xvii
 Chapter 1 Introduction	 1
1.1 Preface	1
1.2 Plate tectonics	2
1.3 Non-Tectonic sources of stress	4
1.3.1 Time varying surface loads	4
1.3.2 Topography loads	7
1.4 Conclusions	11
1.4.1 Summary of results	11
1.4.2 Future research	12
 Chapter 2 Ocean loading effects on stress at near shore plate boundary fault systems	 15
2.1 Introduction	16
2.2 Methods	21
2.2.1 Plate bending stress from ocean loading	21
2.2.2 Ocean loading stress on plate boundary faults	27
2.3 Results	30
2.3.1 Eustatic ocean loading at the San Andreas system	30
2.3.2 Eustatic ocean loading at the Alpine fault system	33
2.3.3 Eustatic ocean loading at the Cascadia subduction system	36
2.3.4 Rapid sea level rise at the Black Sea	38
2.4 Discussion	41
2.5 Conclusions	47
2.6 Appendix	48

	2.6.1	Normal traction on a layered elastic halfspace.....	49
	2.6.2	Including time dependence with a Maxwell viscoelastic model.....	53
	2.6.3	Model benchmarks.....	55
2.7		Acknowledgements.....	57
2.8		References.....	58
Chapter 3		Modulation of the earthquake cycle at the southern San Andreas fault by lake loading.....	64
3.1		Introduction.....	65
	3.1.1	Ancient Lake Cahuilla.....	68
	3.1.2	Salton Trough earthquakes.....	70
3.2		Changes in normal stress due to lake level changes.....	71
	3.2.1	Lithosphere bending model.....	72
	3.2.2	Effect of pore pressure.....	78
	3.2.3	Total effect of lake change on Coulomb stress.....	80
3.3		Deformation and rebound: finding a best-fitting model.....	81
3.4		Stress and Lake Cahuilla.....	87
3.5		Discussions of Lake Cahuilla stress relevance.....	92
3.6		Conclusion.....	97
3.7		Appendix.....	97
	3.7.1	Geological field studies.....	97
	3.7.1.1	Surveys of tufa-covered cliffs.....	98
	3.7.1.2	Survey at Gas Line Road.....	99
	3.7.1.3	Stationary surveys of constructional berms.....	100
	3.7.1.4	Mobile surveys of constructional berms.....	101
	3.7.1.5	Cerro Prieto.....	102
	3.7.2	Suggestions for improvement of data.....	102
3.8		Acknowledgements.....	104
3.9		References.....	105
Chapter 4		Estimates of stress drop and crustal tectonic stress from the February 27, 2010 Maule, Chile earthquake: Implications for fault strength.....	109
4.1		Introduction.....	110
4.2		Minimum stress drop from the February 2010 Maule earthquake.....	112
4.3		Minimum tectonic stress estimate from topography.....	116
4.4		Discussion.....	123
4.5		Conclusions.....	127
4.6		Appendix.....	128
	4.6.1	Method and boundary conditions.....	128
	4.6.2	Stress in a thick elastic plate.....	131
	4.6.3	Benchmarks of limit cases.....	135
	4.6.4	Minimum deviatoric stress in a loaded elastic plate.....	138
4.7		Acknowledgements.....	141
4.8		References.....	142

Chapter 5	Constraints on 3-D stress in the crust from support of mid-ocean ridge topography.....	145
5.1	Introduction.....	146
5.2	Short- and long-wavelength stress at ridges and transforms.....	150
5.3	Methods.....	156
5.4	Results.....	169
5.5	Discussion.....	177
5.6	Conclusions.....	179
5.7	Appendix A: calculation of 3-D stress in a thick elastic plate.....	180
5.8	Appendix B: gravity analysis.....	184
5.9	Acknowledgements.....	191
5.10	References.....	192
Chapter 6	Strength of the lithosphere of the Galilean satellites.....	195
6.1	Introduction.....	196
6.2	Saturation bending moment and yield strength envelope models.....	199
6.3	Maximum observed topographic bending moment.....	205
6.4	An upper bound on the topographic spectrum from the yield strength envelope.....	211
6.5	Discussion.....	215
6.6	Conclusions.....	220
6.7	Acknowledgements.....	221
6.8	References.....	223

LIST OF FIGURES

Figure 1.1	Style of faulting and principal stress orientation.....	3
Figure 1.2	Ancient Lake Cahuilla shoreline in the Salton trough.....	6
Figure 1.3	Global topography and bathymetry.....	8
Figure 2.1	Eustatic sea level since the Last Glacial Maximum.....	16
Figure 2.2	Schematic of thick plate flexure about coastline due to an ocean load ..	19
Figure 2.3	Maximum shear stress perturbation from ocean loading.....	26
Figure 2.4	Ocean loading stress in San Andreas region	31
Figure 2.5	Ocean loading stress in New Zealand.....	34
Figure 2.6	Ocean loading stress in Cascadia region.....	37
Figure 2.7	Ocean loading stress in North Anatolian region	39
Figure 2.A1	Contours of stress components.....	56
Figure 3.1	Ancient Lake Cahuilla region.....	67
Figure 3.2	Lake level history and paleoearthquakes.....	69
Figure 3.3	Schematic diagram of Coulomb stress variation from lake load.....	74
Figure 3.4	Displacement and stress in response to a step water load.....	77
Figure 3.5	Contours of misfit and Predicted vs. observed shoreline elevation.....	84
Figure 3.6	Coulomb stress perturbations due to a single lake cycle.....	88
Figure 3.7	Coulomb stress perturbation from AD 700 - 2000.....	90
Figure 3.8	Coulomb stress perturbation between last two southern SAF ruptures...	91
Figure 3.9	Coulomb stress response since formation of the Salton Sea.....	95
Figure 4.1	Coseismic slip model and RMS fit versus roughness.....	114
Figure 4.2	Schematic illustration of megathrust geometry.....	118
Figure 4.3	Earthquake static shear stress change and topography stress.....	121
Figure 4.A1	Contours of Green's functions for each 3D stress tensor component.....	140
Figure 5.1	Schematic of stress orientations at mid-ocean ridges.....	155
Figure 5.2	Spreading rate along the global mid-ocean ridge.....	156
Figure 5.3	Minimum plastic failure stress, bathymetry, and focal mechanisms.....	159
Figure 5.4	Contours of regime fit versus long-wavelength stress.....	164
Figure 5.5	Regime constraints of ridge-parallel stress.....	166
Figure 5.6	Regime constraints of ridge-perpendicular stress.....	168
Figure 5.7	Summary of tectonic stress constraints.....	172
Figure 5.8	Spreading rate versus elastic thickness and tectonic stress.....	174
Figure 5.9	Regime of topographic stress plus long- wavelength stress fields.....	175
Figure 5.A1	Schematic of loaded elastic plate.....	181
Figure 5.B1	Contours of gravity misfit with elastic thickness and crustal density.....	187
Figure 5.B2	Gravity misfit versus elastic thickness.....	189

Figure 6.1	Diagram of ice shell structure and yield strength envelope models.....	202
Figure 6.2	Response of the lithosphere to a topographic load.....	208
Figure 6.3	Moment saturation for subduction zones on Earth.....	212
Figure 6.4	Impact crater depth versus diameter.....	214
Figure 6.5	Topographic profiles, observed and synthetic.....	217
Figure 6.6	Vertical accuracy of sampled topography.....	219

LIST OF TABLES

Table 3.1a	Lake Cahuilla shoreline sites measured in this study	81
Table 3.1b	Lake Cahuilla shoreline sites measured in previous study	82
Table 3.2a	Location and present-day vertical velocity observed at SCIGN sites.....	85
Table 3.2b	Present-day vertical velocity predicted at SCIGN sites.....	86
Table 5.1	Gravity RMS, elastic thickness, and crustal density in each region.....	158
Table 5.2	World Stress Map regime assignment criteria.....	160
Table 5.3	Constrained ridge-parallel and -perpendicular stress in each region.....	170
Table 6.1	Depth to nodal plane in a moment saturated plate.....	204
Table 6.2	Dimensionless geometric factor depending on Byerlees Law for ice.....	204

ACKNOWLEDGEMENTS

I would like to acknowledge all the people who have assisted me throughout my dissertation research. My advisor, David Sandwell, has been an excellent and supportive mentor and I have learned scads from him about geophysics, science, backpacking spots, childproofing, and much much more. In all my years as a graduate student, I always left his office feeling more confident about my research problems than I was when I went in. He is a model scholar and I am grateful to have had the opportunity to learn from him.

I would also like to thank the many people who have contributed to my research projects. Bridget Smith-Konter, Bruce Bills, and Yehuda Bock were instrumental in accomplishing the fieldwork and GPS processing for the Lake Cahuilla study. J. J. Becker, Danny Brothers, and Afton Van Zandt also cheerfully assisted in the fieldwork for this study, and I am grateful for their willingness to accompany me to the desert. The coseismic stressdrop model of the February 2010 Chile earthquake, as well as the InSAR and GPS observations from which it was derived, were provided by Xiaopeng Tong and Ben Brooks, and it has been a pleasure to collaborate with them on this project.

Additionally, I would like to express my sincere gratitude for the service of my committee members, Bruce Bills, Donna Blackman, Steve Cande, Yuri Fialko, and Xanthippi Markenscoff. In the last few years, they have graciously read drafts of all my papers and each one has offered insightful feedback and challenging questions. I have appreciated their dedication, and I know that I am a better scientist for having had them as role models.

Finally, I would like to thank all the denizens of IGPP for being so supportive of me and my family during my time at SIO. Many thanks to my classmates and officemates, Bettina Goertz-Allmann, Kristin Lawrence, and Karen Weitemeyer for making workdays so enjoyable and engaging. Many more thanks to those who have shared space with me in the last two years: Janine Buehler, Matt Wei, Xiaopeng Tong, Megan Jones, and Dave Stegman have all been fantastically generous and hospitable to my son and I, and I am forever grateful for these small kindnesses that have allowed us to be together.

And to Chad and Oliver, my two favorite boys in the whole world, thank you for being the absolute best part of every day and the best friends a wife or mother could hope for.

Chapter 2, in full, is a reprint of the material as it appears in Luttrell, K., and D. Sandwell (2010), Ocean loading effects on stress at near shore plate boundary fault systems, *Journal of Geophysical Research*, 115, B08411, doi:10.1029/2009JB006541. The dissertation author was the primary investigator and author of this paper.

Chapter 3, in full, is a reprint of the material as it appears in Luttrell, K., D. Sandwell, B. Smith-Konter, B. Bills, and Y. Bock (2007), Modulation of the earthquake cycle at the southern San Andreas fault by lake loading, *Journal of Geophysical Research*, 112, B08411, doi:10.1029/2006JB004752. The dissertation author was the primary investigator and author of this paper.

Chapter 6, in full, is a reprint of the material as it appears in Luttrell, K., and D. Sandwell (2006), Strength of the lithosphere of the Galilean satellites, *Icarus*, 183 (1),

159-167, doi:10.1016/j.icarus.2006.01.015. The dissertation author was the primary investigator and author of this paper.

Chapter 4, in part, is currently being prepared for submission for publication of the material. Luttrell, K., X. Tong, D. Sandwell, and B. Brooks, Estimates of stress drop and crustal tectonic stress from the February 27, 2010 Maule, Chile earthquake: Implications for fault strength. The dissertation author was the primary investigator and author of this material.

Chapter 5, in part, is currently being prepared for submission for publication of the material. Luttrell, K., and D. Sandwell, Constraints on 3-D stress in the crust from support of mid-ocean ridge topography. The dissertation author was the primary investigator and author of this material.

VITA

- 2002 Bachelor of Science, *magna cum laude*, Physics
Texas A&M University
- 2003 Bachelor of Science, *magna cum laude*, Geophysics
Texas A&M University
- 2003 - 2010 Research Assistant, Scripps Institution of Oceanography
University of California, San Diego
- 2007 Teaching Assistant, Scripps Institution of Oceanography
University of California, San Diego
- 2007 - 2010 NASA Earth and Space Science Fellow
University of California, San Diego
- 2010 Doctor of Philosophy, Earth Sciences
University of California, San Diego

PUBLICATIONS

- Luttrell, K., and D. Sandwell (2006), Strength of the lithosphere of the Galilean satellites, *Icarus*, *183* (1), 159-167, doi:10.1016/j.icarus.2006.01.015.
- Luttrell, K., D. Sandwell, B. Smith-Konter, B. Bills, and Y. Bock (2007), Modulation of the earthquake cycle at the southern San Andreas fault by lake loading, *Journal of Geophysical Research*, *112*, B08411, doi:10.1029/2006JB004752.
- Luttrell, K., and D. Sandwell (2010), Ocean loading effects on stress at near shore plate boundary fault systems, *Journal of Geophysical Research*, *115*, B08411, doi:10.1029/2009JB006541.
- Tong, X., D. Sandwell, K. Luttrell, B. Brooks, M. Bevis, M. Shimada, J. Foster, R. Smalley Jr., H. Parra, J. C. Báez Soto, M. Blanco, E. Kendrick, J. Genrich, and D. J. Caccamise II (2010), The 2010 Maule, Chile earthquake: Downdip rupture limit revealed from ALOS interferometry, *Geophysical Research Letters*, *in press*.

- Brothers, D., D. Kilb, K. Luttrell, N. Driscoll, and G. Kent (2010), Potential triggers for large ruptures along the southern San Andreas Fault, *submitted*.
- Luttrell, K., and D. Sandwell (2010), Constraints on 3-D stress in the crust from support of mid-ocean ridge topography, *manuscript in preparation*.
- Luttrell, K., X. Tong, D. Sandwell, and B. Brooks (2010), Estimates of stress drop and crustal tectonic stress from the February 27, 2010 Maule, Chile earthquake: Implications for fault strength, *manuscript in preparation*.

FIELDS OF STUDY

Major Field: Earth Sciences (Geophysics)

Studies in Geophysical Data Analysis
Professors Cathy Constable and Duncan Agnew

Studies in Seismology
Professor Shearer

Studies in Physics of Earth Materials
Professors Yuri Fialko and Duncan Agnew

Studies in Geodynamics
Professor David Sandwell

Studies in Gravity and Geomagnetism
Professors Cathy Constable and Robert Parker

Studies in Geophysical Inverse Theory
Professor Robert Parker

Studies in Radar Interferometry
Professors David Sandwell and Yuri Fialko

Studies in Numerical Methods for Geophysical Partial Differential Equations
Professor Yuri Fialko

ABSTRACT OF THE DISSERTATION

Stress in the Lithosphere from Non-Tectonic Loads
with Implications for Plate Boundary Processes

by

Karen Marie Luttrell

Doctor of Philosophy in Earth Sciences

University of California, San Diego, 2010

Professor David Sandwell, Chair

Stress in the lithosphere from non-tectonic loads is calculated, making use of semi-analytic Fourier models. Sources of non-tectonic stress include coastal lithospheric bending in response to the rise in eustatic sea level since the Last Glacial Maximum, lithospheric rebound and pore pressure changes in response to the intermittent load of Ancient Lake Cahuilla in the Salton trough, stress sustained through the formation and long-term support of local short-wavelength topography, and topography created by the ejecta debris from impact craters on the surface of the icy

Galilean satellites. Stresses from time varying surface water loads are calculated along major plate boundaries globally to determine to what extent, if any, these loads influence the major tectonic processes at work in plate boundary regions, such as the earthquake cycle on major faults. It is determined that the stress perturbations from these loads are generally an order of magnitude smaller than the tectonic stress accumulation rate. Their ability to noticeably affect the seismic cycle is therefore restricted to specific circumstances including when the tectonic loading rate is particularly low, such as along secondary plate boundary fault structures, when the non-tectonic loading rate is particularly high, such as in the case of catastrophic flooding events, or when the fault in question is already critically stressed to a near-failure level. Stresses from local topography are calculated along the global mid-ocean ridge and along the Chilean subduction megathrust. The predicted orientations of these stresses are compared to a presumed ridge-normal and transform-strike-slip faulting regime or the focal mechanism of a single large earthquake, respectively. Quantitative constraints for the coincident tectonic stresses are subsequently established with implications for the strength of the plate boundary faults and the necessity of particular topographic and bathymetric features.

Chapter 1

Introduction

1.1 Preface

2010 has been a year full of reminders of the destructive power of earthquakes. On January 12, 2010 a magnitude 7.0 earthquake occurred near Port-au-Prince, Haiti. The consequent collapse of buildings killed more than 200,000 people, injured an additional 300,000, and left 1.3 million people displaced from their homes. On February 27, 2010 a magnitude 8.8 earthquake occurred off the coast of Maule, Chile, resulting in the deaths of at least 521 people. To date, the Maule event is the fifth largest earthquake since modern recording began, and the largest in this region since the great magnitude 9.5 Chile earthquake in 1960. On April 4, 2010, Easter Sunday, a magnitude 7.2 earthquake occurred near the base of the Sierra El Mayor mountain range south of Mexicali in Baja California, Mexico. Ground motions were felt throughout southern California, USA, including 40 seconds of moderate shaking in San Diego, causing many people to wonder if this was the long expected rupture of the southern San Andreas fault.

The regular occurrence of large earthquakes serves as a reminder that the earth is a dynamic continuously deforming body. The physical quantity driving this deformation is stress, a tensor measure of forces applied to a three dimensional body.

The characterization and quantification of individual sources of stress is an important part of understanding the earth system as a whole.

1.2 Plate tectonics

Plate tectonics is the governing theory of geophysics. It describes the strong outer layer of the earth, or lithosphere, as a patchwork of individual tectonic plates that float upon and slip freely over the relatively fluid asthenosphere. Plate boundaries may be divided into three categories, based on the relative motion of the two contacting plates. Divergent margins are rifting zones where new crust is formed from upwelling mantle material. They are located throughout the oceans and in a few continental regions where spreading is initiating. Convergent margins are collision zones that may result in either an oceanic plate subducting beneath a continent (such as along the west coast of South America) or two continents colliding to uplift a new mountain range (such as the Himalayas of southern Asia). Transform margins occur where two plates slide past one another without much vertical motion, such as the San Andreas fault in California.

Earthquakes generally occur along active plate boundaries, and each type of plate boundary is characterized by a particular dominant style of faulting, though multiple faulting styles may be present in any plate boundary region. Faulting style depends on the relative orientation of the three principal stresses: the most compressive stress, the least compressive stress, and an intermediate stress (Figure 1.1). Normal faulting occurs when the most compressive is the vertical stress, thrust

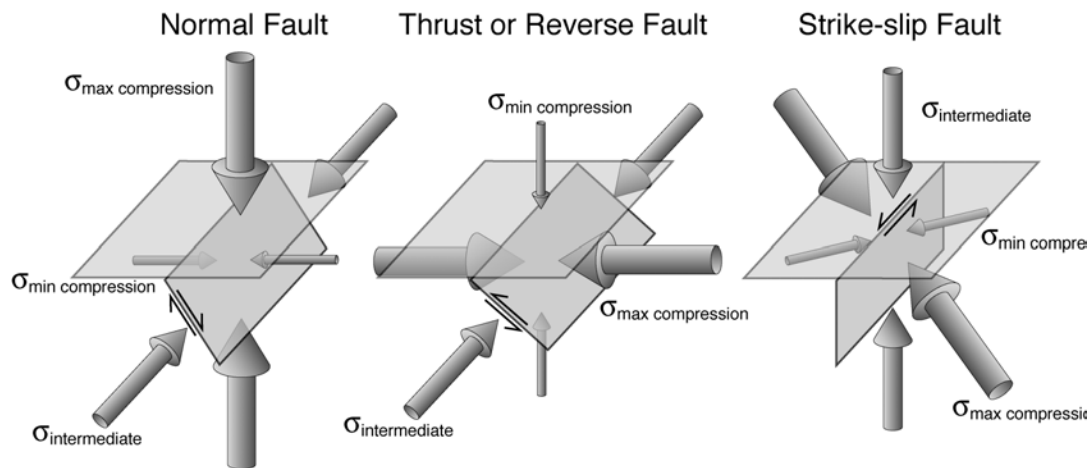


Figure 1.1 Style of faulting and principal stress orientation associated with three types of plate boundary. Small arrow couples show direction of block motion on either side of the fault.

or reverse faulting occurs when the least compressive stress is the vertical stress, and strike-slip faulting occurs when the intermediate stress is the vertical stress.

The physical processes that drive tectonic plates and form the stress field of the lithosphere are largely governed by thermal buoyancy and the force of gravity. Uplifted material at ridges has positive gravitational potential energy that induces an outward gravity sliding force and contributes to seafloor spreading. At convergent margins, older cold oceanic lithosphere is negatively buoyant and subducts beneath less dense continental lithosphere with a sinking slab pull force. In some regions, the base of the lithosphere is mechanically coupled to viscous convection cells in the mantle asthenosphere creating a basal traction that may either drive or inhibit plate motion.

These comprise the main tectonic sources of stress that control the location, style, and plate velocity of each boundary. Much is known about their orientation

from field observations of deformation indicators, from observations of current motion from modern geodetic methods such as GPS (Global Positioning System) and InSAR (Interferometric Synthetic Aperture Radar), and from seismic observations of earthquake focal mechanisms. Less is known about the absolute magnitude of these stresses, but constraints may be constructed through the accurate calculation of local variations in the stress field from non-tectonic sources (for example, the weight of a mountain is well known from its mass and the pull of gravity). Additionally, local plate boundary attributes, such as the exact timing of the earthquake cycle on a particular fault or the specific geometry of a plate boundary region, may be influenced by other non-tectonic sources of stress. It is the characterization and quantification of these non-tectonic loads that motivates this research.

1.3 Non-Tectonic sources of stress

1.3.1 Time varying surface loads

Stress in the lithosphere from non-tectonic loads may be separated into two categories: time varying loads that are applied to the surface, and the emergent load of building and supporting surface topography. A time varying load consists of the deposit or removal of any material with significant mass from the planet surface. This may include loads of sediment or other rock material, but often involves the distribution of water mass. A primary example of this is the Milankovitch climate cycle in which water mass is transferred between the oceans and the polar ice caps on a 10,000 year timescale. The uniform increase in load at the oceans but not on the continents in addition to the unloading at the melted polar ice caps causes the shape of

the earth to change in response to this mass redistribution. At every continental shoreline around the globe, the strong lithosphere will flex in response to this step load, a physically local effect but one that occurs globally.

Several coastlines coincide with major plate boundaries, and it is possible that the additional coast-perpendicular compression and extension from plate bending could sufficiently clamp or unclamp a fault in the region so as to promote or inhibit the earthquake cycle of that fault. If this were the case, it could help resolve some persistent discrepancies between observations of modern day fault slip rates and fault slip rates of the geologic past. In chapter 2, a model of lithospheric bending stress is developed to calculate the response to the rise in eustatic (global mean) sea level since the Last Glacial Maximum ~21,000 years ago.

A second example of a time varying load of water on the surface is the filling and emptying of large lakes. Ancient Lake Cahuilla was a large paleolake that intermittently formed in the Salton trough throughout the late Holocene, controlled by periodic diversions of the Colorado River due to the buildup of sediment in its delta. At its highstand, the weight of Lake Cahuilla would cause the land to flex and subside, and its subsequent desiccation would cause the land to rebound to its pre-lake elevation. The southern end of the San Andreas fault terminates in the middle of Lake Cahuilla, and it is possible that the bending stresses in response to the weight of the water, as well as the increase in pore pressure resulting from the hydration of the crust, were sufficient to affect the seismic cycle of the San Andreas and other faults in the region.

The southern San Andreas fault has been the source of regular large earthquakes throughout the entire period for which we have a sediment record (a little over a thousand years). However the last major rupture on this fault was more than 300 years ago. The questions of whether or not the southern San Andreas fault is “overdue” for a large earthquake, and if so, why the change in behavior, are areas of active research. The study presented in chapter 3 seeks to quantify the magnitude of stress perturbations from Lake Cahuilla on regional faults, particularly on the southern San Andreas, to determine if the lakes of the past could have played an active role in the timing of paleoearthquakes.

As part of this study, it was necessary to gather observations of the modern



Figure 1.2 Ancient Lake Cahuilla shoreline in the Salton trough.

elevation of indicators of the paleoshoreline of Lake Cahuilla (Figure 1.2). Because the highstand of the lake was known to be at a single elevation, the modern differences in the elevation of these points helps to constrain the physical parameters involved in modeling the stresses associated with rebound. Some observations were available from previous studies, but most were obtained from fieldwork carried out in the winter of 2006 specifically for this investigation. This involved identifying shoreline indicators through a combination of remote sensing and field observations, and taking multiple precise campaign GPS measurements of each of these features. Details of this field study may be found in the appendix of chapter 3.

1.3.2 Topography loads

The second category of stress from a non-tectonic load is the stress that is required to build and support local topography (Figure 1.3). An accurate calculation of the magnitude and orientation of this stress field may help constrain the absolute magnitude of plate driving forces. This is accomplished by comparing the short-wavelength variations in the stress orientation predicted by a model of local topographic support with observations of in situ total stress orientation. The size of the long-wavelength tectonic stress components can then be determined as the portion of the stress field that must be added to the local topographic variations in order to satisfy the stress orientation observations.

The success of this study hinges on the ability to accurately compute the short-wavelength stress field. This stress field is presumed to be primarily related to the topographic variations over the same wavelength. At an active mature plate boundary,

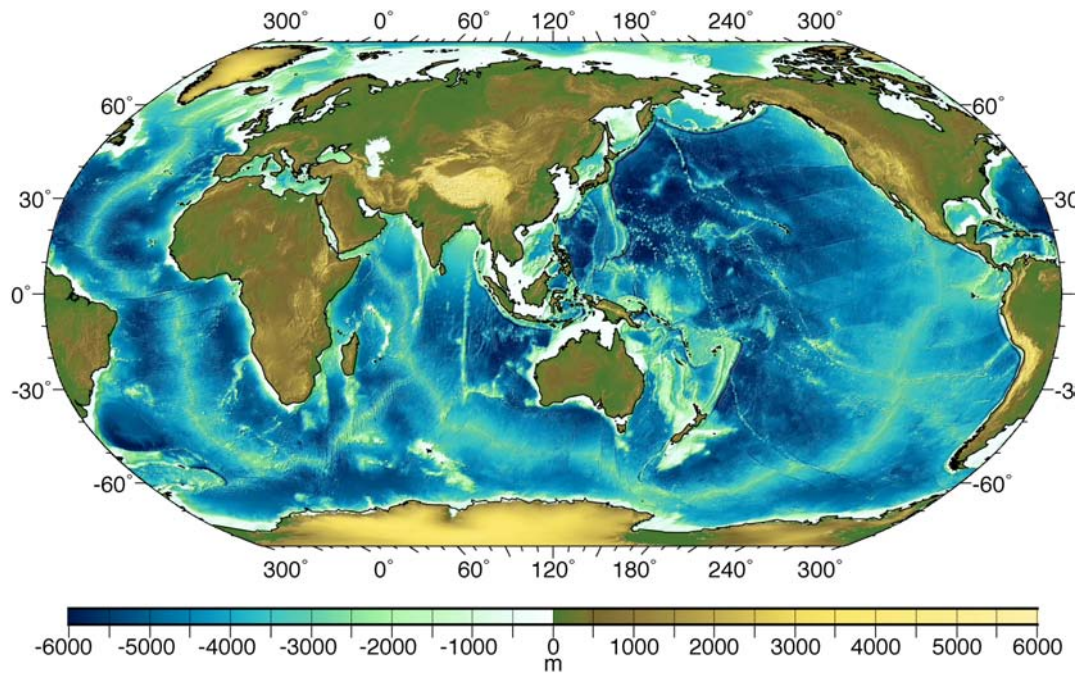


Figure 1.3 Global topography and bathymetry.

topography of this wavelength indicates the accumulation of strain released through a variety of ongoing inelastic deformation processes. If the rheologic form of these processes approximates elastic-perfectly-plastic failure, such that the topography is indicative of the critical transition between sustained elastic stress and dissipated plastic stress, then the short-wavelength variations in stress state may be calculated as those supporting the topographic load on a thick plate with an elastic rheology.

The first step of this calculation is to derive the spectral Green's function for the response of a finite-thickness elastic plate to non-identical but laterally coincident point loads on its surface and base, representing the simplest possible topographic load. This derivation is presented in the appendix of chapter 4 and involves reframing the relevant differential equations in terms of a single scalar potential that must satisfy

the biharmonic equation. This equation is then analytically solved, making use of a computer algebra system. The analytically derived point load solution is then convolved in the Fourier domain with the true two-dimensional shape of the loads at both the surface and base of the plate to obtain the full three-dimensional six-component stress tensor anywhere inside the plate.

The next step of this calculation is the determination of the shapes of the load of topography at the surface of the plate and the supporting buoyant load at the base of the plate, as well as the determination of the appropriate mechanical parameters describing the plate. The surface load is determined from observations of topography and bathymetry. The plate thickness is generally taken to be that of the crust such that the base load can be identified with the Moho (the contact between crust and mantle material). The shape of the buoyant load at the Moho can be determined through flexural analysis, tuning the parameters of crustal thickness, crustal density, and effective elastic thickness with observations of the gravity field. A summary of this method of gravity analysis is presented in appendix B of chapter 5.

The calculation of the local stress field associated with topography has many potential applications, two of which are presented here. In chapter 4, stress variations derived from coastal accretionary wedge topography in the vicinity of the February 2010 Maule, Chile earthquake are used to determine a lower bound on the shear traction supported by the megathrust fault in the rupture region, using the earthquake focal mechanism as the observation of in situ stress orientation across the entire ruptured fault plane. This lower bound of tectonic shear stress is then compared with a model of stress released along the fault plane constrained by observations of

co-seismic surface displacement from GPS and InSAR. The relative magnitude of these two independent estimates of tectonic shear stress has implications for the strength of the fault.

A second application involves calculating the stress from short-wavelength ridge-transform topography along the global mid-ocean ridge. In this study, a normal stress regime is assigned to all spreading ridge segments, while a strike-slip regime is assigned to all transform segments. This is a slightly more complicated problem in that many individual observations of stress orientation must be simultaneously satisfied. However this intricacy also allows more rigorous constraints to be placed on the magnitude of the components of tectonic stress. Particularly, it allows a full constraint to be placed on the magnitude of stress acting in the ridge parallel direction. The simultaneous analysis of all mid-ocean ridge plate boundaries and subregions permits a comparison between margins in different geographic regions and with different spreading rates. Details of this study may be found in chapter 5.

The final study presented here deals in a similar way with the topography created by impact craters on the hard icy outer surface of Europa, one of Jupiter's largest moons, and one of the few planets known to be currently tectonically active. Previous observations had measured the diameter and crest elevation of large debris craters. These observations can be related to a characteristic flexural wavelength and amplitude of deformation supported by bending moments within a thin strong plate of ice. By positing that the sustained crater topography is as high as can be supported by the strength of the ice shell, the observed pattern of crater dimensions can be used to constrain the yield strength envelope of the outer shell of Europa. The thickness of the

rigid brittle-deforming portion is of particular interest because it has many implications for constraining the major processes of planetary dynamics. Details of this study, conducted in an early exploratory phase of the dissertation research and included here for completeness, may be found in chapter 6.

1.4 Conclusions

1.4.1 Summary of results

The calculations of bending stress associated with the rise in eustatic sea level determined that normal stress resolved on nearshore faults is perturbed by a few megapascals over the duration of the loading. In most instances, this is slow enough that ocean loading will not perceptibly alter the seismic cycle. However there are two circumstances in which ocean loading may affect the seismic cycle. Secondary fault structures in plate boundary regions are likely to be affected because they are subject to the same ocean loading stress perturbation, but the tectonic loading rate on these faults is considerably lower than on the primary plate boundary strands. Consequently the perturbation from ocean loading is relatively higher. Also, in cases where sea level rise is much faster than the eustatic rate, such as in the catastrophic flooding of the Black Sea, the same normal stress perturbation is applied in a much shorter time. This particular flooding event very likely triggered ruptures along the entire length of the nearby North Anatolian fault.

Calculations of bending stress in response to the intermittent load of lake Cahuilla on the southern San Andreas fault reveal that resolved Coulomb stress is perturbed by a few tenths of a megapascal. This is a large enough stress that it could

directly trigger the San Andreas fault if it had already been tectonically loaded to a near critical value, but not large enough to noticeably advance or delay the next rupture if the loading occurs in an early or intermediate phase of the seismic cycle.

The two independent estimates of tectonic shear stress in the vicinity of the Maule, Chile earthquake, from observations of stress released in an earthquake and from calculations of stress required to sustain present day topography, are of comparable magnitude, a few megapascals. This suggests that the seismic cycle relieves a quantity of stress similar to the minimum value of tectonic stress, consistent with a weak megathrust fault. These observations are consistent with previous studies that have estimated low shear stress and a low coefficient of friction for the megathrust in this region.

Estimates of tectonic stress at mid-ocean ridges are generally correlated with spreading rate, with higher tectonic stresses being required at slower spreading ridges and lower stress required at faster spreading ridges. Particularly, slower spreading ridges require a non-zero ridge-parallel extension of ~4-8 megapascals, while faster spreading ridges require ridge-parallel extension near zero. In addition to these quantitative constraints, this research suggests that the bathymetric lows in the rift usually associated with transform offsets at mid-ocean ridges are a necessary feature for the long-term activity of an oceanic transform fault.

1.4.2 Future research

Recent seismic observations in the Salton Sea discovered a series of northeast trending normal faults off the southern terminus of the San Andreas fault.

Additionally, these normal faults show offsets that occur during the periodic inundations of Lake Cahuilla. As a follow up to the calculations presented in chapter 2 that consider the direct effect of Lake Cahuilla on the southern San Andreas fault, a two-phased connection may be explored in which the inundation of Lake Cahuilla triggers rupture on one or more normal faults within the lake. The stress response of these ruptures may in turn have a larger effect on the southern San Andreas fault, sufficient to trigger or advance rupture on even a partially loaded fault. This research is the subject of an ongoing collaboration.

The study of time varying surface loads may be extended to consider other surface loads, particularly those related to climate phenomena. This may include seasonal precipitation cycles that add surface loads in the form of mountain snowpack, water levels in mountain lakes and other catchment basins, and increased groundwater heads. It may also include longer-timescale climate variations, such as the El Niño-Southern Oscillation and the Pacific Decadal Oscillation, both of which have been shown to affect precipitation and influence the growth and retreat of glaciers. These loads have the potential to affect not only the earthquake cycle of major plate boundary faults but also the onset of periods of volcanic unrest. This research is the subject of a planned postdoctoral project.

The calculation of stress from topography for the purpose of constraining tectonic stress magnitude can readily be applied to other regions. Specifically, models of topographic stress may be compared to the coseismic rupture of the magnitude 7.9 earthquake near Chengdu, Sichuan province, China on May 12, 2008. This investigation has the potential to yield particularly interesting results as the moment

release from the earthquake is in an oblique-thrust sense. The spatial pattern of rupture style may correspond to the small-scale stress variations associated with local topography. Along the San Andreas fault, a model of small-scale stress from topography may be combined with a model for tectonic stress accumulation and compared to available observations of in situ stress orientation. In some regions, the sum of these two stress components may be sufficient to explain the stress orientations, while in other regions an additional physical mechanism of stress may be required. These projects are the subject of proposed future collaborations.

Chapter 2

Ocean Loading Effects on Stress at Near Shore Plate Boundary Fault Systems

Abstract

Changes in eustatic sea level since the Last Glacial Maximum create a differential load across coastlines globally. The resulting plate bending in response to this load alters the state of stress within the lithosphere within a half flexural wavelength of the coast. We calculate the perturbation to the total stress tensor due to ocean loading in coastal regions. Our stress calculation is fully 3-D and makes use of a semi-analytic model to efficiently calculate stresses within a thick elastic plate overlying a viscoelastic or fluid halfspace. The 3-D stress perturbation is resolved into normal and shear stresses on plate boundary fault planes of known orientation so that Coulomb stress perturbations can be calculated. In the absence of complete paleoseismic indicators that span the time since the Last Glacial Maximum, we investigate the possibility that the seismic cycle of coastal plate-boundary faults was affected by stress perturbations due to the change in sea level. Coulomb stress on onshore transform faults, such as the San Andreas and Alpine faults, is increased by up to 1 to 1.5 MPa respectively, promoting failure primarily through a reduction in normal stress. These stress perturbations may perceptibly alter the seismic cycle of major plate boundary faults, but such effects are more likely to be observed on nearby

secondary faults with a lower tectonic stress accumulation rate. In the specific instance of rapid sea level rise at the Black Sea, the seismic cycle of the nearby North Anatolian fault was likely significantly advanced.

2.1 Introduction

Global mean (eustatic) sea level is temporally subject to many processes. The largest is the Milankovitch cycle whereby water mass is periodically transferred between the global ocean (high sea level) and solid ice buildup at the poles (low sea level). The Last Glacial Maximum (LGM) ended about 21 ka, and since that time eustatic sea level has risen ~ 120 m [Peltier, 2004; Peltier and Fairbanks, 2006] at a rate of up to 1.25 cm/yr, reaching its approximate current level 4 ka (Figure 2.1). As sea level rose, the extra water acted as an additional vertical load to the ocean basins, but not to the continents. In response to this uneven load, the lithosphere at all coastlines globally flexed about the edge of the load at the shoreline.

Many previous studies have focused on the subsidence of ocean basins in

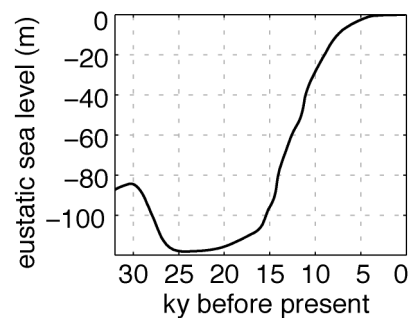


Figure 2.1 Eustatic sea level since the Last Glacial Maximum relative to present day level [Peltier and Fairbanks, 2006].

response to sea level rise as a way of constraining rheologic models of earth structure [e.g., *Lambeck and Chappell*, 2001; *Lambeck et al.*, 2002a; *Peltier and Drummond*, 2008], but these analyses are not repeated here. Instead, this study focuses on the stresses induced in the near-shore lithosphere as it flexes about coastlines globally. These flexure-induced stresses cause a perturbation to the total stress state in the lithosphere within half a flexural wavelength of the coast, both offshore and onshore (Figure 2.2).

It is possible that the change in the lithospheric stress state from ocean loading-induced flexure impacted the ongoing tectonic processes in coastal regions, particularly where the coastal region overlaps a plate boundary or other feature of geophysical interest. It is therefore the principal aim of this study to investigate the potential impact to plate boundary processes, particularly the shear faulting cycle, from the perturbing stress from sea level rise since the LGM. If we assume this stress perturbation is independent of other sources of stress in a region, we may make this determination by calculating the stress of a flexing thick plate resolved onto a particular fault plane.

Estimates of fault slip rate from geologic and geodetic methods show consistent discrepancies [e.g., *Bennett et al.*, 2004; *Matmon et al.*, 2005]. Several studies have addressed this discrepancy by adjusting either the geologic or geodetic rate with the hope of reconciling the two numbers [e.g., *Bennett et al.*, 2004; *Hetland and Hager*, 2006; *Oskin et al.*, 2007]. Other studies, however, have suggested that the difference in the geologic and geodetic estimates of fault slip rate may be revealing subtle details of the long-term faulting process [e.g., *Chery and Vernant*, 2006; *Dolan*

et al., 2007; *Hampel and Hetzel*, 2006; *Hetzel and Hampel*, 2005; *Luttrell et al.*, 2007]. If the stress perturbations from ocean loading throughout the Milankovich cycle are large enough, they may influence the seismic cycle of coastal faults sufficiently that the slip rate and recurrence interval of earthquakes on those faults would be perceptibly altered. This would be an example of a physical process external to the seismic cycle affecting the faulting process. There are not currently many paleoseismic indicators that sufficiently span the time since the LGM in a way that would allow these predictions to be rigorously tested, though a few studies do offer some observations of long-term fault behavior [e.g., *Rockwell et al.*, 2009]. We therefore present a model-based analysis of the stress changes ocean loading is likely to create and the impact such perturbations would have on observable paleoseismic indicators, so as to better understand the influence sea level rise may have on long-term plate boundary behavior.

Several studies have addressed the response of the earth to surface loads of water that come and go over various time scales and investigated their role in seismic triggering. The seasonal response to meters of precipitation in Japan and the Himalayas alters stress by a few kPa and has been shown to affect seismicity rate [*Bettinelli et al.*, 2008; *Bollinger et al.*, 2007; *Heki*, 2001; *Heki*, 2003]. The filling of new reservoirs with tens of meters of water can trigger seismicity not only from the immediate elastic response but also from the temporal flow of pore fluids in the crust, which may perturb stress by a few tens of kPa for several years after filling [e.g., *Gahalaut et al.*, 2007; *Simpson et al.*, 1988]. In a few cases, hundreds of meters of water removed as entire lakes empty affect stresses both by altering the pore pressure

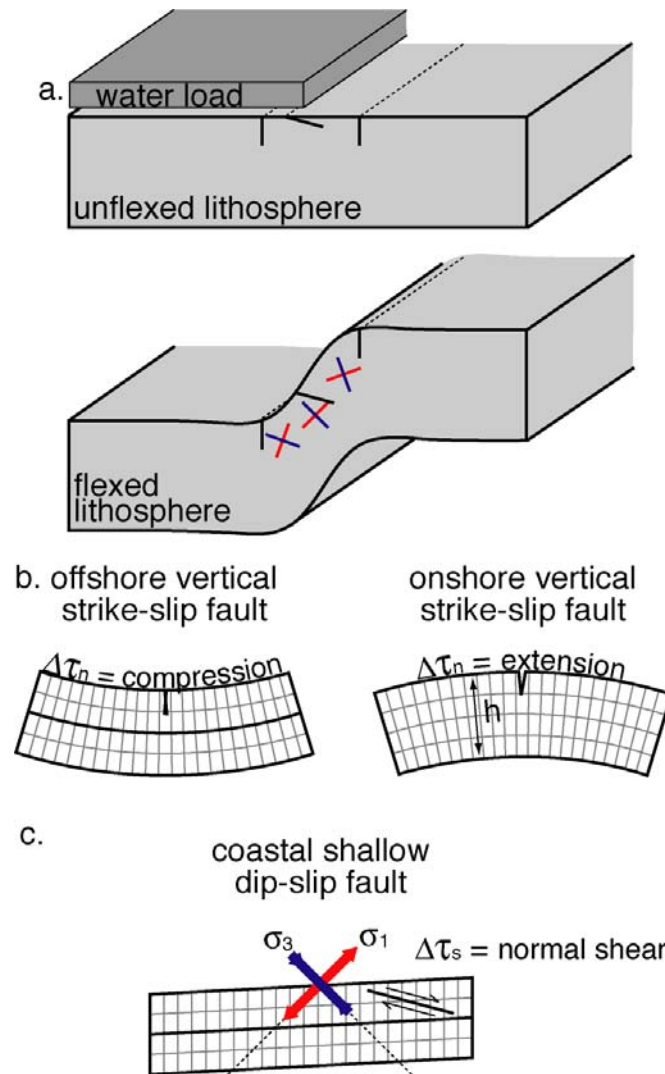


Figure 2.2 (a) Schematic of thick plate flexure about coastline due to an ocean load. Red and blue bars show direction of maximum (extension) and minimum (compression) principal stresses from flexure about coastline. The short black lines show the location of an onshore and offshore vertical fault as well as a near-shore shallow dipping fault, and the dotted lines represent the surface trace of these faults. Ocean loading will perturb stress on an offshore or onshore (b) vertical strike-slip fault differently from a shallow-dipping coastal dip-slip fault (c). For vertical strike-slip faults, the normal stress component is dominant. For a shallow dipping dip-slip fault, the shear stress component may also play a role.

in the crust and inducing flexure in the lithosphere. These changes alter stress by a few MPa over thousands of years [*Hampel and Hetzel, 2006; Hetzel and Hampel, 2005*] or a few hundred kPa over hundreds of years [*Luttrell et al., 2007*] and can affect the slip rate of nearby faults. On the largest and longest scale, glacial rebound following the removal of kilometers of ice may alter stresses tens of MPa for many thousand years following unloading and can reactivate seismicity on previously dormant faults [e.g., *Grollmund and Zoback, 2000; Ivins et al., 2003; Johnston et al., 1998*]. Additionally, there have been numerous investigations of regional subsidence and flexure associated with sea level rise that have not calculated the perturbing contribution to the stress state [e.g., *Ivins et al., 2007; Kendall et al., 2003; Lambeck and Purcell, 2005*]. The load considered in this study acts over the same time period as polar ice cap melting, but it has a smaller amplitude and is more widespread since the change in sea level is global. The largest flexure-induced stresses are present only within a flexural wavelength of the coastline, generally a few hundred km. For this reason, our analysis more closely resembles the cases of local lake unloading than widespread glacial rebound.

In the sections that follow, we develop the model used to calculate bending stress from ocean loading globally and the method of resolving this into Coulomb stress on a particular fault plane. We then more closely examine the stress predictions at two coastal transform boundaries (San Andreas fault and Alpine fault) and a near-shore subduction boundary (Cascadia subduction zone). We also examine a special instance of ocean loading stress on a coastal transform in response to a very rapid sea

level rise (North Anatolian fault). Finally, we discuss the implications of our calculations for the understanding of long-term fault behavior.

2.2 Methods

2.2.1 Plate bending stress from ocean loading

The stress perturbation from ocean loading is just one component of the total stress tensor in a region. In addition to the lithostatic stress that increases with depth and remains constant over time, a region is also subject to the broad tectonic stress that drives plate motions and changes over geologic timescales (10^6 yr). The ocean loading component we calculate changes on the timescale of the Milankovitch cycles ($10^4 - 10^5$ yr). Local stresses associated with the earthquake cycle of a particular fault evolve over the timescale of the recurrence interval of that fault ($10^2 - 10^4$ yr). Because all of these sources of stress act over very different timescales, we can calculate their effects independently from one another and add them linearly to get the total stress σ_{ij} , as seen below,

$$\sigma_{ij} = (\rho g z) \mathbf{I}_{ij} + \tau_{ij}^{tectonic} + \tau_{ij}^{ocean\ loading} + \tau_{ij}^{faults} \quad (2.1)$$

where ρ is the density, g is gravity, z is the vertical coordinate, \mathbf{I}_{ij} is the identity matrix, and τ_{ij} represents a stress deviation from the lithostatic state from various

sources. We can therefore calculate the effect of stress change from ocean loading $\Delta\tau_{ij}^{ocean\ loading}$ on the total stress $\Delta\sigma_{ij}$ without needing to specify forms for the regional tectonic or local earthquake cycle stresses (hereafter we shall refer to stress perturbation from ocean loading as $\Delta\tau_{ij}$). This is only possible because the ocean loading strains are small so we can assume a linear stress-strain relationship.

We model stress perturbations from ocean loading by first calculating the full 3-D stress tensor from a vertical surface load in a thick elastic plate overlying a Maxwell viscoelastic halfspace. The plate is both uniformly thick and uniformly strong. We make no assumptions about the orientations of the principal axes of the stress tensor, nor do we assume any of the six Cartesian stress components are zero, particularly $\tau_{xz} \neq \tau_{yz} \neq 0$. The calculations are done using a semi-analytic Fourier model [Luttrell *et al.*, 2007; Smith and Sandwell, 2004] such that vertical displacements and derivatives are calculated from analytic solutions and horizontal displacements and derivatives are calculated in the Fourier domain (see Appendix for a summary of model details). This is equivalent to calculating the analytic Green's function response to a point load and then convolving that response with the true 2-D shape of the load. The semi-analytic model is advantageous because use of the 2-D Fast Fourier Transform allows fast model calculations with true load geometry. However the rheologic vertical stratification is necessarily simple to allow an analytic vertical solution. Also, the horizontal wavelength of the load distribution is numerically restricted to be less than the width of the grid used for computation. This

model has previously been benchmarked against known analytic solutions [see *Luttrell et al.*, 2007].

For the model input, we use a eustatic sea level curve since the LGM that takes into account multiple local data sets from around the world as well as a model of isostasy to account for changes in basin volume as the lithosphere flexes under the weight of the water (Figure 2.1) [*Peltier*, 2004; *Peltier and Fairbanks*, 2006]. The bathymetry of the seafloor is determined from the new SRTM30_PLUS global topography/bathymetry grid [*Becker et al.*, 2009], which is particularly accurate in shallow coastal areas (depth $< 300\text{m}$) where ship soundings are abundant. The true load geometry, therefore, is known exactly. This exact load shape is input into our model without simplification, accounting for the migration of the shoreline as sea level rises.

As previously mentioned, the assumption that these stress components add linearly to the regional background state of stress (Eq. 2.1) allows us to study the stress perturbations induced by ocean loading without having to specify anything about the other sources of stress present in a region. We are primarily interested in the change in stress over time, not the absolute stress state itself. Therefore, we generally take the initial stress to be that at the time of the LGM, though this choice is of course arbitrary and we could equally examine any time period of interest.

For the elastic plate, we assume a Young's modulus of 70 GPa and a Poisson's ratio of 0.25. The only two model parameters to consider are the thickness of the elastically strong plate h and the viscosity of the underlying halfspace η . However, because the eustatic sea level rise is so gradual, any time delay in the flexural response

due to the viscous asthenosphere would be negligible for a viscosity of 10^{20} Pa s or less (corresponding to a Maxwell relaxation time of about 200 yr). The asthenosphere viscosity in a plate boundary region is typically less than 10^{20} Pa s by as much as two orders of magnitude [e.g., *James et al.*, 2000; *Lambeck and Purcell*, 2005]. In general, therefore, we examine the fully relaxed response, equivalent to an elastic plate over a fluid halfspace. (A special case of rapid ocean loading is treated in Section 2.3.4).

The choice of plate thickness is important because h affects the flexural rigidity and flexural wavelength. Consequently, a thicker bending plate will affect a larger area around the coastline, whereas stresses in a thinner plate will be more localized. Global post-glacial rebound studies generally suggest a plate 65 km or thicker is appropriate for continents and a 50 km thick plate is appropriate for ocean basins [e.g., *Lambeck and Chappell*, 2001; *Lambeck et al.*, 2002b], but along tectonically active coastal margins a thinner plate of 40 km or less may be more appropriate [e.g., *James et al.*, 2000]. For the purposes of this study we examine stress perturbations in a plate of intermediate thickness, $h = 50$ km, corresponding to a flexural wavelength about 500 km. The magnitude of the stress perturbations also depends on the depth of observation within the plate relative to the plate thickness (z/h), with larger bending stresses near the surface and smaller stresses closer to the center of the plate (see Appendix). We choose an observation depth of 10 km, which is a typical seismogenic depth on the transform faults considered here and is approximately the depth of the base of the elastic zone of the Cascadia subduction zone [*Fluck et al.*, 1997].

The extent to which a fault in a coastal region is affected by plate bending stresses from ocean loading depends not only on the thickness of the flexing plate, as mentioned above, but also on the shape of the coastline and the location of the boundary. We calculated the fully relaxed global stress perturbation in a 50 km thick plate due to 120 m of sea level rise, using the exact shape of the ocean basin without any simplification of the coastline. The maximum shear stress, $(\sigma_1 - \sigma_3)/2$, where σ_1 and σ_3 are the maximum and minimum principal stresses, is shown in Figure 2.3 and gives an idea of the “size” of the stress perturbation, allowing a simple comparison of the effects of geography. The areas of greatest potential stress perturbation are within a few hundred km of the coast, both on- and offshore [Kendall *et al.*, 2003], where an optimally oriented fault could experience a 1.2 MPa change in shear stress in addition to a pressure change of similar magnitude. Anywhere a tectonic plate boundary (shown as red lines) coincides with a coastline, there is the potential for the faults associated with that boundary to be influenced by the rise in sea level. Far offshore features like mid-ocean ridges and deep ocean subduction zones are unaffected by ocean loading (Figure 2.3b) because the ocean load is uniform there and no bending stresses are induced. A coastal subduction zone may or may not be affected depending on its proximity to the coast. An onshore transform fault, however, such as the San Andreas, North Anatolian, or Alpine fault, is well positioned to experience large stress perturbations from ocean loading.

Bending stresses from ocean loading are particularly pronounced in regions where the narrow strips of water or land have a width equal to about half the flexural

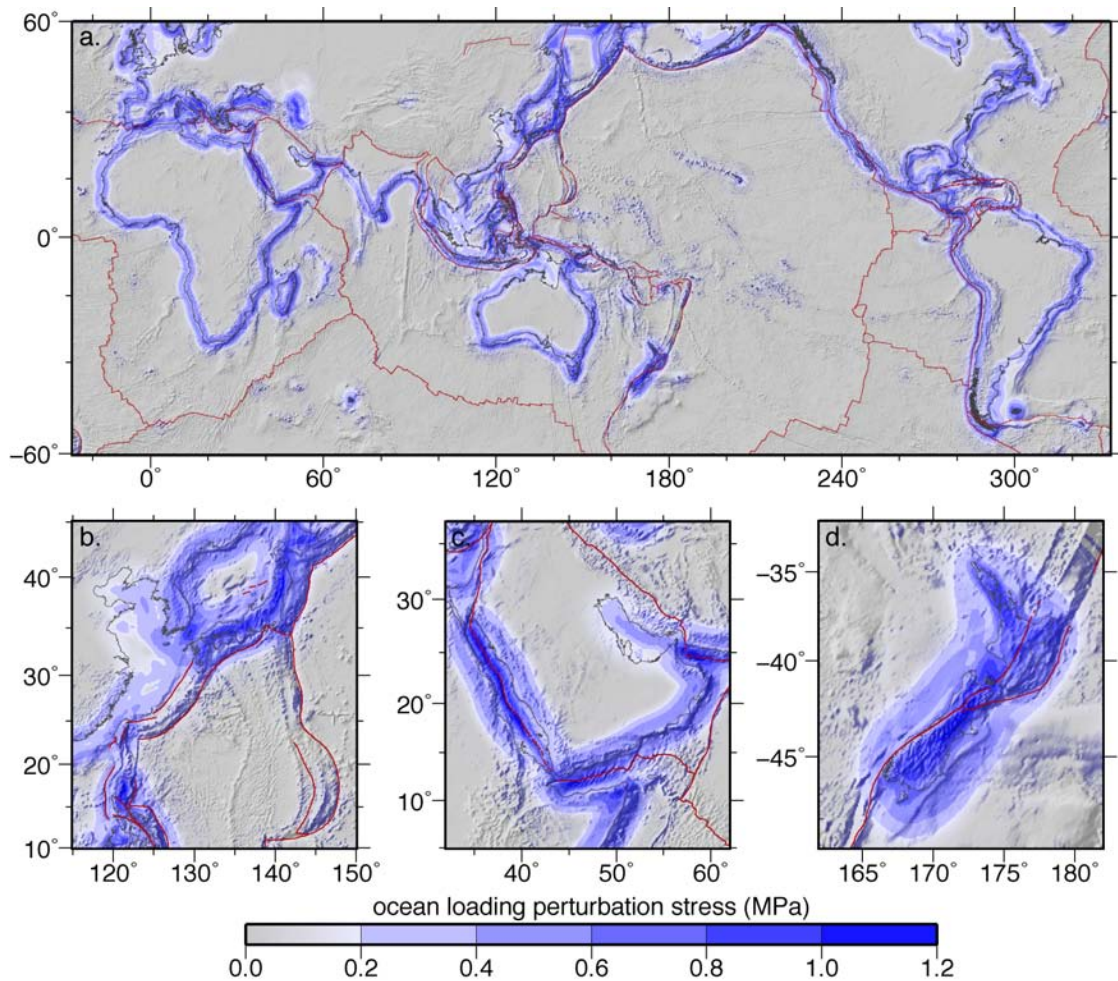


Figure 2.3 (a) Maximum shear stress perturbation from ocean loading on a 50 km thick plate. Optimally oriented faults could experience up to a 1.2 MPa change in shear stress at all coastlines globally in addition to a pressure change of similar magnitude. Tectonic plate boundaries (red) in coastal regions may be affected by the stress perturbations. (b) Deep sea subduction zones will not be affected by ocean loading, but near-land subduction zones may be affected depending on their proximity to the coast. (c) In narrow gulfs where the width of the water load is close to half the flexural wavelength, bending stress magnitude may be higher. (d) Loading on multiple sides of a narrow land mass of width close to half the flexural wavelength also concentrates the bending stress, resulting in higher magnitudes.

wavelength. In these cases, the geometry of the load concentrates the stress of bending. This is the case at the Red Sea (Figure 2.3c), where the 250 km width of the gulf happens to correspond to the half flexural wavelength of a 50 km thick plate, making the maximum shear stress there larger than it is a comparable distance offshore in the open ocean. This stress concentration is less pronounced, however, when a thinner plate is used to calculate bending stresses, which is likely more appropriate in a rifting zone. Similarly, stress on a narrow strip of land such as the islands of New Zealand or Japan may be as much as fifty percent larger than stress a comparable distance inland from a continental coastline if their width is similar to the half flexural wavelength (Figure 2.3d). Again, however, this stress concentration phenomenon is sensitive to the choice of model plate thickness. Though the coastal stresses from ocean loading are present globally, we shall focus in this study on the San Andreas fault (SAF), Alpine fault, North Anatolian fault (NAF), and Cascadia subduction zone (CSZ) systems as representatives of major transform and subduction boundaries under different loading conditions.

2.2.2 Ocean loading stress on plate boundary faults

We use the above model to calculate the perturbation to the six components of the 3-D Cartesian stress tensor $\Delta\tau_{ij}$. We interpret the 3-D change in stress by calculating differential Coulomb stress resolved on a fault plane of known orientation, $\Delta\tau_c$ [e.g., *King and Cocco*, 2001; *King et al.*, 1994].

$$\Delta\tau_c = \Delta\tau_s + \mu_f \Delta\tau_n \quad (2.2)$$

In this equation, μ_f is the effective coefficient of friction and $\Delta\tau_n$ and $\Delta\tau_s$ are the normal and shear stresses from the perturbing stress tensor $\Delta\tau_{ij}$ on a plane with normal vector n_i , defined as in *Fialko et al.* [2005] as

$$\Delta\tau_n = \Delta\tau_{ij} n_i n_j \quad (2.3)$$

$$\Delta\tau_s = \Delta\tau_{ij} n_i t_j. \quad (2.4)$$

where we use the standard summation notation, such that a variable with a single subscript i or j is a vector, a variable with two subscripts ij is a tensor, and a repeated index indicates summation over the spatial coordinates. Calculating normal stress requires only a choice of the normal to the plane n_i , but calculating shear stress requires choosing both the orientation of the plane and the direction within the plane in which the shear stress is resolved t_i . This will generally be the expected direction of slip on a fault so for the strike-slip SAF, t_i is horizontal along strike, but for the oblique-thrust CSZ, t_i dips in the direction of convergence 69° east of north [*Demets et al.*, 1990; *Demets et al.*, 1994]. A positive or negative change in Coulomb stress indicates that failure along that plane would be promoted or inhibited such that the timing of the subsequent rupture on that fault would be advanced or delayed. Normal stress is positive in extension and negative in compression, while the sense of stress

indicated by positive and negative shear stress is context dependent. However, we choose the sign such that a positive change in either normal or shear stress always increases Coulomb stress, and vice versa. It is worth noting that in regions where normal stress perturbation dominates, the effect on Coulomb stress will be mitigated by the coefficient of friction, but shear stress perturbations have a direct effect on Coulomb stress independent of the coefficient of friction.

The sign and magnitude of the Coulomb stress perturbation on a fault is influenced both by the orientation and presumed sense of slip on that fault and the orientation of the principal stresses of the ocean loading perturbation $\Delta\tau_{ij}$. The intermediate principal stress σ_2 is generally parallel to the coast. Near the shoreline the maximum (extension) and minimum (compression) principal stresses, σ_1 and σ_3 , are perpendicular to the coast and plunge roughly 45° away from and toward the ocean, respectively, in the top half of the plate (Figure 2.2a). Further onshore, the principal stresses rotate slightly toward the land, while further offshore they rotate slightly away from the land. Change in normal stress resolved on a vertical onshore fault is extensional because the maximum principal stress is more horizontal (Figure 2.2b, right). Conversely, normal stress on an offshore fault becomes more compressional (Figure 2.2b, left). For a vertical strike-slip fault the change in shear stress is much smaller than the change in normal stress. For a shallow dip-slip fault, however, shear stress may be large enough to contribute to Coulomb stress perturbation (Figure 2.2c). The sense of the change in shear stress will depend on the dip of the fault relative to the orientation of the principal stresses. Shear stress on a

coastal fault dipping toward the land is perturbed in a normal shear sense as long as the dip of the fault is shallower than the dip of the compressional principal stress.

2.3 Results

2.3.1 Eustatic ocean loading at the San Andreas system

The San Andreas fault system accommodates 40 mm/yr of right lateral slip, approximately 80 % of the relative Pacific – North American plate motion [e.g., *Demets et al.*, 1990; *Fay and Humphreys*, 2005]. The principal strand of the fault runs within 100 km of the coastline along most of its 500 km length. We calculate the stress change at 10 km depth within a 50 km thick plate in response to 120 m of sea level rise. Figure 2.4a shows the regional variations in normal stress resolved on a vertical fault plane striking 50° west of north, the mean trend of the SAF and the various subparallel auxiliary faults that make up the plate boundary. As expected, the regional effect of ocean loading on vertical faults is extension (positive normal stress) onshore and compression (negative normal stress) offshore. These zones of perturbed stress have magnitudes up to 1.5 MPa and follow the coastline, coinciding with the flexural bulge onshore and flexural moat offshore. Stress on a vertical fault running along the shoreline would be perturbed very little by ocean loading. Offshore faults such as those in the borderland of southern California would experience normal compression due to sea level rise. Based on the location of the fault trace, the central and southern portions of the SAF would experience more normal extension than the northern SAF and some smaller faults like the Hayward, San Jacinto, and Elsinore faults could experience similar or greater stress perturbations.

The SAF is not, of course, a single plane but rather has significant variation in strike and dip in the central and southern segments (Figure 2.4c). It dips southwest in the central section, north of the “big bend”, and dips northeast south of the “big bend” [Scheirer *et al.*, 2007]. We calculate the normal, shear, and Coulomb stresses resolved on the main SAF strand applying Eq. (2.2 – 2.4), using the varying orientation and assuming a horizontal in-plane shear direction. Because the strike of the fault roughly

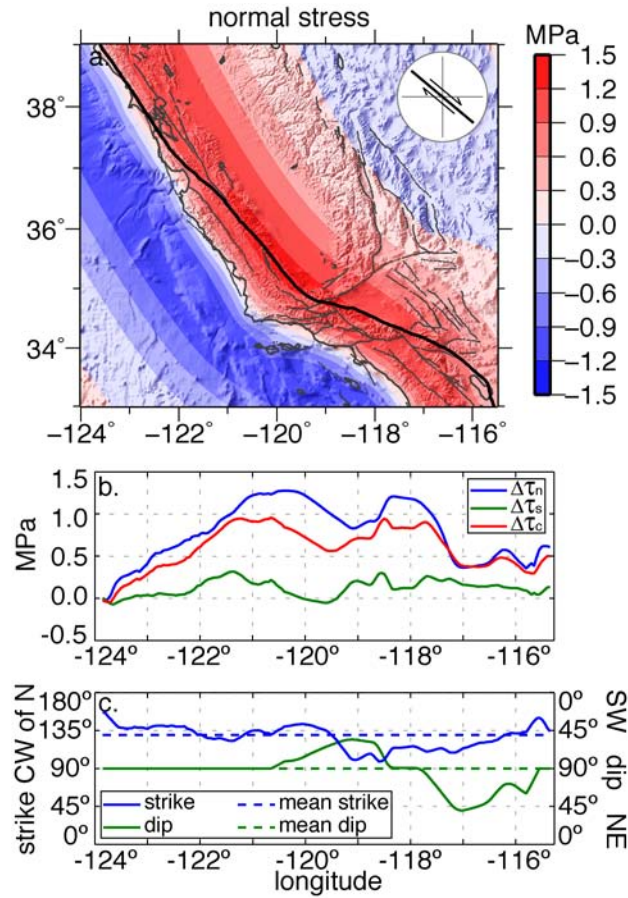


Figure 2.4 (a) San Andreas region ocean loading perturbation to normal stress resolved on a vertical plane striking 50° W of N. Actual SAF trace shown (thick black line). Positive and negative normal stress represent extensional and compressional perturbations, respectively. (b) Normal (blue), shear (green), and Coulomb stress (red) resolved onto the actual SAF plane with varying orientation (c) along its length.

follows the shape of the coastline, variations in the dip of the fault have greater influence on stress than variations in strike, decreasing the magnitude of the normal stress (Figure 2.4b). Along the strike-slip SAF, normal stress is about four times larger than shear stress and is the dominant component of Coulomb stress. Assuming an effective coefficient of friction of $\mu_f = 0.6$, Coulomb stress along the SAF is perturbed by 0.5 – 1 MPa, promoting failure.

A Coulomb stress increase of 1 MPa during the time of eustatic sea level rise corresponds to a loading rate increase of 0.1 kPa/yr, a factor of 300 smaller than the tectonic loading rate of around 30 kPa/yr [*Smith and Sandwell, 2003*]. Over a 300-year seismic cycle, ocean loading would contribute about 30 kPa Coulomb stress. This very small increase in the loading rate on the main fault strand will not noticeably speed up the seismic cycle. However a change in normal stress of 1 MPa or greater may noticeably weaken (strengthen) the coastal faults onshore (offshore) during times of high sea level relative to times of low sea level. This will be particularly noticeable if fault strength is generally low (10 MPa or less) and remains constant over many seismic cycles. We would expect to see onshore faults have a shorter recurrence interval in recent times than during the LGM, possibly observable on the main strand of the SAF but more likely on the various subparallel secondary faults in the region. Simultaneously, slip on offshore faults would be inhibited, making the recurrence interval longer in recent times relative to the LGM.

2.3.2 Eustatic ocean loading at the Alpine Fault system

Most coastal regions of continents will behave similarly to the San Andreas region when bending in response to a rise in sea level. In areas where loading occurs on either a narrow strip of ocean or around a narrow strip of land of width comparable to half the flexural wavelength, however, the resulting bending stresses may be amplified due to the geometry of the load. One example of this is at the North and South Islands of New Zealand, which are approximately 200 km wide. The region is tectonically complicated because the islands mark the transition between the Pacific plate subducted beneath the Australian plate in the north and the Australian plate subducted beneath the Pacific in the south. The 480 km long Alpine fault is the main expression of this plate boundary on the South Island, accommodating 27 ± 5 mm/yr of dextral strike-slip and 0 – 12 mm/yr of fault normal shortening, about 75 % of the total Pacific-Australia plate motion predicted by global models [Norris and Cooper, 2001].

At the northern South Island, the Alpine fault splays into several subparallel faults in the Marlborough Fault System, each accommodating some portion of the slip budget, the largest of which is the Hope fault, carrying 23 mm/yr of strike slip. Additionally as much as 4.1 mm/yr of strike-slip may be accommodated on the Porters Pass fault, which runs parallel to the Alpine fault east of the Southern Alps and has produced several large ($M > 7$) earthquakes in the Holocene, though there have been no historic ruptures on this fault [Howard *et al.*, 2005]. The orientation of these faults varies significantly along strike. At the far south, the Alpine fault is mostly a single steeply dipping segment, and almost purely strike slip. In central South Island, the

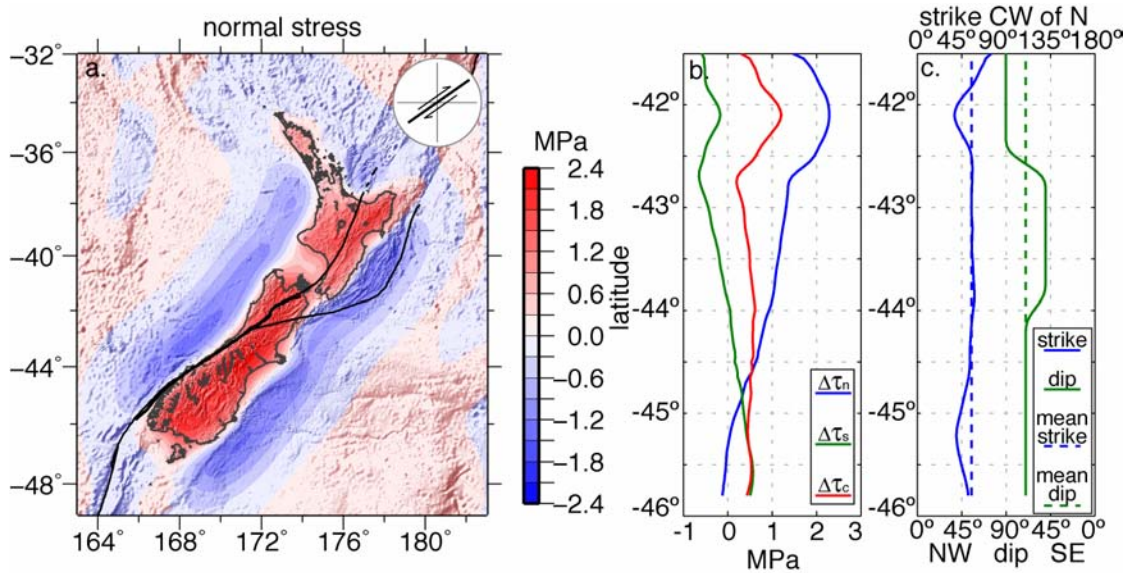


Figure 2.5 (a) New Zealand region ocean loading perturbation to normal stress resolved on a vertical plane striking 55° E of N. Actual Alpine fault trace shown (thick black line). Positive and negative normal stress represent extensional and compressional perturbations, respectively. (b) Normal (blue), shear (green), and Coulomb stress (red) resolved onto the Alpine fault plane with varying orientation (c) along its length.

Alpine consists of many right-stepping segments, dipping ~50° to the southeast, and has a large convergent component. Further north, the faults of the Marlborough system are vertical and dextral [Robinson, 2004].

Figure 2.5a shows the regional variations in normal stress in response to 120 m sea level rise using the same model parameters as in the previous section and resolved on a vertical fault plane striking 55° east of north. In general, onshore regions experience an extensional perturbation to normal stress whereas offshore regions experience additional compression, just as in the previous section. The magnitude of the onshore perturbation, however, may be up to 2.4 MPa, which is sixty percent greater than the normal stress perturbation in the SAF region. This is due to the island

being loaded on both sides and being the right width such that the bending effects from each coast overlap and add constructively. Along the trace of the Alpine fault (Figure 2.5 b and c) bending stress magnitude varies. In the southern South Island, the Alpine fault runs very near the coastline in the nodal region, such that the perturbation in normal stress on a steeply dipping fault is 1 MPa or less. In the central South Island the fault has a shallower dip, which tends to decrease the normal stress perturbation, but the fault trace also runs inland, closer to the onshore flexural bulge. The normal stress perturbation in this section is therefore about 1.2 MPa. In the northern Marlborough faults region, change in normal stress is large both because the faults are located in the flexural bulge and because these faults are nearly vertical, such that normal stress is perturbed up to 2 MPa or more in this section.

Assuming a coefficient of friction of $\mu_f = 0.6$ and taking into account the shear stress effects due to changes in the strike of the fault relative to the strike of the coastline, Coulomb stress along the fault is perturbed by 0.5 – 1.0 MPa. This is similar to the Coulomb stress perturbation at the SAF, so again we expect that this change will be insignificant compared to the tectonic loading rate. However because the normal stresses are higher, particularly in the inland sections of the South Island, it is possible that the strength of the Marlborough faults and Porters Pass faults would be decreased during times of high sea level leading to increased seismic activity and perhaps average slip rate relative to times of low sea level.

2.3.3 Eustatic ocean loading at the Cascadia subduction system

A third type of coastal plate boundary geometry to consider is the case of a very shallow dipping subduction zone in which the seismogenic zone of the main fault may straddle both sides of the coastline. The Cascadia subduction zone in the Pacific Northwest forms the main boundary between the subducting Juan De Fuca plate and the overriding North America plate. The leading edge of subduction roughly follows the coastline about 100 km offshore, and the base of the locked zone is downdip at a depth around 10 km (Figure 2.6) [*Fluck et al.*, 1997; *Wang et al.*, 2003]. Using the same parameters as in the previous sections, we calculate the fully relaxed stress change in response to 120 m of sea level rise and resolve normal stress onto a plane dipping 15° to the east and striking 5° west of north. Normal stress is perturbed by up to 0.6 MPa, but in an opposite sense on different parts of the fault. On the shallow offshore portion, failure is inhibited by increased compression, whereas on the downdip extension of the fault beneath the continent failure is promoted by extension on the fault.

The magnitude of normal stress perturbation along the CSZ is about half the magnitude of the perturbation along the SAF to the immediate south, principally because of the shallow dip of the fault. Note, however, that for a similar locking depth the area of a 15° dipping fault will be 3.8 times greater than the area of a vertical fault, so the change in integrated fault strength could be greater at a subduction zone than on a transform fault. The shear stress perturbation along the CSZ is larger than along the SAF, mostly because the sense of shear on the CSZ is thrust motion as opposed to strike-slip, and tends to inhibit failure along the coastline. A smaller coefficient of

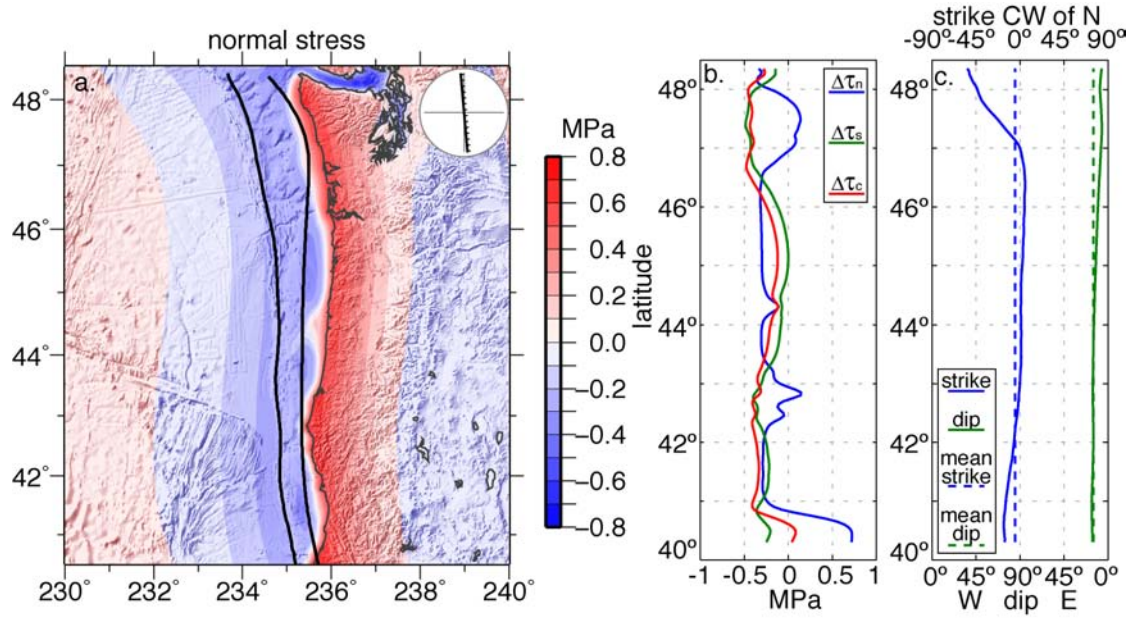


Figure 2.6 (a) Cascadia region ocean loading perturbation to normal stress resolved on a plane striking 5° W of N and dipping 15° E. CSZ surface trace and approximate location of fault plane at 10 km depth are shown (thick black lines). Positive and negative normal stress represent extension and compression, respectively. (b) Normal (blue), shear (green), and Coulomb stress (red) resolved onto the actual CSZ plane at 10 km depth with varying orientation (c) along its length.

friction in this region, $\mu_f = 0.4$ [Goldfinger *et al.*, 2008], makes the Coulomb stress perturbation at 10 km depth near the shoreline about -0.4 MPa inhibiting failure, smaller than at either the SAF or AFNZ and corresponding to a stress perturbation rate of -0.04 kPa/yr, much smaller than the tectonic loading rate. Because the fault zone straddles the coastline, the relative strengthening and weakening of different sections of the fault could possibly lead to a shift in the type of rupture on the CSZ. When sea level is high, the CSZ would preferably fail in deeper segments below the continent, whereas in times of low sea level, the CSZ would preferable rupture the shallower offshore portions of the fault zone.

2.3.4 Rapid sea level rise at the Black Sea

Thusfar we have considered stress perturbations from the steady and gradual increase of eustatic sea level since the LGM. There are, however, cases where water levels, either globally or locally, rose significantly faster than the global post-LGM average. In these instances, the more rapid loading may have had a greater impact on the seismic cycle of nearby faults. In particular, we consider the case of the inundation of the Black Sea, which may have impacted the seismic cycle of the nearby North Anatolian fault.

At the LGM, the connection between the Black Sea and the global ocean was blocked. The subsequent water level of the sea was isolated from eustatic sea level rise until the two reconnected sometime around 10 ka before present. The exact timing and mechanism of reconnection are the subject of ongoing research, but it is generally agreed that shortly before marine reconnection the level of the Black Sea was significantly low (~100 m). Following reconnection the water level rose ~70 m to the level of the global ocean within a few years to a few hundred years [e.g., *Chepalyga, 2007; Hiscott et al., 2007; Major et al., 2006; Ryan, 2007; Ryan et al., 1997*]. Either way, loading at the Black Sea happened at least an order of magnitude faster than in the global ocean. The strike-slip North Anatolian fault (NAF) lies within 100 km of the southern coast of the Black Sea and is well located to be affected by the rapid water level rise (Figure 2.7a).

When calculating stresses from a more rapidly increasing load, the time evolution of the stress response becomes dependent more on the viscous relaxation rate of the asthenosphere rather than on the loading rate. Initially we assume a thick elastic plate over a viscoelastic halfspace with a shear modulus of $\mu = 28$ GPa and a Maxwell relaxation time $\tau_m = 2\eta/\mu$ of 50 yr, corresponding to viscosity

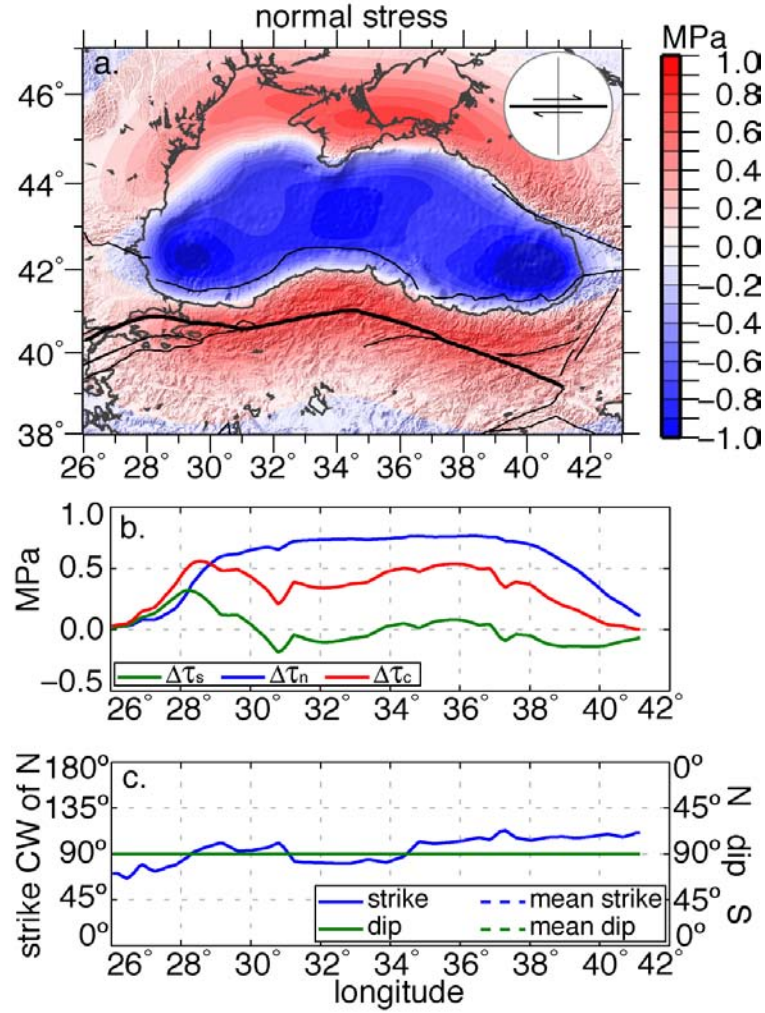


Figure 2.7 (a) North Anatolian region perturbation to normal stress following inundation of the Black Sea resolved on a vertical plane striking E - W. Actual NAF trace shown (thick black line). Positive and negative normal stress represent extension and compression, respectively. (b) Normal (blue), shear (green), and Coulomb stress (red) resolved onto the actual NAF plane with varying orientation (c) along its length.

$\eta = 2.2 \times 10^{19}$ Pa s. Full relaxation from the sudden Black Sea rise should be complete within five Maxwell times, or about 250 yrs, though eustatic sea level rise would continue to perturb stress at the NAF. Figure 2.7a shows the fully relaxed regional normal stress from 70 m of inundation calculated on a vertical plane striking East-West at 10 km depth within a 50 km thick elastic plate, and Figure 2.7b shows the normal, shear, and Coulomb stress perturbations along the NAF assuming a vertical plane with varying strike (Figure 2.7c). The change in normal stress along the NAF is positive with a maximum magnitude of 0.8 MPa. Along most of the NAF the shear stress contributions are relatively minor, so the maximum Coulomb stress perturbation is about 0.5 MPa promoting failure, assuming the coefficient of friction $\mu_f = 0.6$. Offshore, the stress perturbations have the opposite sign but an even larger magnitude.

When averaged over the full $5\tau_m$ relaxation time, this suggests an additional Coulomb stress rate of 2 kPa/yr, more than an order of magnitude greater than the eustatic perturbation rate. A viscoelastic material, however, will respond even more rapidly soon after the load is emplaced and will retard with time. The immediate elastic response to the Black Sea filling increases Coulomb stress along the NAF by about 75 kPa. There is also much uncertainty in the appropriate halfspace viscosity for this region. If η were larger, the rapid loading rate would be offset by the slower stress evolution, and the perturbation to Coulomb stress rate on the NAF would more resemble that of eustatic loading on the SAF. However if η were smaller by a factor of three, the Maxwell relaxation time would be reduced to about 17 years and the

Coulomb stress rate on the NAF would increase by an average 7.2 kPa/yr following inundation. This is about a quarter of the tectonic loading rate. If this were the case, it would certainly impact the seismic cycle, especially immediately after loading, bringing the NAF significantly closer to failure.

It is possible that soon after the Black Sea level rose all portions of the NAF would have ruptured, regardless of where they had been in their seismic cycle. This could have initiated fault behavior similar to that seen today in which temporally close large earthquakes rupture nearly the entire span of the NAF within about a century [e.g., *Hartleb et al.*, 2006]. Since the time of this water level rise, around 30 seismic cycles have elapsed, so the NAF synchronized rupture we see today is unlikely to be in continued response to the Black Sea increase. But if the paleoseismic record could be extended back to the time of the Black Sea filling, we should be able to clearly observe a marked difference in faulting behavior during the period after Black Sea level rise.

2.4 Discussion

The ultimate way to test these predictions would be to compare them to a set of paleoseismic data that spanned the last glacial cycle. The paleoseismic observations would need to show either specific ruptures or mean recurrence interval with enough temporal resolution to be able to distinguish between activity at the LGM, activity in the early Holocene, and activity in the late Holocene. If a record were long enough, we would expect to see, e.g., an increase in onshore transform fault activity since the LGM. Unfortunately, complete datasets spanning this interval are largely unavailable.

Some paleoseismic records at the SAF or NAF may go back a few thousand years [e.g., *Fumal et al.*, 2002; *Hartleb et al.*, 2006], but these are unable to yield any information about the effect of changing sea level because this is still after the global oceans reached modern levels. In the Dead Sea region, a long paleoseismic record showing some earthquake clustering exists for the late Pleistocene [*Marco et al.*, 1996], but no datasets span the time since the LGM. Recent paleoseismic studies at the Manteigas-Bragança fault in northern Portugal identified a cluster of events 14.5 – 11 ka [*Rockwell et al.*, 2009]. This sinistral fault lies 120 km inland and has a very low slip rate (< 1 mm/yr), and the increase in activity coincides with the most rapid sea level rise. As such, these ruptures may have been promoted by the extra extensional stress provided by bending in response to the seawater load.

Perhaps the most temporally consistent paleoseismic indicators come from some locations, such as at the CSZ, where a marine turbidite record may be used as a proxy for earthquake record [*Goldfinger et al.*, 2003]. Because these rely on offshore sediment cores, they tend to be more complete and extend further back than paleoseismic records from trenching. The record from offshore Cascadia extends 9 ka and it is tempting to look for an ocean loading signal in these data. In fact, *Goldfinger et al.* [2008; 2003] do calculate a different recurrence interval for the northern SAF and CSZ over the last 3ka ($\tau_r \sim 215$ yr) versus the last 9ka ($\tau_r \sim 260$ yr). If these differences were real, they would suggest that the seismic cycle at the northern SAF and CSZ sped up slightly as sea level rose, which would be consistent with our prediction that flexure in response to sea level rise promotes failure onshore. However these observations are not robust and the authors themselves caution against drawing

any conclusions about long-term fault behavior from this dataset. Future paleoseismic studies may be able to either extend existing records to the late Pleistocene, or further establish records on very low-slip faults, thus providing a record that could better test for the influence of sea level rise on plate boundary behavior. For the time being, however, the question of “was ocean loading important” remains unclear.

Instead we focus on the question “could ocean loading have been important”? There are two ways to interpret the calculated change in Coulomb stress. If faults are weak, i.e. they consistently slip when accumulated shear stress reaches a low threshold value (~ 10 MPa) [e.g., *Zoback et al.*, 1987], then either increasing or decreasing the normal stress on the fault by a megapascal or more through the process of ocean loading could be an important change that modulates fault behavior. As sea level rises and falls in response to the Milankovitch cycles, the normal stress on coastal faults will also vary cyclically, promoting onshore fault failure when ocean levels are high, inhibiting onshore fault failure when ocean levels are low, and vice versa for offshore faults. Indeed, if a record of plate boundary activity spanning the Pleistocene were available, we would expect cyclically enhanced and muted failure of coastal faults following the oscillating ocean loading. If, however, faults are very strong or fault strength has little consistency beyond a few seismic cycles, variations in stress accumulation rate may be more important, in which case the few pascals per year difference will probably not noticeably alter the seismic cycle at plate boundary faults.

In either case, because the ocean loading perturbation to normal stress is relatively uniform across the flexural bulge, we expect all the faults in a plate boundary region to experience roughly the same bending stress from ocean loading.

Any perturbation to the seismic cycle would be more evident on a secondary fault structure with a low tectonic loading rate than on the principal strand of the plate boundary. Thus in the San Andreas region, for example, we expect ocean loading to noticeably promote failure on the faults of the eastern California shear zone or the Los Angeles basin but to inhibit failure on the Garlock fault due to its orientation and sense of slip. It is also possible that coastal faults at passive continental margins could be influenced, or even reactivated, by ocean loading.

We can extend the analysis of the SAF, Alpine fault, and CSZ presented here to infer the effect of sea level rise in other regions. In general, we expect seismic activity to increase onshore and decrease offshore. Particularly, we expect muted activity in regions where the ocean load is narrow, such as in the fledgling rift zones or other narrow gulfs, and enhanced activity in regions where the ocean load surrounds a narrow strip of land, such as at the Italian peninsula, the islands of Japan, or the isthmus of Central America. This amplification of the ocean loading effect depends upon the features having a width comparable to half the flexural wavelength of the bending plate, and will therefore vary from region to region. At coastal subduction zones we might anticipate a cyclic shift between deep and shallow activity following the variations in sea level. This effect ought to be particularly noticeable on the islands of Japan, which both override a subducting plate and are loaded by changes in sea level on multiple sides.

The model calculations presented in this study are dependent upon the choice of some physical parameters. A thicker plate would result in more widespread stresses of smaller magnitude, and vice versa. A more or less viscous halfspace has

ramifications for the temporal importance of the loading rate relative to the relaxation rate, as discussed in the previous section. We have assumed a halfspace viscosity corresponds to a single relaxation time, regardless of the wavelength of the load. Such an assumption may be a simplification of the true physics involved in viscous relaxation, but it is appropriate in this case because the load primarily consists of a single wavelength, that of the flexural wavelength of the plate. We have also assumed the thick plate is a perfect elastic solid, corresponding to a Poisson's ratio of 0.25, but this number may be higher. We compared the model output for a Poisson's ratio of $\nu = 0.25$ and $\nu = 0.5$, corresponding to an incompressible elastic solid, and found that increasing the Poisson's ratio increases the magnitude of all the stresses by about twenty percent. Since the stress patterns produced also do not change, the overall effect of a variation in Poisson's ratio is small and would not alter the interpretation of the modeled stresses. The model presented here is particularly well suited for calculating stresses from relatively small, short-wavelength loads, such that a flat earth approximation is valid and the physical processes involved can be acceptably characterized as linear. As such, it would be inadequate for investigation of broader loads such as post-glacial rebound in the polar regions, where additional physics would be required.

There have also been certain simplifications of loading processes in that while focusing on the loading of water mass accumulated in the oceans, we have neglected any mass unloading caused by ice melting that happens over the same time period. While the large scale continental ice sheets may be far enough removed from most active plate boundaries to affect the ocean loading process, there may have been

considerable ice mass stored in mountain glaciers that existed in proximity to coastal plate boundaries. Had we included this additional source of onshore unloading, offshore compression and onshore extension would still be predicted for coastal regions, only the magnitude of onshore extension would increase by an amount related to the size and proximity of the glacier. In such a case, activity at onshore faults would be even greater at sea level highstands relative to the times of glacial maximum and an observable signal would be even more likely.

Another implication of this study is a reemphasis that a seismic cycle can be modulated by factors external to it. The consistent discrepancies in fault slip estimates from geologic and geodetic methods may be reconcilable as the various estimation methods evolve and improve. However, persistent discrepancies may reveal actual temporal variation in instantaneous slip rate [*Bennett, 2007*] and thus subtle details of the long-term faulting process, including the transfer of plate boundary slip between different active fault strands. Stress perturbations from sea level rise and their effect on seismic cycles could be significant enough that a geologic estimate of slip rate estimated over this time period would be expected to differ from a modern geodetic slip rate. At onshore transform boundaries such as the SAF, Alpine Fault, or NAF, we would generally expect $v_{\text{geologic}} < v_{\text{geodetic}}$. Again, this ocean loading-induced slip rate discrepancy would be more pronounced on low-slip secondary faults than on principal plate boundary strands. When trying to understand long-term fault system behavior, we find it may be at least as important to consider stresses external to the system as to consider subtle seismic cycle stresses internal to the system. Particularly we reemphasize the ability of climate systems to interact with tectonic systems.

2.5 Conclusions

We have investigated the theoretical role of eustatic sea level changes in modulating the seismic cycle at coastal plate boundary systems. Sea level rise induces bending about coastlines globally, reducing the magnitude of normal stress so as to “unclamp” onshore faults and promote failure while altering normal stress on offshore faults so as to inhibit failure. A nearshore transform fault will experience a 1 – 2 MPa change in normal stress over this time period, promoting failure onshore and inhibiting it offshore, corresponding to a change in Coulomb stress accumulation rate of ~ 100 Pa/yr. This rate is about 100 times smaller than the tectonic loading rate on major plate boundaries and will therefore not alter the stress buildup on a fault. However, the total magnitude of normal stress change may perceptibly weaken or strengthen coastal faults, particularly if the background fault strength is low and remains constant over many seismic cycles, thus altering the quantity of tectonically accumulated stress required for the fault to rupture.

For coastal transform faults, those onshore will be weaker during periods of high sea level (such as today) relative to periods of low sea level (such as during the LGM), corresponding to a more rapid seismic cycle. Offshore transform faults will be relatively stronger when sea level is high, with less activity relative to times of low sea level. It is possible that these non-tectonic influences on the seismic cycle could be detected at major plate boundary faults such as the SAF or AFNZ. However it is more likely that the influence of plate bending in response to ocean loading would be observable on secondary faults with a much lower tectonic loading rate. In locations

where sea level rise was much faster than the global average, such as in the catastrophic flooding of the Black Sea, the same normal stress perturbation of up to 1 MPa develops over a much shorter period of time, determined by the relaxation time of the asthenosphere. Following this event, the Coulomb stress accumulation rate on the onshore North Anatolian Fault increased by as much as 2 kPa/yr for a few hundred years. This rapid decrease in fault strength would likely have encouraged all segments of the NAF to rupture soon after the load was emplaced, though it is unlikely that this pattern of rupture would persist over tens of seismic cycles to be related to the synchronicity of NAF ruptures observed today.

2.6 Appendix

We calculate the full 3-D stress tensor from a vertical surface load on a thick elastic plate overlying a Maxwell viscoelastic halfspace. The model is semianalytic in that we convolve the response of a unit point load on a thick elastic plate overlying a viscoelastic halfspace with the true load distribution in the Fourier domain. It is this delta function response that we now further derive.

The 3-D problem is solved analytically in the vertical and time dimensions (z, t) while the solutions in the horizontal dimensions (x, y) are developed in the Fourier transform domain. This semianalytic method allows us to take full advantage of the convolution theorem and the numerical efficiency of the Fast Fourier Transform, while maintaining an arbitrarily complex surface load distribution. The disadvantage is that the rheology is restricted to stacked homogeneous layers.

The original solution of the Boussinesq problem [*Boussinesq*, 1885] was for vertical tractions on a homogeneous elastic halfspace. *Steketee* [1958] used this solution to balance the anomalous vertical tractions resulting from a force couple model. *Smith and Sandwell* [2004] followed these methods to develop a solution for vertical tractions on an elastic plate over a viscoelastic halfspace, again using the solution to correct anomalous vertical tractions resulting from a force couple model. *Luttrell et al.* [2007] adapted this Boussinesq-like vertical traction calculation to calculate displacement and stress in the lithosphere near the southern San Andreas fault in response to the time varying load of Ancient Lake Cahuilla.

We develop the solution in two parts (for further details of development and testing, see *Smith and Sandwell* [2004]). First, we derive the solution for displacement and stress in a layered elastic halfspace (homogeneous layer with Lamé parameters μ_1 and λ_1 over a homogeneous elastic halfspace with Lamé parameters μ_2 and λ_2). Second, we use the Correspondence Principle to simulate viscoelastic behavior in the lower halfspace by allowing the effective shear modulus μ_2 to vary with the time elapsed since loading t relative to the Maxwell time of the halfspace τ_m .

2.6.1 Normal traction on a layered elastic halfspace

Following the method of *Steketee* [1958], we let displacement and stress be a function of the Galerkin vector potential Γ_i ,

$$u_i = \Gamma_{i,kk} - \alpha \Gamma_{k,ki}, \quad (2.A1)$$

$$\tau_{ij} = \lambda(1 - \alpha)\delta_{ij}\Gamma_{l,kl} + \mu(\Gamma_{i,kkj} + \Gamma_{j,kki}) - 2\mu\alpha\Gamma_{k,kij}, \quad (2.A2)$$

where α is a constant yet to be determined and stress τ_{ij} has been related to strain and displacement u_i through an elastic constitutive equation with Lamé parameters λ and μ . Note that we use the standard summation notation, such that a variable with a single subscript is a vector, a variable with two subscripts is a tensor, a repeated index indicates summation over the spatial coordinates, and an index following a comma indicates differentiation with respect to that spatial coordinate. Because our point source is a purely normal traction on the free surface of a layered halfspace, it turns out that we need only retain the third component of the Galerkin vector, such that $\Gamma_x = \Gamma_y = 0$ and $\Gamma_z = \Gamma$, which we shall now call the Galerkin potential.

The equilibrium equations for a body in the absence of internal body forces or acceleration are $\tau_{ij,j} = 0$. When we write these as a function of Galerkin potential, we find that with a clever choice of $\alpha = (\lambda + \mu)/(\lambda + 2\mu)$, the Galerkin potential must satisfy the biharmonic equation $\nabla^4 \Gamma = 0$. After taking the 2-D horizontal Fourier transform of this equation, the solution form is recognized as

$$\Gamma(\mathbf{k}, z) = (A + Cz)e^{2\pi|\mathbf{k}|z} - (B + Dz)e^{-2\pi|\mathbf{k}|z}, \quad (2.A3)$$

where $|\mathbf{k}| = \sqrt{k_x^2 + k_y^2}$ is the horizontal wavenumber and (A, B, C, D) are coefficients to be determined by the boundary conditions. Our layered model consists of an elastic

layer of thickness h (z positive up) over an elastic halfspace, and the solution will require a Galerkin potential for each layer related to stress and displacement by the elastic moduli of that layer ($\Gamma_1, \mu_1, \lambda_1, \alpha_1$ in the upper layer, $\Gamma_2, \mu_2, \lambda_2, \alpha_2$ in the lower halfspace).

There are three boundary conditions that must be met for our layered elastic halfspace: (1) a normal traction $\tau_{applied}$ is applied at the free surface and is partially balanced by a gravitational restoring force, but shear tractions must be zero;

$$\begin{aligned}\tau_{zz1}\big|_{z=0} &= -\tau_{applied} + \rho_1 g W_1\big|_{z=0} \\ \tau_{xz1}\big|_{z=0} &= \tau_{yz1}\big|_{z=0} = 0\end{aligned}\tag{2.A4}$$

(2) all components of displacement and stress must be continuous across the boundary between the layer and the halfspace (note that we have shifted notation for displacement such that $u_x = U$, $u_y = V$, and $u_z = W$);

$$\begin{aligned}U_1\big|_{z=-h} &= U_2\big|_{z=-h} & \tau_{xz1}\big|_{z=-h} &= \tau_{xz2}\big|_{z=-h} \\ V_1\big|_{z=-h} &= V_2\big|_{z=-h} & \tau_{yz1}\big|_{z=-h} &= \tau_{yz2}\big|_{z=-h} \\ W_1\big|_{z=-h} &= W_2\big|_{z=-h} & \tau_{zz1}\big|_{z=-h} &= \tau_{zz2}\big|_{z=-h}\end{aligned}\tag{2.A5}$$

(3) at infinite depth, all stress and displacement components must go to zero.

$$\begin{aligned}
\tau_{xz2}\big|_{z \rightarrow \infty} &= \tau_{yz2}\big|_{z \rightarrow \infty} = \tau_{zz2}\big|_{z \rightarrow \infty} = 0 \\
U_2\big|_{z \rightarrow \infty} &= V_2\big|_{z \rightarrow \infty} = W_2\big|_{z \rightarrow \infty} = 0
\end{aligned}
\tag{2.A6}$$

The boundary conditions (2.A4-2.A6) can be rewritten in terms of the Galerkin potential (2.A1-2.A3) resulting in a set of equations with eight coefficients, (A_1, B_1, C_1, D_1) and (A_2, B_2, C_2, D_2) . The third boundary condition is solved by ensuring $B_2 = D_2 = 0$, so we are left finally with six coefficients $(A_1, B_1, C_1, D_1, A_2, C_2)$ and six equations

$$\begin{aligned}
\tau_{xz1}\big|_{z=0} &= 0 \\
\tau_{zz1}\big|_{z=0} &= -\tau_{\text{applied}} + \rho_1 g W_1\big|_{z=0}
\end{aligned}
\qquad
\begin{aligned}
U_1\big|_{z=-h} &= U_2\big|_{z=-h} \\
W_1\big|_{z=-h} &= W_2\big|_{z=-h} \\
\tau_{xz1}\big|_{z=-h} &= \tau_{xz2}\big|_{z=-h} \\
\tau_{zz1}\big|_{z=-h} &= \tau_{zz2}\big|_{z=-h}
\end{aligned}
\tag{2.A7}$$

(Note that there is some redundancy in the algebra because we are describing a solution with cylindrical symmetry in a Cartesian coordinate system). We algebraically solve this system of equations using the computer algebra capabilities of MATLAB (see *Smith and Sandwell* [2004, Appendix A] for the solutions to the coefficients $(A_1, B_1, C_1, D_1, A_2, C_2)$). MATLAB also delivers C-code for the rather complicated algebraic forms that can be directly used in computation, although the code does need to be modified to ensure that there are no growing exponential functions to cause numerical problems. We can then use Eq. (2.A1-2.A3) to calculate

stress and displacement as a function of k_x , k_y , z , and $\tau_{applied}(k_x, k_y)$, the Fourier transform of the applied load, and inverse Fourier transform to get numerical solutions for the stress and displacement components in the space domain.

Because the horizontal dimensions are solved in the Fourier domain, the horizontal boundary conditions require that stress and strain be periodic. We deal with this by tapering the edges of our flat earth grids to zero, thus ensuring periodicity in all directions. This means that we are restricted to examining features of interest of characteristic wavelength smaller than the length of the grid. For a typical regional grid of 2048x2048 elements at a grid spacing of 30 arcseconds (~ 1 km), this means we are limited to features with characteristic wavelength less than ~ 1000 km. This resolution is sufficient since we are focused on the coastline transitions along a specific segment of a plate boundary.

2.6.2 Including time dependence with a Maxwell viscoelastic model

A viscoelastic Maxwell body is made up of an elastic element and a viscous element connected in series. Its constitutive equation is

$$\dot{\epsilon} = \frac{1}{\mu} \dot{\sigma} + \frac{1}{\eta} \sigma, \quad (2.A8)$$

where σ and ϵ are stress and strain respectively, μ and η are the shear modulus and viscosity respectively, and the over dot indicates the time derivative. Making use of

the Correspondence Principle, we take the Laplace transform of (2.A8) (where s is the Laplace domain variable) and solve for stress

$$\sigma(s) = \frac{\mu s}{s + \frac{\mu}{\eta}} \varepsilon(s). \quad (2.A9)$$

If we let the effective shear modulus be

$$\mu_2(s) = \frac{\mu(s)s}{s + \frac{\mu}{\eta}}, \quad (2.A10)$$

we can then write

$$\sigma(s) = \mu_2(s) \varepsilon(s), \quad (2.A11)$$

which is in the same form as an elastic constitutive relation. Note that when we solve for an effective lower shear modulus μ_2 , we must also solve for an effective Lamé parameter λ_2 so that the bulk modulus of the halfspace remains constant.

We can analytically inverse Laplace transform (2.A10) and get

$$\mu_2(t) = \mu \left(\frac{e^{-\frac{t}{\tau_m}}}{2 - e^{-\frac{t}{\tau_m}}} \right), \quad (2.A12)$$

where we have assumed a single Maxwell relaxation time τ_m for the material regardless of the wavelength of the load, defined by

$$\tau_m = \frac{2\eta}{\mu}. \quad (2.A13)$$

So given a time since loading and a Maxwell relaxation time, we can compute the effective Lamé parameters of the lower halfspace and then use those in the layered elastic solutions for stress and displacement.

2.6.3 Model benchmarks

The end member cases of this model have been benchmarked against known solutions. The elastic half space end member should match the analytic displacement solutions of *Love* [1929], and the elastic plate over a fluid end member should approximate the numerical displacement and stress solutions for flexure of a thin elastic plate [*Turcotte and Schubert*, 2002]. The model has been found to be in good agreement with both sets of solutions [*Luttrell et al.*, 2007; *Smith and Sandwell*, 2004]. Additionally, we present here contours of the fully-relaxed stress components as a function of depth and distance perpendicular to a straight coastline, parallel to the

y-axis, that has been loaded on one side ($x < 0$) by 120 m of water (Figure 2.A1). All three components of normal stress are in compression underneath the load and in extension “onshore” in the top half of the plate, with stronger magnitudes near the

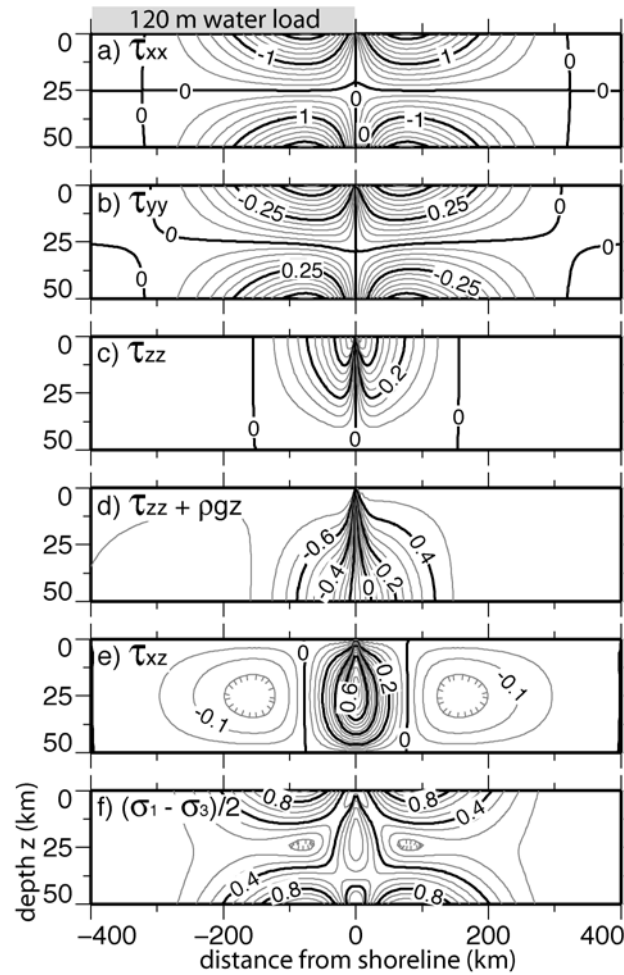


Figure 2.A1 Contours of stress components, in units of MPa, as a function of depth and distance perpendicular to a coastline that has been loaded on one side by 120 m of water and allowed to fully relax. Horizontal normal components of bending stress perpendicular to (a) and parallel to (b) shoreline. (c) Vertical normal component of bending stress. (d) Vertical normal component of bending stress plus stress from a buoyant mantle deflection. (e) Vertical shear stress component perpendicular to the shoreline (note the other two shear stress components τ_{xy} and τ_{yz} are negligible for a straight coastline oriented along the y-axis). (f) Maximum shear stress induced by bending stresses across the coastline.

surface, away from the nodal plane. The component of vertical shear stress perpendicular to the coastline is maximized in a narrow zone at the coastline and is stronger in the middle of the plate than at the surface. The maximum shear stress, $(\sigma_1 - \sigma_3)/2$, where σ_1 and σ_3 are the maximum and minimum principal stresses, reflects the patterns of the other stress components with high magnitudes near the surface offshore and onshore, and high magnitudes at depth at the coastline. When computed for an elliptical disc-shaped load of the same dimensions, these stress components match those published in *Ivins et al.* [2003], *Klemann and Wolf* [1998], and *Johnston et al.* [1998], though we note the vertical normal stress τ_{zz} of those models corresponds to the vertical normal stress of our bending model with an additional stress due to the buoyancy of the deflected mantle, $\tau_{zz} + \rho_m g W$.

2.7 Acknowledgements

We thank B. Bills, T. Rockwell, B. Smith-Konter, and B. Meade for their helpful conversations and feedback in the development of this manuscript. Thoughtful reviews by E. Ivins, K. Heki, and an Associate Editor greatly improved the manuscript. This research was supported by the NASA Earth and Space Science Fellowship Program and by the National Science Foundation (EAR 0811772).

Chapter 2, in full, is a reprint of the material as it appears in Luttrell, K., and D. Sandwell (2010), Ocean loading effects on stress at near shore plate boundary fault systems, *Journal of Geophysical Research*, 115, B08411, doi:10.1029/2009JB006541. The dissertation author was the primary investigator and author of this paper.

2.8 References

- Becker, J.J., D.T. Sandwell, W.H.F. Smith, J. Braud, B. Binder, J. Depner, D. Fabre, J. Factor, S. Ingalls, S.H. Kim, R. Ladner, K. Marks, S. Nelson, A. Pharaoh, R. Trimmer, J. Von Rosenberg, G. Wallace, and P. Weatherall (2009), Global Bathymetry and Elevation Data at 30 Arc Seconds Resolution: SRTM30_PLUS, *Marine Geodesy*, 32 (4), 355-371, doi: 10.1080/01490410903297766.
- Bennett, R.A. (2007), Instantaneous slip rates from geology and geodesy, *Geophysical Journal International*, 169 (1), 19-28, doi: 10.1111/j.1365-246X.2007.03331.x.
- Bennett, R.A., A.M. Friedrich, and K.P. Furlong (2004), Codependent histories of the San Andreas and San Jacinto fault zones from inversion of fault displacement rates, *Geology*, 32 (11), 961-964.
- Bettinelli, P., J.P. Avouac, M. Flouzat, L. Bollinger, G. Ramillien, S. Rajaure, and S. Sapkota (2008), Seasonal variations of seismicity and geodetic strain in the Himalaya induced by surface hydrology, *Earth and Planetary Science Letters*, 266 (3-4), 332-344, doi:10.1016/j.epsl.2007.11.021.
- Bollinger, L., F. Perrier, J.P. Avouac, S. Sapkota, U. Gautam, and D.R. Tiwari (2007), Seasonal modulation of seismicity in the Himalaya of Nepal, *Geophysical Research Letters*, 34 (L08304), doi:10.1029/2006GL029192.
- Boussinesq, J. (1885), *Application des Potentiels a l'Etude de l'Equilibre et du Mouvement des Solides Elastiques*, 508 pp., Gauthier-Viallars, Paris.
- Chepalyga, A. (2007), The Late Glacial Great Flood in the Ponto-Caspian Basin, in *The Black Sea Flood Question: Changes in Coastline, Climate, and Human Settlement*, edited by V. Yanko-Hombach, A. Gilbert, N. Panin, and P. Dolukhanov, pp. 63-88, Springer, Dordrecht, The Netherlands.
- Chery, J., and P. Vernant (2006), Lithospheric elasticity promotes episodic fault activity, *Earth Planet. Sci. Lett.*, 243 (1-2), 211-217.
- Demets, C., R.G. Gordon, D.F. Argus, and S. Stein (1990), Current Plate Motions, *Geophys. J. Int.*, 101 (2), 425-478.
- Demets, C., R.G. Gordon, D.F. Argus, and S. Stein (1994), Effect of Recent Revisions to the Geomagnetic Reversal Time-Scale on Estimates of Current Plate Motions, *Geophysical Research Letters*, 21 (20), 2191-2194.
- Dolan, J.F., D.D. Bowman, and C.G. Sammis (2007), Long-range and long-term fault interactions in Southern California, *Geology*, 35 (9), 855-858, doi: 10.1130/G23789A.1.

Fay, N.P., and E.D. Humphreys (2005), Fault slip rates, effects of elastic heterogeneity on geodetic data, and the strength of the lower crust in the Salton Trough region, southern California, *J. Geophys. Res.*, *110* (B09401).

Fluck, P., R.D. Hyndman, and K. Wang (1997), Three-dimensional dislocation model for great earthquakes of the Cascadia subduction zone, *Journal of Geophysical Research-Solid Earth*, *102* (B9), 20539-20550.

Fumal, T.E., M.J. Rymer, and G.G. Seitz (2002), Timing of large earthquakes since AD 800 on the Mission Creek strand of the San Andreas fault zone at Thousand Palms Oasis, near Palm Springs, California, *Bull. Seismol. Soc Am.*, *92* (7), 2841-2860.

Gahalaut, K., V.K. Gahalaut, and M.R. Pandey (2007), A new case of reservoir triggered seismicity: Govind Ballav Pant reservoir (Rihand dam), central India, *Tectonophysics*, *439* (1-4), 171-178, doi: 10.1016/j.tecto.2007.04.003.

Goldfinger, C., K. Grijalva, R. Burgmann, A.E. Morey, J.E. Johnson, C.H. Nelson, J. Gutierrez-Pastor, A. Ericsson, E. Karabanov, J.D. Chaytor, J. Patton, and E. Gracia (2008), Late Holocene rupture of the northern San Andreas fault and possible stress linkage to the Cascadia subduction zone, *Bulletin of the Seismological Society of America*, *98* (2), 861-889, doi: 10.1785/0120060411.

Goldfinger, C., C.H. Nelson, and J.E. Johnson (2003), Holocene earthquake records from the Cascadia subduction zone and northern San Andreas Fault based on precise dating of offshore turbidites, *Annu. Rev. Earth Planet. Sci.*, *31*, 555-577, doi: 10.1146/annurev.earth.31.100901.141246.

Grollimund, B., and M.D. Zoback (2000), Post glacial lithospheric flexure and induced stresses and pore pressure changes in the northern North Sea, *Tectonophysics*, *327* (1-2), 61-81.

Hampel, A., and R. Hetzel (2006), Response of normal faults to glacial-interglacial fluctuations of ice and water masses on Earth's surface, *J. Geophys. Res.*, *111* (B06406).

Hartleb, R.D., J.F. Dolan, O. Kozaci, H.S. Akyuz, and G.G. Seitz (2006), A 2500-yr-long paleoseismologic record of large, infrequent earthquakes on the North Anatolian fault at Cukurcimen, Turkey, *Geological Society of America Bulletin*, *118* (7-8), 823-840.

Heki, K. (2001), Seasonal modulation of interseismic strain buildup in northeastern Japan driven by snow loads, *Science*, *293* (5527), 89-92.

Heki, K. (2003), Snow load and seasonal variation of earthquake occurrence in Japan, *Earth Planet. Sci. Lett.*, *207* (1-4), 159-164.

Hetland, E.A., and B.H. Hager (2006), Interseismic strain accumulation: Spin-up, cycle invariance, and irregular rupture sequences, *Geochemistry Geophysics Geosystems*, 7.

Hetzel, R., and A. Hampel (2005), Slip rate variations on normal faults during glacial-interglacial changes in surface loads, *Nature*, 435 (7038), 81-84.

Hiscott, R., A. Aksu, P. Mudie, M. Kaminski, T. Abrajano, D. Yasar, and A. Rochon (2007), The Maramara Sea Gateway since ~16 ky BP: Non-catastrophic causes of Paleooceanographic Events in the Black Sea at 8.4 and 7.15 ky BP, in *The Black Sea Flood Question: Changes in Coastline, Climate, and Human Settlement*, edited by V. Yanko-Hombach, A. Gilbert, N. Panin, and P. Dolukhanov, pp. 63-88, Springer, Dordrecht, The Netherlands.

Howard, M., A. Nicol, J. Campbell, and J.R. Pettinga (2005), Holocene paleoearthquakes on the strike-slip Porters Pass Fault, Canterbury, New Zealand, *New Zealand Journal of Geology and Geophysics*, 48 (1), 59-74.

Ivins, E.R., R.K. Dokka, and R.G. Blom (2007), Post-glacial sediment load and subsidence in coastal Louisiana, *Geophysical Research Letters*, 34 (L16303), doi:10.1029/2007GL030003.

Ivins, E.R., T.S. James, and V. Klemann (2003), Glacial isostatic stress shadowing by the Antarctic ice sheet, *Journal of Geophysical Research-Solid Earth*, 108 (B12), 2560, doi:10.1029/2002JB002182.

James, T.S., J.J. Clague, K.L. Wang, and I. Hutchinson (2000), Postglacial rebound at the northern Cascadia subduction zone, *Quaternary Science Reviews*, 19 (14-15), 1527-1541.

Johnston, P., P. Wu, and K. Lambeck (1998), Dependence of horizontal stress magnitude on load dimension in glacial rebound models, *Geophys. J. Int.*, 132 (1), 41-60.

Kendall, R., J.X. Mitrovica, and R. Sabadini (2003), Lithospheric thickness inferred from Australian post-glacial sea-level change: The influence of a ductile crustal zone, *Geophysical Research Letters*, 30 (9), 1461, doi:10.1029/2003GL017022.

King, G.C.P., and M. Cocco (2001), Fault interaction by elastic stress changes: New clues from earthquake sequences, in *Advances in Geophysics*, Vol. 44, pp. 1-38.

King, G.C.P., R.S. Stein, and J. Lin (1994), Static Stress Changes and the Triggering of Earthquakes, *Bull. Seismol. Soc Am.*, 84 (3), 935-953.

Lambeck, K., and J. Chappell (2001), Sea level change through the last glacial cycle, *Science*, 292 (5517), 679-686.

Lambeck, K., T.M. Esat, and E.K. Potter (2002a), Links between climate and sea levels for the past three million years, *Nature*, *419* (6903), 199-206.

Lambeck, K., and A. Purcell (2005), Sea-level change in the Mediterranean Sea since the LGM: model predictions for tectonically stable areas, *Quaternary Science Reviews*, *24* (18-19), 1969-1988.

Lambeck, K., Y. Yokoyama, and T. Purcell (2002b), Into and out of the Last Glacial Maximum: sea-level change during Oxygen Isotope Stages 3 and 2, *Quaternary Science Reviews*, *21* (1-3), 343-360.

Love, A.E.H. (1929), The stress produced in a semi-infinite solid by pressure on part of the boundary, *Proc. Roy. Soc. Lond. A*, *228*, 377-420.

Luttrell, K., D. Sandwell, B. Smith-Konter, B. Bills, and Y. Bock (2007), Modulation of the earthquake cycle at the southern San Andreas fault by lake loading, *J. Geophys. Res.*, *112* (B08411), doi:10.1029/2006JB004752.

Major, C.O., S.L. Goldstein, W.B.F. Ryan, G. Lericolais, A.M. Piotrowski, and I. Hajdas (2006), The co-evolution of Black Sea level and composition through the last deglaciation and its paleoclimatic significance, *Quaternary Science Reviews*, *25* (17-18), 2031-2047.

Marco, S., M. Stein, A. Agnon, and H. Ron (1996), Long-term earthquake clustering: A 50,000-year paleoseismic record in the Dead Sea Graben, *J. Geophys. Res.*, *101* (B3), 6179-6191.

Massonnet, D., and K.L. Feigl (1998), Radar interferometry and its application to changes in the earth's surface, *Reviews of Geophysics*, *36* (4), 441-500.

Matmon, A., D.P. Schwartz, R. Finkel, S. Clemmens, and T. Hanks (2005), Dating offset fans along the Mojave section of the San Andreas fault using cosmogenic Al-26 and Be-10, *Geological Society of America Bulletin*, *117* (5-6), 795-807.

Norris, R.J., and A.F. Cooper (2001), Late Quaternary slip rates and slip partitioning on the Alpine Fault, New Zealand, *Journal of Structural Geology*, *23* (2-3), 507-520.

Oskin, M., L. Perg, D. Blumentritt, S. Mukhopadhyay, and A. Iriondo (2007), Slip rate of the Calico fault: Implications for geologic versus geodetic rate discrepancy in the Eastern California Shear Zone, *J. Geophys. Res.*, *112* (B03402).

Peltier, W.R. (2004), Global glacial isostasy and the surface of the ice-age earth: The ice-5G (VM2) model and grace, *Annu. Rev. Earth Planet. Sci.*, *32*, 111-149, doi: 10.1146/annurev.earth.32.082503.144359.

Peltier, W.R., and R. Drummond (2008), Rheological stratification of the lithosphere: A direct inference based upon the geodetically observed pattern of the glacial isostatic

adjustment of the North American continent, *Geophysical Research Letters*, 35 (L16314), doi:10.1029/2008GL034586.

Peltier, W.R., and R.G. Fairbanks (2006), Global glacial ice volume and Last Glacial Maximum duration from an extended Barbados sea level record, *Quaternary Science Reviews*, 25 (23-24), 3322-3337.

Robinson, R. (2004), Potential earthquake triggering in a complex fault network: the northern South Island, New Zealand, *Geophys. J. Int.*, 159 (2), 734-748, doi: 10.1111/j.1365-246X.2004.02446.x.

Rockwell, T., J. Fonseca, C. Madden, T. Dawson, L.A. Owen, S. Vilanova, and P. Figueiredo (2009), Paleoseismology of the Vilariça Segment of the Manteigas-Bragança Fault in Northeastern Portugal, in *Palaeoseismology: Historical and Prehistorical Records of Earthquake Ground Effects for Seismic Hazard Assessment*, edited by K. Reicherter, A.M. Michetti, and P.G. Silva, pp. 237-258, doi: 10.1144/SP316.15, The Geological Society of London, London.

Ryan, W.B.F. (2007), Status of the Black Sea Flood Hypothesis, in *The Black Sea Flood Question: Changes in Coastline, Climate, and Human Settlement*, edited by V. Yanko-Hombach, A. Gilbert, N. Panin, and P. Dolukhanov, pp. 63-88, Springer, Dordrecht, The Netherlands.

Ryan, W.B.F., W.C. Pitman, C.O. Major, K. Shimkus, V. Moskalenko, G.A. Jones, P. Dimitrov, N. Gorur, M. Sakinc, and H. Yuce (1997), An abrupt drowning of the Black Sea shelf, *Marine Geology*, 138 (1-2), 119-126.

Scheirer, D., G. Fuis, and V. Langenheim (2007), Constructing a Model of a Dipping Southern San Andreas Fault, Southern California, *Eos Trans. AGU*, 88(52), Fall Meet. Suppl.

Simpson, D.W., W.S. Leith, and C.H. Scholz (1988), Two Types of Reservoir-Induced Seismicity, *Bull. Seismol. Soc Am.*, 78 (6), 2025-2040.

Smith, B., and D. Sandwell (2003), Coulomb stress accumulation along the San Andreas Fault System, *J. Geophys. Res.*, 108 (B6), 2296.

Smith, B., and D. Sandwell (2004), A three-dimensional semianalytic viscoelastic model for time-dependent analyses of the earthquake cycle, *J. Geophys. Res.*, 109 (B12401), doi:10.1029/2004JB003185.

Steketee, J.A. (1958), On Volterra's dislocations in a semi-infinite elastic medium, *Can. J. Phys.*, 36, 192-205.

Turcotte, D.L., and G. Schubert (2002), *Geodynamics*, 456 pp., Cambridge Univ. Press, New York.

Wang, K., R. Wells, S. Mazzotti, R.D. Hyndman, and T. Sagiya (2003), A revised dislocation model of interseismic deformation of the Cascadia subduction zone, *J. Geophys. Res.*, *108* (B1), 2026, doi:10.1029/2001JB001227.

Zoback, M.D., M.L. Zoback, V.S. Mount, J. Suppe, J.P. Eaton, J.H. Healy, D. Oppenheimer, P. Reasenber, L. Jones, C.B. Raleigh, I.G. Wong, O. Scotti, and C. Wentworth (1987), New Evidence on the State of Stress of the San-Andreas Fault System, *Science*, *238* (4830), 1105-1111.

Chapter 3

Modulation of the earthquake cycle at the southern San Andreas fault by lake loading

Abstract

Changes in the level of Ancient Lake Cahuilla over the last 1500 years in the Salton Trough alter the state of stress by bending the lithosphere in response to the applied lake load and by varying the pore pressure magnitude within the crust. The recurrence interval of the lake is similar to the recurrence interval of rupture on the southern San Andreas and San Jacinto faults, both of which are partially covered by the lake at its highstand. Furthermore, four of the last five ruptures on the southern San Andreas fault have occurred near a time of substantial lake level change. We investigate the effect of Coulomb stress perturbations on local faults due to changing level of Lake Cahuilla to determine a possible role for the lake in affecting the timing of fault rupture. Coulomb stress is calculated with a 3-D model of an elastic plate overlying a viscoelastic half-space. Plate thickness and half-space relaxation time are adjusted to match observed vertical deformation since the last lake highstand. The lake cycle causes positive and negative Coulomb stress perturbations of 0.2 - 0.6 MPa on the southern San Andreas within the lake, and 0.1 - 0.2 MPa on the southern San Andreas outside the lake. These Coulomb stress perturbations are comparable to

stress magnitudes known to have triggered events at other faults along the North America-Pacific plate boundary.

3.1 Introduction

The San Andreas Fault system forms part of the boundary between the North American and Pacific plates, accommodating a total of about 40 mm/yr of right lateral slip [e.g., *Fay and Humphreys*, 2005]. The southern portion of the San Andreas Fault system lies in the Salton Trough, a broad region of Southern California that includes the southern San Andreas Fault (SAF), the southern San Jacinto Fault (SJF), the Imperial Fault (IF), and the Salton Sea. The Salton Trough is also a transitional tectonic regime between opening motion along a constructive plate margin in the Gulf of California and transform motion along the SAF system. This complex tectonic setting has the potential to produce large earthquakes, but the last 300 years have seen no major ruptures on the SAF and SJF, and only one major earthquake on the IF [*Fialko*, 2006; *Fumal et al.*, 2002; *Gurrola and Rockwell*, 1996; *Shifflett et al.*, 2002; *Thomas and Rockwell*, 1996].

The exact timing of a rupture on a fault is complicated and difficult to predict. However, the general readiness of a fault to fail can be characterized by the state of stress on that fault and changes to that stress, expressed through the Coulomb failure criteria [e.g., *King et al.*, 1994]. Non-tectonic perturbations to the state of stress on a fault may also alter the Coulomb stress, and thus the timing of the next event. In Japan, the changing vertical load of seasonally snow-covered mountains produces seasonal subsidence and seismicity [*Heki*, 2001; *Heki*, 2003]. On a much longer

timescale, flexure of the lithosphere beneath the Fennoscandian ice sheet in the North Sea has been proposed as a mechanism to modulate stresses, affecting faulting style and seismicity [*Grollmund and Zoback, 2000*]. Another non-tectonic source of stress perturbation, acting over intermediate timescales, is the vertical load caused by the filling and emptying of surface lakes.

In this study we wish to investigate the feasibility of stress perturbations at the Salton Trough in response to Ancient Lake Cahuilla influencing the timing of rupture on nearby faults. Numerous studies have used vertical surface deformation in response to lake loads to constrain subsurface rheology [e.g., *Bills et al., 2007; 1994; Kaufmann and Amelung, 2000*], but few have examined their effect on faulting. Other studies have shown that induced seismicity may occur in response to reservoir level changes, either by direct response of elastic stress following loading, or by delayed increase of pore pressure and decrease of effective normal stress [e.g., *Simpson et al., 1988*]. *Hetzel and Hampel [2005]* and *Hampel and Hetzel [2006]* examined lithospheric rebound in response to unloading in the Great Basin by the regression of Lake Bonneville and considered two mechanisms that affect the earthquake cycle. The direct removal of mass decreases vertical stress causing a decrease in slip rate on the normal Wasatch Fault. Lithospheric rebound following the removal of mass alters horizontal stress promoting a faster slip rate. They found the combination of these mechanisms explain a Late Pleistocene increase in slip rate on the Wasatch and adjacent normal faults. Both the temporal and spatial scales of lake change we consider in this study are between those of reservoirs and Lake Bonneville. As such,

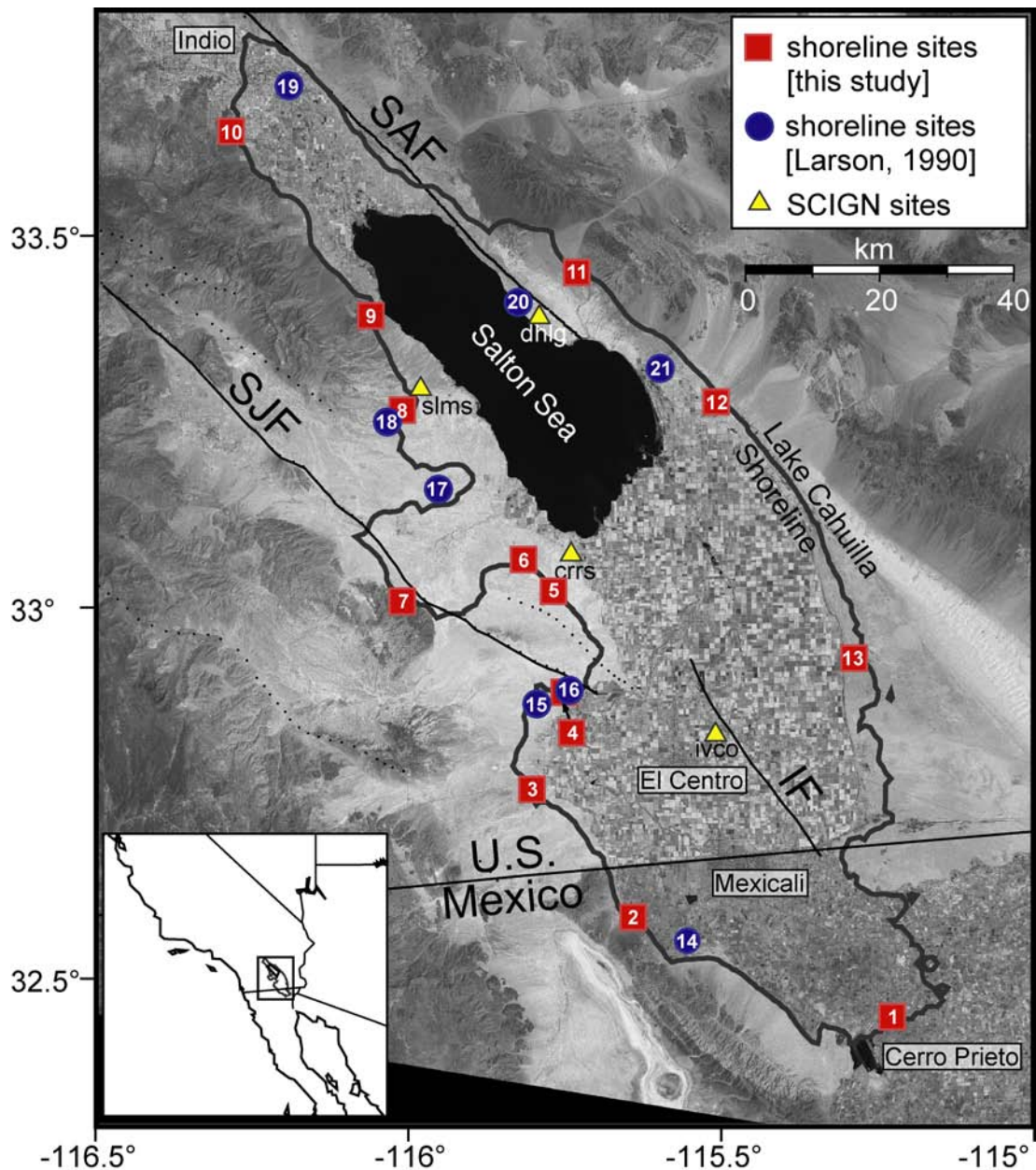


Figure 3.1 Ancient Lake Cahuilla region showing approximate location of the ancient shoreline (13 m above sea level), San Andreas Fault (SAF), San Jacinto Fault (SJF), and Imperial Fault (IF). Other local faults not mentioned in the text are shown as dotted lines for reference. Sites of shoreline elevation surveys from this study are shown as red squares. Sites from *Larson* [1990] are shown as blue circles. Site numbers correspond to Table 3.1. Locations of SCIGN continuous GPS stations within Ancient Lake Cahuilla are shown as yellow triangles (Table 3.2).

we consider both the effects of 3-D lithosphere deformation and of changes in pore pressure, but we consider only lithospheric rebound to be time-dependent.

3.1.1 Ancient Lake Cahuilla

Ancient Lake Cahuilla is a freshwater lake (180 km x 50 km) that has periodically formed when the Colorado River drained north into the Salton Trough region of southern California instead of along its current course South through northern Mexico into the Sea of Cortez. At times of its highstands at 13 m above sea level [Waters, 1983], Lake Cahuilla extended from present-day Indio, California in the north to Cerro Prieto, Baja California Norte, Mexico in the south (Figure 3.1) covering parts of the southern SAF, SJF, and IF to a maximum depth of 90 m.

The direction of flow of the Colorado River is controlled by the deposition of sediment at the river delta, which over time builds to form a natural dam. When enough sediment is deposited that the river is blocked from its southern course to the sea, flow turns northward into the Salton Trough and Lake Cahuilla forms quickly, filling in just 20 years to its maximum height of 13 m, controlled by the height of the sill at the southernmost edge [e.g., *Gurrola and Rockwell*, 1996; *Thomas and Rockwell*, 1996; *Waters*, 1983]. When in time the northern course becomes blocked by sediment, the Colorado resumes southern flow and the lake evaporates and becomes fully dry in approximately 60 years. The timing and duration of the last four lake highstands over the last 1300 years was studied by dating organic material from outcrop lake sediments and constraining these estimates to match the historical record (Figure 3.2) [*Gurrola and Rockwell*, 1996; *Sieh and Williams*, 1990; *Waters*, 1983].

Waters [1983] presents evidence for at least three clear highstands between the years AD 700 and 1500; furthermore *Gurrola and Rockwell* [1996] find three partial or total lakefall events between AD 1500 and 1700, represented in Figure 3.2 as a single falling event at the time the most recent lake began falling, between AD 1675 – 1687. While geologists do not yet agree on the timing and duration of even the most recent highstand, the changes in the volume of the lake are well constrained by the topography of the basin and the height of the sill. The most recent, though minor, change in lake level is the historically documented formation of the man-made Salton Sea in 1906, at a present-day elevation of 71 m below sea level [see *Oglesby*, 2005 and references therein].

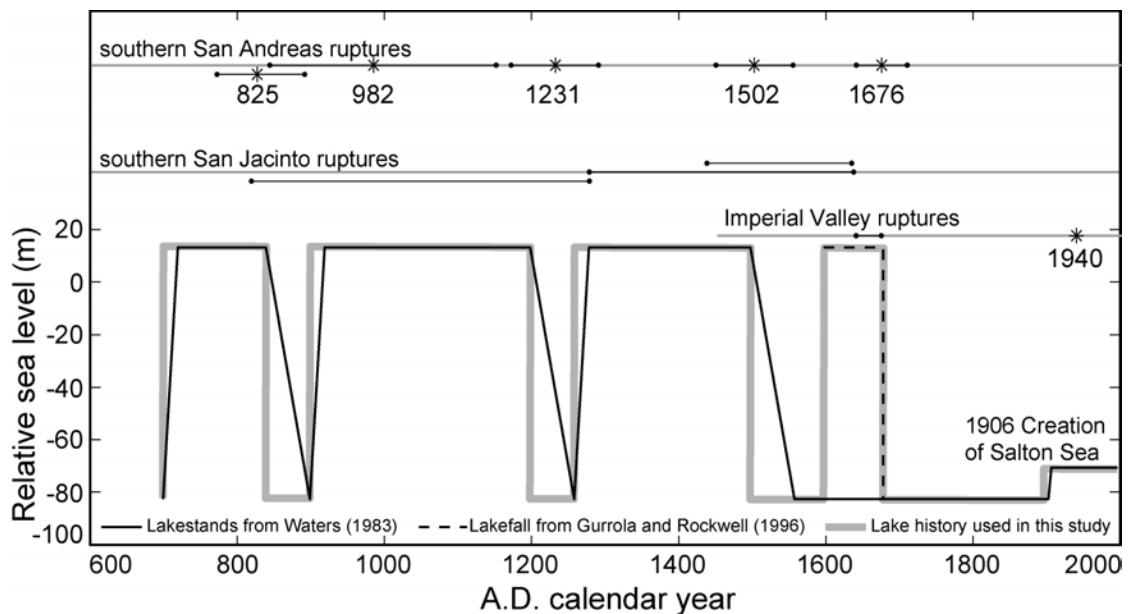


Figure 3.2 Lake level history from *Waters* [1983] (solid line) and *Gurrola and Rockwell* [1996] (dashed line), including the formation of the Salton Sea in 1906. The history used for models in this study is shown with a thick grey line. The last five southern SAF ruptures [*Fumal et al.*, 2002], last three southern SJF ruptures [*Gurrola and Rockwell*, 1996], and last two IF ruptures [*Thomas and Rockwell*, 1996] are also shown.

3.1.2 Salton Trough earthquakes

The recurrence interval of the filling and draining of Lake Cahuilla is similar to the recurrence interval of major ruptures on the Southern SAF of 260 ± 100 years [Shifflett *et al.*, 2002] and documented activity on the SJF [Gurrola and Rockwell, 1996] (Figure 3.2). The occurrence of five ruptures on the southern SAF have been estimated between AD 1641-1711, 1450-1555, 1170-1290, 840-1150, and 770-890 with best averaged estimates of 1676, 1502, 1231, 982, and 825 respectively [Fumal *et al.*, 2002; Sieh and Williams, 1990]. The identification of these events at multiple sites along the SAF suggests that each of these was a major event rupturing at least the southernmost 200 km of the SAF. The last three ruptures on the southern SJF occurred between 1440 and 1637, 1280 and 1440-1640, and 820 and 1280 [Gurrola and Rockwell, 1996]. The most recent event is known to have occurred just before the ~1480-1660 inundation of Lake Cahuilla (T. Rockwell, personal communication, 2006) (see Figure 3.2). None of these events were historically recorded; all have been inferred from paleoseismology. The most recent major event on the IF was the historically recorded 1940 Imperial Valley earthquake ($M_w = 7.0$). Prior to that, an event has been identified late within the last highstand of Lake Cahuilla. No other major slip events are observed in the available sediment record (since AD 1450) [Thomas and Rockwell, 1996].

The similar recurrence intervals between lake level changes and major earthquakes could be mere coincidence. However, it is possible that there is a physical connection between the two phenomena. One possibility is that vertical

motions associated with the major ruptures cause changes in the outflow direction of the Colorado River. In this case, the ruptures trigger the lake level changes. A second, more interesting possibility is that the change in stress due to the vertical load of the lake volume trigger the major events. It is the feasibility of this second possible connection that we explore in this study. If this model is correct, it could greatly impact our understanding of ruptures along the southern SAF system. In addition, one could calculate whether changing the configuration of the Salton Sea as proposed by the Salton Sea Authority (<http://www.saltonsea.ca.gov/>) would increase or decrease the probability of a major rupture on the southern SAF, which is believed to be late in the seismic cycle [Fialko, 2006].

3.2 Changes in normal stress due to lake level changes

Slip on the upper locked portion (2 – 12 km) of a transform fault may be triggered by a reduction in fault stability, commonly characterized by a change in Coulomb stress [e.g., *King and Cocco*, 2001; *King et al.*, 1994; *Reasenber and Simpson*, 1992],

$$\sigma_c = \sigma_s - \mu_f \sigma_n. \quad (3.1)$$

This includes both tectonic shear loading, in which deep slip gives rise to shear stress accumulation σ_s , and fault strength, equal to the coefficient of friction μ_f times the effective normal stress on the fault plane σ_n . We propose that changes in lake level

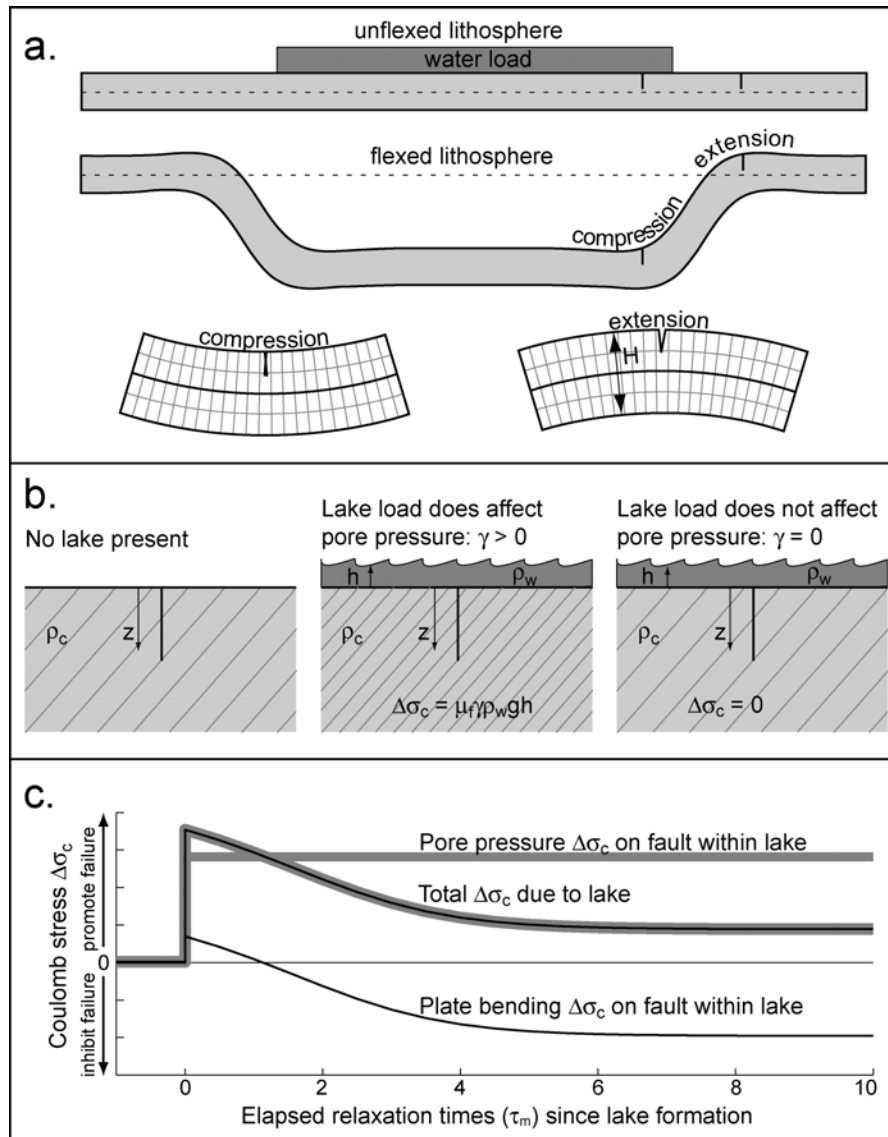
modulate the earthquake cycle by changing the effective normal stress on major fault planes at seismogenic depth. We consider two types of perturbation to normal stress: those induced solely from the weight of the surface load, and those induced because the load is a fluid that interacts with a porous crust.

3.2.1 Lithosphere bending model

Immediately after Lake Cahuilla fills, the Earth will respond to the weight of the surface load approximately as an elastic half-space. The spatial variations in the vertical load are defined by the lake depth, which is known from the topography of the Salton Trough. Convolving this load with the analytic flexure solution for the point response of an elastic half-space [*Love*, 1929] provides the exact displacement and stress. *Larson* [1990] calculated the displacement and stress due to changes in the level of Lake Cahuilla on an elastic half-space and found only small Coulomb stress changes at seismogenic depth (~ 10 kPa). Since this is 15 times smaller than shear stress associated with induced seismicity at other reservoirs, that study concluded that it is unlikely that this stress could trigger seismic activity. However, *Larson* [1990] also showed that the elastic half-space model provided a poor fit to the lake rebound data derived from present-day shoreline measurements. A thin elastic plate flexure model with an elastic thickness of about 40 km could better explain the shoreline rebound data.

Figure 3.3a is a diagram of the lithosphere response to a vertical load considered in this study. A lake load having width comparable to the flexural wavelength of the elastic plate is applied. Initially the Earth responds as an elastic

Figure 3.3 (a) Schematic representation of Coulomb stress variation by lithosphere flexure under a vertical load of lake water. Tick marks indicate faults inside and outside the lake boundary. In regions of compression, faults experience negative Coulomb stress perturbation, inhibiting failure. In regions of extension, faults experience positive Coulomb stress perturbation, promoting failure. (b) Schematic representation of Coulomb stress variation by change in pore pressure due to lake level change showing crust with pore pressure and no lake (left), crust with increased pore pressure in the presence of a lake (middle), and crust with unchanged pore pressure in the presence of a lake (right). An increase in lake level increases Coulomb stress, promoting failure. (c) Time evolution of Coulomb stress perturbation on a fault within the lake after a rise in lake level over ten half-space relaxation times (τ_m). Pore pressure (thick grey line) responds instantaneously by increasing Coulomb stress. Plate flexure (dashed black line) has a small elastic response (instantaneous) increasing Coulomb stress, followed by a viscoelastic response (time dependent) decreasing Coulomb stress by a magnitude on the order of the increase caused by changes in pore pressure. The combined effects (thick grey and black line) are most important within the first five relaxation times after a change in lake level.



half-space, but when the duration of the load exceeds the relaxation timescale of the asthenosphere, the plate bends. Consider a fault running parallel to the shoreline as shown in Figure 3.3a. At a seismogenic depth, for example 5 km, the downward flexing of the plate landward of the shoreline will cause extension (a decrease in normal stress), while the upward flexing of the plate within the lake will cause compression.

We can calculate the magnitude of a Coulomb stress perturbation from a change in water-level load by convolving the response of a unit point load on a thick elastic plate overlying a viscoelastic half-space with the true load distribution. We calculate the full 3-D problem semi-analytically using a method developed by *Smith and Sandwell* [2003; 2004]. For both the plate and the half-space, we assume a Young's modulus of 70 GPa, a Poisson's ratio of 0.25, and a mantle material density of 3300 kg m^{-3} . The free parameters that we vary are elastic plate thickness H , half-space Maxwell relaxation time ($\tau_m = 2\eta/\mu$ where η and μ are the viscosity and shear modulus, respectively), and vertical load history. In the case of vertical loading by changing levels of water, the load $\rho_w g h(x, y)$ is known exactly in both spatial extent and magnitude because the topography is exactly known.

We check the full 3-D model by considering a 2-D thin-elastic-plate approximation. The 3-D response should approximately match the thin elastic plate solution at infinite time and the elastic half-space solution at zero time. The vertical deflection $W(x)$ of a thin elastic plate of flexural rigidity D [N m] and flexural parameter α [m] in response to a step function vertical load of magnitude V_0 [N m²]

is found by integrating the line-load solution [Turcotte and Schubert, 2002, equation 3-130] from the shoreline ($x = 0$) to infinite distance into the lake. The result is

$$W(x) = \frac{V_0 \alpha^4}{8D} \left(1 - e^{-|x|/\alpha} \cos \frac{|x|}{\alpha} \right) \text{sign}(x), \quad (3.2)$$

where we have removed the mean deflection. The horizontal (normal) stress due to this load at a distance z_0 above the nodal plane is

$$\sigma_{xx} = \frac{3V_0 \alpha^2}{H^2} \left(\frac{z_0}{H} \right) e^{-|x|/\alpha} \sin \left(\frac{|x|}{\alpha} \right) \text{sign}(x). \quad (3.3)$$

Figure 3.4 compares the analytical thin-plate flexure solution (dashed curves) for stress and displacement with the numerically calculated thick-plate flexure solution (solid curves). Figure 3.4a shows the applied step load of magnitude equivalent to 1 m of mantle density material, such that we expect a vertical displacement of 1 m beneath the load. Both the vertical deflection (Figure 3.4c) and the horizontal stress (Figure 3.4d) are antisymmetric about the edge of the step load at $x = 0$. The thick-plate solution shows almost exactly the same behavior as the thin-plate solution. There is a minor difference at the coastline where the thick-plate solution shows an undulation due to local 3-D elastic stress effects. There is one major difference between the two solutions; the thin-plate solution has no horizontal displacement $U(x)$ (Figure 3.4b), while the thick-plate solution has a net negative motion near the coastline. The good

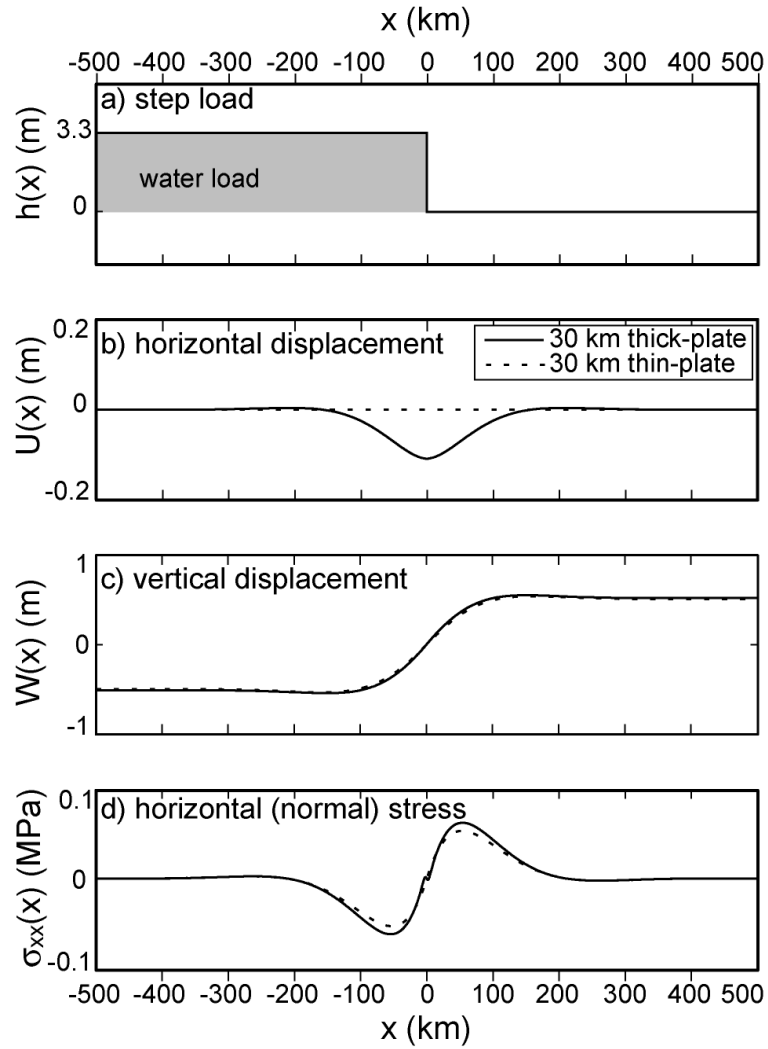


Figure 3.4 Displacement and stress of an elastic plate in response to a step water load. Solid line represents numerically calculated thick-plate flexure solution used throughout this study. Dashed line represents the analytic thin-plate flexure solution (Equations 3.1 and 3.2). Both solutions are calculated for a 30 km plate. Horizontal axis shows distance from edge of lake load. Vertical axis shows (a) applied water load, (b) horizontal surface displacement $U(x)$, (c) vertical surface displacement $W(x)$, and (d) horizontal (normal) stress $\sigma_{xx}(x)$ at seismogenic depth (5 km). The thin-plate flexure solution predicts no horizontal displacement. The thick-plate flexure solution shows an undulation in horizontal stress at the coastline due to local 3-D elastic stress effects.

overall match between these solutions for vertical displacement and horizontal stress suggests that the thin-plate solution is adequate. However, the thick-plate solution also includes a viscoelastic response to accurately model the loading history. Moreover, it can accurately accommodate realistic coastlines. Computations of both solutions require the same amount of computer time.

To provide a spatially accurate loading history, we use high-resolution (1 km) topography. Land elevations were derived from the Shuttle Radar Topography Mission data [<http://www2.jpl.nasa.gov/srtm/>] while elevations within the Salton Sea were derived by interpolating between digitized contours of bathymetry. The accurate topography accounts for the horizontal shifts in the coastline as lake level rises. Displacement and stress are computed at 1 km grid spacing and Coulomb stress is calculated on a vertical fault plane striking 45° West of North, the general trend of the SAF system.

3.2.2 Effect of pore pressure

With the addition or removal of a load of water on the crust, the loading material interacts with the loaded material creating additional stresses. The presence of water in a fault may, for example, affect the coefficient of friction μ_f by altering fault minerals. In our analysis, we assume a constant coefficient of friction, $\mu_f = 0.6$ [Byerlee, 1978]. The lake load may also alter the stress on a fault by changing the effective normal stress, illustrated in Figure 3.3b. The effective horizontal normal stress σ_n on a fault is the difference between the inward pressure (primarily

lithostatic) and the outward pore pressure due to the water-filled crust. If the lake level is increased by h and the water is free to percolate to seismogenic depth, then in time the pore pressure at that depth will increase by an amount $\Delta p = \rho_w g \Delta h$ to reach hydraulic equilibrium, where p is pore pressure, ρ_w is the water density (1000 kg m^{-3}), and g is the acceleration of gravity (9.8 m s^{-2}). This is equivalent to the “drained” pore pressure [e.g., *Roeloffs*, 1988a; *Roeloffs*, 1988b]. However, the system may not be able to reach equilibrium if, for example, the pore spaces in the crust are not fully connected to seismogenic depth. In this case, the change in normal stress due to lake rise is

$$\Delta \sigma_n = -\gamma \rho_w g h, \quad (3.4)$$

where $\gamma \in [0,1]$ is a dimensionless parameter describing the ability of pore fluids to percolate at depth ($\gamma = 0$ for no fluid movement to depth, $\gamma = 1$ for hydrostatic pore pressure change at depth). The maximum magnitude of the direct Coulomb stress change is $\Delta \sigma_c = \mu_f \rho_w g h$. For the 90 m of lake level change associated with Lake Cahuilla and pore pressure fully able to penetrate to seismogenic depths ($\gamma = 1$), the increase in Coulomb stress will be 500 kPa.

Though we use the equilibrated change in pore pressure, we assume that the time required for the crust to reach this equilibrium is much less than the timescale of lithospheric rebound. Thus we treat changes in pore pressure at depth as concurrent with lake level changes. This simplifies the problem to one relaxation time rather than

two. Under this assumption, the predicted rate of change of Coulomb stress at a time of lake level change is an upper bound, as is the magnitude of Coulomb stress perturbation. Another simplifying assumption we make is to neglect lateral flow of pore fluids, such that beneath the lake, change in pore pressure is directly proportional to the change in water level directly above, and outside the lake there is no change in pore pressure. Including lateral flow would make the spatial pattern of predicted stress change more diffuse across lake shorelines.

3.2.3 Total effect of lake change on Coulomb stress

Both the direct pore pressure and indirect plate bending effects should be considered when calculating the change in Coulomb stress induced by Lake Cahuilla. It is interesting to note that the spatial and temporal variations in stress at seismogenic depth will be rather complex functions. If the fault is beneath the lake, the pore-pressure effect will cause a step-increase in Coulomb stress, but this will decay to near zero after several viscoelastic relaxation times because of downward flexure of the plate (Figure 3.3c). A fault far from the lake that is not influenced by the direct hydrostatic effect will experience only the indirect effect of increasing Coulomb stress as the plate bends. A fault running between the high and low shorelines will experience a complicated time variation in stress because the shoreline changes position by up to 100 km as the lake fills. At seismogenic depth, Coulomb stress change due to plate bending is about equal in magnitude and opposite in sign to Coulomb stress change due to an increase in pore pressure.

3.3 Deformation and rebound: finding a best-fitting model

To constrain the model parameters of plate thickness (H) and relaxation time (τ_m), we measured the vertical rebound of the Lake Cahuilla area since the last lake fall by measuring the current elevation of observed ancient shoreline features (see Appendix). The ancient shoreline elevation data collected from our survey are shown in Table 3.1a, along with data published in *Larson* [1990] (Table 3.1b). Data in Table 3.1a were collected with a GPS receiver measuring height above the reference ellipsoid (WGS84) and corrected to height above sea level with the GEOID03 model [<http://www.ngs.noaa.gov/GEOID/GEOID03/>]. The ellipsoidal heights were estimated by 1 Hz instantaneous positioning [*Bock et al.*, 2000] of the field GPS receiver relative to the known geodetic coordinates of California Real Time Network (CRTN – <http://sopac.ucsd.edu/projects/realtime/>) sites. Data in Table 3.1b from

Table 3.1a Location and elevation (relative to GEOID03) of Lake Cahuilla shoreline sites measured in this study.

Number in Figure 3.1	Location	Latitude	Longitude	Elevation \pm Error (m)
1	Cerro Prieto	32.448	-115.223	10.323 ± 0.299
2	Mexicali	32.582	-115.642	11.486 ± 0.387
3	Yuha Basin	32.753	-115.798	13.205 ± 0.083
4	Dry Wash	32.887	-115.745	12.862 ± 0.084
5	Superstition Hills	33.023	-115.766	11.773 ± 0.178
6	Elmore Ranch	33.063	-115.814	16.754 ± 0.391
7	Fish Creek Mountains	33.009	-116.006	12.079 ± 0.060
8	Salton City	33.266	-116.006	13.877 ± 0.379
9	Travertine Rock	33.391	-116.058	12.331 ± 0.146
10	La Quinta	33.637	-116.280	11.788 ± 0.056
11	Salt Creek Fan	33.452	-115.729	13.845 ± 0.047
12	Gas Line Road	33.277	-115.499	12.416 ± 0.086
13	Southeast Sand Bar	32.932	-115.285	11.841 ± 0.459

Larson [1990] were collected by leveling to known benchmarks that denote height above sea level. We find that the two approaches agree very well, and that the largest uncertainty in the shoreline height measurement is related to identification of the shoreline marker. (See Appendix).

We computed models of the vertical rebound due to lake loading for a plate thickness between 10 and 100 km and a half-space relaxation time between 20 yrs and 200 yrs (corresponding to half-space viscosity $\eta = \mu\tau_m / 2$ of $10^{19} - 10^{20}$ Pa s, given a shear modulus $\mu = 28$ GPa). For each of these possible models, we compared the values of deformation expected at each of the 21 sites from Table 3.1 with the observed elevations above sea level. We can only detect the pattern and relative amplitude of the deformation; we cannot calculate the absolute elevation, thus our model has three free parameters: the plate thickness, the relaxation time, and an absolute vertical offset between the model-predicted and observed elevations.

We computed the sum of squared residuals, where z_{mi} and z_{oi} are the modeled and observed elevations at each point, ε_i is the error of each observed measurement,

Table 3.1b Location and elevation of Lake Cahuilla shoreline sites from *Larson* [1990].

Number in Figure 3.1	Description	Latitude	Longitude	Elevation \pm Error (m)
14	A	32.55	-115.55	12.2 ± 0.1
15	C	32.87	-115.79	12.7 ± 0.1
16	F	32.89	-115.74	12.8 ± 0.1
17	D	33.16	-115.95	12.7 ± 0.1
18	G	33.25	-116.03	13.1 ± 0.1
19	B	33.70	-116.19	12.2 ± 0.1
20	H	33.41	-115.82	13.8 ± 0.1
21	E	33.32	-115.60	12.7 ± 0.1

and N is the total number of points (21),

$$\chi^2 = \frac{1}{N} \sum_{i=1}^N \frac{(z_{mi} - z_{oi})^2}{\varepsilon_i}, \quad (3.5)$$

and found no single best-fitting model (Figure 3.5a). Contours of misfit as a function of (H, τ_m) reveal a trade-off between plate thickness and relaxation time (i.e., half-space viscosity). A thinner plate can fit the data well with a more viscous half-space, while a thicker plate requires a less viscous half-space to fit the data equally well. Figure 3.5b shows the field-observed elevations from Table (3.1a) and (3.1b) (diamonds and squares, respectively) along with their error bars plotted against the expected present-day model-predicted elevation for two equally best-fitting models, $(H = 20 \text{ km}, \tau_m = 90 \text{ yr})$ and $(H = 35 \text{ km}, \tau_m = 30 \text{ yr})$ (blue and red, respectively).

It is possible to further constrain the model (H, τ_m) pairs by examining the vertical velocity that each predicts for today. For long relaxation times (thin plates), we expect that the Salton Trough would still be experiencing significant rebound from the last lake highstand, however this constraint depends heavily on the timing of the last lake fall. We identified four continuous GPS receivers from the Southern California Integrated GPS Network (SCIGN) [Hudnut *et al.*, 2002] that are well within the bounds of Lake Cahuilla and would experience near-maximum uplift since the last lake fall (see Figure 3.1). Table 3.2a gives the locations and current vertical velocities of these sites (<http://sopac.ucsd.edu/cgi-bin/refinedJavaTimeSeries.cgi>). We also

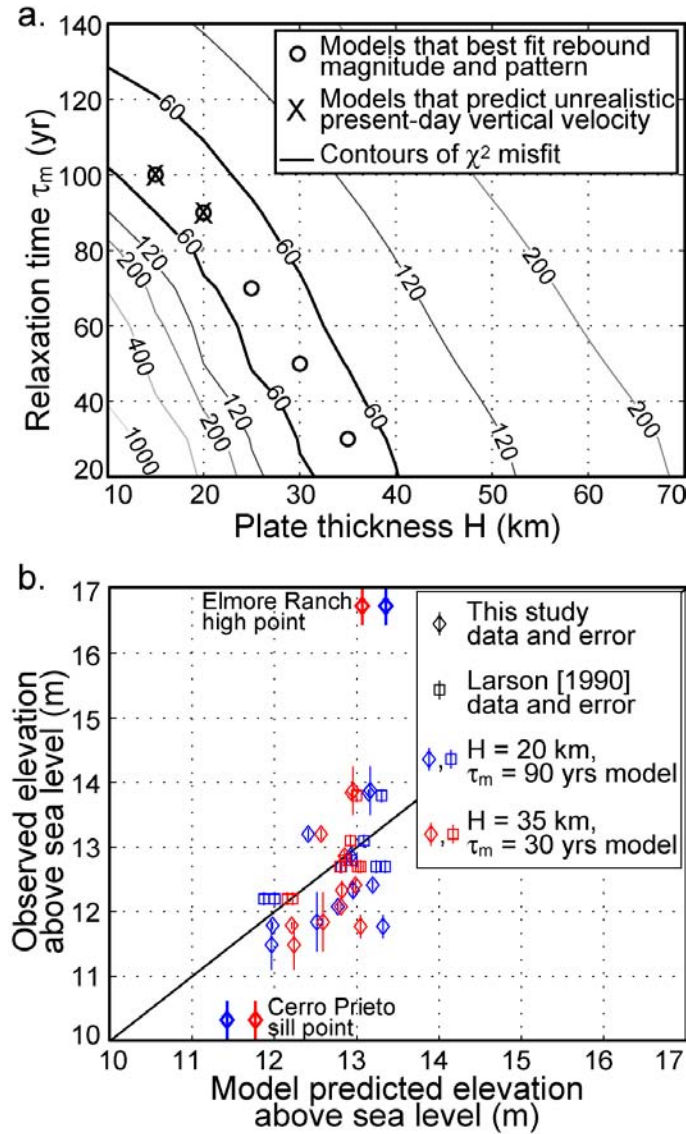


Figure 3.5 (a) Contours of χ^2 misfit for models with different (H, τ_m) values. Circles show (H, τ_m) pairs that fit the observed elevation data equally well. X's show (H, τ_m) pairs that predict vertical velocity today much higher than the observed velocity. (b) Predicted vs. observed shoreline elevation at points given in Table 3.1. Observed elevation and error bars from this study (diamonds) and *Larson* [1990] (squares) is plotted on the vertical axis. Horizontal axis represents predicted elevation at each site calculated for two models with an equally low χ^2 value: a thinner plate ($H = 20$ km) with a more viscous half-space ($\tau_m = 90$ yr) (blue), and a thicker plate ($H = 35$ km) with a less viscous half-space ($\tau_m = 30$ yr) (red). Diagonal black line shows a perfect fit between observed and predicted elevation.

Table 3.2a Location and present-day vertical velocity observed at four SCIGN sites.

SCIGN site	dhlg	slms	crrs	ivco
Latitude	33.390	33.292	33.070	32.829
Longitude	-115.788	-115.978	-115.735	-115.507
Observed velocity (mm/yr)	-1.7	-1.3	-1.8	-3.1

calculate the vertical velocity that each best-fitting (H, τ_m) model pair predicts today at each SCIGN site (Table 3.2b). The predominant vertical signal in this region is subsidence from the Salton Trough opening. Knowing the magnitude of Salton Trough subsidence, both expected from modeling (maximum -4 mm/yr, [Smith and Sandwell, 2003]) and observed from geodesy (~ -1 mm/yr, Table 3.2a), we determine that if the lake area were rebounding at anything more than a rate of 5 mm/yr, we would be able to observe the rebound at these four SCIGN sites. Hence all models that predict vertical uplift greater than 5 mm/yr at these points can be discounted (Figure 3.5a). This leaves us with two (H, τ_m) pairs to consider as model end members: $(H = 25 \text{ km}, \tau_m = 70 \text{ yr})$ and $(H = 35 \text{ km}, \tau_m = 30 \text{ yr})$. It is important to note that other non-tectonic signals, for example a subsidence signal due to groundwater pumping for agriculture, could mask the rebound signal. However a groundwater signal would be more localized than the broad rebound deformation signal, so if such a signal had large enough amplitude to mask significant rebound, we would not expect agreement at the four SCIGN sites. We are therefore confident that no significant lake rebound is occurring today in the Salton Trough.

Around the lake, low rebound is expected at the far south and north and high rebound is expected in the east and west, closest to the deepest part of the lake (the

Table 3.2b Present-day vertical velocity predicted at four SCIGN sites by five best-fitting model (H, τ_m) pairs.

Model (H, τ_m)	Predicted velocity at SCIGN site (mm/yr)			
	dhlg	slms	crrs	ivco
$H = 15 \text{ km}, \tau_m = 100 \text{ yr}^a$	15.6	14.8	16.2	10.8
$H = 20 \text{ km}, \tau_m = 90 \text{ yr}^a$	10.7	10.3	11.1	8.1
$H = 25 \text{ km}, \tau_m = 70 \text{ yr}$	5.2	5.1	5.4	4.2
$H = 30 \text{ km}, \tau_m = 50 \text{ yr}$	1.1	1.1	1.1	0.9
$H = 35 \text{ km}, \tau_m = 30 \text{ yr}$	0.02	0.02	0.02	0.02

^a Models predicting uplift greater than 5 mm/yr (untenable)

current Salton Sea). The lowest point is the sill site at Cerro Prieto, shown in bold in Figure 3.5b. This is the single most important site because its elevation essentially sets the magnitude of the entire modeled rebound. It also has the second largest misfit, and no model we consider is able to fit both this point and the points closer to the present day Salton Sea. Our estimation of the sill elevation is consistent with other estimates [e.g., *Oglesby*, 2005], and the next lowest point at Mexicali (40 km northwest) is also lower than the models predict. It is possible that a geothermal plant near Cerro Prieto is causing local subsidence and making the measured sill height anomalously low. However the observation that both Cerro Prieto and Mexicali are low suggests a plate of uniform thickness may not be appropriate in the spreading region. The bulk of the data do not support the magnitude of rebound suggested by the sill point.

The point with the worst misfit is the highest at Elmore Ranch. We do expect a large amount of rebound here because of its close proximity to the deepest part of the lake load, but there are other points at which equally high rebound is expected that

have a much lower elevation and smaller misfit (e.g. Superstition Hills, Salton City, Larson points 17, 20, and 21). This leads us to believe that either 1) the feature we measured at this point was not created by the most recent Lake Cahuilla highstand, 2) there are other tectonic sources of deformation at this location (e.g., interaction with an unmapped fault), or 3) we did measure the correct features but plate inhomogeneities (e.g., variable thickness, dike upwellings, cracks in the plate) are making this area rebound more than predicted. The effect of excluding the two furthest outlying points from our fit would be that the data would prefer a slightly thicker plate over a slightly more viscous half-space. The effect on the level of Coulomb stress perturbation on the SAF would be very small (e.g., 0.1 MPa difference).

3.4 Stress at Lake Cahuilla

Before we consider fault stress perturbations due to real loading history, it is instructive to examine the response to a single lake cycle. Figure 3.6a shows the pattern of Coulomb stress for a vertical fault plane parallel to the SAF, due to the rise of the lake at time $t = 0\tau_m$ and the fall of the lake at $t = 10\tau_m$ for a plate thickness $H = 30$ km at 5 km depth. Figure 3.6b shows the Coulomb stress perturbation predicted at Bombay Beach, CA at the southern end of the SAF and within the boundaries of Lake Cahuilla, likely subject to pore pressure changes. Figure 3.6c shows Coulomb stress perturbation at Indio, CA, further north along the SAF and outside the shoreline of Lake Cahuilla, beyond the region affected by pore pressure

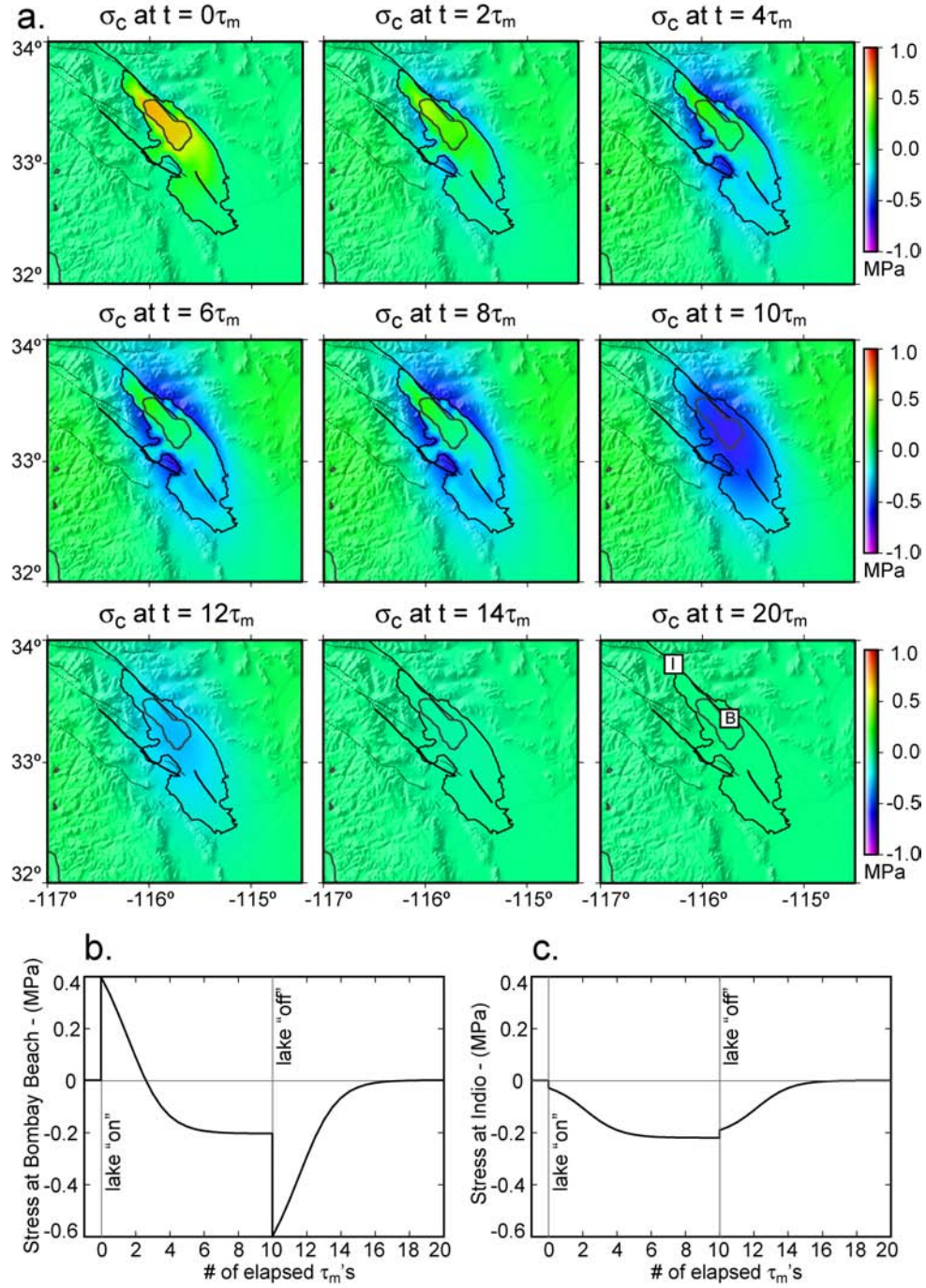


Figure 3.6 (a) Coulomb stress perturbations due to a single cycle of lake formation and desiccation. The lake fills at $0\tau_m$, remains full, and falls at $10\tau_m$. Negative Coulomb stress decreases the likeliness of rupture. Locations of Bombay Beach, CA (B) and Indio, CA (I) on the SAF are also shown. (b) Perturbation of Coulomb stress at Bombay Beach, within Lake Cahuilla. (c) Perturbation of Coulomb stress at Indio, outside of Lake Cahuilla.

variations. (Location of Bombay Beach (B) and Indio (I) is shown in the last frame of Figure 3.6a.) At $0\tau_m$, the pore pressure effect proportional to the depth of the lake is the dominant signal. By $2\tau_m$ much of the pore pressure effect has been negated by the bending of the lithosphere. The plate bending response is fully relaxed by $6\tau_m$. At $10\tau_m$, the lake load is removed and the Coulomb stress within the lake drops significantly, however outside of the lake, the Coulomb stress increases slightly due to the elastic response of the lithosphere. By $16\tau_m$ the lithosphere is fully relaxed again. As part of our analysis, we considered the difference in stress between treating lake changes as instantaneous and treating them as gradual, as suggested by *Waters* [1983] (Figure 3.2). We found the difference in total Coulomb stress perturbation is small, but the difference in Coulomb stress rate is more significant. Fluid effects rather than rebound effects dominate the early stress behavior after a lake level change, so neglecting time-dependent lake level change affects stress in essentially the same way as neglecting time-dependent pore pressure response, a scenario previously discussed (see Section 3.2).

We calculate Coulomb stress perturbation due to the lake history shown in Figure 3.2, between A.D. 700 – 2000. Figure 3.7a shows Coulomb stress at Bombay Beach for a lithosphere with hydrostatic pore pressure ($\gamma = 1$) for end member models ($H = 25$ km, $\tau_m = 70$ yr, blue) and ($H = 35$ km, $\tau_m = 30$ yr, red). Over this period, perturbations of $\pm 0.4 - 0.6$ MPa are expected. Figure 3.7b shows Coulomb stress at Bombay Beach without the effect of pore pressure ($\gamma = 0$). The perturbations in Coulomb stress are, in general, smaller and less sudden. Figure 3.7c shows Coulomb

stress at Indio, outside of the Lake Cahuilla shoreline and away from the effects of pore pressure. The perturbation magnitude is much smaller (0.2 MPa) due to

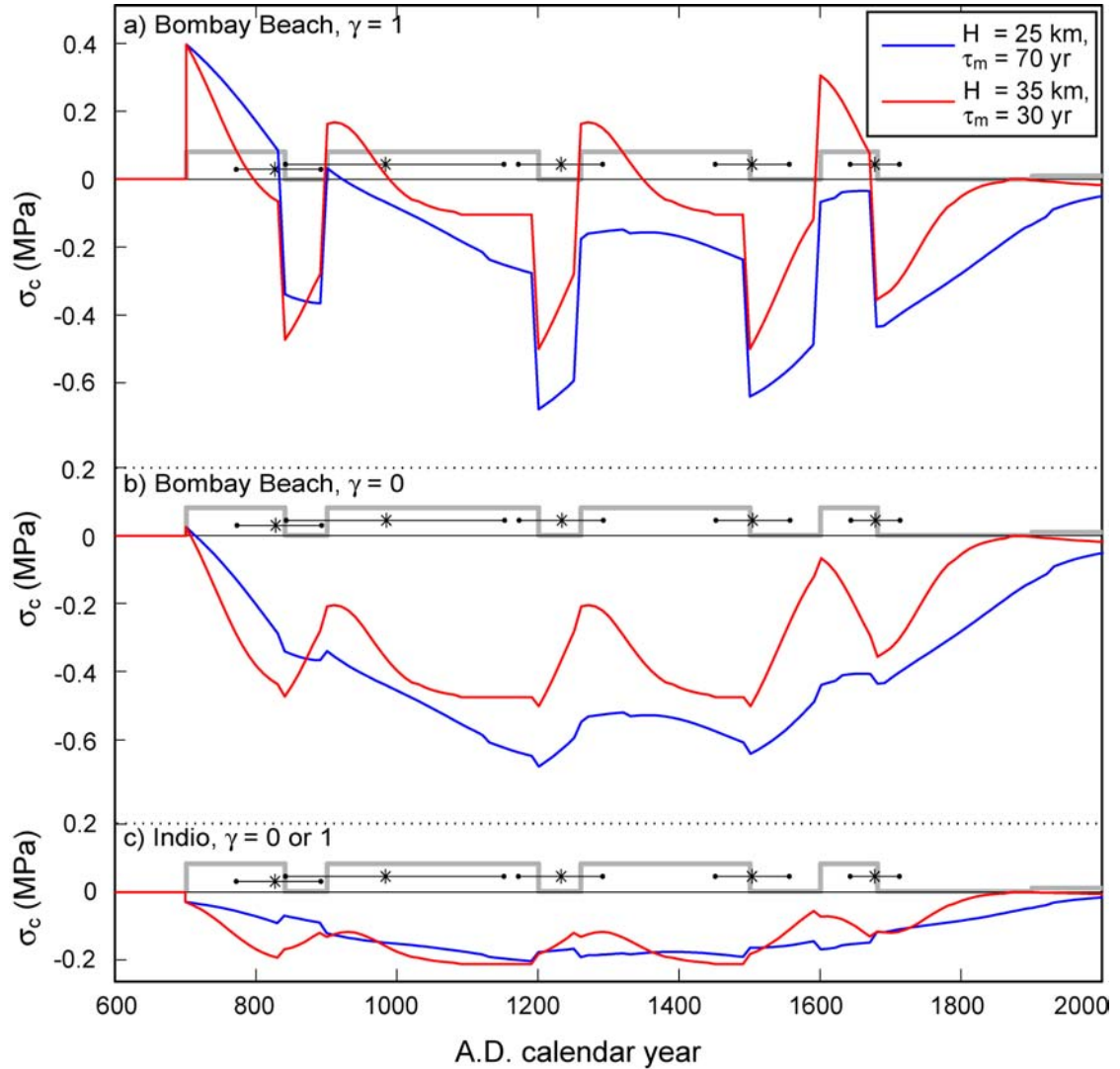


Figure 3.7 Coulomb stress perturbation from AD 700 - 2000 at (a) Bombay Beach within the lake with full pore pressure effect ($\gamma = 1$), (b) Bombay Beach with no pore pressure effect ($\gamma = 0$), and (c) and Indio outside of the lake with no pore pressure effect. Blue and red lines show stress from models with ($H = 25$ km, $\tau_m = 70$ yr), and ($H = 35$ km, $\tau_m = 30$ yr), respectively. Thick grey line shows timing of the lake level changes and black stars show timing and error of the last five Southern SAF ruptures (see Figure 3.2).

increased distance from the deepest load.

Figure 3.8a shows the regional difference in Coulomb stress from Lake Cahuilla (not including tectonic stress) between the most recent two southern SAF ruptures (1502 and 1676) calculated for ($H = 25$ km, $\tau_m = 70$ yr). During this time, the entire Lake Cahuilla region experiences an increase in modeled Coulomb stress.

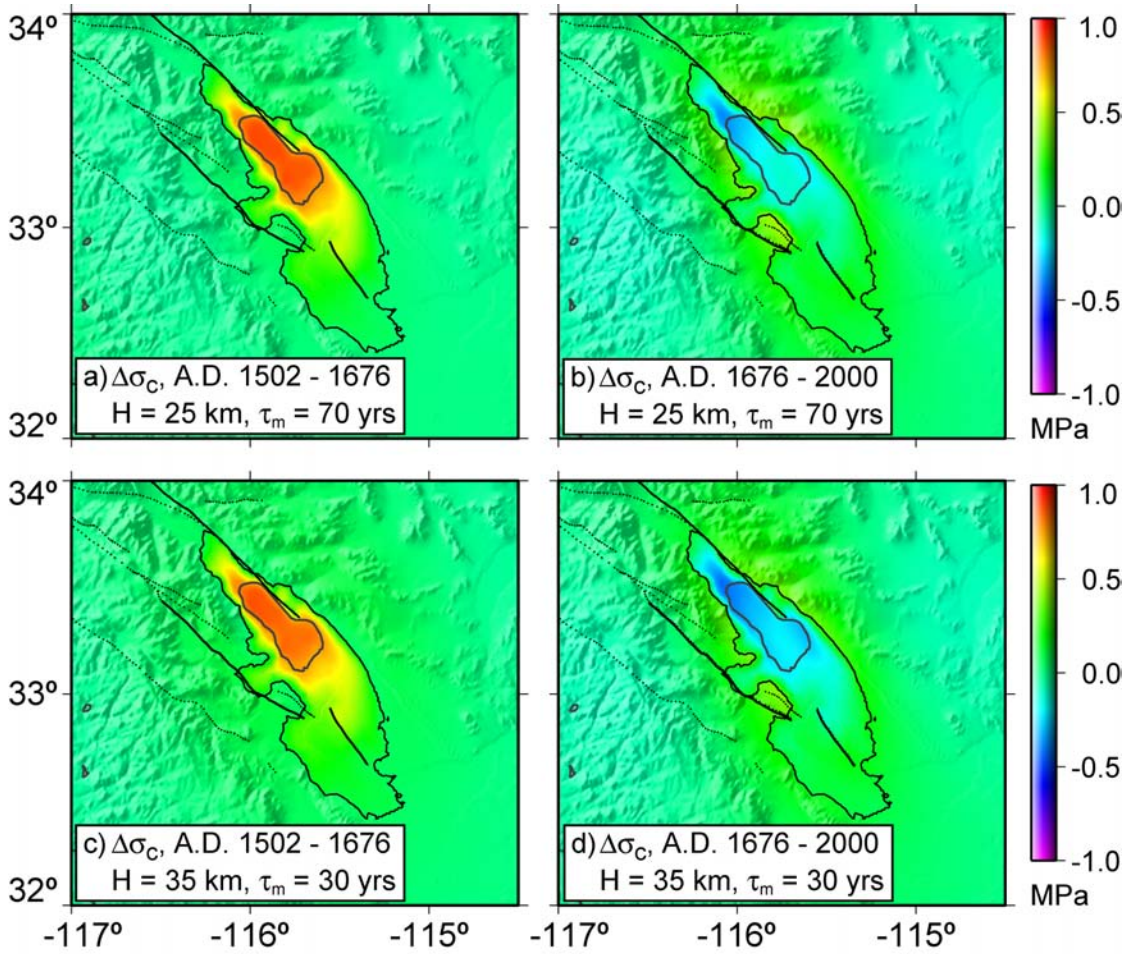


Figure 3.8 Coulomb stress perturbation in MPa between the last two Southern SAF ruptures (a and c) and since the most recent rupture (b and d) for two plausible model (H, τ_m) pairs: ($H = 25$ km, $\tau_m = 70$ yr, a and b), and ($H = 35$ km, $\tau_m = 30$ yr, c and d). Positive Coulomb stress perturbation promotes failure, negative inhibits failure.

Coulomb stress at Bombay Beach on the SAF increases by 0.2 – 0.6 MPa depending on the effect of pore pressure. The SJF and IF experience smaller stress increases of 0.2 - 0.4 MPa. Figure 3.8b shows the stress perturbation since the last rupture. Within the lake, stress decreases due to the pore pressure effect. Around the lakeshore, particularly at the SJF, stress increases. Figures 3.8c and 3.8d show Coulomb stress perturbation between the last two ruptures and since the most recent rupture calculated for ($H = 35$ km, $\tau_m = 30$ yr). The main differences between the two model predictions are 1) the magnitudes tend to be higher for the shorter relaxation time, and 2) the plate deformation effect is broader for the thicker plate.

3.5 Discussion of Lake Cahuilla stress relevance

The magnitude of Coulomb stress perturbation due to the changes in the level of Lake Cahuilla is, as expected, about 10 times smaller than tectonic loading that occurs between major earthquakes. It is, however, of comparable size to other effects that have been suggested to enact triggering. The postseismic deformation following the 1992 Landers earthquake, for example, led to Coulomb stress changes of 0.1 - 0.2 MPa in the vicinity of the 1999 Hector Mine earthquake, contributing to its failure [Freed and Lin, 2001]. Stress perturbation following lake level changes is certainly large enough to contribute to the stress budget on a given fault, but it is likely to only make an observable difference to faults that are critically stressed from tectonic loading (late in the seismic cycle).

We would expect events to be triggered at times of increasing Coulomb stress following great tectonic loading (~ 1 recurrence interval since the last event). This could happen either: 1) shortly after lake level rise, due to an increase in pore pressure, or 2) in the time after a lake fall, due to fault-normal extension. Conversely, during times of low or falling Coulomb stress, we expect periods of quiescence. Four of the last five events are near times of lake level change, however it is difficult to draw firm conclusions about a physical connection due to the large error bars in both lake history and timing of paleo-events.

Better constraints are needed for both fault slip history and lake level history to determine if lake loading has been important in the real history of Salton Trough seismicity. For ruptures that occur near times of lake level change, knowing whether the rupture happened before, during, or after lake transition is key to understanding a possible causal relationship. In addition, knowing the date of a paleo-event (either seismic or lake related) to within one half-space relaxation time and understanding which lake falls were complete or partial will help refine the influence of lithospheric bending. We also expect that perturbations in Coulomb stress would trigger higher quantities of smaller events ($M < 5$) in addition to affecting the timing of very large events ($M > 7$). If the paleo-activity level were known with certainty, it would be an additional source of information to evaluate the lake loading effect.

There has recently been much discussion in the literature about the need to reconcile fault slip rates interpreted from geologic measurements with those interpreted from geodetic ones [see *Bennett et al.*, 2004; *Matmon et al.*, 2005, and references therein]. There are two timescales that affect the earthquake cycle: the

earthquake recurrence interval, which may be tens to thousands of years, and the Maxwell relaxation time, which may be tens to hundreds of years. Any perturbation of the earthquake cycle over longer geologic time periods requires another physical mechanism beyond those considered part of the earthquake cycle. It is over these longer timescales that fault slip rates along the San Andreas system seem to vary. Mechanisms that have been proposed to reconcile slip rate discrepancies include: transfer of slip rate between the SAF and the SJF [*Bennett et al.*, 2004], use of a more realistic rheology and rupture history [*Hetland and Hager*, 2006], higher geologic slip rate by finding more paleo-slip on faults [*Oskin et al.*, 2007], actual variations in slip rate caused by variations in fault strength and loading rate [*Chery and Vernant*, 2006], and actual variation in slip rate by changing normal stress in response to a vertical load [*Hampel and Hetzel*, 2006; *Hetzel and Hampel*, 2005]. The results of this study suggest that slip rate may in fact vary over timescales greater than or equal to the recurrence interval. Our hypothesis that lake loads modulate the earthquake cycle is a tenable explanation rooted in well-understood physics, and could be extended to include other vertical loads on a broader spatial scale such as the differential load of rising sea level on a plate boundary.

An interesting result of this analysis is the implications it suggests to the current Salton Sea. To control salinity and water elevation at the Salton Sea, a mid-lake dam has been proposed by the Salton Sea Authority to isolate the northern and southern portions of the lake, just north of Bombay Beach, which would involve some drawdown of lake level. Figure 3.9 shows the Coulomb stress perturbation today due to the 1906 formation of the Salton Sea, including the effect of pore pressure. The

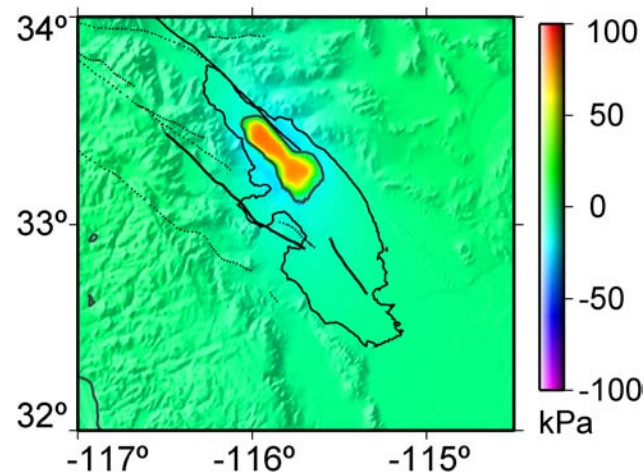


Figure 3.9 Coulomb stress response in kPa since formation of the Salton Sea in 1906. Maximum perturbation amplitude is ~ 90 kPa.

highest stresses of 0.1 MPa are within the lake itself. This model, with ($H = 35$ km, $\tau_m = 30$ yr), predicts only a slight decrease in Coulomb stress around the margins of the lake. While the stresses associated with the Salton Sea are smaller than those associated with Ancient Lake Cahuilla, our analysis suggests the possible seismic impact of sudden changes in lake level should be considered in addition to the hazards of a dam nearby a major active fault.

This analysis makes two simplifying assumptions about pore pressure resulting from lake level change. First, it assumes that pore fluids can move vertically but not horizontally. Including horizontal flow would make the effect of pore pressure more diffuse, decreasing its influence within the lake and increasing its influence outside the lake boundary. Second, we assume that the changes in pore pressure occur instantaneously at all depths along a fault. Percolation of pore fluids is likely to be a time dependent diffusive process. The error incurred by neglecting this time

dependence will depend on its relation to the time dependence of lithospheric relaxation. If the fluid-flow relaxation time is much shorter than subsurface relaxation time from this load, then instantaneous fluid flow is a reasonable simplification. If the fluid-flow timescale is comparable to or longer than that of subsurface relaxation, then their combined Coulomb stress perturbation magnitude may be smaller by up to an order of magnitude.

Modeling lithospheric bending with an elastic plate over a viscoelastic half-space is certainly a simplification of real subsurface rheology. This model does not include variations in viscosity as the geotherm increases with depth or variations in plate thickness expected in a complex tectonic region. Investigations at Lake Bonneville [*Bills et al.*, 1994] and Lake Lahontan [*Bills et al.*, 2007], 900 km to the northeast, inverted rebound data for viscosity and layer thickness of 7 – 10 layers and observed distinct upper crust, lower crust, and upper mantle viscosities (10^{24} Pa s, 10^{18-19} Pa s, and 10^{20-18} Pa s respectively). However the rebound signal at those lakes is 10s of m, more than an order of magnitude larger than the signal at Lake Cahuilla where rebound data are best fit by a 25 – 35 km plate over a halfspace of viscosity 10^{19} Pa s. Investigations of deformation following the 1938 filling of Lake Meade, 300 km to the north-northeast, found the 0.2 m pattern of subsidence could be fit equally well by a two-layer model (30 km elastic crust over viscoelastic half-space with viscosity 10^{18} Pa s) and a three-layer model (10 km elastic upper crust and a 20 km viscoelastic lower crust with viscosity $> 10^{20}$ Pa s over a viscoelastic half-space with viscosity 10^{18} Pa s) [*Kaufmann and Amelung*, 2000]. Increasing model complexity to include 10 viscoelastic layers minimally affected the fit to rebound data. The results of these

studies suggest that while Lake Cahuilla rebound data are likely insufficient for detailed analysis of subsurface rheology, they are satisfactory for estimating first-order rheologic parameters for the purpose of calculating bending stresses.

3.6 Conclusion

We have explored the possibility of stress changes due to changes in pore pressure and isostatic rebound in response to the transient existence of Lake Cahuilla affecting the earthquake cycle on nearby faults by hastening or delaying rupture. Over the last 1300 years of lake rise and fall, Coulomb stress on the southern SAF has been perturbed 0.2 – 0.6 MPa within the lake and 0.1 – 0.2 MPa outside the lake. This stress perturbation is an order of magnitude smaller than Coulomb stress associated with tectonic loading. Therefore, lake perturbations are likely to modulate the earthquake cycle only when faults are near critically stressed. Though the similarity in recurrence interval for the southern SAF and the filling/falling of Lake Cahuilla is intriguing and the lake-related mechanisms of stress perturbation are non-trivial, firm conclusions cannot be made without better constraints on the paleo history for the Salton Trough region.

3.7 Appendix

3.7.1 Geological field studies

The following are descriptions of the field studies carried out between January 2006 and January 2007 around the Ancient Lake Cahuilla shoreline. Sites were

identified and features measured using a variety of techniques, each described here along with their respective sources and magnitudes of error.

We made extensive use of a dual-frequency GPS receiver (Ashtech Z-12) sampling at 1 Hz to estimate precise ellipsoid heights of a number of site locations relative to the known geodetic coordinates of California Real Time Network (CRTN) sites, where coverage was available (<http://sopac.ucsd.edu/projects/realtime/>). In other locations we set up temporary 1 Hz base stations. Using the Geodetics RTD software in post-processing mode, we estimated receiver coordinates by instantaneous positioning, as described by *Bock et al.* [2000], of about 15-60 minutes of 1 Hz data collected at each field site. In this approach, each epoch of 1 Hz GPS observations of field receiver and CRTN site(s) are analyzed independently to estimate a series of 3-D geodetic coordinates, which are then averaged using robust statistics. Ellipsoid heights are converted to elevations (geoid/orthometric heights) using the GEOID03 model [<http://www.ngs.noaa.gov/GEOID/GEOID03/>].

3.7.1.1 Surveys of tufa-covered cliffs

Along the western side of Lake Cahuilla there are several locations where the lake was bounded by high cliffs at the edge of the Fish Creek and Santa Rosa Mountains. During lake highstand, tufa deposits (layers of CaCO_3 deposited in warm freshwater in the presence of blue-green algae [e.g., *Nelson et al.*, 2005; *Oglesby*, 2005]) form along the cliffs at and below the waterline. These watermarks exist today and are easily recognized as the line between the dark outer deposit growth and the bare rock underneath. We measured this at three sites (Fish Creek Mountains,

Travertine Rock, and La Quinta). In some sections, there were two tufa substances on the rocks: 1) an older, more friable beige layer that covered the rocks to a higher level, and 2) a more recent sturdy black layer that covered the beige layer up to a height of a few feet below the height of the beige layer. The beige layer may represent a previous highstand at a different level, or perhaps deposits from early in the lake highstand from before it subsided. For this study, we measured the height of the sturdy black layer of tufa. Though regionally the tufa line is quite flat, at close range there is some variation in its height depending on, for example, erosion since deposition, degree of shelter, and local wave energy. Since we were looking for the highest stand of the lake, we measured the height of the highest tufa within each 10-ft section.

The heights were determined by using a leveling scope to sight to a particular feature to determine its height above the nearby GPS receiver. The processed GPS height is relative to the WGS84 reference ellipsoid and has an error of less than 5 mm. At each point, the height of the feature relative to the receiver was added to the GPS height above WGS84 and the GEOID03 correction to determine feature height above sea level. For each site, a single elevation was determined as the median of the local maximum measurements and the error is half the interquartile range.

3.7.1.2 Survey at Gas Line Road

Aerial photos of the Gas Line Road site show distinct color changes parallel to the expected shoreline location reoccurring periodically westward (toward the Salton Sea). We surveyed the highest (most eastward) color change visible in the aerial

photos and found a mostly-flat region with small (1 - 2 m) hills. We observed a regional delineation in the appearance of surface rocks, parallel to the 13-m National Elevation Data Set (NED) contour (approximate expected location of the Lake Cahuilla shoreline). Toward the Salton Sea, surface rocks were well-rounded, grey in color, and had a typical size of a few inches. Away from the Salton Sea, surface rocks were jagged, pink in color, and of the same typical size. We interpreted the well-rounded rocks as having spent much more time in water compared to the jagged rocks, and we interpreted the transition point between rounded and jagged rocks as the highest point where Lake Cahuilla waters were able to round the stones existing on its shore. A few hundred meters to the north, the color change visible in aerial photos no longer marks a transition between two types of rocks. Rather, it marks a transition between well-rounded, grey-colored pebbles and hard-packed sand with no pebbles on the surface. We measured the height of these features by taking GPS measurements at three locations along a 700 m stretch of shoreline and using a leveling scope to sight horizontally from the GPS stations to 10 other points exactly on the edge of the shoreline feature.

3.7.1.3 Stationary surveys of constructional berms

Constructional sand berms are formed around lake edges by deposition of sediment carried by currents within a lake [e.g., *Adams et al.*, 1999; *Currey*, 1982]. Their crest is at or near the elevation of the lake. At four sites (Mexicali, Dry Wash, Elmore Ranch, and Salt Creek Fan) we identified the sand berms at the shoreline from their lighter color in aerial photography and LANDSAT images. In the field, we

measured the elevation of the berm crest, away from vehicle tracks and other human demolition of the feature. The actual survey was conducted in the same manner as the Gas Line Road survey, sighting from a feature to a stationary GPS receiver with a leveling scope. Post analysis, we found the error involved with knowing the elevation of the berm crest is tolerably small (< 0.1 m). The biggest problem with these sites is constraining the relationship between berm crest elevation today and water level at the time of lake highstand (see below).

3.7.1.4 Mobile surveys of constructional berms

At four sites (Yuha Basin, Superstition Hills, Salton City, and Southeast Sandbar) sand berms were identified in the same manner as the stationary survey sites (see above) but were measured in a different way. In an attempt to expedite the survey, we mounted a GPS receiver sampling at 1 Hz on a low stable rolling platform that could be pulled by hand along and across the crest of a berm, ideally yielding many more data points, all at the desired elevation over a much shorter time. Post analysis however, we found that in a linear mobile survey, the desired elevation signal is somewhat masked by coexistent and unrelated dips and bumps in topography which would be easily avoided in a static survey. Thus the potential advantage of more data was nullified by the noise in that data, leading to larger errors (0.1 – 0.5 m) in elevation measurements at these sites. As with the stationary berm surveys, this error does not include the difficulty in constraining the relationship between berm crest elevation today and water level at the time of lake highstand (see below).

3.7.1.5 Cerro Prieto

The sill point at the southern end of Lake Cahuilla is the single most important point for establishing the magnitude of vertical rebound. To establish its location and elevation, we first examined contours of Shuttle Radar Topography Mission (SRTM) and National Elevation Data Set (NED) topography. While the NED 13-m contour closes south of Mexicali, Mexico, the SRTM 13-m contour is open between Lake Cahuilla and the Sea of Cortez. According to SRTM topography (3 minute resolution), Lake Cahuilla is only isolated from the Sea of Cortez at elevations at or below 10.0 ± 0.299 m by a narrow 2 km wide strip of land east of Cerro Prieto volcano. NED likely has considerable errors outside of the US so we used remotely-derived SRTM for our analysis. However, the SRTM may have broad errors in elevation.

We verified the accuracy of the SRTM elevations by comparing it with both Geoscience Laser Altimeter System (GLAS) tracks (vertical resolution < 2 cm, [Fricker *et al.*, 2005]) crossing the sill and GPS tracks taken from a receiver mounted to the roof of a vehicle driving across the sill region (this study). Based on these comparisons, we determined SRTM elevation requires a uniform offset correction of 0.323 m in the vicinity of the sill.

3.7.2 Suggestion for improvement of data

With improved accuracy and abundance of rebound measurements, we could acquire a more complete picture of the spatial extent and magnitude of Coulomb stress perturbations on faults in the study region. Currently, our least reliable data are those

at sand berm sites. One way to improve our understanding of these sites would be to have LIDAR coverage with which to conduct a statistical analysis of the height, width, and extent of the berms. We were able to explore this potential method at Durmid Hill, a region of tectonic uplift on the SAF east of the Salton Sea. During Lake Cahuilla highstands, portions of it stood above the water level as an island, and it was covered by the B4 Airborne Laser Swath Mapping (ALSM) topography survey, flown along the SAF and SJF with 0.5-m footprint resolution and 0.1 m height accuracy [Bevis *et al.*, 2005]. In these data and in the field, we observe concentric recessional terraces spreading out from the hill. In a histogram of the relevant section of topographic data, we were able to identify these terraces as distinct peaks because of the extra land at these elevations. If we had similar data around the Lake Cahuilla shoreline at each local setting, we could use statistical analyses to better understand the diffusive processes involved in berm profile evolution.

In contrast to sand berm sites, tufa sites are much easier to identify and measure with small error for several reasons: 1) unlike berms and sorted surface rocks, tufa deposits change very little over 300 years, 2) tufa deposits extend along the entire length of the host cliff allowing for maximum redundancy in sampling, and 3) tufa deposits have little local variation in elevation. However, the greatest limitation in our shoreline elevation survey is the unknown relationship between the current elevation of a measured feature and the water elevation at the time of lake highstand. In the case of sand berms, this error is caused by erosion and diffusion so that the height of the feature today is likely not the same as it was at the time of the lake highstand. In the case of tufa deposits, this error is caused by the fact that the high line of tufa may

form slightly higher or lower than the actual water level. We expect errors of this sort to be, at most, a few meters and count them as the most significant source of noise in our data

3.8 Acknowledgements

We thank Steven Micklethwaite and an anonymous reviewer for their help in improving the manuscript. We also thank Yuri Fialko and Donna Blackman for providing careful in-house reviews. We are grateful to Daniel Brothers, Joseph Becker, and Afton Van Zandt, who assisted in the fieldwork for this project. This research was supported by the National Science Foundation (OCE-0326707) and the Academic Senate of the University of California.

Chapter 3, in full, is a reprint of the material as it appears in Luttrell, K., D. Sandwell, B. Smith-Konter, B. Bills, and Y. Bock (2007), Modulation of the earthquake cycle at the southern San Andreas fault by lake loading, *Journal of Geophysical Research*, 112, B08411, doi:10.1029/2006JB004752. The dissertation author was the primary investigator and author of this paper.

3.9 References

- Adams, K.D., S.G. Wesnousky, and B.G. Bills (1999), Isostatic rebound, active faulting, and potential geomorphic effects in the Lake Lahontan basin, Nevada and California, *Geol. Soc. Am. Bull.*, *111* (12), 1739-1756.
- Bennett, R.A., A.M. Friedrich, and K.P. Furlong (2004), Codependent histories of the San Andreas and San Jacinto fault zones from inversion of fault displacement rates, *Geology*, *32* (11), 961-964.
- Bevis, M., K. Hudnut, R. Sanchez, C. Toth, D. Grejner-Brzezinska, E. Kendrick, D. Caccamise, D. Raleigh, H. Zhou, S. Shan, W. Shindle, A. Yong, J. Harvey, A. Borsa, F. Ayoub, R. Shrestha, B. Carter, M. Sartori, D. Phillips, and F. Coloma (2005), The B4 Project: Scanning the San Andreas and San Jacinto Fault Zones, *Eos Trans. AGU*, *86*(52), Fall Meet. Suppl., Abstract H34B-01.
- Bills, B., K.D. Adams, and S.G. Wesnousky (2007), Viscosity structure of the crust and upper mantle in western Nevada from isostatic rebound patterns of the Late Pleistocene Lake Lahontan high shoreline, *J. Geophys. Res.*, *in press*.
- Bills, B.G., D.R. Currey, and G.A. Marshall (1994), Viscosity Estimates for the Crust and Upper-Mantle from Patterns of Lacustrine Shoreline Deformation in the Eastern Great-Basin, *J. Geophys. Res.*, *99* (B11), 22059-22086.
- Bock, Y., R.M. Nikolaidis, P.J. de Jonge, and M. Bevis (2000), Instantaneous geodetic positioning at medium distances with the Global Positioning System, *J. Geophys. Res.* (B12), 28223-28253.
- Byerlee, J. (1978), Friction of Rocks, *Pure Appl. Geophys.*, *116* (4-5), 615-626.
- Chery, J., and P. Vernant (2006), Lithospheric elasticity promotes episodic fault activity, *Earth Planet. Sci. Lett.*, *243* (1-2), 211-217.
- Currey, D.R. (1982), Lake Bonneville: Selected features of relevance to neotectonic analysis, *Open File Rep. 82-1070*, 31 pp., U.S. Geol. Surv.
- Fay, N.P., and E.D. Humphreys (2005), Fault slip rates, effects of elastic heterogeneity on geodetic data, and the strength of the lower crust in the Salton Trough region, southern California, *J. Geophys. Res.*, *110* (B09401).
- Fialko, Y. (2006), Interseismic strain accumulation and the earthquake potential on the southern San Andreas fault system, *Nature*, *441* (7096), 968-971.
- Freed, A.M., and J. Lin (2001), Delayed triggering of the 1999 Hector Mine earthquake by viscoelastic stress transfer, *Nature*, *411* (6834), 180-183.

- Fricker, H.A., A. Borsa, B. Minster, C. Carabajal, K. Quinn, and B. Bills (2005), Assessment of ICESat performance at the Salar de Uyuni, Bolivia, *Geophys. Res. Lett.*, **32** (L21S06).
- Fumal, T.E., M.J. Rymer, and G.G. Seitz (2002), Timing of large earthquakes since AD 800 on the Mission Creek strand of the San Andreas fault zone at Thousand Palms Oasis, near Palm Springs, California, *Bull. Seismol. Soc Am.*, **92** (7), 2841-2860.
- Grollmund, B., and M.D. Zoback (2000), Post glacial lithospheric flexure and induced stresses and pore pressure changes in the northern North Sea, *Tectonophysics*, **327** (1-2), 61-81.
- Gurrola, L.D., and T.K. Rockwell (1996), Timing and slip for prehistoric earthquakes on the Superstition Mountain Fault, Imperial Valley, southern California, *J. Geophys. Res.*, **101** (B3), 5977-5985.
- Hampel, A., and R. Hetzel (2006), Response of normal faults to glacial-interglacial fluctuations of ice and water masses on Earth's surface, *J. Geophys. Res.*, **111** (B06406).
- Heki, K. (2001), Seasonal modulation of interseismic strain buildup in northeastern Japan driven by snow loads, *Science*, **293** (5527), 89-92.
- Heki, K. (2003), Snow load and seasonal variation of earthquake occurrence in Japan, *Earth Planet. Sci. Lett.*, **207** (1-4), 159-164.
- Hetland, E.A., and B.H. Hager (2006), Interseismic strain accumulation: Spin-up, cycle invariance, and irregular rupture sequences, *Geochemistry Geophysics Geosystems*, **7**.
- Hetzel, R., and A. Hampel (2005), Slip rate variations on normal faults during glacial-interglacial changes in surface loads, *Nature*, **435** (7038), 81-84.
- Hudnut, K.W., Y. Bock, J.E. Galetzka, F.H. Webb, and W.H. Young (2002), The Southern California Integrated GPS Network (SCIGN), in *Seismotectonics in Convergent Plate Boundary*, edited by Y. Fujinawa, and A. Yoshida, pp. 167-189, Terra Sci., Tokyo.
- Kaufmann, G., and F. Amelung (2000), Reservoir-induced deformation and continental rheology in vicinity of Lake Mead, Nevada, *J. Geophys. Res.*, **105** (B7), 16341-16358.
- King, G.C.P., and M. Cocco (2001), Fault interaction by elastic stress changes: New clues from earthquake sequences, in *Advances in Geophysics*, Vol. 44, pp. 1-38.
- King, G.C.P., R.S. Stein, and J. Lin (1994), Static Stress Changes and the Triggering of Earthquakes, *Bull. Seismol. Soc Am.*, **84** (3), 935-953.

Larson, K.M. (1990), Precision, accuracy, and tectonics from the Global Positioning System, Ph.D. thesis, 269 pp., Univ. of Calif. San Diego, La Jolla.

Love, A.E.H. (1929), The stress produced in a semi-infinite solid by pressure on part of the boundary, *Proc. Roy. Soc. Lond. A*, 228, 377-420.

Matmon, A., D.P. Schwartz, R. Finkel, S. Clemmens, and T. Hanks (2005), Dating offset fans along the Mojave section of the San Andreas fault using cosmogenic Al-26 and Be-10, *Geological Society of America Bulletin*, 117 (5-6), 795-807.

Nelson, S.T., M.J. Wood, A.L. Mayo, D.G. Tingey, and D. Eggett (2005), Shoreline Tufa and Tufaglomerate from Pleistocene Lake Bonneville, Utah, USA: stable isotopic and mineralogical records of lake conditions, processes, and climate, *J. Quaternary Sci.*, 20 (1), 3-19.

Oglesby, L.C. (2005), *The Salton Sea: geology, history, potential problems, politics, and possible futures of an unnatural desert salt lake*, *Memoirs of the Southern California Academy of Sciences*, vol. 10, 240 pp., Southern California Academy of Sciences, Los Angeles.

Oskin, M., L. Perg, D. Blumentritt, S. Mukhopadhyay, and A. Iriondo (2007), Slip rate of the Calico fault: Implications for geologic versus geodetic rate discrepancy in the Eastern California Shear Zone, *J. Geophys. Res.*, 112 (B03402).

Reasenber, P.A., and R.W. Simpson (1992), Response of Regional Seismicity to the Static Stress Change Produced by the Loma-Prieta Earthquake, *Science*, 255 (5052), 1687-1690.

Roeloffs, E.A. (1988a), Fault Stability Changes Induced beneath a Reservoir with Cyclic Variations in Water Level, *J. Geophys. Res.*, 93 (B3), 2107-2124.

Roeloffs, E.A. (1988b), Hydrologic Precursors to Earthquakes - a Review, *Pure and Applied Geophysics*, 126 (2-4), 177-209.

Shifflett, H., M.G. Gray, R. Grannell, and B.L. Ingram (2002), New evidence on the slip rate, renewal time, and late Holocene surface displacement, southernmost San Andreas fault, Mecca Hills, California, *Bull. Seismol. Soc Am.*, 92 (7), 2861-2877.

Sieh, K.E., and P.L. Williams (1990), Behavior of the Southernmost San-Andreas Fault During the Past 300 Years, *J. Geophys. Res.*, 95 (B5), 6629-6645.

Simpson, D.W., W.S. Leith, and C.H. Scholz (1988), Two Types of Reservoir-Induced Seismicity, *Bull. Seismol. Soc Am.*, 78 (6), 2025-2040.

Smith, B., and D. Sandwell (2003), Coulomb stress accumulation along the San Andreas Fault System, *J. Geophys. Res.*, 108 (B6), 2296.

Smith, B., and D. Sandwell (2004), A three-dimensional semianalytic viscoelastic model for time-dependent analyses of the earthquake cycle, *J. Geophys. Res.*, *109* (B12401), doi:10.1029/2004JB003185.

Thomas, A.P., and T.K. Rockwell (1996), A 300- to 550-year history of slip on the Imperial fault near the US-Mexico border: Missing slip at the Imperial fault bottleneck, *J. Geophys. Res.*, *101* (B3), 5987-5997.

Turcotte, D.L., and G. Schubert (2002), *Geodynamics*, 456 pp., Cambridge Univ. Press, New York.

Waters, M.R. (1983), Late Holocene Lacustrine Chronology and Archaeology of Ancient Lake Cahuilla, California, *Quat. Res.*, *19* (3), 373-387.

Chapter 4

Estimates of stress drop and crustal tectonic stress from the February 27, 2010 Maule, Chile earthquake: Implications for fault strength

Abstract

The great February 27, 2010 M_w 8.8 earthquake off the coast of southern Chile ruptured a 606 km length of subduction zone. In this study we make two independent estimates of shear stress in the crust in the region of the Chile earthquake. First, we use a coseismic slip model constrained by geodetic observations from InSAR and GPS to derive a spatially variable estimate of the change in static shear stress along the ruptured fault. Second, we use a static force balance model to constrain the crustal shear stress required to support observed accretionary wedge topography and the stress orientation indicated by the earthquake focal mechanism. This includes the derivation of a semi-analytic solution for the stress field exerted by surface and Moho topography loading the crust. We find that the deviatoric stress exerted by topography is minimized in the limit when the crust is considered an incompressible elastic solid, with a Poisson's ratio of 0.5. This places a lower bound on the critical stress state maintained by the crust supporting plastically deformed accretionary wedge topography. We estimate the shear stress change from the Maule event ranged from -6 MPa (stress increase) to 14 MPa (stress drop), with a maximum depth-averaged shear stress drop of 4 MPa. We separately estimate that the plate driving forces acting

in the region, regardless of their exact mechanism, must contribute at least 15 MPa trench-parallel compression, and trench-perpendicular compression must exceed trench-parallel compression by at least 12 MPa. This corresponds to a depth-averaged shear stress of at least 7 MPa. The comparable magnitude of these two independent shear stress estimates is consistent with the interpretation that the section of the megathrust fault ruptured in the Maule earthquake is weak, with the seismic cycle relieving much of the total sustained shear stress in the crust, and an equal portion of plate-driving stress being transmitted through the mantle.

4.1 Introduction

On February 27, 2010 an earthquake of magnitude 8.8 struck off the coast of Maule, Chile. At least 500 people were killed and damage to homes was widespread across the region in the aftermath of the mainshock and subsequent aftershocks [National Earthquake Information Center of the U.S. Geological Survey, hereafter referred to as NEIC]. This event represents the latest release of strain energy built up along the locked megathrust zone created by the Nazca plate subducting beneath the South American plate at a rate of 70 mm/yr.

Low stress drops and the absence of a strong fault-related heat flow anomaly along the San Andreas fault in California suggest that the stress stored and released over the seismic cycle is much lower than the large in situ stresses that are both observed in borehole measurements and predicted from laboratory faulting experiments [e.g., *Byerlee*, 1978; *Scholz*, 2000; *Zoback*, 2000]. These observations may be reconciled if faults in general, or perhaps the SAF specifically, are weak with a

coefficient of friction ~ 0.1 . However other lines of evidence, such as the angle between the principal stress axes and a particular fault trace, have led to inconsistent interpretations of fault friction [Hardebeck and Michael, 2004]. At subduction zones, observations of the reactivation of outer rise normal faults have shown that while these faults are weaker than newly formed faults, they still have coefficient of friction of 0.6, in line with the predictions of laboratory experiments [Billen *et al.*, 2007].

Previous studies have estimated the shear stress at subduction zone megathrusts by balancing tectonic driving stress with lithostatic pressure from topography. Lamb [2006] estimated the mean shear stress required to support the elevation of the high Andes at ~ 37 MPa and ~ 15 MPa in northern and southern Chile respectively, consistent with estimates from previous thermal modeling studies in megathrust regions. Of this stress, approximately even portions were transmitted through the crust and mantle. Seno [2009] used a similar force balance method and estimated that mean shear stress along subduction zones is generally tens of megapascals, with the value in northern Chile on the higher end of that range, greater than 80 MPa. Zhong and Gurnis [1994] used a dynamic model of developing trench topography to estimate shear stress on subduction faults in the range of 15 to 30 MPa. Other studies have used observations of present-day topography to constrain the effective coefficient of friction on subduction thrusts to be less than 0.2 [Cattin *et al.*, 1997] or 0.03 to 0.09 [Lamb, 2006].

In this study we provide independent estimates of both the stress change on the rupture surface from a major earthquake and the minimum crustal tectonic stress required to support the topography immediately above that fault. The complete

InSAR coverage over the rupture area of the Maule event provides a unique opportunity to derive a detailed slip model needed to estimate the spatially variable stress change from the event. In addition, we present a new formulation to directly estimate the minimum 3-D stress field exerted by local surface and Moho topography, constrained by gravity observations. We can then determine the minimum value of stress in the crust applied by tectonic forces required to both offset the stress exerted by topography and maintain a stress field orientation consistent with that of the stress released in the earthquake. This idea is similar to previous studies that have estimated tectonic stress by balancing the loading of topography [e.g., *Lamb*, 2006], but it has the advantage of deriving its estimate from the short-wavelength topography immediately above the ruptured megathrust region. In this way, the estimate more directly samples the stress in the crust at the seismogenic portion of the subduction zone, rather than relying on stress beneath the high Andes being transmitted several hundred kilometers back to the shallow megathrust region. By estimating both of these quantities independently, we have the opportunity to, in this one instance, make a direct comparison of the stress released in a major earthquake with a lower bound on the absolute stress present in the crust. In doing so, we are able to constrain the fraction of seismic stress release relative to total stress in the crust and discuss the implications for the strength of the megathrust fault in the Maule area.

4.2 Minimum stress drop from the February 2010 Maule earthquake

The coseismic displacement from the 2010 Maule, Chile earthquake was observed in unprecedented detail using interferometric synthetic aperture radar

(InSAR). Several factors contribute to the quality of these observations. First, scene pairs acquired with the Advanced Land Observatory Satellite (ALOS) have improved coherence relative to those acquired from satellites operating a shorter wavelength radar. Second, recent processing advances allow interferograms to be made from scenes acquired in ScanSAR mode. This is especially important because the descending passes made days after the mainshock were recorded in ScanSAR mode and record the deformation along the entire coastline in a single track. Third, because the region of interest is a shallow dipping subduction zone, spatial variations in coseismic slip on the fault are better mapped onto spatial variations in surface displacement than they are when using InSAR to look at, for example, horizontal slip on a vertical fault plane. However, this also means the shallowest portions of the fault lie offshore where displacement is unobservable by InSAR. Because interferometry is unable to determine the absolute line of sight displacement, observations of coseismic displacement from a network of GPS stations in the region are required to constrain the absolute offset. (These interferograms were first published in *Tong et al.* [2010] and are available, along with the slip model results, online at ftp://topex.ucsd.edu/pub/chile_eq/chile_insar.zip).

Tong et al. [2010] inverted these geodetic data to model coseismic slip on a single dipping plane 670 km long by 260 km wide, approximating the geometry of the shallow megathrust with a strike N 16° E and a 15° dip to the east. The inversion assumes an isotropic homogeneous elastic half-space [*Fialko*, 2004; *Okada*, 1985] and resolves in-plane slip onto rectangular patches approximately 20 km by 20 km. The model shows that slip occurred primarily in two patches (Figure 4.1a), predominantly

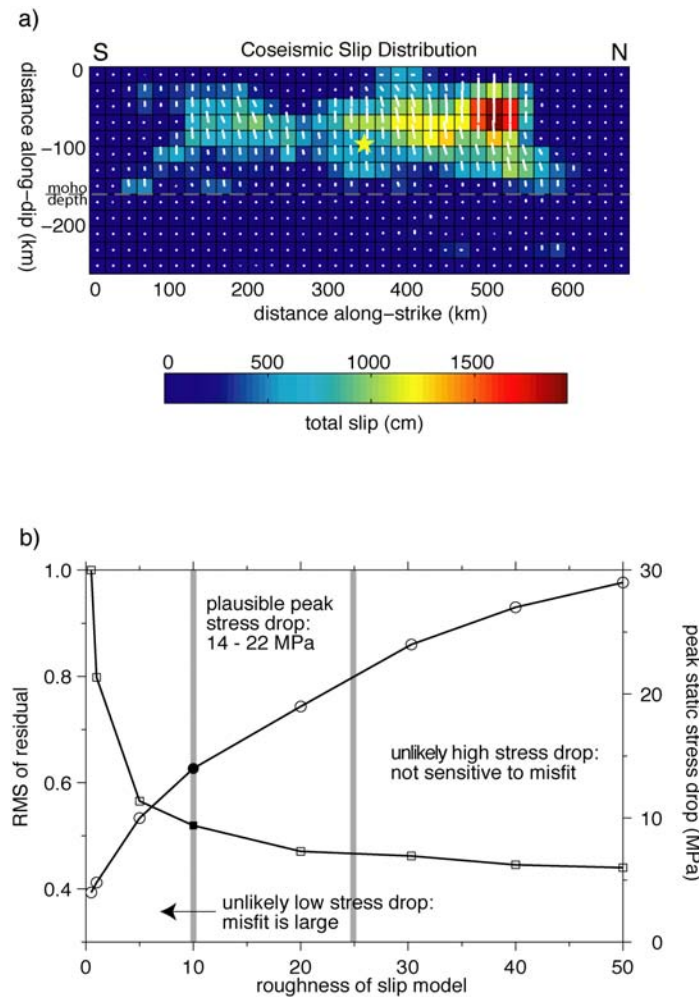


Figure 4.1 (a) Coseismic slip model from joint inversion of GPS and InSAR data (Tong *et al.* [2010]). The magnitude and direction of slip (hanging wall motion relative to foot wall) are indicated by the colored squares and white bars respectively. The yellow star shows the location of the epicenter, and dashed gray line indicates the Moho at ~40 km depth. A non-negativity constraint was applied in the inversion of the geodetic data to allow only thrust and right-lateral strike slip. (b) RMS fit of inverted slip model to geodetic observations (squares) and peak stress drop of stress change derived from slip model (circles) as a function of nondimensional model roughness parameter. Peak stress drop location is at the main slip asperity north of the hypocenter. Increasing model roughness decreases misfit and increases peak stress drop. Models with roughness parameter above 10 provide an acceptable fit to geodetic data, while models with roughness parameter above 25 cannot be justified with geodetic observations. This corresponds to a likely peak stress drop between 14 and 22 MPa. The filled symbols indicate the roughness value of the stress change model shown in Figure 4.3a. We interpret this as a lower bound of stress drop estimated from geodetic inversion.

in the up-dip direction with a small component of right-lateral motion. The largest slip of 17 m occurred in a patch north of the epicenter, while a smaller patch south of the epicenter slipped up to 11 m. The geodetic moment release of this model is 1.53×10^{22} Nm (M_w 8.72), compared with the seismic moment of 1.8×10^{22} Nm [NEIC]. The smaller geodetic moment is probably due to an underestimate of slip where there is a lack of observations offshore. Interestingly, the model indicates that coseismic slip is confined above the Moho ($\sim 35 - 45$ km [Sick *et al.*, 2006; Yuan *et al.*, 2002]), a result that is robust to variations in assumed fault geometry [Tong *et al.*, 2010].

We compute the static shear stress drop from the earthquake based on the interpolated slip model using a Fast Fourier Transform (FFT) method [Andrews, 1980; Ripperger and Mai, 2004] that neglects the effect of the free surface boundary condition for inclined faults. This method has usually been used on vertical fault planes, so we tested its efficacy on a simple shallow dipping thrust fault by comparing the static stress drop of the FFT method with that of an exact half-space formulation [Okada, 1992]. We found the effect of neglecting the half-space boundary condition was at most about twenty percent near the top edge of the fault (0-3 km depth), with the disagreement between the two solutions decreasing with depth. Below 5 km depth, the static stress drop estimations from the FFT and half-space methods agree fairly well. We then estimated the static shear stress drop in the dip-slip direction from the full slip model (Figure 4.1a) using the FFT method. Stress drop resolved in the strike-slip direction may be safely neglected since the coseismic slip was dominated by thrust motion.

Both the fit of the slip model to the geodetic observations and the estimated static stress drop depend on the roughness of the slip model, i.e., the second derivative of slip on the fault plane (Figure 4.1b). The ~20 km resolution of our slip model is limited by the resolution of the geodetic inversion, such that increasing model roughness only improves fit to the data up to a certain point, beyond which the data can no longer justify the increase in model complexity. As slip model roughness increases, the calculated peak static stress drop also increases as the patches of slip and stress release become more localized. We therefore identify a range of acceptable slip models that provide a reasonable fit to the geodetic observations. This corresponds to a range of likely peak stress drop, though strictly it is a lower bound on the possible stress drop. Figure 4.3a shows a stress drop model from within this range. The static stress change varies approximately from 14 MPa (stress drop) to -6 MPa (stress increase) over the fault plane. As expected the variation of the static stress drop follows the variation of the slip model and a significant portion of the stress drop is contributed from thrust motion at the northern asperity.

4.3 Minimum tectonic stress estimate from topography

Topography formation is subject to many different processes. In the region of the Maule earthquake, the topography may be divided by wavelength into two portions. The long-wavelength topography across the coast of South America (i.e. wavelengths greater than 2π times the depth of compensation) is dominated by the rise from the offshore subduction trench to the high Andes and is supported by a combination of isostatic compensation and dynamic buoyancy due to convecting

upper mantle material. The short-wavelength topography (i.e. wavelengths less than ~350 km) in the megathrust region is dominated by an accretionary wedge of material scraped from the subducting slab. This wedge is built through processes of plastic deformation such that the state of stress supporting this topography is maintained at the level of critical failure [Dahlen, 1990]. The height of this critical wedge topography is limited by the portion of the lithosphere that can sustain shear stress (i.e. the depth to the brittle-ductile transition). Based on the observation of *Tong et al.* [2010] that coseismic slip for the Maule earthquake appears to be negligible below the fore-arc Moho, we infer that the stress state of critical plastic failure is sustained throughout the crust in this region and that the height of the short-wavelength topography is related to this critical stress level.

We can calculate the three-dimensional stress state exerted by the load of this short-wavelength topography at the surface of a uniformly thick plate and the corresponding short-wavelength buoyant load from the shape of the Moho, which can be inferred from gravity observations (Figure 4.2, Appendix A). We measure the critical stress in the crust by calculating the second invariant of the deviatoric stress tensor, i.e., the Von Mises stress. We show in Appendix A that the smallest deviatoric stress the wedge topography could exert in the crust is that in which the surface topography (and its corresponding Moho topography) acts as a load on an incompressible elastic plate. For topography at wavelengths comparable to the crustal thickness, this gives a lower bound on the size of the deviatoric stress sustained by the deformed crust. If the plastic deformation processes of topography formation preserve

the volume of the undeformed crust, then the in situ stress state at this wavelength may be equal to the stress state exerted by the load of topography.

However, we know more about the stress state than simply that it supports the observed topography. The orientation of the in situ stress tensor in the ruptured fault region is represented by the centroid moment tensor solution of the Maule event [NEIC]. By adding a regionally-uniform horizontal stress field (representing the depth-averaged tectonic plate-driving stress in the crust) to the minimum topography-supporting stress tensor, we can determine the smallest magnitude of additional stress required to align the stress field in that region with the in situ stress orientation indicated by the earthquake focal mechanism. The absolute magnitude of the tectonic stress, regardless of the physical processes generating that stress, must be at least this big. When resolved onto the dipping megathrust fault plane, this provides a minimum

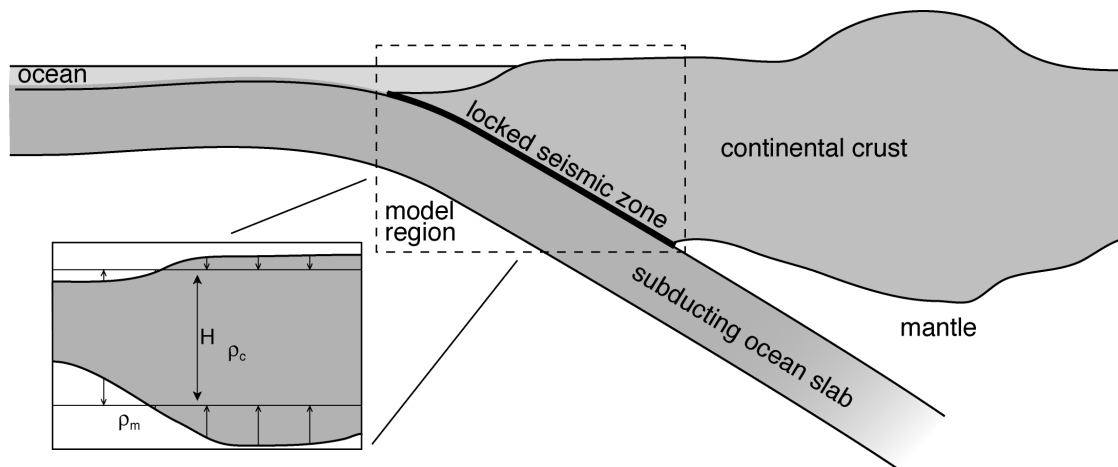


Figure 4.2 schematic illustration of megathrust geometry showing the locked seismogenic zone between the subducting slab and the continental crust. 3-D calculation of minimum stress required to support the short-wavelength topography is calculated in the region within the dashed box. Inset schematic shows a thick plate loaded by surface and Moho topography, the geometry used in the 3-D stress calculation.

estimate of the depth-averaged shear stress along the crustal plate interface.

In order to calculate the stress state exerted by topography, the surface topography and bathymetry [*Becker et al.*, 2009] is first high-pass filtered using a cosine taper between spherical harmonics 100 and 140 (corresponding to wavelengths between 300 km and 400 km). The shape of the Moho is related to the surface topography by flexure, constrained by observations of the gravity anomaly in the region that have also been high-pass filtered [continent region from *Pavlis et al.*, 2008; ocean region from *Sandwell and Smith*, 2009]. For a 40 km thick crust, consistent with the estimates of *Yuan et al.* [2002], *Sick et al.* [2006], and the CRUST 2.0 model [*Laske et al.*, 2001], the ~250 mGal anomaly across the region is fit to an RMS of 33 mGal with an elastic thickness of 3 km and a density of 2500 kg/m³. This density is likely lower than the bulk density of the crust in this region, but because the calculation of topography stress depends only on the product of density and topography, any set of elastic thickness and crustal density parameters that sufficiently reproduces the gravity is an adequate representation of the spatial distribution of the load at the Moho.

We calculate the minimum stress required to support topography along the locked interface between the subducting slab and the overriding crust, using the same fault geometry as the coseismic stress drop model in the previous section. The orientation of the minimum stress tensor along this plane is shown in Figure 4.3b, where the stress state at each point is represented as a lower-hemisphere projection “beachball”, with the tension principal stress axis oriented through the shaded quadrants and the pressure axis oriented through the unshaded quadrants. The

compatibility of the computed stress field at each point with the stress orientation indicated by the Maule event can be quantified by assigning each location a goodness-of-fit value $\xi \in [0,1]$ (indicated by the color of the shaded quadrant of each beachball) such that

$$\xi = \begin{cases} 0 & \text{if model and event stress regimes differ} \\ \left(\vec{v}_1^{model} \cdot \vec{v}_1^{event} + \vec{v}_2^{model} \cdot \vec{v}_2^{event} + \vec{v}_3^{model} \cdot \vec{v}_3^{event} \right) / 3 & \text{else} \end{cases} \quad (4.1)$$

where \vec{v}_i^{model} and \vec{v}_i^{event} are the eigenvectors (principal stress axes) of the 3-D stress tensor of the model and event respectively. The definition of stress regime involves the plunge angle of each principal stress axis, following the convention of the World Stress Map catalog [e.g., *Zoback*, 1992]. The mean of this parameter over each location on the faultplane $\bar{\xi}$ tests the fit of each modeled stress field.

The minimum stress needed to support the surface and Moho topography does not predict the focal mechanism of the Maule event: the mean fit across the faultplane is $\bar{\xi} = 0.198$. Offshore in the trench region, the minimum stress state is generally in a thrust regime, while onshore in the coastal foothills it is in a normal or strike-slip regime. When this topography-only stress state is resolved into reverse-slip shear stress on the megathrust fault plane (Figure 4.3b), we observe that the regions in which shear stress is negative (indicating that reverse slip is not favored) strongly correspond to the regions in which the topography-exerted stress orientation is not in a thrust regime.

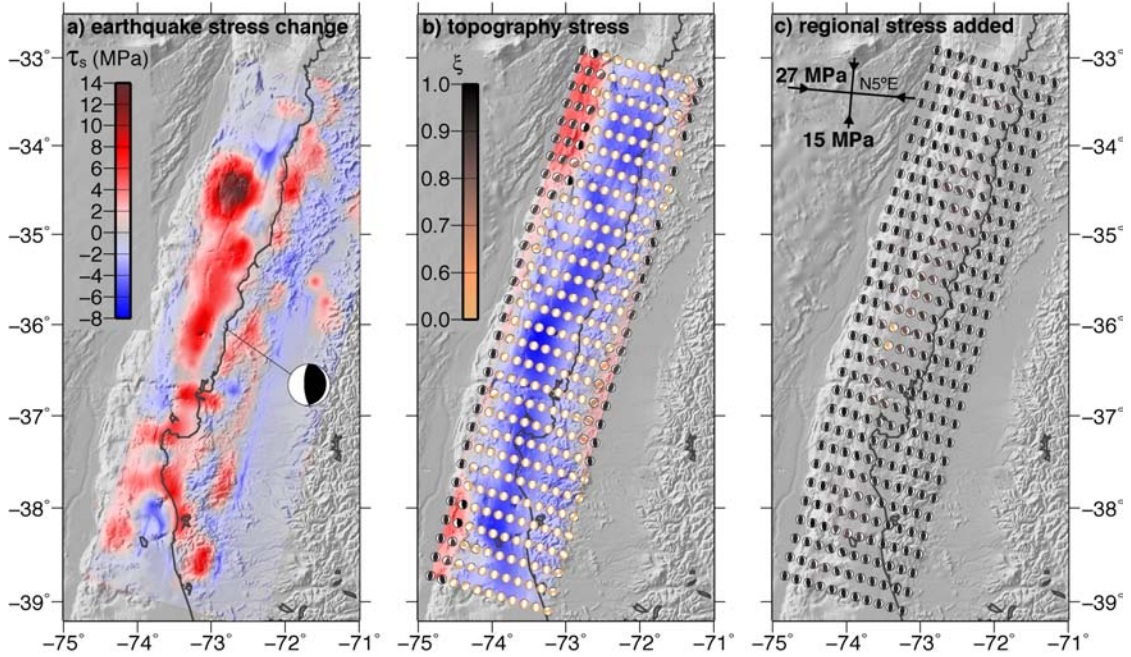


Figure 4.3 (a) Static shear stress change from Maule, Chile earthquake derived from slip model shown in Figure 1. Positive (negative) shear stress values correspond to stress release (build up). Focal mechanism from the Maule event is shown with a line to the mainshock hypocenter. (b) magnitude (shading) and orientation (beachballs) of minimum deviatoric stress field exerted by surface and Moho topography on the crust. Magnitude is indicated as the dip-slip shear stress resolved onto the same dipping fault plane as in (a), using the same color scale. Positive (negative) shear stress values indicate reverse (normal) dip-slip motion preferred. 3-D orientation of stress tensor indicated by lower-projection beachballs calculated at depth along the dipping fault plane. Color of shaded quadrants indicates goodness-of-fit parameter ξ , describing fit to focal mechanism of the Maule event. (c) Orientation of smallest stress field capable of both supporting short-wavelength topography and maintaining stress orientation consistent with that of the Maule event throughout rupture region. Color of shaded quadrants again indicates value of ξ . Stress field consists of that shown in (b) with an additional 27 MPa compression at 95° EofN and 17 MPa compression at 5° EofN.

To reconcile this stress mismatch, we add a regionally uniform horizontal stress field, representing the sum of any applied long-wavelength tectonic forces, consisting of three free parameters (two principal horizontal stress magnitudes and an orientation angle of the axes), to the minimum topography-supporting stress field. We search this parameter space and define the conditions that maximize $\bar{\xi}$, the fit between the model stress field and the Maule event. There are two requirements in order for the combined stress field to be aligned with that of the earthquake. First, there must be a trench-parallel compression of at least 15 MPa above lithostatic pressure. Second, trench-perpendicular compression must exceed trench-parallel compression by at least 12 MPa for a total of at least 27 MPa of trench-perpendicular compression. Any added stress that satisfies both of these conditions will result in a properly oriented thrust-regime stress field along the entire megathrust faultplane.

The orientation of the stress field that includes the smallest satisfactory additional stress (15 MPa compression at 5° EofN and 27 MPa compression at 95° EofN) is shown in Figure 4.3c. The mean fit of the stress field orientation improves to $\bar{\xi} = 0.914$ with the additional stress, indicating that most of the faultplane is now in a stress field consistent with the orientation of the Maule event. Though the strike and regime of the theoretical fault planes fit well, the theoretical dip angle does not align perfectly with the actual fault dip because our calculation has no knowledge of the pre-existing plane of weakness that is the subducting slab interface. Also, the oblique rake of the focal mechanism is only fit well in the shallowest portions of the fault where the vertical shear stress components are of comparable size to the normal stress

components. Deeper in the crust, where these stress components are smaller, the slightly counterclockwise-rotated stress orientation with non-oblique theoretical rake provides the best fit, as defined in equation 4.1, to the actual oblique focal mechanism.

A trench-perpendicular compression of 27 MPa resolved onto a 15° dipping plane corresponds to 7 MPa of resolved reverse-slip shear stress. This balances the minimum value of the topography-only shear stress, ensuring that the total stress field favors reverse dip-slip over normal dip-slip. However ensuring a thrust regime throughout the faultplane requires trench-parallel compression to exceed vertical compression. The 15 MPa of trench-parallel compression corresponds to the largest amount by which the vertical normal stress (σ_{zz}) exceeds the trench-parallel normal stress ($\sim \sigma_{yy}$) across the faultplane. In order to maintain a properly oriented stress field, the regional driving tectonic stress must maintain at least 12 MPa deviatoric stress.

4.4 Discussion

The stress drop of a single earthquake can vary widely, from $\sim 10^{-1}$ to 10^2 MPa [e.g., *Allmann and Shearer*, 2009; *Hardebeck and Aron*, 2009]. The peak value of our slip model-derived estimate at 14 MPa is on the higher end of this range, well above the 3-4 MPa median stress drop estimated from the corner frequency of the seismic spectra for a global catalog of events. However the depth averaged stress drop estimate of 4 MPa may be a better quantity to compare with seismic estimates of stress drop. This depth-averaged estimate is consistent with previous observations that

intraplate earthquakes deep in the subducted slab in Chile have a higher stress drop around 9 MPa, while interplate earthquakes along the contact megathrust zone between the plates have a lower stress drop around 3 MPa [Leyton *et al.*, 2009]. Previous studies have disagreed over whether there is any correlation between event stress drop and event magnitude, depth, or regime. Larger stress drops have been associated with thrust events along the San Andreas fault in California [Hardebeck and Aron, 2009], but a global study of stress drops found rather that stress drop is larger for strike-slip events than thrust events, though it could be that some of the assumptions of a seismic estimation of stress drop (e.g., a circular slip patch, constant rupture velocity) break down for very large earthquakes [Allmann and Shearer, 2009].

The comparison of our crustal tectonic stress estimate with our stress drop estimate from the Maule event has some implications for our understanding of fault strength in the region. A stress drop larger than the tectonic stress estimate would be unphysical because the earthquake cannot relieve more stress than it has accumulated, therefore it would be an indication that the tectonic stress estimate was too low. If the minimum crustal tectonic stress was much larger than the earthquake stress drop, this would indicate that in this portion of the Chilean subduction zone the stress perturbations associated with the earthquake cycle involve only a fraction of the absolute stress in the lithosphere, consistent with a “strong” fault. If the tectonic stress and stress drop are of similar size, then this could indicate that the seismic cycle does relieve the bulk of the above-lithostatic stress carried in the lithosphere, consistent with a relatively “weak” fault.

In order to directly compare resolved dip-slip shear stress estimates, we must take the depth average of the modeled earthquake stress change through the crust (top 40 km depth, or 154 km along dip). The along-fault depth-average shear stress drop at the northern asperity is about 4 MPa, compared with at least 7 MPa resolved tectonic shear stress required to support topography. If these numbers represent the actual stresses sustained by the fault and relieved through the seismic cycle, then our estimates indicate a fairly weak crustal fault in which major earthquakes relieve much of the total stress. In this case, the bulk of the plate driving stress would be transmitted across the plate boundary through the mantle. A weak crustal fault would be consistent with modeling studies that indicate a low effective coefficient of friction (less than 0.2) is required on subduction thrust faults in order to be consistent with observations of forearc topography [Cattin *et al.*, 1997; Lamb, 2006]. However, because these are both strictly minimum estimates we cannot say for sure that the Chilean subduction thrust is weak. We rather conclude that the only way the Chilean subduction thrust can be strong is if the tectonic stress magnitude in the crust is much larger than the minimum stress required to sustain the observed topography and stress regime, meaning a substantial portion of plate driving stress is transmitted through the crust.

Our tectonic mean crustal shear stress estimate is a minimum for two reasons. First, the assumption of material incompressibility calculates the stress state with the smallest possible deviatoric stress that the topography as a load could exert, such that our calculation of the short-wavelength stress is a minimum. However such an assumption may be appropriate when considering the support of short-wavelength

topography. *Dahlen* [1981] proposed that the deviatoric stress in unflexed regions of oceanic lithosphere is the minimum state required to support topography and found that this corresponded to the case of an incompressible material, though this was not explicitly stated. If this is the case, then our calculation may closely estimate the variations in the magnitude of sustained stress at this wavelength.

The second reason our mean crustal shear stress estimate is a minimum is because we have made no assumptions about the forces responsible for advancing the slab toward subduction. Any stress responsible for net plate motion that is sustained through the crust must be in addition to the minimum long-wavelength stress we have identified as necessary to support the observed topography and stress regime. It is interesting that our minimum estimate of crustal shear stress is about half that of previous estimates of tectonic shear stress throughout the entire plate that focused on the balance of long-wavelength topography with tectonic stress [*Lamb*, 2006; *Seno*, 2009; *Zhong and Gurnis*, 1994]. This could indicate that plate strength is equally proportioned through the crust and mantle, but with the mantle portion being principally responsible for gross plate motion and the crustal portion primarily maintaining the topography and seismogenic cycle.

We observe that the slip distribution from this event occurred just north of the extent of the slip from the 1960 event [*Barrientos and Ward*, 1990]. This is in a region with a high positive gravity anomaly, particularly in comparison to the region of the 1960 event further south. This appears inconsistent with the observations of *Song and Simon* [2003] that great earthquakes tend to occur in regions of strongly negative trench parallel gravity anomaly (TPGA) while regions of high TPGA should

be relatively quiescent. It is possible that the processes governing the spatial variation in frictional properties that may be responsible for prior observations of this correlation across several subduction zones globally are not operating in this region. More likely the gravity high present here onshore and along the coast is indicative of the transition to continental crust, such that the observations of *Song and Simon* [2003] are limited to the offshore near-trench portions of subduction zones.

4.5 Conclusions

In this study we have made two independent estimates of shear stress in the crust in the region of the M_w 8.8 Maule, Chile earthquake. In the first, we have combined observations from InSAR and GPS to develop a coseismic slip model for the event and used this model to calculate the spatially variable static shear stress change along the fault from the rupture. We estimate the stress change from this event varied between -6 MPa (stress increase) to 14 MPa (stress drop). When averaged through the crust, this corresponds to a maximum shear stress drop of 4 MPa.

In the second, we have calculated the stress field exerted by surface and Moho topography loading the crust and have related that to the critical stress level sustained in the support of the accretionary wedge topography in the rupture region. We observe that long-wavelength plate-driving forces, regardless of their exact mechanism, must contribute at least enough stress in the crust to both support the observed topography variations and ensure the 3-D orientation of the stress field is consistent with that indicated by the focal mechanism of the Maule event. We can therefore identify the following constraints on the tectonically applied stress in the

crust at this location: trench-parallel compression must be at least 15 MPa, and trench perpendicular compression must exceed trench parallel compression by at least 12 MPa for a total of at least 27 MPa of trench-perpendicular compression. When resolved into dip-slip shear stress on the subduction fault plane, this corresponds to a mean crustal shear stress of at least 7 MPa.

The comparable magnitudes of these two independent estimates suggests that the seismic cycle relieves a quantity of stress similar to that required to sustain the observed topography and stress orientation, consistent with a weak megathrust fault. The fault may be stronger if the additional driving stress responsible for gross plate motion is transmitted through both the crust and mantle, as opposed to solely through the mantle. These observations are consistent with previous studies that estimate a low coefficient of friction for subduction faults as well as low mean shear stress along the subduction interface of southern Chile in particular. Detailed geodetic imaging of the coseismic slip from the Maule event as well as the development of a force balance model derived specifically to constrain the magnitude of crustal tectonic stress has allowed us to specifically investigate the stress state in a narrow geographic region. We are thus able to place strict lower bounds on the absolute magnitude of the deviatoric stress in the lithosphere at this location.

4.6 Appendix

4.6.1 Method and boundary conditions

This appendix contains the derivation of the 3D stress field generated by top and bottom loading of an elastic plate of thickness h . Solutions to the Boussinesq

problem for balancing vertical tractions on a surface were originally developed for an elastic halfspace [*Boussinesq*, 1885; *Steketee*, 1958]. More recently, similar methods have been followed to derive solutions for balancing vertical tractions on the surface of an elastic plate overlying a viscoelastic halfspace [*Luttrell and Sandwell*, 2010; *Luttrell et al.*, 2007; *Smith and Sandwell*, 2004]. Here we again follow the approach of *Steketee* [1958] to solve a Boussinesq-like problem in which we apply two distinct loads to the surfaces of an elastic plate.

The model is semianalytic in that the Green's function stress from a vertical point load at the top and bottom of the plate is analytically derived (below) and then numerically convolved with the actual 2-D shape of the load to get the 3-D stress field. This method of calculation is advantageous because it is numerically efficient, though it does require the vertical structure of the model earth to be simple. The loads at the top and bottom of the plate ($f(x, y)$ at $z = 0$ and $g(x, y)$ at depth $z = h$, respectively) may be arbitrarily intricate and need not be related, though Moho shape is generally related to surface topography through flexure. The only restrictions on the loads come from the Fast Fourier Transform convolution, which requires that the zero-wavenumber component of the force be zero and that the computational region be wider than the longest wavelength we are interested in. The compensation of very long-wavelength loads can be adequately described by thin plate flexure, while the compensation of short-wavelength loads can be described by an elastic halfspace. We are primarily interested in the intermediate-wavelength loads between these domains.

The response of a plate to a vertical point load is radially symmetric, therefore only four boundary conditions are needed to describe the system. Shear tractions must

vanish at the surfaces and vertical normal tractions are defined by the applied loads.

We treat the distributed loads as horizontally varying but applied at a single depth.

$$\sigma_{xz}(\vec{x}, 0) = 0 \quad (4.A1.1)$$

$$\sigma_{xz}(\vec{x}, h) = 0 \quad (4.A1.2)$$

$$\sigma_{zz}(\vec{x}, 0) = -f(\vec{x}) \quad (4.A1.3)$$

$$\sigma_{zz}(\vec{x}, h) = -g(\vec{x}) \quad (4.A1.4)$$

Stress is positive in extension and negative in compression, and z is positive up. If $f(\vec{x})$ and $g(\vec{x})$ are positive numbers, both applied normal stresses are compressive (negative). Note that despite the inherent radial symmetry of the problem, we continue the derivation in Cartesian coordinates for simplicity, and note here that additional boundary conditions requiring the other vertical shear stress σ_{yz} also vanish are appropriate but redundant. Numerical FFTs are done in Cartesian coordinates on a global one-minute Mercator-projected grid divided into strips of latitude, and individual strips are merged using a cosine taper to reduce any effect from latitude seams.

4.6.2 Stress in a thick elastic plate

As in *Luttrell and Sandwell* [2010], we let displacement and stress be a function of the Galerkin vector potential Γ_i ,

$$u_i = \Gamma_{i,kk} - \alpha \Gamma_{k,ki}, \quad (4.A2)$$

$$\sigma_{ij} = \lambda(1 - \alpha) \delta_{ij} \Gamma_{l,kkl} + \mu (\Gamma_{i,kkj} + \Gamma_{j,kki}) - 2\mu \alpha \Gamma_{k,kij}, \quad (4.A3)$$

where α is a constant yet to be determined and stress above the lithostatic state σ_{ij} has been related to strain and displacement u_i through an elastic constitutive equation with Lamé parameters λ and μ . Note that we use the standard summation notation, such that a variable with a single subscript is a vector, a variable with two subscripts is a tensor, a repeated index indicates summation over the coordinates, and an index following a comma indicates differentiation with respect to that coordinate. Because the applied point loads are purely normal and applied on a horizontal free surface, we need only retain the third component of the Galerkin vector, such that $\Gamma_x = \Gamma_y = 0$ and $\Gamma_z = \Gamma$, which we call the Galerkin potential.

When the equilibrium equations for a body in the absence of internal body forces or acceleration $\sigma_{ij,j} = 0$ are written in terms of the Galerkin potential, we find that by letting $\alpha = (\lambda + \mu)/(\lambda + 2\mu)$, the Galerkin potential must satisfy the

biharmonic equation $\nabla^4 \Gamma = 0$. After taking the 2-D horizontal Fourier transform of this equation, the solution form is recognized as

$$\Gamma(\vec{k}, z) = (A + B\beta z)e^{\beta z} + (C + D\beta z)e^{-\beta z}, \quad (4.A4)$$

where $\beta = 2\pi|\vec{k}| = 2\pi\sqrt{k_x^2 + k_y^2}$ is the horizontal wavenumber and (A, B, C, D) are coefficients to be determined by the boundary conditions (equation 4.A1).

We may now express the components of the stress tensor (equation 4.A3) in terms of the Young's modulus E , Poisson's ratio ν , horizontal wavenumber, and the Galerkin potential coefficients. The stress components relevant to the boundary conditions (equation 4.A1) are

$$\sigma_{xz}(\vec{k}, z) = -i\pi k_x \frac{E\beta^2}{1-\nu^2} \left[(A + B(2\nu + \beta z))e^{\beta z} + (C + D(-2\nu + \beta z))e^{-\beta z} \right] \quad (4.A5.1)$$

$$\sigma_{zz}(\vec{k}, z) = \frac{E\beta^3}{2(1-\nu^2)} \left[(-A + B(1 - 2\nu - \beta z))e^{\beta z} + (C + D(1 - 2\nu + \beta z))e^{-\beta z} \right] \quad (4.A5.2)$$

This system of four equations and four unknowns can now be solved using a computer algebra system (Mathematica). The coefficients of the Galerkin potential are found to be

$$\Phi = \frac{v^2 - 1}{E\beta^3(1 + 2\beta^2 h^2 - \cosh 2\beta h)} \quad (4.A6.1)$$

$$A = \Phi \left[\begin{array}{l} f(\vec{k}) \left[-2\nu(2\beta h + \sinh 2\beta h) + (-2\nu(1 - \cosh 2\beta h) - 2\beta^2 h^2) \right] + \\ g(\vec{k}) \left[4\nu(\beta h \cosh \beta h + \sinh \beta h) + 2(1 - 2\nu)\beta h \sinh \beta h \right] \end{array} \right] \quad (4.A6.2)$$

$$B = \Phi \left[\begin{array}{l} f(\vec{k}) \left[(1 - \cosh 2\beta h) + (2\beta h + \sinh 2\beta h) \right] + \\ g(\vec{k}) \left[2\beta h \sinh \beta h - 2(\beta h \cosh \beta h + \sinh \beta h) \right] \end{array} \right] \quad (4.A6.3)$$

$$C = \Phi \left[\begin{array}{l} f(\vec{k}) \left[-2\nu(2\beta h + \sinh 2\beta h) - (-2\nu(1 - \cosh 2\beta h) - 2\beta^2 h^2) \right] + \\ g(\vec{k}) \left[4\nu(\beta h \cosh \beta h + \sinh \beta h) - 2(1 - 2\nu)\beta h \sinh \beta h \right] \end{array} \right] \quad (4.A6.4)$$

$$D = \Phi \left[\begin{array}{l} f(\vec{k}) \left[(1 - \cosh 2\beta h) - (2\beta h + \sinh 2\beta h) \right] + \\ g(\vec{k}) \left[2\beta h \sinh \beta h + 2(\beta h \cosh \beta h + \sinh \beta h) \right] \end{array} \right] \quad (4.A6.5)$$

When substituted back into equations 4.A4 and 4.A3, the six components of the stress tensor can be written as

$$\begin{aligned} \sigma_{xx}(k_x, k_y, z) = & f(\vec{k}) \left[\frac{k_x^2}{|\vec{k}|^2} (C_f - S_f) - 2\nu S_f \frac{k_y^2}{|\vec{k}|^2} \right] \\ & + g(\vec{k}) \left[\frac{k_x^2}{|\vec{k}|^2} (C_g - S_g) - 2\nu S_g \frac{k_y^2}{|\vec{k}|^2} \right] \end{aligned} \quad (4.A7.1)$$

$$\begin{aligned}\sigma_{yy}(k_x, k_y, z) = f(\vec{k}) & \left[\frac{k_y^2}{|\vec{k}|^2} (C_f - S_f) - 2\nu S_f \frac{k_x^2}{|\vec{k}|^2} \right] \\ & + g(\vec{k}) \left[\frac{k_y^2}{|\vec{k}|^2} (C_g - S_g) - 2\nu S_g \frac{k_x^2}{|\vec{k}|^2} \right]\end{aligned}\quad (4.A7.2)$$

$$\sigma_{zz}(k_x, k_y, z) = f(\vec{k})[-C_f - S_f] + g(\vec{k})[-C_g - S_g] \quad (4.A7.3)$$

$$\sigma_{xy}(k_x, k_y, z) = \frac{k_x k_y}{|\vec{k}|^2} \left\{ f(\vec{k})[C_f - S_f + 2\nu S_f] + g(\vec{k})[C_g - S_g + 2\nu S_g] \right\} \quad (4.A7.4)$$

$$\sigma_{xz}(k_x, k_y, z) = \frac{ik_x}{|\vec{k}|} \left[f(\vec{k})S'_f + g(\vec{k})S'_g \right] \quad (4.A7.5)$$

$$\sigma_{yz}(k_x, k_y, z) = \frac{ik_y}{|\vec{k}|} \left[f(\vec{k})S'_f + g(\vec{k})S'_g \right] \quad (4.A7.6)$$

where $\vec{k} = (k_x, k_y)$ is the horizontal wavenumber, ν is Poisson's ratio, and depth dependence for the normal stress components and the horizontal shear stress components is given by the transfer functions

$$C_f = \frac{2\beta^2 h \zeta \cosh \beta z - \beta z \sinh \beta z - \beta z \sinh \beta(h + \zeta)}{1 + 2\beta^2 h^2 - \cosh 2\beta h} \quad (4.A8.1)$$

$$C_g = \frac{2\beta^2 h z \cosh \beta \zeta - \beta \zeta \sinh \beta \zeta - \beta \zeta \sinh \beta (h + z)}{1 + 2\beta^2 h^2 - \cosh 2\beta h} \quad (4.A8.2)$$

$$S_f = \frac{2\beta h \sinh \beta z + \cosh \beta z - \cosh \beta (h + \zeta)}{1 + 2\beta^2 h^2 - \cosh 2\beta h} \quad (4.A8.3)$$

$$S_g = \frac{2\beta h \sinh \beta \zeta + \cosh \beta \zeta - \cosh \beta (h + z)}{1 + 2\beta^2 h^2 - \cosh 2\beta h} \quad (4.A8.4)$$

where z is the depth from the top of the plate and $\zeta = h - z$ is the distance from the bottom of the plate. The transfer functions related to the bottom load $g(\vec{k})$ are depth-inverted versions of those related to the top load $f(\vec{k})$, such that any occurrence of z and ζ are interchanged. The transfer functions for the vertical shear stress components are related to those in equation 4.A8 by derivatives with respect to depth, such that

$$S'_{(f,g)} = -\frac{1}{\beta} \frac{d}{dz} [C_{(f,g)} + S_{(f,g)}]. \quad (4.A9)$$

4.6.3 Benchmarks of limit cases

We numerically compared the stress solutions above to those of *Love* [1929] for a point load in an elastic halfspace, and confirmed that stress calculations match to

within a factor of 10^{-3} . We also show that in the long wavelength limit, these solutions reduce to the 2D stress solutions for a thin elastic plate in which topography is exactly Airy compensated, such that $g(x, y) = f(x, y)$. We can simplify the full 3-D solution for the Airy compensation case where $g(x, y) = f(x, y)$, such that the stress solution given in equations 4.A7 – 4.A9 reduces to

$$\sigma_{xx} = f(\vec{k}) \left[\frac{k_x^2}{|\vec{k}|^2} [C - S] - 2\nu S \frac{k_y^2}{|\vec{k}|^2} \right] \quad (4.A10.1)$$

$$\sigma_{yy} = f(\vec{k}) \left[\frac{k_y^2}{|\vec{k}|^2} [C - S] - 2\nu S \frac{k_x^2}{|\vec{k}|^2} \right] \quad (4.A10.2)$$

$$\sigma_{zz} = f(\vec{k}) [-C - S] \quad (4.A10.3)$$

$$\sigma_{xy} = f(\vec{k}) \frac{k_x k_y}{|\vec{k}|^2} [C - S + 2\nu S] \quad (4.A10.4)$$

$$\sigma_{xz} = i \frac{k_x}{|\vec{k}|} f(\vec{k}) S', \quad (4.A10.5)$$

$$\sigma_{yz} = i \frac{k_y}{|\vec{k}|} f(\vec{k}) S', \quad (4.A10.6)$$

with transfer functions given by

$$C = \frac{\beta\zeta \cosh \beta z + \beta z \cosh \beta\zeta}{\sinh \beta h + \beta h} \quad (4.A11.1)$$

$$S = \frac{\sinh \beta z + \sinh \beta\zeta}{\sinh \beta h + \beta h} \quad (4.A11.2)$$

$$S' = -\frac{1}{\beta} \frac{d}{dz} [C + S] \quad (4.A11.3)$$

In the limit as $\beta \rightarrow 0$, the transfer function for the vertical shear stresses S' approaches zero, while the transfer functions for the horizontal shear stress and normal stresses, C and S , both approach $1/2$. The long wavelength stresses, therefore, become

$$\sigma_{xx} = -f(\vec{k})v \frac{k_y^2}{|\vec{k}|^2}, \quad (4.A12.1)$$

$$\sigma_{yy} = -f(\vec{k})v \frac{k_x^2}{|\vec{k}|^2}, \quad (4.A12.2)$$

$$\sigma_{xy} = f(\vec{k}) \nu \frac{k_x k_y}{|\vec{k}|^2}, \quad (4.A12.3)$$

with the applied load $\sigma_{zz} = -f(\vec{k})$ and the vertical shear stresses $\sigma_{xz} = \sigma_{yz} = 0$. These are the Cartesian stresses for a load within a thin elastic plate [e.g., *Dahlen*, 1981]. Based on these three benchmark comparisons, we are confident that the more general 3-D solution is correct.

4.6.4 Minimum deviatoric stress in a loaded elastic plate

The solutions of equation 4.A7 serve as Green's functions allowing the full 3-D stress tensor to be computed by a simple convolution in the Fourier domain. We seek the conditions for which the deviatoric stress given by this solution is minimized.

The second invariant of the deviatoric stress tensor $\tau_{ij} = \sigma_{ij} - \frac{1}{3}\sigma_{kk}$ is given by

$$II_\tau = \frac{1}{6} \left[(\sigma_{xx} - \sigma_{yy})^2 + (\sigma_{xx} - \sigma_{zz})^2 + (\sigma_{yy} - \sigma_{zz})^2 \right] + \sigma_{xy}^2 + \sigma_{xz}^2 + \sigma_{yz}^2 \quad (4.A13)$$

In terms of the transfer functions of equations 4.A8-4.A9, this becomes

$$II_\tau = \frac{1}{3} \left[3 \left(f(\vec{k}) C_f + g(\vec{k}) C_g \right)^2 - 3 \left(f(\vec{k}) S'_f + g(\vec{k}) S'_g \right)^2 \right. \\ \left. + \left(f(\vec{k}) S_f + g(\vec{k}) S_g \right)^2 (1 - 2\nu)^2 \right] \quad (4.A14)$$

which is minimized when $\nu = 1/2$, corresponding to an incompressible elastic solid. *Dahlen* [1981] similarly showed that in the 2-D case, the second invariant of the deviatoric stress from Airy compensated topography at mid-ocean ridges was minimized for $\nu = 1/2$, though this was never explicitly stated. Our analysis extends the results of *Dahlen* [1981] to three dimensions. Note that the form of the second invariant is the same as the stress used to define the von Mises yield condition. Therefore if the material has an elastic-plastic rheology and it has been stressed to its yield strength, then the minimum stress used in our models is also the maximum stress that can be maintained in the crust.

The dimensionless Green's functions for an Airy compensated load $g(\vec{k}) = f(\vec{k})$ on an incompressible elastic plate at depth $z = \frac{h}{4}$ are shown in Figure 4.A1. The wavenumbers have been scaled by the plate thickness h and the stress components have been scaled by the applied load $f(\vec{k})$. In the long-wavelength (zero-wavenumber) limit, the vertical shear stresses are zero and the vertical normal stress is the same as the size of the applied load. At this same limit, the horizontal stress components no longer depend upon the size of the horizontal radial wavenumber $|\vec{k}|$, but rather only depend upon the relative sizes of the two horizontal wavenumber components k_x and k_y , consistent with stress in a thin elastic plate. In the short-wavelength (infinite-wavenumber) limit, all stress components go to zero.

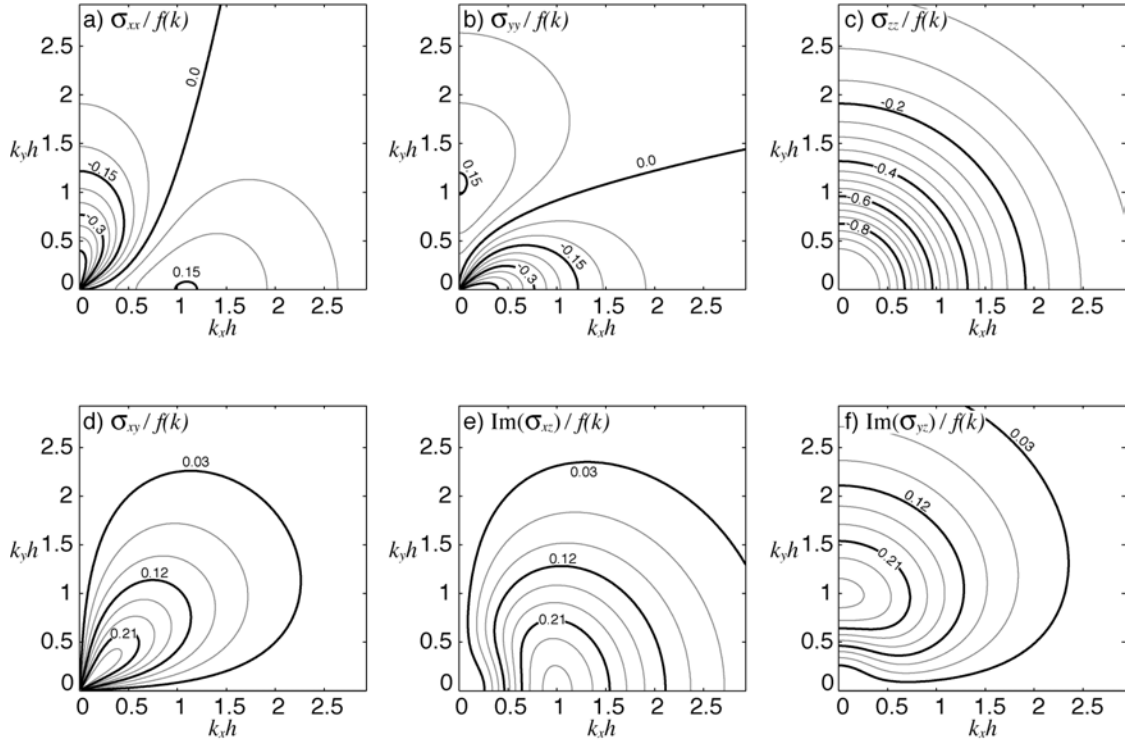


Figure 4.A1 Contours of Green's functions for each 3D stress tensor component assuming an Airy compensated load $g(\vec{k}) = f(\vec{k})$ on an incompressible elastic plate $\nu = \frac{1}{2}$ at depth $z = \frac{h}{4}$. Dimensionless horizontal wavenumber is scaled by the plate thickness h , and the dimensionless stress values are scaled by the size of the load $f(\vec{k})$. The Green's functions of the vertical shear stress components σ_{xz} and σ_{yz} are purely imaginary, so the imaginary component is plotted.

Fortran code to calculate the 3-D stress field due to an arbitrary surface topography load is provided at the following ftp location (ftp://topex.ucsd.edu/chile_topo_stress).

4.7 Acknowledgements

This research was supported by NASA Geodetic Imaging NNX09AD12G, the NASA Earth and Space Science Fellowship Program, and NSF EAR0811772.

Chapter 4, in part, is currently being prepared for submission for publication of the material. Luttrell, K., X. Tong, D. Sandwell, and B. Brooks, Estimates of stress drop and crustal tectonic stress from the February 27, 2010 Maule, Chile earthquake: Implications for fault strength. The dissertation author was the primary investigator and author of this material.

4.8 References

- Allmann, B.P., and P.M. Shearer (2009), Global variations of stress drop for moderate to large earthquakes, *Journal of Geophysical Research-Solid Earth*, 114.
- Andrews, D.J. (1980), A Stochastic Fault Model .1. Static Case, *Journal of Geophysical Research*, 85 (NB7), 3867-3877.
- Barrientos, S.E., and S.N. Ward (1990), The 1960 Chile Earthquake - Inversion for Slip Distribution from Surface Deformation, *Geophysical Journal International*, 103 (3), 589-598.
- Becker, J.J., D.T. Sandwell, W.H.F. Smith, J. Braud, B. Binder, J. Depner, D. Fabre, J. Factor, S. Ingalls, S.H. Kim, R. Ladner, K. Marks, S. Nelson, A. Pharaoh, R. Trimmer, J. Von Rosenberg, G. Wallace, and P. Weatherall (2009), Global Bathymetry and Elevation Data at 30 Arc Seconds Resolution: SRTM30_PLUS, *Marine Geodesy*, 32 (4), 355-371, doi: 10.1080/01490410903297766.
- Billen, M., E. Cowgill, and E. Buer (2007), Determination of fault friction from reactivation of abyssal-hill faults in subduction zones, *Geology*, 35 (9), 819-822.
- Boussinesq, J. (1885), *Application des Potentiels a l'Etude de l'Equilibre et du Mouvement des Solides Elastiques*, 508 pp., Gauthier-Viallars, Paris.
- Byerlee, J. (1978), Friction of Rocks, *Pure Appl. Geophys.*, 116 (4-5), 615-626.
- Cattin, R., H. LyonCaen, and J. Chery (1997), Quantification of interplate coupling in subduction zones and forearc topography, *Geophysical Research Letters*, 24 (13), 1563-1566.
- Dahlen, F.A. (1981), Isostasy and the Ambient State of Stress in the Oceanic Lithosphere, *Journal of Geophysical Research*, 86 (NB9), 7801-7807.
- Dahlen, F.A. (1990), Critical Taper Model of Fold-and-Thrust Belts and Accretionary Wedges, *Annual Review of Earth and Planetary Sciences*, 18, 55-99.
- Fialko, Y. (2004), Probing the mechanical properties of seismically active crust with space geodesy: Study of the coseismic deformation due to the 1992 M(w)7.3 Landers (southern California) earthquake, *Journal of Geophysical Research-Solid Earth*, 109 (B3).
- Hardebeck, J.L., and A. Aron (2009), Earthquake Stress Drops and Inferred Fault Strength on the Hayward Fault, East San Francisco Bay, California, *Bulletin of the Seismological Society of America*, 99 (3), 1801-1814.

- Hardebeck, J.L., and A.J. Michael (2004), Stress orientations at intermediate angles to the San Andreas Fault, California, *Journal of Geophysical Research-Solid Earth*, 109 (B11).
- Lamb, S. (2006), Shear stresses on megathrusts: Implications for mountain building behind subduction zones, *Journal of Geophysical Research-Solid Earth*, 111 (B7).
- Laske, G., G. Masters, and C. Reif (2001), CRUST 2.0: A New Global Crustal Model at 2x2 Degrees, <http://igppweb.ucsd.edu/~gabi/rem.html>.
- Leyton, F., J. Ruiz, J. Campos, and E. Kausel (2009), Intraplate and interplate earthquakes in Chilean subduction zone: A theoretical and observational comparison, *Physics of the Earth and Planetary Interiors*, 175 (1-2), 37-46.
- Love, A.E.H. (1929), The stress produced in a semi-infinite solid by pressure on part of the boundary, *Proc. Roy. Soc. Lond. A*, 228, 377-420.
- Luttrell, K., and D. Sandwell (2010), Ocean Loading Effects on Stress at Near Shore Plate Boundary Fault Systems, *J. Geophys. Res.*, *paper in press*.
- Luttrell, K., D. Sandwell, B. Smith-Konter, B. Bills, and Y. Bock (2007), Modulation of the earthquake cycle at the southern San Andreas fault by lake loading, *J. Geophys. Res.*, 112 (B08411), doi:10.1029/2006JB004752.
- Okada, Y. (1985), Surface Deformation Due to Shear and Tensile Faults in a Half-Space, *Bulletin of the Seismological Society of America*, 75 (4), 1135-1154.
- Okada, Y. (1992), Internal Deformation Due to Shear and Tensile Faults in a Half-Space, *Bulletin of the Seismological Society of America*, 82 (2), 1018-1040.
- Pavlis, N.K., S.A. Holmes, S.C. Kenyon, and J.K. Factor (2008), An Earth gravitational model to degree 2160, *General Assembly, Eur. Geosci. Union*.
- Ripperger, J., and P.M. Mai (2004), Fast computation of static stress changes on 2D faults from final slip distributions, *Geophysical Research Letters*, 31 (18).
- Sandwell, D.T., and W.H.F. Smith (2009), Global marine gravity from retracked Geosat and ERS-1 altimetry: Ridge segmentation versus spreading rate, *Journal of Geophysical Research-Solid Earth*, 114.
- Scholz, C.H. (2000), Evidence for a strong San Andreas fault, *Geology*, 28 (2), 163-166.
- Seno, T. (2009), Determination of the pore fluid pressure ratio at seismogenic megathrusts in subduction zones: Implications for strength of asperities and Andean-type mountain building, *Journal of Geophysical Research-Solid Earth*, 114.

Sick, C., M. Yoon, K. Rauch, A. Buske, S. Lüth, M. Araneda, B. Klaus, G. Chong, P. Giese, C. Krawczyk, J. Mechie, H. Meyer, O. Oncken, C. Reichert, M. Schmitz, S. Shapiro, M. Stiller, and P. Wigger (2006), Seismic Images of Accretive and Erosive Subduction Zones from the Chilean Margin, in *The Andes: Frontiers in Earth Sciences*, edited by O. Oncken, G. Chong, G. Franz, P. Giese, H. Götze, V. Ramos, M. Strecker, and P. Wigger, pp. 147-169, DOI: 10.1007/978-3-540-48684-8_7, Springer, Berlin.

Smith, B., and D. Sandwell (2004), A three-dimensional semianalytic viscoelastic model for time-dependent analyses of the earthquake cycle, *J. Geophys. Res.*, *109* (B12401), doi:10.1029/2004JB003185.

Song, T.R.A., and M. Simons (2003), Large trench-parallel gravity variations predict seismogenic behavior in subduction zones, *Science*, *301* (5633), 630-633.

Steketee, J.A. (1958), On Volterra's dislocations in a semi-infinite elastic medium, *Can. J. Phys.*, *36*, 192-205.

Tong, X., D. Sandwell, K. Luttrell, B. Brooks, M. Bevis, M. Shimada, J. Foster, R. Smalley, H. Parra, J.C. Baez Soto, M. Blanco, E. Kendrick, J. Genrich, and D. Caccamise (2010), The 2010 Maule, Chile earthquake: Downdip rupture limit revealed by space geodesy, *Geophys. Res. Lett.*, *in press*.

Yuan, X., S.V. Sobolev, and R. Kind (2002), Moho topography in the central Andes and its geodynamic implications, *Earth and Planetary Science Letters*, *199* (3-4), 389-402.

Zhong, S.J., and M. Gurnis (1994), Controls on Trench Topography from Dynamic-Models of Subducted Slabs, *Journal of Geophysical Research-Solid Earth*, *99* (B8), 15683-15695.

Zoback, M.D. (2000), Earth science - Strength of the San Andreas, *Nature*, *405* (6782), 31-32.

Zoback, M.L. (1992), 1st-Order and 2nd-Order Patterns of Stress in the Lithosphere - the World Stress Map Project, *Journal of Geophysical Research-Solid Earth*, *97* (B8), 11703-11728.

Chapter 5

Constraints on 3-D stress in the crust from support of mid-ocean ridge topography

Abstract

The direction of crustal stresses acting at mid-ocean ridges is well characterized, but the magnitude of these stresses is poorly constrained. We present a method by which the absolute magnitude of these stresses may be constrained using seafloor topography and gravity. The topography is divided into a short-wavelength portion, created by rifting, magmatism, and transform faulting, and a long-wavelength portion associated with the cooling and subsidence of the oceanic lithosphere. The short-wavelength surface and Moho topography are used to calculate the spatially varying 3-D stress tensor in the crust by assuming that in creating this topography, the deviatoric stress reached the elastic-plastic limiting stress; the Moho topography is constrained by short-wavelength gravity variations. Under these assumptions, an incompressible elastic material gives the smallest plastic failure stress associated with this topography. This short wavelength topographic stress generally predicts the wrong style of earthquake focal mechanisms at ridges (i.e., normal) and transform faults (i.e. strike-slip). However, the addition of an in-plane regional stress field is able to reconcile the combined crustal stress with both the ridge and transform focal mechanisms. By adjusting the magnitude of the regional stress, we determine a lower

bound for in situ ridge-perpendicular extension of 25 to 40 MPa along the slow-spreading mid-Atlantic ridge, 40 to 50 MPa along the ultra slow-spreading ridges in the western Indian ocean, and 10 to 30 MPa along the fast-spreading ridges of the southeastern Indian and Pacific oceans. Furthermore we constrain the magnitude of ridge-parallel extension to be between 4 to 8 MPa in the Atlantic ocean, -1 to 7 MPa in the western Indian ocean, and -1 to 3 MPa in the southeastern Indian and Pacific oceans. These observations suggest that a deep transform valley is an essential feature of the ridge-transform spreading center.

5.1 Introduction

The more than 50,000 km long global mid-ocean ridge is the morphologic result of rifting, magmatism, and transform faulting associated with seafloor spreading driven by plate tectonic forces. The magnitude of the resistive stresses needed to produce spreading and the associated topography is poorly constrained, especially along the remote ocean ridges where in situ stress measurements are largely unavailable [Heidbach *et al.*, 2008]. Bathymetry and gravity are two global data sets that could be used to constrain crustal stress in the spreading environment. To first order, the cross sectional shape of the spreading axis has either an axial valley or axial high depending on spreading rate and magma supply [Macdonald, 1982; Small and Sandwell, 1994]. Along slower spreading ridges, the axial valley is often shallower at the center of a ridge segment and systematically deepens towards the adjacent ridge-transform intersections [Blackman and Forsyth, 1989]. First order ridge segments are usually oriented perpendicular to the spreading direction and are offset by transform

faults with a characteristic spacing that also depends on spreading rate [*Macdonald et al.*, 1988]. Second-order offsets in some cases overlap and curve toward one another in the overlapping section. Most of these features seem to be spreading rate dependent [e.g., *Chen*, 1992; *Chen*, 1996; *Dick et al.*, 2003; *Purdy et al.*, 1992; *Sandwell and Smith*, 2009; *Small and Sandwell*, 1994].

In regions where adjacent offset ridges are connected by an orthogonal transform fault, that transform often coincides with a deep valley [*Gregg et al.*, 2007]. These deep oceanic transform valleys exhibit some of the steepest topography gradients anywhere on Earth's surface. It has long been the subject of debate whether transform faults at mid-ocean ridges are necessarily inherited structures from the pre-rifted plate or whether these features can evolve emergently from the processes that incite ridge development [e.g., *Choi et al.*, 2008; *Gerya*, 2010; *Oldenburg and Brune*, 1972; *Sandwell*, 1986]. Though recent studies have been able to identify emergent origins for a ridge-transform spreading morphology, none have reproduced the consistently deep topography of transforms.

While much is known about the orientation of the stress field at mid-ocean ridges, less is known about its magnitude. Primary observations of principal stress axes indicated by focal mechanisms show that the stress field at mid-ocean ridges is primarily 2-D and dominated by ridge-perpendicular extension. However *Gudmundsson* [1995] showed that various morphological characteristics of ridge-transform systems are better explained when the long-wavelength component of stress at mid-ocean ridges is one of biaxial extension, with both ridge-perpendicular and ridge-parallel stresses, rather than uniaxial extension in the ridge-perpendicular

direction alone. Possible origins of this ridge-parallel component include thermal stress [*Choi et al.*, 2008; *Sandwell*, 1986], flexural stress response to changes in spreading direction [*Pockalny et al.*, 1996], and plane stress resulting from isostatic compensation of the long-wavelength topography [*Neves et al.*, 2004]. Several studies have worked to constrain the ratio of ridge-normal stress to transform shear stress using the observations of ridge axis curvature towards a ridge-transform intersection [e.g., *Grindlay and Fox*, 1993; *Phipps-Morgan and Parmentier*, 1984], and more recent models have related the ratio of ridge-parallel thermal stress to ridge-perpendicular spreading-induced stress to spreading-rate dependent expressions of ridge-transform intersection morphology [*Choi et al.*, 2008]. While these forward-modeling studies help identify and describe the physical mechanisms guiding the evolution of ridge transform systems, they generally only refer to relative stress quantities and are unable to constrain the absolute magnitude of stress.

The aim of this study is to establish absolute constraints on the size of the long wavelength stress field along the entire global mid-ocean ridge, both the ridge-perpendicular and ridge-parallel components. We do this by estimating the absolute stress field associated with short-wavelength variations in bathymetry, including the ridge crest, median valley, and low transform valley. This estimate assumes that spreading plate boundary topography is critically strained beyond the plastic limit such that the actual stress state is the minimum deviatoric stress necessary to support the topography [e.g., *Dahlen*, 1981], which is an end member of the stress in a thick elastic plate loaded by topography. Part of this calculation also involves a global gravity flexure analysis to determine the variation of the elastic thickness parameter

along the global mid-ocean ridge and constrain the strength of the brittle oceanic lithosphere.

Based on this stress estimate, we may place absolute upper and lower constraints on the magnitude of long-wavelength ridge-parallel stress, whether in compression or extension, and an absolute lower bound on the magnitude of ridge-perpendicular extension. We do this by requiring the total deviatoric stress field along ridge or transform segment to be in a normal or strike-slip stress regime, respectively, consistent with the observations of earthquake focal mechanisms. The dominant factor in this analysis is the relative depth of the ridge and transform bathymetry across a particular region, but it is also sensitive to other local bathymetric features such as the presence of flanking bathymetric highs and the curvature of spreading segments at ridge-transform intersections.

Through our analysis we find a spreading rate dependence for the long-wavelength stress components such that the strength of the oceanic lithosphere, the magnitude of ridge-parallel extension, and the magnitude of ridge-perpendicular extension are all systematically higher at slower spreading centers and lower at fast spreading centers. Another result of our analysis is the suggestion that the low bathymetry observed at transform zones is a necessary feature of ridge-transform morphology, playing an important part in the mechanics of the region. The absolute magnitude of plate boundary forces has implications for efforts at modeling specific regional processes.

5.2 Short- and long-wavelength stress at ridges and transforms

A mid-ocean ridge consists of alternating segments of uplifted spreading ridge axis with stress in a normal regime and low, slipping transforms with stress in a strike-slip regime. If we initially assume that principal axes of the 3-D in situ stress tensor are aligned so that they are approximately vertical σ_v , ridge-perpendicular σ_{\perp} , and ridge-parallel σ_{\parallel} , then the stress state at the normal ridge axis requires

$$\sigma_v < \sigma_{\parallel} < \sigma_{\perp} \quad (5.1)$$

while the stress state at the transform offsets requires

$$\sigma_{\parallel} < \sigma_v < \sigma_{\perp} \quad (5.2)$$

where stress is positive in extension. We then divide the stresses into a short-wavelength topography-related component σ_{topo} and a long-wavelength plate-driving component $\Delta\sigma$, and find

$$\sigma_{v_{topo}} < \sigma_{\parallel_{topo}} + \Delta\sigma_{\parallel} < \sigma_{\perp_{topo}} + \Delta\sigma_{\perp} \quad (5.3)$$

at the ridges and

$$\sigma_{\parallel_{topo}} + \Delta\sigma_{\parallel} < \sigma_{v_{topo}} < \sigma_{\perp_{topo}} + \Delta\sigma_{\perp} \quad (5.4)$$

at the transforms. If we then assume the long-wavelength stress components are uniform across adjacent ridge and transform segments, then by calculating the components of short-wavelength topography stress we can place the following constraints on the size of the long-wavelength stress components:

$$\left(\sigma_{V_{topo}} - \sigma_{\parallel topo}\right)_{ridge} < \Delta\sigma_{\parallel} < \left(\sigma_{V_{topo}} - \sigma_{\parallel topo}\right)_{transform} \quad (5.5)$$

$$\begin{aligned} \Delta\sigma_{\perp} &> \left(\sigma_{\parallel topo} + \Delta\sigma_{\parallel} - \sigma_{\perp topo}\right)_{ridge} \\ \Delta\sigma_{\perp} &> \left(\sigma_{V_{topo}} - \sigma_{\perp topo}\right)_{transform} \end{aligned} \quad (5.6)$$

The condition on the ridge-perpendicular stress can always be met by increasing its value. Therefore this analysis can only place a lower bound on ridge-perpendicular stress. The ridge-parallel component, however, is constrained on both sides by the topography stress components at the ridge and transform segments. To first order, both constraints are satisfied when the depth of the transform valley exceeds the depth of the ridge axis (axial valley or axial high). However, they are also sensitive to other local bathymetric features, such as the presence of flanking bathymetric highs and the curvature of spreading segments, because it is the difference between the vertical and ridge-parallel components of the short-wavelength stress variations that makes up the key constraint.

The first step to estimating these bounding stress values is to divide the in situ stress field in the lithosphere into a short-wavelength component and a long-wavelength component. The unknown long-wavelength portion is comprised of all the stresses resulting from plate driving, including ridge push, slab pull, basal traction, etc., and may be safely assumed to be regionally homogeneous over the scale of individual adjacent ridge-transform segments, ~300 km or less. Specifically at the mid-ocean ridge, this long-wavelength component may be identified with the ridge push force. (It is most convenient to consider the lithostatic component of the stress field separately from the deviations from the lithostatic state, and any reference to the total stress field or long-wavelength component of the stress field throughout this study should be interpreted as the total or long-wavelength portion of the non-lithostatic component of the stress field.) The short-wavelength component of the in situ stress field consists of all the local processes of buoyant uplift, failure by brittle faulting or magmatic extension, gradual thermal cooling, etc., that define the individual characteristics of each ridge, transform, or non-transform offset segment. Though the long- and short-wavelength physical mechanisms may not be truly independent over geologic time, at a given instant (e.g., the present day) we may calculate their effects independently and superpose them linearly to infer the in situ stress state.

We assume that the short-wavelength (segment scale or less) variations in the stress field are expressed in the topographic features in the same spectral band, such that the stress field variations at this wavelength may be uniquely identified by the topographic structure. At mid-ocean ridges, the topographic features in this

wavelength band include the ridge crests, the axial highs or valleys, the low transform valleys and fracture zones, and the adjacent transform-flanking ridges. These features form over time through a complicated sequence of brittle and plastic deformation events that can be difficult to forward-model [e.g., *Buck et al.*, 2005; *Chen*, 1996; *Macdonald et al.*, 1996; *Menard*, 1984; *Pockalny et al.*, 1996]. However, regardless of the exact nature of this deformation, we assume that deformation at the active mid-ocean ridge plate boundary has reached a critical plastic limit such that the topography could not be any greater, and any additional applied stress would result in gross plate motion.

We must then determine the stress field that is supporting the short-wavelength topography, assuming it has reached a plastic limit. The height of the topography is set by the depth to the brittle-ductile transition, as only stresses in the brittle portion of the lithosphere will be sustained long-term. In the oceans, this transition is coincident with the 600° C isotherm which, depending on spreading rate and the presence of any hydrothermal cooling processes, may be as shallow as 3 km or as deep as 13 km [e.g., *Gregg et al.*, 2007], but largely coincides with the thickness of the crust near spreading ridges [*Buck et al.*, 2005]. For our purposes, therefore, the Moho may be considered the depth of compensation for this topography, such that all short-wavelength topography-supporting stress is sustained above this depth. If we assume that oceanic crust deforms according to an elastic-perfectly-plastic rheology, then the stress state supporting the observed topography at the critical elastic-plastic transition may be calculated by considering the elastic plate stresses associated with that topography.

We calculate the short-wavelength stress variations from topography within a finite thickness elastic plate that is loaded at its surface and base using a semi-analytic model (see Appendix A). The surface load is the weight of the observed short-wavelength topography, including the weight of the seawater above. The base load is that of the buoyant forces acting at or near the depth of compensation, including principally the compositional buoyancy above the actual Moho but also including any thermal buoyancy acting at these scales. As a force balance problem, the weight of the surface topography must be supported either by the buoyancy at the depth of the Moho or by the strength of the oceanic crust. For plastic failure, the critical quantity is the second invariant of the deviatoric stress tensor, sometimes known as the Von Mises stress. For an elastic stress state, this invariant quantity depends only on the applied loads and the Poisson's ratio of the material. A material with a Poisson's ratio of 0.5, corresponding to an incompressible elastic solid, has the smallest possible Von Mises stress associated with a given load [Luttrell *et al.*, 2010]. Because we intend to establish firm constraints on the absolute magnitude of the in situ stress state at the mid-ocean ridge, we proceed by calculating the stress state in an incompressible material so that the lower bounds we calculate may be taken as a firm minimum.

We can then use the pattern of local stress variations to determine constraints on the size of the long-wavelength stresses, as in equations 5.5 and 5.6. Figure 5.1 illustrates this schematically. The gray shaded bathymetry shown is from a region of the southern mid-Atlantic ridge. The colored regions are defined by contours of high-pass filtered bathymetry at a 300 m interval, such that the high red regions are at least 300 m above the low blue regions and at least 600 m above the very low purple

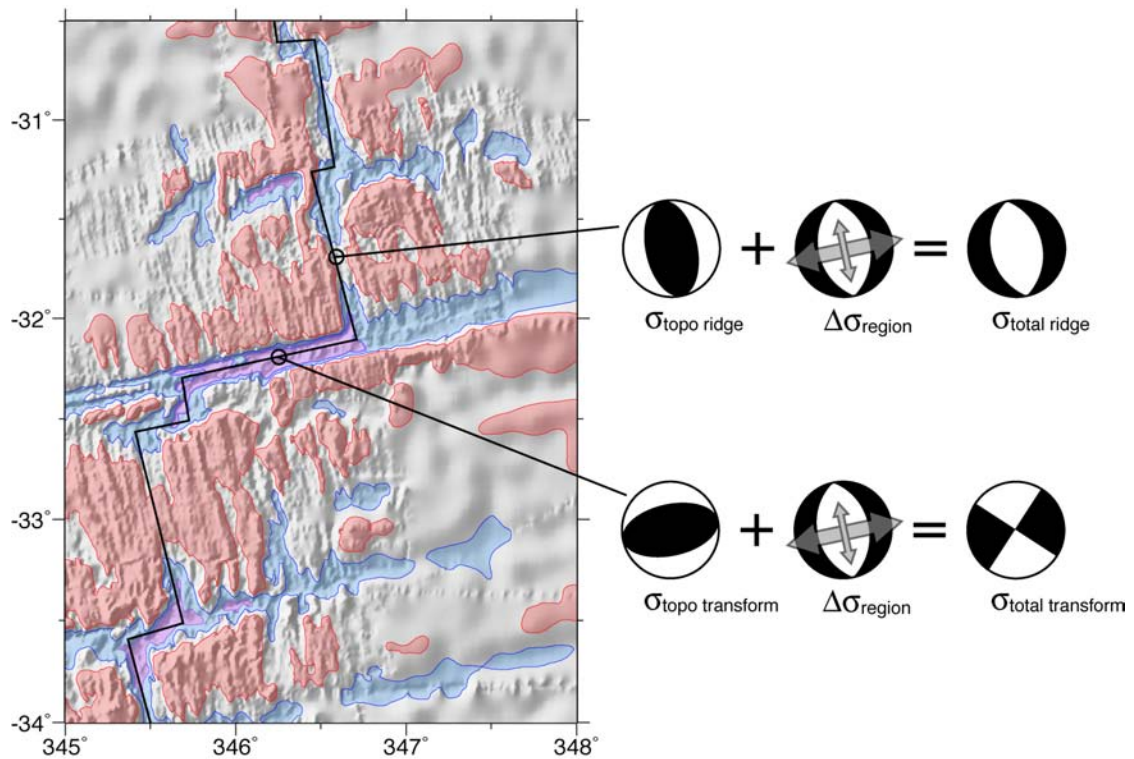


Figure 5.1 Schematic of short- and long-wavelength stress orientations at mid-ocean ridge and transform segments. Gray shaded bathymetry shown for a small region of the south Atlantic (within subregion 14 in Figure 5.2). Contours of high-pass filtered bathymetry are shown as shaded regions, with red, blue, and purple indicating high, low, and very-low regions respectively. Contour interval is 300 m. Black line indicates the plate boundary. Schematic focal mechanisms illustrate the individual orientations of short- and long-wavelength stress components, as well as the total stress, at both ridge and transform segments.

regions. At both the low ridge axis and transform valley, the stress state from topography would be in a thrust regime with orientation determined by the geometry of the adjacent high topography. The long-wavelength stress across the entire region is likely one of ridge-perpendicular extension with a normal regime. This extension must be large enough that the total regime at the ridge axis is normal, but not so large that the total regime at the transform also becomes normal.

5.3 Methods

We begin by identifying the wavelengths of topography that can be related to the stress state in the crust. We high-pass filter the bathymetry [Becker *et al.*, 2009] and gravity data [Sandwell and Smith, 2009] between spherical harmonics 100 and 140, corresponding to wavelengths between 300 and 400 km. This is long enough to include all the flexural features of the lithosphere, but short enough to remove the effects of any deep mantle processes. We then determine the best single depth location and approximate shape of the buoyant load at the depth of compensation by

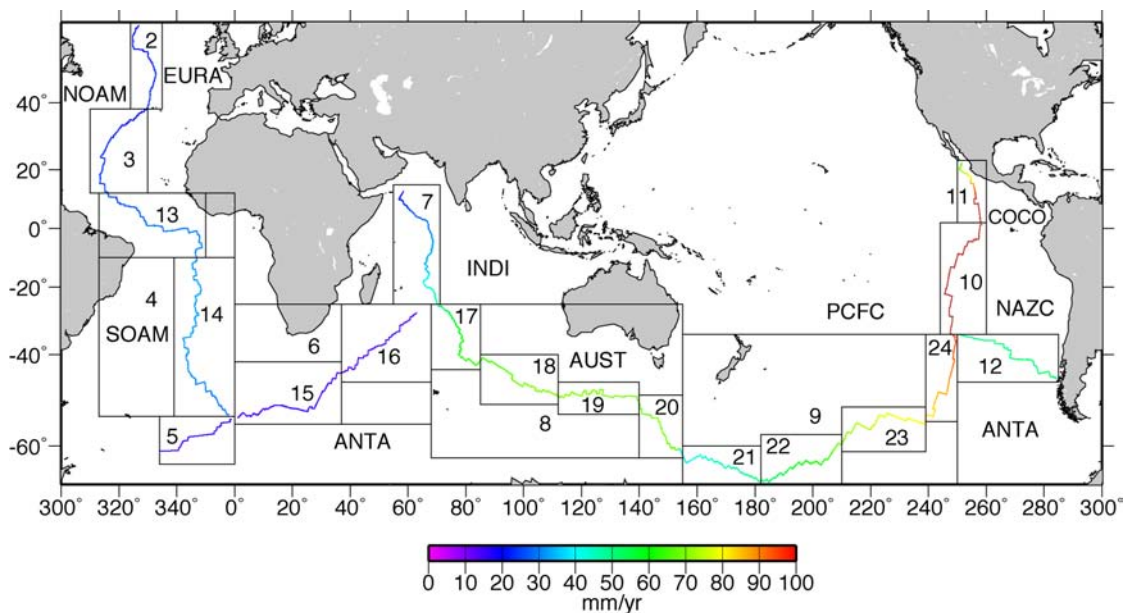


Figure 5.2 Spreading rate along the global mid-ocean ridge [DeMets *et al.*, 2010] and plate boundaries and subregions considered in this study. The numbers in each box correspond to the regions listed in Tables 5.1 and 5.3. Labels correspond to major tectonic plates: NOAM – North American, EURA – Eurasian, SOAM – South American, AFRC – African, ANTA – Antarctic, IND – Indian, AUST – Australian, PCFC – Pacific, NAZC – Nazca, and COCO – Cocos.

calculating the gravity field from a plate whose base load is related to the surface load through flexure (Appendix B; [Watts, 2001]). Modeled gravity is then compared to gravity observations at locations that are both within 30 km of the plate boundary and where bathymetry data are from ship soundings, to ensure the compared gravity fields are derived from independent data. We identify the optimal values of crustal density and elastic thickness for each spreading plate boundary individually, as well as for several plate subregions divided based on spreading behavior (Figure 5.2 and Table 5.1).

With these regional parameters, we estimate the spatial variation in the 3-D stress field by calculating the stress tensor throughout a thick elastic plate loaded by high-pass filtered bathymetry on the surface and by a deformed buoyant short-wavelength Moho at 7 km depth. The six components of the 3-D stress tensor are calculated using a semi-analytic model consisting of an analytically-derived Green's function for surface point loads convolved with the actual 2-D shape of the loads (Appendix A). A strong elastic plate with small but finite thickness loaded in this way is subject to large bending stresses that can obscure the bathymetry-related features we are attempting to isolate. For this reason, we integrate the stress components over the plate depth, which eliminates the horizontal compression and extension bending stresses that are approximately anti-symmetric with depth. The vertical shear tractions associated with bending, which are approximately symmetric with depth, are also reduced through this averaging.

Table 5.1 Gravity RMS, elastic thickness, and crustal density values at each plate boundary and subregion.

Number in Figure 5.1	Plate Boundary	Best T_e (km)	Best ρ_c (kg/m ³)	Best RMS (mGal)	Acceptable T_e (km)	RMS of acceptable T_e and ρ_c (mGal)	Spreading rate ^a (mm/yr)
1	Whole earth	5	3000	8.767	6	9.052	---
2 ^b	NOAM-EURA	10	2800	11.312	5	11.417	21.7
3	NOAM-AFRC	5	2900	9.381	5	9.515	22.8
4	SOAM-AFRC	5	3000	9.239	6	9.721	30.3
13	SOAM-AFRC 1	8	2900	9.687	8	9.994	28.4
14	SOAM-AFRC 2	3	3000	8.151	4	8.811	31.8
5 ^b	SOAM-ANTA	4	3000	12.269	5	13.257	15.3
6	AFRC-ANTA	6	3000	14.854	7	16.278	14.7
15	AFRC-ANTA 1	7	3000	14.938	8	16.530	15.1
16	AFRC-ANTA 2	5	3000	14.339	6	14.953	14.4
7	AFRC-INDI	8	2900	11.776	7	11.955	33.1
8	AUST-ANTA	2	3000	5.025	3	5.214	65.9
17	AUST-ANTA 1	2	3000	6.316	2	6.528	58.8
18	AUST-ANTA 2	2	3000	3.789	3	3.890	68.1
19	AUST-ANTA 3	2	3000	5.304	3	5.605	69.9
20 ^b	AUST-ANTA 4	2	2900	4.168	2	4.216	66.5
9	PCFC-ANTA	3	3000	6.114	5	6.332	67.6
21 ^b	PCFC-ANTA 1	5	2700	11.485	3	11.572	46.4
22	PCFC-ANTA 2	2	2900	3.658	2	3.733	59.2
23	PCFC-ANTA 3	4	3000	7.524	5	7.974	76.2
24	PCFC-ANTA 4	2	2800	4.679	2	4.679	88.5
10	PCFC-NAZC	3	2700	3.455	2	3.493	137.5
11	PCFC-COCO	11	2600	6.067	8	6.302	92.8
12	NAZC-ANTA	3	3000	8.571	4	8.749	50.7

^a spreading rate calculated from MORVEL plate velocities [DeMets *et al.*, 2010].^b denotes regions with few constrained gravity points at the plate boundary

We calculate the transitional failure stress associated with the sustained topography as the square root of the second invariant of the deviatoric component of this depth averaged stress tensor (Von Mises stress). This critical failure stress ranges from near zero in the flattest least-deformed regions (e.g., along the East Pacific Rise) to about 70 MPa in the steepest regions along deep transform valleys (e.g., the Romanche or Udintsev valleys), where the deviatoric stress must be quite large to

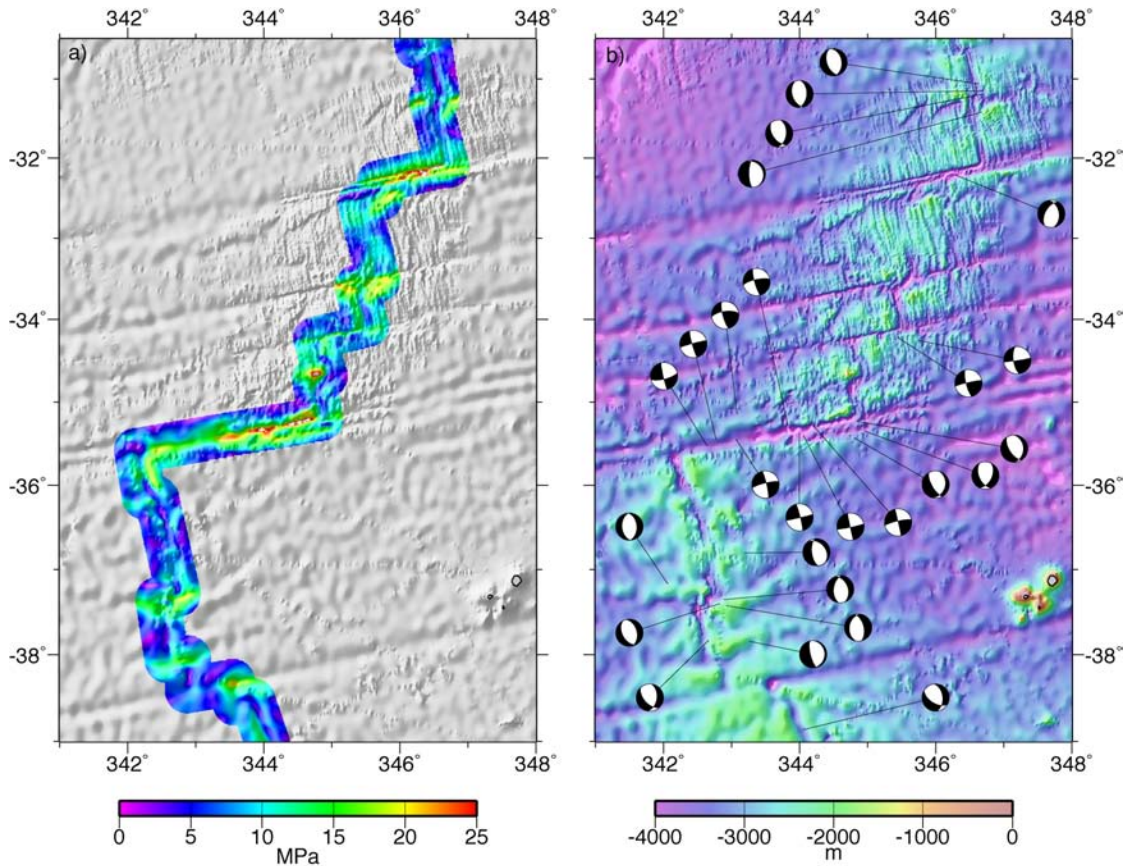


Figure 5.3 (a) Smallest plastic failure stress associated with short-wavelength topography, measured by the square root of the second invariant of the deviatoric stress field. (b) bathymetry along a portion of the southern mid-Atlantic ridge (within subregion 14 in Figure 5.2) with focal mechanisms from the WSM catalogue [Heidbach *et al.*, 2008].

Table 5.2 World Stress Map regime assignment criteria [after *Zoback, 1992*]

Regime	Plunge ϕ of pressure axis	Plunge ϕ of intermediate axis	Plunge ϕ of tension axis
normal	$\phi > 52^\circ$		$\phi < 35^\circ$
oblique normal/strike-slip	$40^\circ < \phi < 52^\circ$		$\phi < 20^\circ$
strike-slip	$\phi < 40^\circ$ $\phi < 20^\circ$	$\phi > 45^\circ$ $\phi > 45^\circ$	$\phi < 20^\circ$ $\phi < 40^\circ$
oblique thrust/strike-slip	$\phi < 20^\circ$		$40^\circ < \phi < 52^\circ$
thrust	$\phi < 35^\circ$		$\phi > 52^\circ$
undefined	any other configuration		

sustain the high load gradient. Figure 5.3a shows the critical plastic failure stress in a region of the southern mid-Atlantic ridge. Failure stress is ~ 25 MPa in the deep narrow transform valley, $\sim 15 - 20$ MPa at the ridge-transform intersections, and $5 - 10$ MPa along the spreading ridge axis.

These depth-averaged short-wavelength variations in the stress field are used to constrain the magnitude of the total stress field. We add a spatially-uniform horizontal 2-D stress field to the bathymetry-supporting stress field and determine the stress regime at each point, defined by the relative plunge angles of the principal stress axes (see Table 5.2), as in the World Stress Map project [*Zoback, 1992*]. We consider two sources of observations of the stress regime along the mid-ocean ridge. In the first, we assume that the appropriate regime along the entire length of every spreading ridge axis segment is normal, while the appropriate regime along all offset transform segments is strike-slip. The endpoints of each ridge and transform segment are digitized from gravity and bathymetry data [*Sandwell and Smith, 2009*] and the sample

locations along each segment are interpolated at a regular interval (~ 10 km), resulting in ~ 8000 observations of stress regime evenly sampling the entire mid-ocean ridge. The clear advantage of this dataset is that it gives a complete and uniform sampling of the global mid-ocean ridge. The disadvantage is that it a priori presumes the stress regime based on a morphology that requires some subjective judgment to define. We quantitatively define the fit between the regimes of a modeled stress field and the observed stress regimes with a goodness of fit parameter $\xi \in [0,1]$,

$$\xi = \begin{cases} 1 & \text{if model and observation stress regimes match} \\ 0.25 & \text{if observed stress regime is strikeslip and model} \\ & \text{stress regime is oblique normal/strike-slip} \\ 0 & \text{else} \end{cases} \quad (5.7)$$

The second observation set we consider is the information in the World Stress Map (WSM) catalogue [Heidbach *et al.*, 2008]. Along the mid-ocean ridge, this consists of 881 earthquake focal mechanisms, a subset of which are shown in Figure 5.3b. The advantage of this dataset is that it is based on observations of a direct in situ stress-related event (earthquake) rather than a presumed in situ stress-related process (deformation and formation of the ridge axis). Another advantage is that it includes information on the full 3-D orientation of the stress field, and can thus better constrain our calculations. The first major disadvantage is that the observations are not evenly distributed: slow-spreading regions tend to have many more large earthquakes than faster-spreading regions. The second major disadvantage is that because the

observations are located using seismic waves at stations far away from the events, they are subject to a mislocation error of up to 20-40 km [*Pan et al.*, 2002]. This mislocation is large enough that, e.g., a strike-slip earthquake that occurred on a transform valley could appear to be located off the plate boundary where the stress regime may be quite different. Because of these key limitations, we restrict our use of the WSM focal mechanisms to qualitative comparison and rely on the assigned ridge-transform stress regime for quantitative constraints.

The additional 2-D stress is defined by three parameters: the two perpendicular principal stresses and the orientation angle of those stresses. Initially we allowed the orientation angle to vary freely, but found no evidence that an orientation other than ridge-perpendicular and ridge-parallel was warranted. For the remainder of the analysis, we therefore focus on constraining the magnitude of long-wavelength stress aligned with the spreading direction at each point, defined by the MORVEL plate motions [*DeMets et al.*, 2010].

For each added long-wavelength stress field, we define a value of ξ at each point along the plate boundary and take the average value at all the ridges or transforms within a region or subregion separately, to get $\bar{\xi}_{ridge}$ and $\bar{\xi}_{transform}$. We then average these two values to get $\bar{\xi}$, the parameter of fit for each region. This averaging is important because the true constraint on the size of the long-wavelength stress depends upon the simultaneous fitting of both ridge and transform data. Averaging the fits to each individually adjusts for a region having a disproportionate quantity of ridge or transform observations.

Figure 5.4 Contours of mean model fit at both ridges and transforms ($\bar{\xi}$) as a function of added ridge-perpendicular and ridge-parallel stress ($\Delta\sigma_{\perp}$ and $\Delta\sigma_{\parallel}$ respectively) for each plate boundary and subregion. Contour interval is 0.05. Quantitative fit is defined as in equation 5.7. Constrained values of $\Delta\sigma_{\perp}$, $\Delta\sigma_{\parallel}$, and $\bar{\xi}_{\max}$ for each region are summarized in Table 5.3 and Figure 5.7.

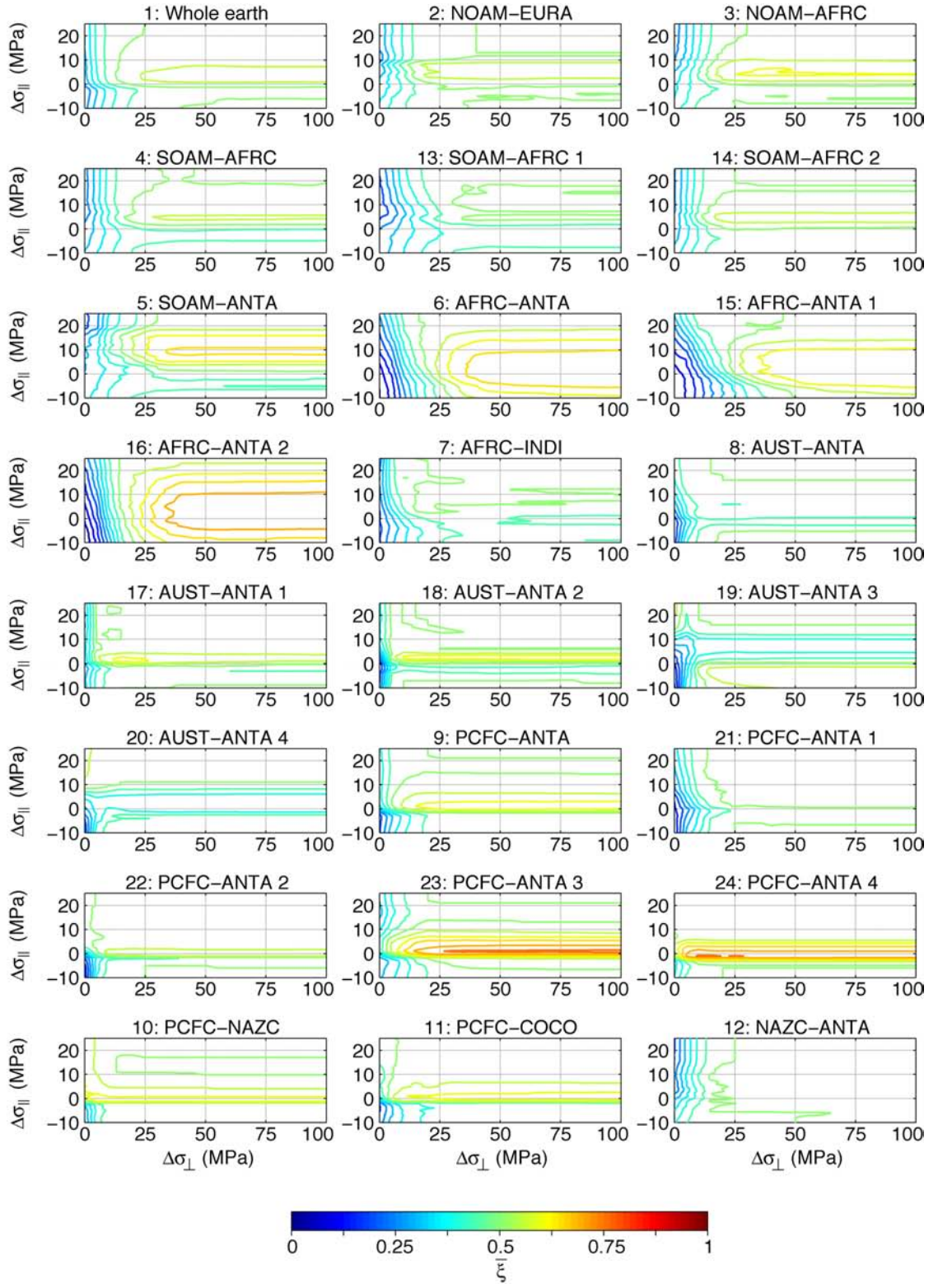


Figure 5.5 Mean model fit at ridges (blue), transforms (green), and both (red) over each plate boundary and subregion as a function of long-wavelength ridge-parallel stress ($\Delta\sigma_{\parallel}$), assuming a ridge-perpendicular extension of 100 MPa. Horizontal black line indicates the threshold value for determining the range of best-fitting stress, $0.98 \bar{\xi}_{\max}$. Vertical lines capped with right- and left-pointing arrows indicate the minimum and maximum value of $\Delta\sigma_{\parallel}$ that optimizes model fit at both ridges and transforms.

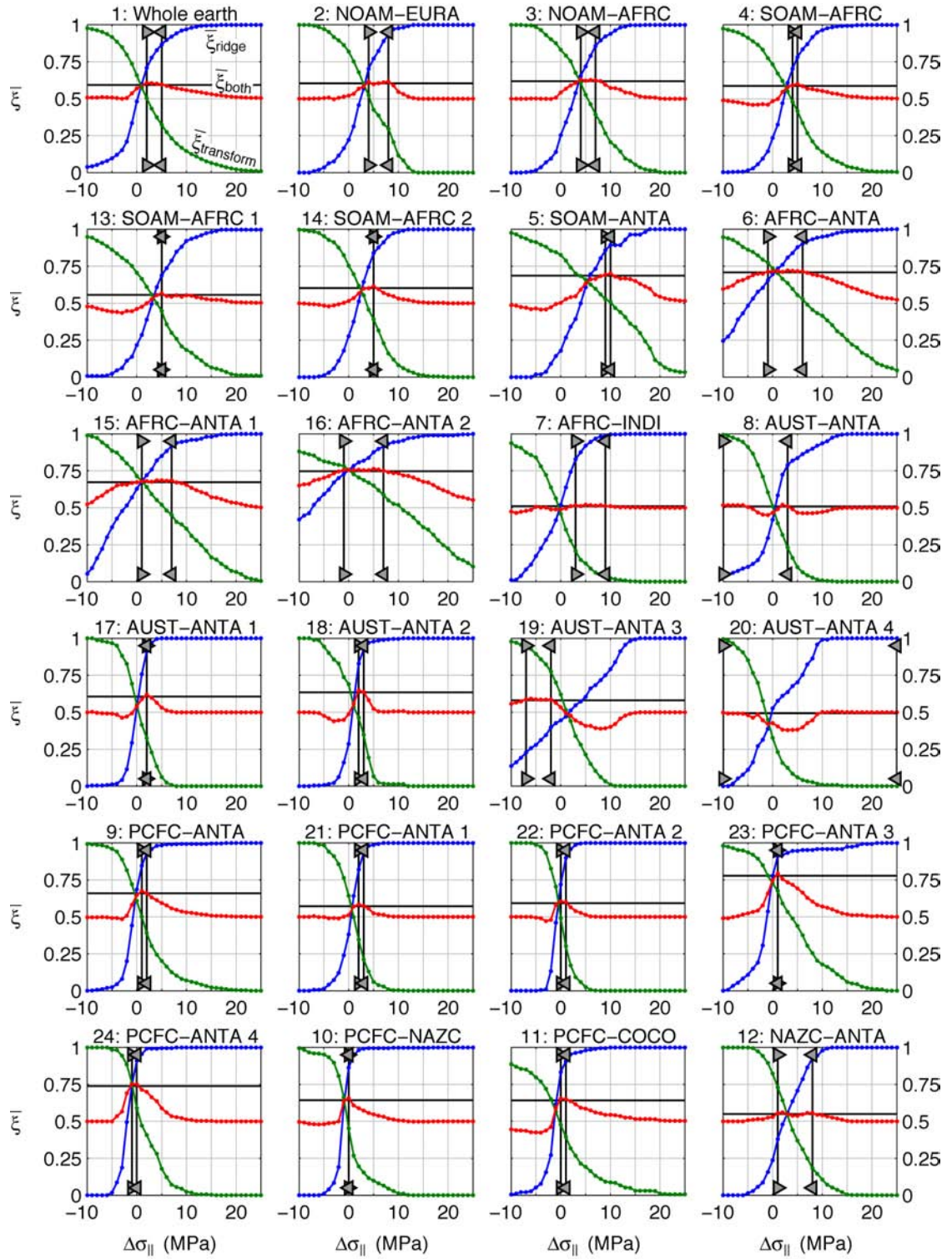
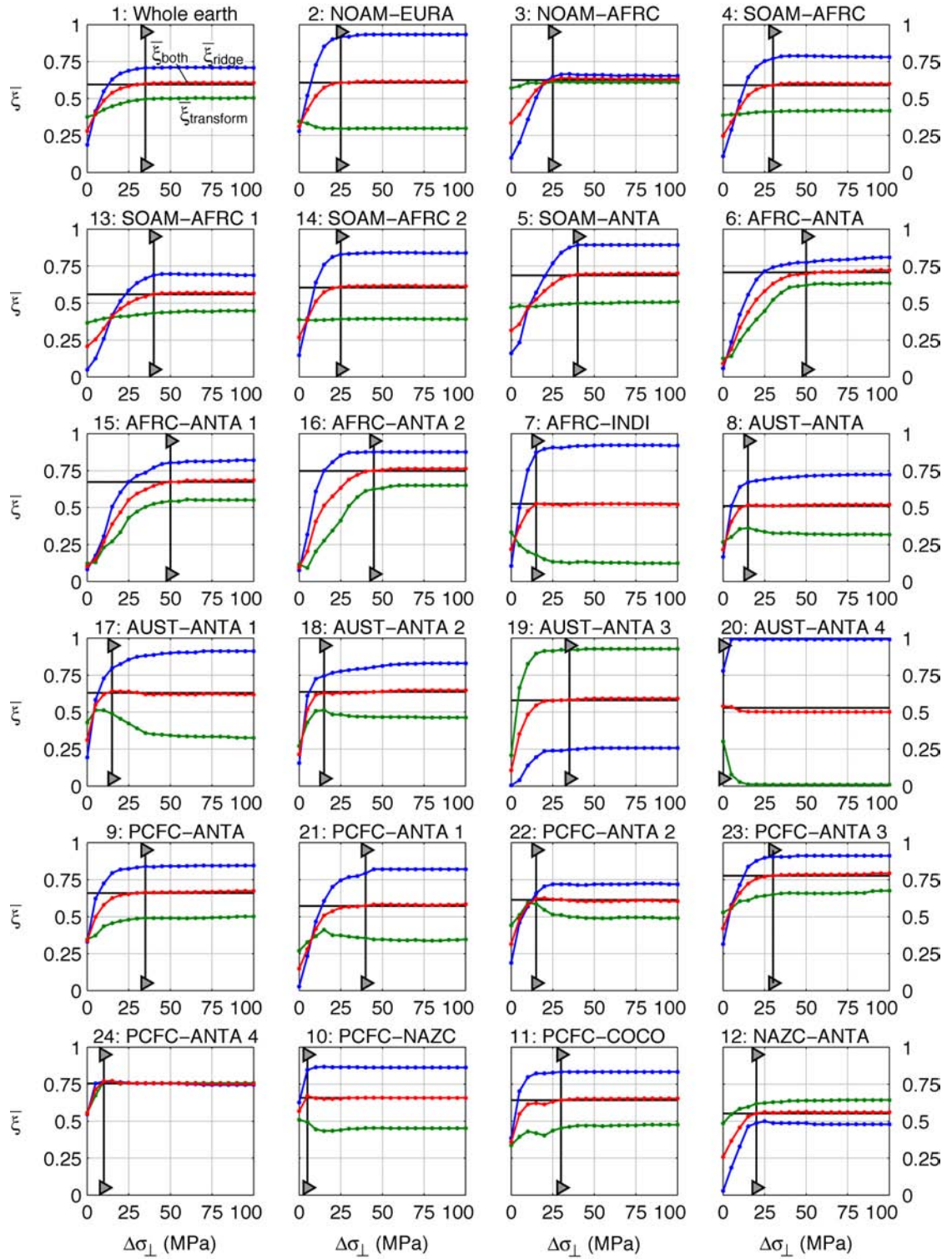


Figure 5.6 Mean model fit at ridges (blue), transforms (green), and both (red) over each plate boundary and subregion as a function of long-wavelength ridge-perpendicular stress ($\Delta\sigma_{\perp}$), assuming the optimal ridge-parallel extension value in each region, listed in Table 5.3. Horizontal black line indicates the threshold value for determining the minimum ridge-perpendicular stress, $0.98 \bar{\xi}_{\max}$. Vertical line capped with right-pointing arrows indicates the minimum value of $\Delta\sigma_{\perp}$ that optimizes the fit at both ridges and transforms.



5.4 Results

Figure 5.4 shows contours of the mean fit $\bar{\xi}$ at each plate boundary and subregion as a function of the long-wavelength ridge-perpendicular and ridge-parallel stresses ($\Delta\sigma_{\perp}$ and $\Delta\sigma_{\parallel}$). At most of the regions, there is an easily discernable maximum $\bar{\xi}$ contour with a defined minimum ridge-perpendicular value and defined minimum and maximum ridge-parallel values. Because the constraint on $\Delta\sigma_{\perp}$ depends upon the determined value for $\Delta\sigma_{\parallel}$ (equation 5.6), we first determine the constraint on $\Delta\sigma_{\parallel}$ by examining a profile of $\bar{\xi}$ versus $\Delta\sigma_{\parallel}$ at a value of $\Delta\sigma_{\perp} = 100$ MPa (Figure 5.5). For each region, the blue and green curves show the value of $\bar{\xi}$ averaged over all the ridges and transforms, respectively, within that region. In most regions, some ridge-parallel extension is required to bring all the ridge points in to a normal stress regime. This is an effect of the deep median valleys at some ridge segments, evidenced by the stronger need for ridge-parallel extension at slower spreading regions like AFRC-ANTA than at faster spreading regions like PCFC-NAZC. In the absence of any ridge-parallel stress, most regions fit at least half of the defined transform points, with successively more being fit as ridge-parallel stress becomes more compressive.

The true test of our model is its ability to simultaneously accurately predict regions of ridge normal and transform strike-slip stress regimes. The red line in Figure 5.5 is the average of $\bar{\xi}_{ridge}$ and $\bar{\xi}_{transform}$, which weights the ridge and transform fits evenly and compensates for any regional difference in the relative abundance of

Table 5.3 Best mean model fit, with corresponding range of long-wavelength ridge-parallel stress and minimum ridge-perpendicular stress.

Number in Figure 5.1	Plate Boundary	$\bar{\xi}_{\max}$	$\Delta\sigma_{\parallel}$ (MPa)	$\Delta\sigma_{\perp}$ (MPa)
1	Whole earth	0.606	2-5	35
2	NOAM-EURA	0.619	4-8	25
3	NOAM-AFRC	0.638	4-7	25
4	SOAM-AFRC	0.602	4-5	35
13	SOAM-AFRC 1	0.569	5	40
14	SOAM-AFRC 2	0.616	5	25
5	SOAM-ANTA	0.701	9-10	40
6	AFRC-ANTA	0.723	-1-6	50
15	AFRC-ANTA 1	0.686	1-7	50
16	AFRC-ANTA 2	0.762	-1-7	45
7 ^a	AFRC-INDI	0.536	3-9 ^a	15 ^a
8 ^a	AUST-ANTA	0.521	-10-3 ^a	15 ^a
17	AUST-ANTA 1	0.643	2	15
18	AUST-ANTA 2	0.651	2-3	15
19	AUST-ANTA 3	0.592	-7- -2	35
20 ^a	AUST-ANTA 4	0.541	-10-25 ^a	0 ^a
9	PCFC-ANTA	0.673	1-2	35
21	PCFC-ANTA 1	0.583	2-3	40
22	PCFC-ANTA 2	0.625	0-1	15
23	PCFC-ANTA 3	0.793	1	30
24	PCFC-ANTA 4	0.770	-1-0	10
10	PCFC-NAZC	0.670	0	5
11	PCFC-COCO	0.654	0-1	30
12	NAZC-ANTA	0.563	1-8	20

^a denotes regions with $\bar{\xi}_{\max} < 0.550$, such that constraints on $\Delta\sigma_{\parallel}$ and $\Delta\sigma_{\perp}$ are unreliable

ridge or transform segments. In most regions this curve reaches a clear broad maximum value $\bar{\xi}_{\max}$ somewhere in the range of 0-10 MPa ridge-parallel extension.

We define the width of this maximum as the range of $\Delta\sigma_{\parallel}$ values for which

$\bar{\xi} > 0.98\bar{\xi}_{\max}$. This threshold is indicated by the horizontal black line, and the

satisfying $\Delta\sigma_{\parallel}$ range is indicated by the vertical black lines capped with right- and left-pointing arrows. The values of $\Delta\sigma_{\parallel}$ and $\bar{\xi}_{\max}$ for each plate boundary and subregion are listed in Table 5.3. In most regions, $\Delta\sigma_{\parallel}$ is constrained to a narrow range of slightly extensional stress values. In three regions, AFRC-INDI, AUST-ANTA, and AUST-ANTA 4 (regions 7, 8, and 20), $\bar{\xi}_{\max}$ is 0.550 or below, indicating that in these regions there is no single long-wavelength stress that can be added to our calculated topographic stress and satisfactorily simultaneously fit the expected regime of both ridge and transform regions. Because the models fail in these regions, they are subsequently omitted from the rest of the analysis. The only region which requires ridge-parallel compression is AUST-ANTA 3 (region 19), consisting of the intermediate-fast spreading discordant section of the plate boundary.

Once the values of $\Delta\sigma_{\parallel}$ have been determined, we can evaluate profiles of $\bar{\xi}$ versus $\Delta\sigma_{\perp}$ at the best value of $\Delta\sigma_{\parallel}$ for each region. In Figure 5.6, the blue and green lines again show profiles of $\bar{\xi}_{\text{ridge}}$ and $\bar{\xi}_{\text{transform}}$ respectively, and the red line shows their average. Generally, $\bar{\xi}$ increases rapidly with $\Delta\sigma_{\perp}$ up to a point, after which it tapers to a maintained maximum level $\bar{\xi}_{\max}$. Once again we define the threshold for determining the value of $\Delta\sigma_{\perp}$ such that $\bar{\xi} > 0.98\bar{\xi}_{\max}$, indicated by the horizontal black line in each region subplot. The vertical black line with right-pointing triangle endcaps indicates the minimum $\Delta\sigma_{\perp}$ value at which this threshold is reached (values summarized in Table 5.3). In general, ridge-perpendicular extension

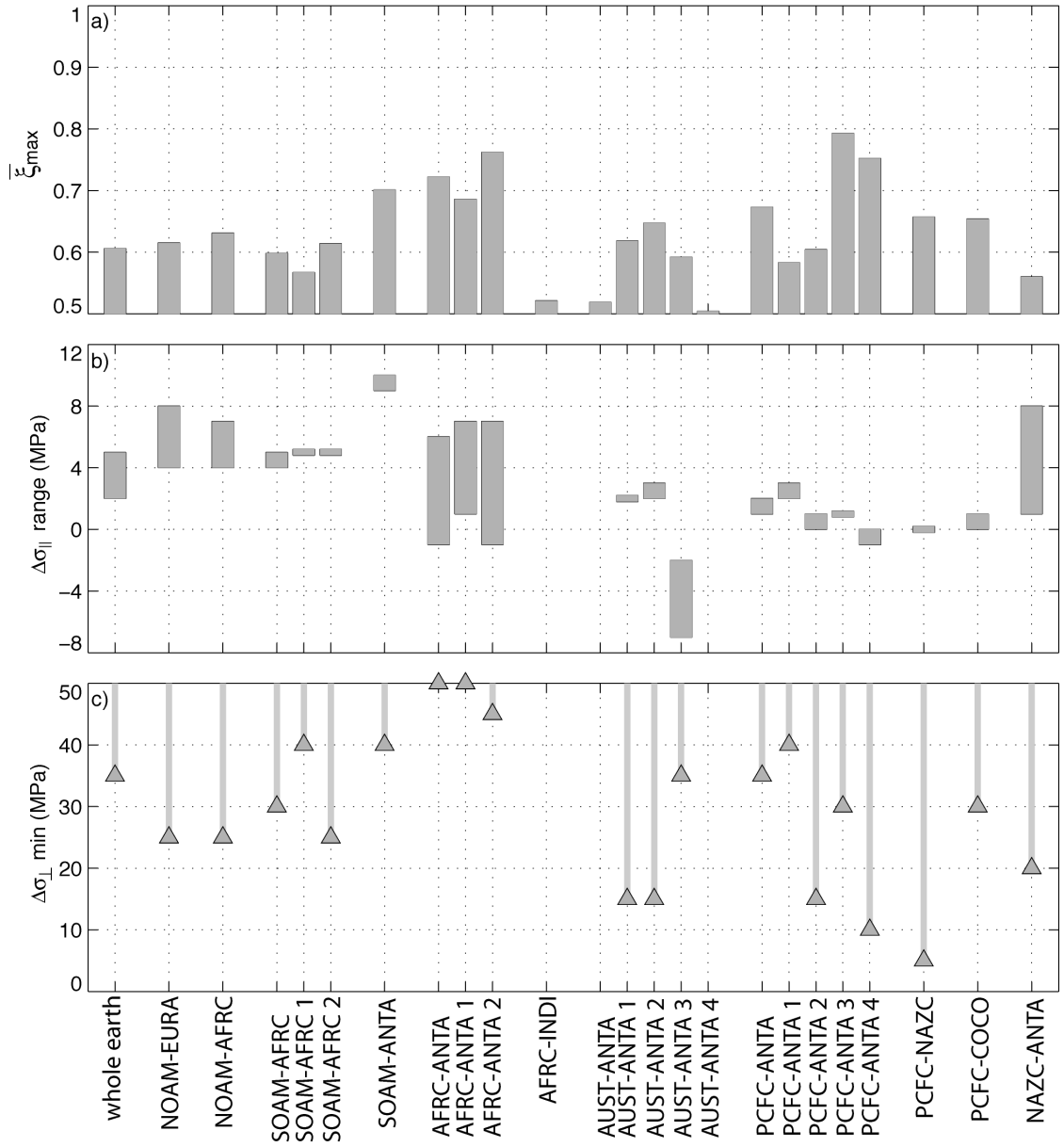


Figure 5.7 Summary of regional variation of (a) $\bar{\xi}_{\max}$, (b) long-wavelength ridge-parallel stress ($\Delta\sigma_{\parallel}$) range, and (c) minimum ridge-perpendicular stress ($\Delta\sigma_{\perp}$). (Values given in Table 5.3). Values of $\Delta\sigma_{\parallel}$ and $\Delta\sigma_{\perp}$ are not shown for AFRC-INDI, AUST-ANTA, and AUST-ANTA 4 (regions 7, 8, and 20) because these regions with $\bar{\xi}_{\max} < 0.550$ are poorly constrained.

must be at least 5 – 50 MPa to simultaneously fit the regime at both ridges and transforms.

The constrained values of $\bar{\xi}_{\max}$, $\Delta\sigma_{\perp}$, and $\Delta\sigma_{\parallel}$ are summarized in Figure 5.7.

Examining these results, we begin to notice a relationship between the constrained stress magnitude and spreading rate. The slower-spreading mid-Atlantic segments generally require 4 – 8 MPa ridge-parallel extension, while the faster-spreading Pacific segments generally require 0 – 3 MPa ridge-parallel extension, or even slight compression. Once again we notice the unusual result of the discordant zone of AUST-ANTA 3 requiring 2 – 7 MPa ridge-parallel compression. Constraints on the ridge-perpendicular component are somewhat more varied. The slow-spreading Atlantic segments require at least 25-40 MPa ridge-perpendicular extension and the ultra-slow spreading regions of the AFRC-ANTA plate boundary require at least 45-50 MPa extension. The faster-spreading Pacific segments are more varied, requiring 5-40 MPa ridge-perpendicular extension.

Figure 5.8 clarifies the relationship between spreading rate and elastic thickness, $\Delta\sigma_{\perp}$, and $\Delta\sigma_{\parallel}$. A clear decrease in elastic thickness is observed with spreading rate down to ~2 km at 70 mm/yr, after which the dependence tapers off, such that the fastest spreading regions still maintain finite strength with a 2 km elastic thickness. One exception seems to be the 8 km elastic thickness predicted for the PCFC-COCO plate boundary. The ridge-parallel stress shows a similar pattern of decreasing with spreading rate up to about 80 mm/yr, and then leveling off around 0 MPa for faster spreading regions. In this case, the clear exception is again the strong

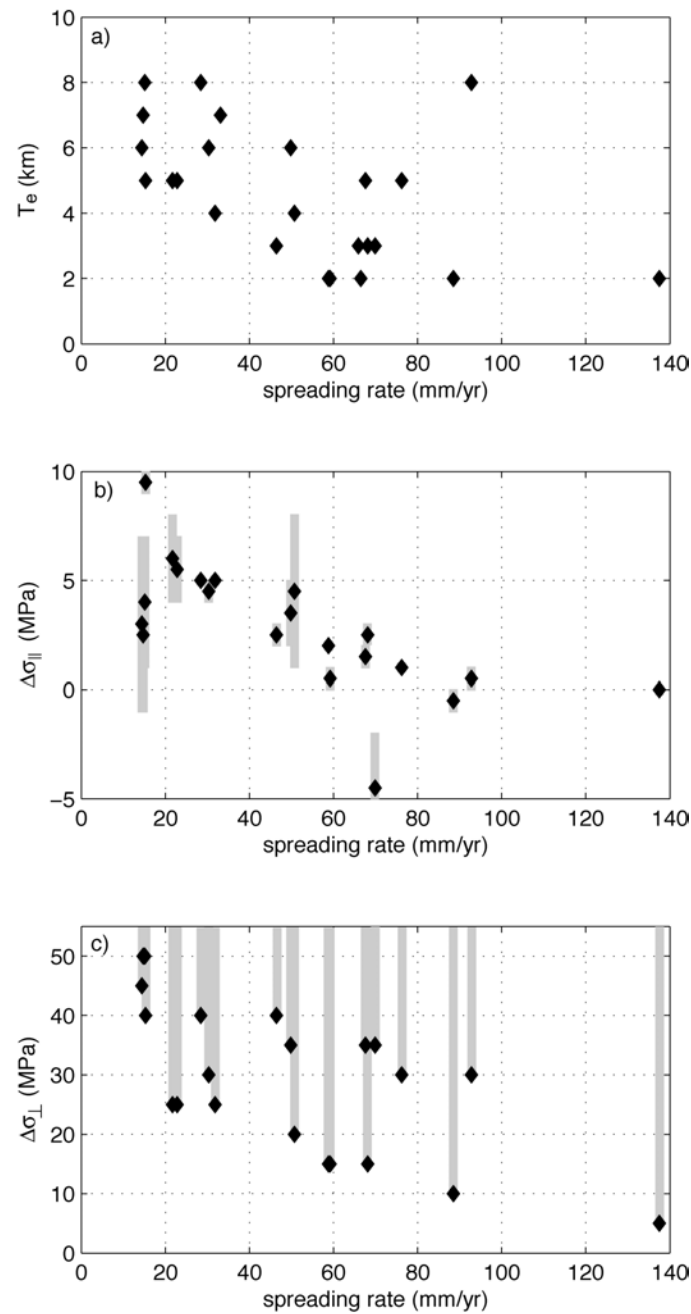


Figure 5.8 Spreading rate versus (a) elastic thickness, (b) range of ridge-parallel stress ($\Delta\sigma_{||}$), and (c) minimum ridge-perpendicular stress ($\Delta\sigma_{\perp}$) for each plate boundary and subregion. (Values given in Tables 5.1 and 5.3). The value of $\Delta\sigma_{||}$ plotted in (b) is the midpoint of the acceptable range.

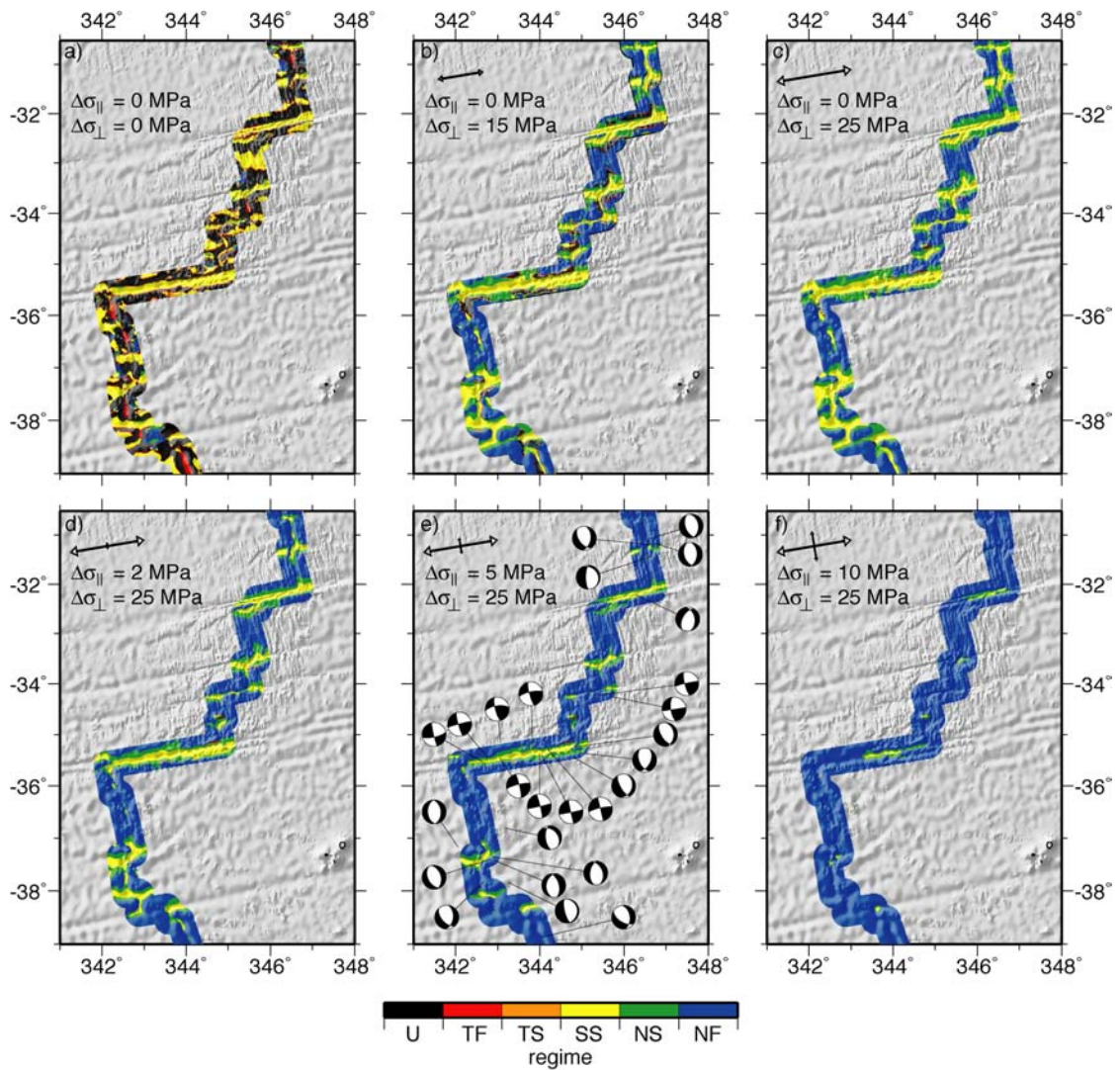


Figure 5.9 Spatial distribution of stress regime for topographic stress variations added to various long-wavelength stress fields, for the same area as shown in Figure 5.3. Thrust, strike-slip, and normal regime indicated by red, yellow, and blue respectively. Oblique thrust and oblique normal regime indicated by orange and green respectively. Black regions indicate the regime of the stress orientation is undefined. (Regime definition criteria are summarized in Table 5.2). (a) Stress regime from short-wavelength topography alone with no additional long-wavelength stress. Stress regime with (b) insufficient $\Delta\sigma_{\perp}$ (15 MPa) and (c) minimum sufficient $\Delta\sigma_{\perp}$ (25 MPa). Stress regime with minimum sufficient $\Delta\sigma_{\perp}$ and (d) too little $\Delta\sigma_{\parallel}$ (2 MPa), (e) optimal $\Delta\sigma_{\parallel}$ (5 MPa), and (f) too much $\Delta\sigma_{\parallel}$ (10 MPa). WSM focal mechanisms shown atop best-fitting total stress field (e), with strike-slip regime predicted at low transform offsets and normal regime predicted nearly everywhere else.

compression required by the discordant zone in the southern ocean. The trend is less pronounced for ridge-perpendicular stress, but it still shows a steady decrease in minimum $\Delta\sigma_{\perp}$ value through 90 mm/yr.

It is illustrative to examine the predicted stress regime along the plate boundary in mapview. Figure 5.9 shows the predicted stress regime for the same small region of the southern mid-Atlantic ridge computed from short-wavelength topography plus a range of long-wavelength tectonic stress fields. Regime is color coded with blue and yellow indicating normal and strike-slip regimes, red indicating thrust regime, green and orange indicating oblique normal and oblique thrust regimes, and black indicating a regime unable to be classified by the criteria in Table 5.2. For topography stress alone (Figure 5.9a), the lowest regions are in a thrust or strike-slip regime, while much of the flanking seafloor is in an unclassifiable orientation. This is due to the large vertical shear stresses associated with a bending plate. As $\Delta\sigma_{\perp}$ increases, the slightly off-axis regions attain a normal regime, but the predicted strike-slip regime is still too widespread (Figure 5.9c). As $\Delta\sigma_{\parallel}$ increases, the ridges become more consistently normal until an optimal balance is found between a normal regime at the ridge axes and a strike-slip regime at the transform valleys, flanked by narrow transitional regions of oblique normal-strike-slip regime (Figure 5.9e). As $\Delta\sigma_{\parallel}$ continues to increase, the entire region is moved into a normal regime (Figure 5.9f).

5.5 Discussion

Several studies have used numerical models to identify the processes required to initiate new plate spreading and form the pattern of mostly-perpendicular ridge and transform segments observed throughout the modern ocean [Gerya, 2010]. However, though such models can reproduce the characteristic segment spacing and spreading rates associated with various types of plate spreading, including the uplifted topography of ridge flanks, they have not reproduced the bathymetric lows of the transform offsets. This suggests that transform valleys are not necessarily a part of spreading initiation, but rather may play an important role in maintaining a transform offset once initiated. It could be that as a ridge transform system is developing, those protero-offsets that coincide with deep bathymetry, formed by any active inelastic deformation process at that time, are the offsets that persevere, while those whose formation does not coincide with a bathymetric valley are preferentially abandoned. Thus bathymetric valleys, though not necessarily present at the initiation of plate spreading, may be an important part of the development of a mature ridge-spreading system.

Though the calculations presented here do not account for preexisting fault structures, the orientation of the fault planes at the normal ridge axis align with the planes of maximum shear stress of the predicted 3-D stress tensor. However, the predicted planes of maximum shear stress at transform offsets, even though the regime is strike-slip, strike 45° away from the observed transform. The orientation of these transform segments is primarily defined by the preexisting need to connect the broken ends of the spreading axis, forcing the fault to be aligned with principal extension in

the ridge-perpendicular direction. This observation agrees with previous studies suggesting that oceanic transform faults sustain very low shear stresses and may be poorly seismically coupled [e.g., *Behn et al.*, 2002].

A curious result is that the discordant zone of the Australian-Antarctic plate boundary seems to require ridge-parallel compression in order to simultaneously fit the stress regime at both ridges and transforms. An alternative interpretation of this constraint is that the ridges require large ridge-parallel extension (15 MPa or more) in order to bring even the ridges into a normal stress regime. With this much ridge-parallel extension, none of the transforms would remain in a strike-slip regime. This model result is likely a reflection of the anomalously low bathymetry in this region [e.g., *Forsyth et al.*, 1987; *Holmes et al.*, 2010], related to an anomalously low temperature and magma supply.

The regions of AFRC-INDI, AUST-ANTA, and subregion AUST-ANTA 4 are the locations where the predictions of this model are least successful. These subregions make up a long section of ridge in the eastern Indian ocean spreading at an intermediate rate. Model indications suggest that ridges at AFRC-INDI require non-zero ridge-parallel extension, but that transforms at this plate boundary require non-zero ridge-parallel compression. These two non-compatible conditions may reflect the presence of lower ridge topography with a deep axial valley in the northern section of this plate boundary contrasted with rugged topography with densely-spaced fracture zones in the southern section. Model results at AUST-ANTA may also be divided into two sections by the slope of $\bar{\xi}_{ridge}$ as a function of $\Delta\sigma_{||}$ (Figure 5.5). The western half

(regions 17 and 18) requires the ridge-parallel extension (or compression) to be near zero in order to fit both the ridges and transforms. The eastern half (regions 19 and 20), including the discordant zone, exhibits a much shallower slope of $\bar{\xi}_{ridge}$, requiring a much higher extension in order to fit all the ridge points, but also allowing many of the ridge points to be fit even with ridge-parallel compression. This is principally indicative of the great variety of ridge-transform morphology along this plate boundary.

5.6 Conclusions

We have demonstrated that the rapid variation in stress regime between spreading ridge and transform segments may be forward modeled as the sum of two stresses: a long-wavelength regionally uniform tectonic driving stress and a short-wavelength regionally varying stress related to the support of observable bathymetric features. The short-wavelength stress variations may be calculated as those of the critical elastic-plastic failure transition, measured by the second invariant of the deviatoric stress. This plastic failure stress ranges from 0 – 70 MPa, depending on the ruggedness of the bathymetry. Along most spreading plate boundaries, we are able to satisfactorily model the observed variations in stress regime between normal ridges and strike-slip transforms. This suggests that short-wavelength bathymetry features, particularly a transform valley that is deeper than the nearby ridge axis topography, may be a necessary feature for the long-term endurance of an oceanic transform fault.

We further use the calculations of the short-wavelength component to place constraints on the 2-D long-wavelength plate driving stress, and thus on the total in situ stress tensor. We find that ridge perpendicular extension globally must exceed the sustained critical yield stress of deformation by at least 10 – 30 MPa of extension along fast spreading ridges, 25 – 40 MPa extension along slow spreading ridges, 40 – 50 MPa extension along ultra-slow spreading ridges. Additionally, we determine that ridge-parallel stress along fast-spreading segments must be near zero, between 1 MPa compression and 3 MPa extension. Ridge-parallel stress along slow segments must be between 4 – 8 MPa extension, and ridge-parallel stress along ultra-slow segments must be between 1 MPa compression and 7 MPa extension.

5.7 Appendix A: calculation of 3-D stress in a thick elastic plate

The 3-D stress throughout a loaded thick elastic plate may be calculated semi-analytically by numerically convolving the 2-D shape of the surface and base loads with an analytically calculated Green's function response of a thick elastic plate to non-identical point loads. For the full derivation of this Green's function, see the Appendix of *Luttrell et al.* [2010]. The solution is summarized here.

Given an arbitrary surface load $f(x, y)$ at $z = 0$ and an arbitrary Moho load $g(x, y)$ at depth $z = h$ loading an elastic plate (Figure 5.A1), the six components of the stress tensor can be calculated in the Fourier domain by

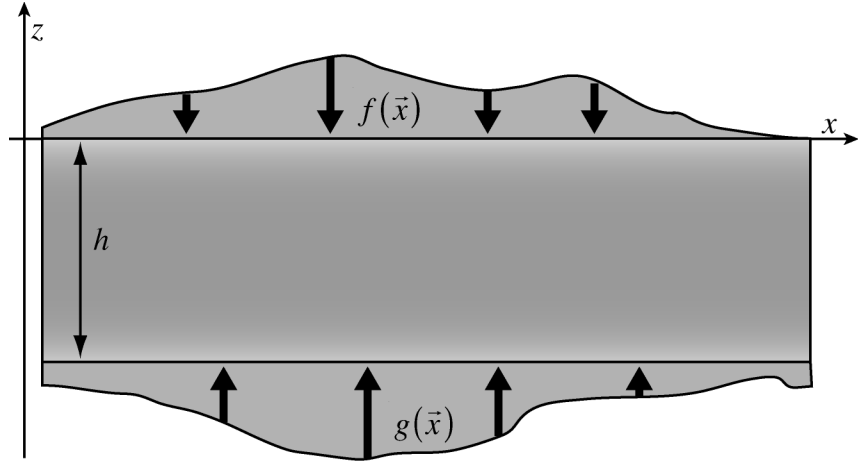


Figure 5.A1 Schematic of elastic plate with thickness h with arbitrarily shaped non-identical loads at the surface $f(\vec{x})$ and base $g(\vec{x})$.

$$\begin{aligned} \sigma_{xx}(k_x, k_y, z) = f(\vec{k}) & \left[\frac{k_x^2}{|\vec{k}|^2} (C_f - S_f) - 2\nu S_f \frac{k_y^2}{|\vec{k}|^2} \right] \\ & + g(\vec{k}) \left[\frac{k_x^2}{|\vec{k}|^2} (C_g - S_g) - 2\nu S_g \frac{k_y^2}{|\vec{k}|^2} \right] \end{aligned} \quad (5.A1)$$

$$\begin{aligned} \sigma_{yy}(k_x, k_y, z) = f(\vec{k}) & \left[\frac{k_y^2}{|\vec{k}|^2} (C_f - S_f) - 2\nu S_f \frac{k_x^2}{|\vec{k}|^2} \right] \\ & + g(\vec{k}) \left[\frac{k_y^2}{|\vec{k}|^2} (C_g - S_g) - 2\nu S_g \frac{k_x^2}{|\vec{k}|^2} \right] \end{aligned} \quad (5.A2)$$

$$\sigma_{zz}(k_x, k_y, z) = f(\vec{k}) [-C_f - S_f] + g(\vec{k}) [-C_g - S_g] \quad (5.A3)$$

$$\sigma_{xy}(k_x, k_y, z) = \frac{k_x k_y}{|\vec{k}|^2} \left\{ f(\vec{k}) [C_f - S_f + 2\nu S_f] + g(\vec{k}) [C_g - S_g + 2\nu S_g] \right\} \quad (5.A4)$$

$$\sigma_{xz}(k_x, k_y, z) = \frac{ik_x}{|\vec{k}|} \left[f(\vec{k}) S'_f + g(\vec{k}) S'_g \right] \quad (5.A5)$$

$$\sigma_{yz}(k_x, k_y, z) = \frac{ik_y}{|\vec{k}|} \left[f(\vec{k}) S'_f + g(\vec{k}) S'_g \right] \quad (5.A6)$$

where $\vec{k} = (k_x, k_y)$ is the horizontal wavenumber, ν is Poisson's ratio. Depth dependence for the normal stress components and the horizontal shear stress component is given by the transfer functions

$$C_f = \frac{2\beta^2 h \zeta \cosh \beta z - \beta z \sinh \beta z - \beta z \sinh \beta (h + \zeta)}{1 + 2\beta^2 h^2 - \cosh 2\beta h} \quad (5.A7)$$

$$C_g = \frac{2\beta^2 h z \cosh \beta \zeta - \beta \zeta \sinh \beta \zeta - \beta \zeta \sinh \beta (h + z)}{1 + 2\beta^2 h^2 - \cosh 2\beta h} \quad (5.A8)$$

$$S_f = \frac{2\beta h \sinh \beta z + \cosh \beta z - \cosh \beta (h + \zeta)}{1 + 2\beta^2 h^2 - \cosh 2\beta h} \quad (5.A9)$$

$$S_g = \frac{2\beta h \sinh \beta \zeta + \cosh \beta \zeta - \cosh \beta (h + z)}{1 + 2\beta^2 h^2 - \cosh 2\beta h} \quad (5.A10)$$

where $\beta = 2\pi|\vec{k}|$ is the radial wavenumber, z is the depth from the top of the plate, and $\zeta = h - z$ is the distance from the bottom of the plate. The two transfer functions related to the bottom load $g(\vec{k})$ are depth-inverted versions of those related to the top load $f(\vec{k})$, such that any occurrence of z and ζ are interchanged. The transfer functions for the vertical shear stress components are related to those in equations 5.A7 – 5.A10 by derivatives with respect to depth, such that

$$S'_{(f,g)} = -\frac{1}{\beta} \frac{d}{dz} [C_{(f,g)} + S_{(f,g)}]. \quad (5.A11)$$

These solutions reduce to those of *Love* [1929] in the elastic halfspace limit and match the 2-D solutions in the long wavelength limit as $\beta \rightarrow 0$.

Equations 5.A1-5.A6 serve as Green's functions allowing the full 3-D stress tensor to be computed by a simple convolution in the Fourier domain. The second invariant of the deviatoric stress tensor $\tau_{ij} = \sigma_{ij} - \frac{1}{3}\sigma_{kk}$ is given by

$$II_{\tau} = \frac{1}{6} \left[(\sigma_{xx} - \sigma_{yy})^2 + (\sigma_{xx} - \sigma_{zz})^2 + (\sigma_{yy} - \sigma_{zz})^2 \right] + \sigma_{xy}^2 + \sigma_{xz}^2 + \sigma_{yz}^2 \quad (5.A12)$$

In terms of the transfer functions 5.A7-5.A11, this becomes

$$II_{\tau} = \frac{1}{3} \left[\frac{3 \left(f(\vec{k}) C_f + g(\vec{k}) C_g \right)^2 - 3 \left(f(\vec{k}) S'_f + g(\vec{k}) S'_g \right)^2}{+ \left(f(\vec{k}) S_f + g(\vec{k}) S_g \right)^2 (1 - 2\nu)^2} \right] \quad (5.A13)$$

which is minimized when $\nu = \frac{1}{2}$, corresponding to an incompressible elastic solid.

Dahlen [1981] similarly showed that in the two-dimensional case, the second invariant of the deviatoric stress from Airy compensated topography at mid ocean ridges was minimized for $\nu = \frac{1}{2}$, though this was never explicitly stated. Our analysis extends the results of *Dahlen* [1981] to three dimensions.

5.8 Appendix B: gravity analysis

Calculation of the stress state sustaining short-wavelength bathymetry variations requires both observations of the surface bathymetry, from satellite and ship tracks [*Becker et al.*, 2009], and an estimate of the buoyant load acting at the base of the finite-thickness elastic plate. This buoyancy may be derived from heterogeneities in either thermal structure or composition, either of which result in a density anomaly indicated in observations of gravity [*Sandwell and Smith*, 2009]. We use these gravity observations to determine a reasonable structure for the shape of the buoyant load at the base of the lithosphere [e.g., *Watts*, 2001]. We model the shape of the buoyant load as a filtered version of the surface load, with support of the surface topography coming from a combination of Airy compensation and the flexural strength of the

elastic plate, effectively tuning the shape of the Moho with the elastic thickness of the crust.

We calculate the gravity anomaly using the first two terms of the gravity expansion of *Parker* [1972] for a homogeneous single-layer crust of density ρ_c overlying a homogenous mantle of density ρ_m such that the total anomaly $g_{total} = g_{surface} + g_{Moho}$. The gravity anomaly at the surface, $z = z_s$, is given by

$$g_{surface} = f_{topo} G \rho_c e^{-\beta(a_{obs}-z_s)} \quad (5.B1)$$

where G is the gravitational constant, f_{topo} is the load of topography, a_{obs} is the altitude of observation (in this case, the sea surface at $z = 0$), and $\beta = 2\pi|\vec{k}|$ is the radial wavenumber. The gravity anomaly at the Moho, $z = h + z_s$, is given by

$$g_{Moho} = f_{topo} G (\rho_c - \rho_m) \Phi e^{-\beta(a_{obs}-h-z_s)} \quad (5.B2)$$

where the transfer function Φ is given by

$$\Phi = \frac{-\rho_c}{\rho_m - \rho_c} \left[1 + \frac{D\beta^4}{g(\rho_m - \rho_c)} \right]^{-1} \quad (5.B3)$$

where g is the mean surface gravity, and the flexural rigidity D depends on the elastic thickness T_e , Young's modulus E , and Poisson's ratio ν as

$$D = \frac{ET_e^3}{12(1-\nu)} \quad (5.B4)$$

For our gravity calculations, we use a mean ocean depth of 3 km, a mantle density of 3300 kg/m³, a Young's modulus of 70 GPa, and a Poisson's ratio of 0.5. The choice of Poisson's ratio is made to be consistent with the stress calculations of this study (Appendix A) and has little impact on the gravity analysis, as it only appears within the flexural rigidity such that the difference in gravity anomaly of a material with $\nu = 0.25$ and $\nu = 0.5$ is about 7%. There are two parameters that we allow to vary: the density and elastic thickness of the crust. We use a crustal thickness of 6.5 km [Laske *et al.*, 2001], recognizing that the gravity-topography transfer function is relatively insensitive to crustal thickness at the short wavelengths considered here.

We calculate the global gravity field for a crustal density between 2400 - 3000 kg/m³ and elastic thickness between 0 - 20 km. We then compare the model with the high-pass filtered gravity data only at points where the bathymetry data are from ship soundings and that are within 30 km either side of the ridge or transform segment [Sandwell and Smith, 2009]. These precautions ensure that our analysis is focused on the plate boundary and that the observed and model gravity are largely derived from independent data. We then calculate the RMS misfit, defined as

$$RMS = \sqrt{\frac{\sum_{i=1}^N (g_i^{observation} - g_i^{model})^2}{N}}, \quad (5.B5)$$

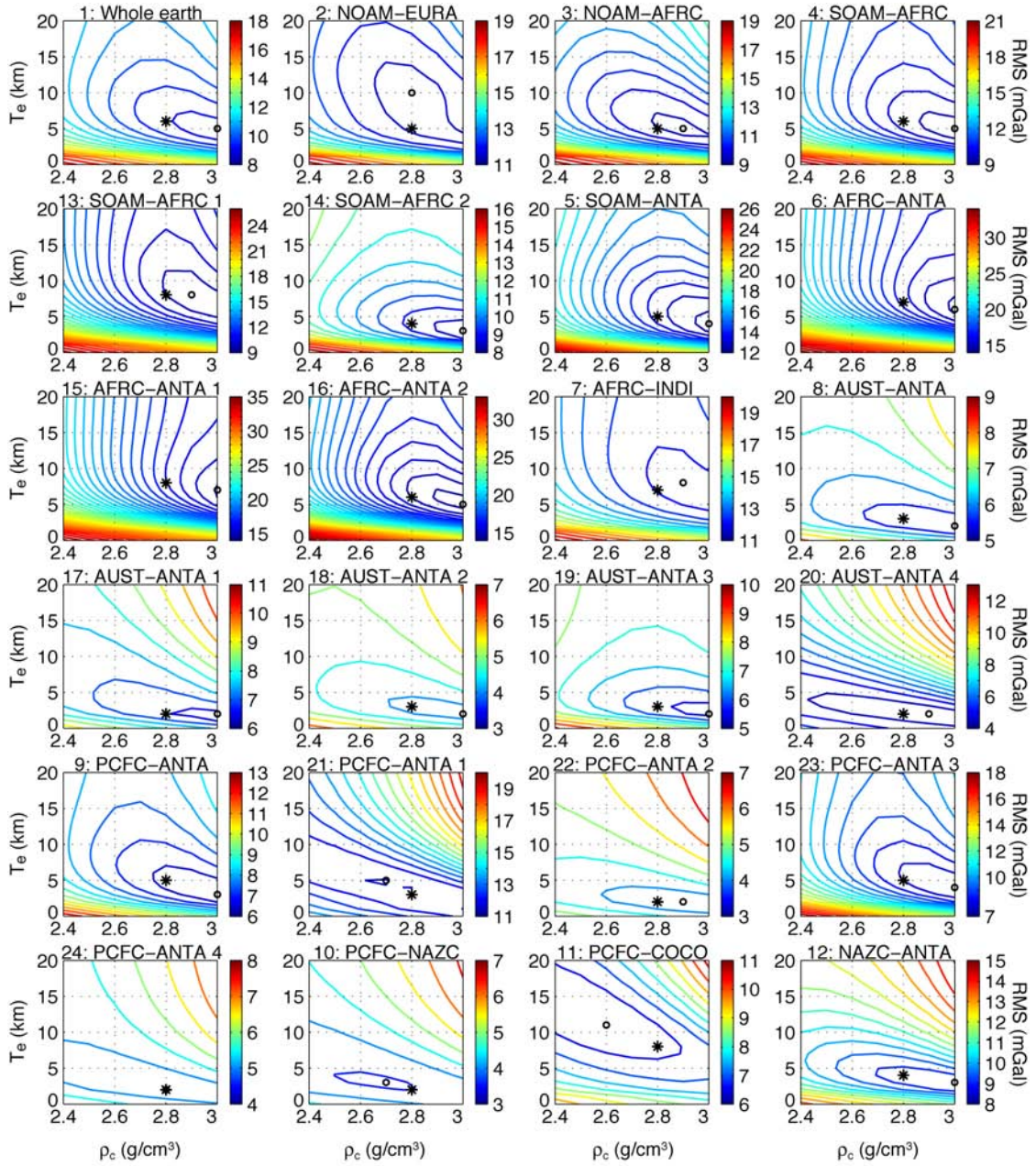
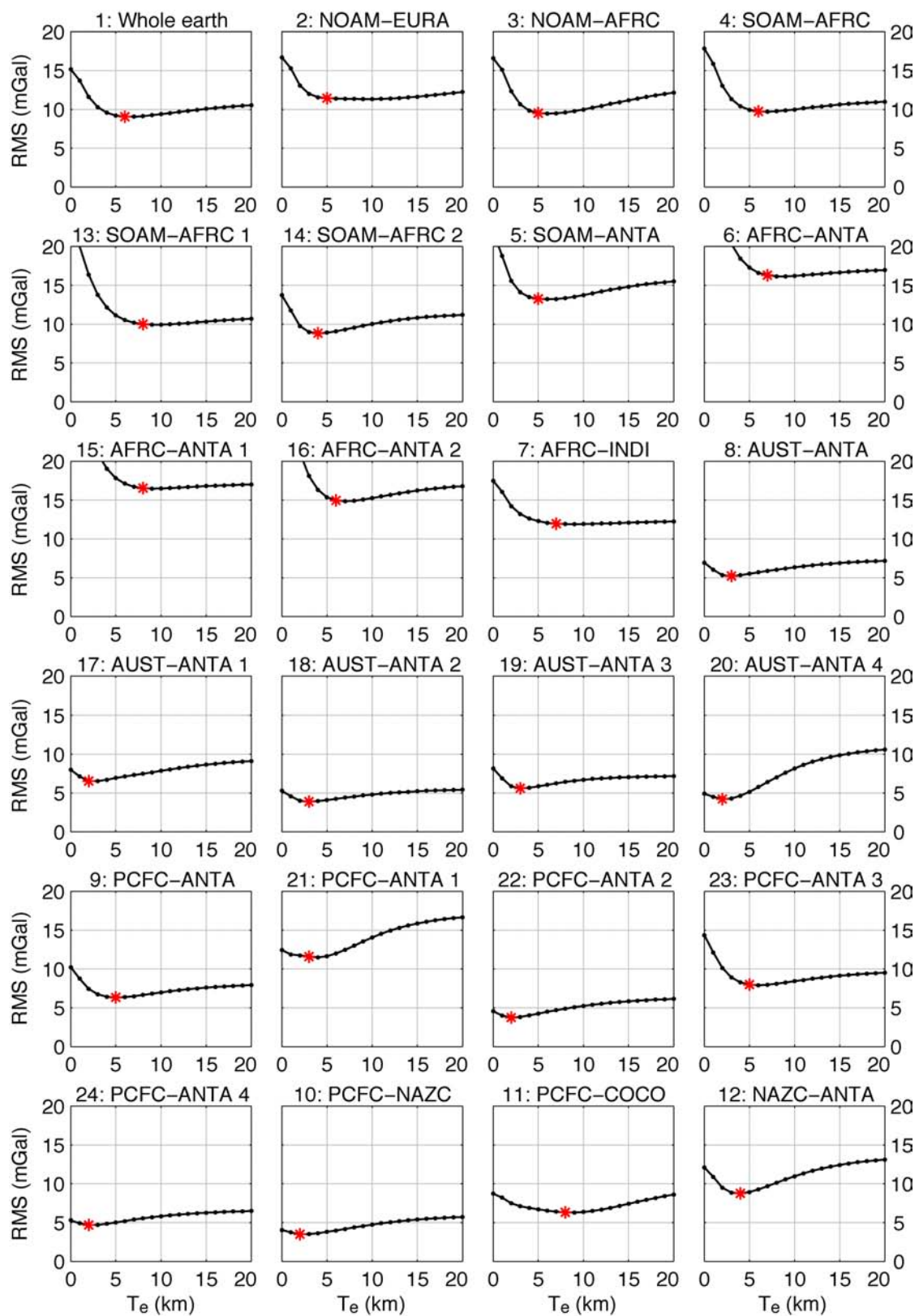


Figure 5.B1 Contours of RMS misfit between gravity model and data for each plate boundary and subregion as a function of crustal density and elastic thickness. Contour interval is 0.5 mGal. Black circle indicates the absolute lowest RMS value. Black star indicates best model with crustal density 2800 kg/m³. Optimal parameters for each region and their corresponding RMS values are listed in Table 5.1.

Figure 5.B2 RMS misfit between gravity model and data for each plate boundary and subregion as a function of elastic thickness, assuming a crustal density of 2800 kg/m^3 . Red star indicates lowest elastic thickness value that minimizes RMS.



for the global mid-ocean ridge and for each plate boundary separately (Figure 5.2), and determine the best fitting values of crustal density and elastic thickness (Table 5.1, Figure 5.B1). As usual, we find there is a tradeoff to gravity fit between density and elastic thickness. Though the strict minimum RMS often corresponds to the highest considered density (3000 kg/m^3), we find the difference in RMS from a density of 2800 kg/m^3 is negligible and select this as our preferred crustal density.

We then determine the most suitable elastic thickness for each region (Figure 5.B2). In regions where the minimum RMS is broad and spans several elastic thickness values, we select the smallest suitable value. Generally the optimal elastic thickness ranges from 2 - 8 km. The fast-spreading sections of the mid-ocean ridge in the Pacific ocean require a smaller elastic thickness of 2 km, while the slower-spreading sections of the mid-Atlantic ocean are fit with a higher elastic thickness, ~5 km. The ultra-slow boundaries in the southwestern Indian ocean are strongest, with a best elastic thickness of 7 km. These values generally agree with those of *Cochran* [1979], who found gravity profiles across the mid-Atlantic ridge to be best fit with a crustal density of 2600 kg/m^3 and an elastic thickness of 9 km, while profiles across the East Pacific Rise required a smaller elastic thickness. At plate boundaries NOAM-EURA, SOAM ANTA, AUST-ANTA 4, and PCFC-ANTA 1 (regions 2, 5, 20, and 21), the constrained gravity observations are particularly sparse. However the optimized parameters from these limited data are consistent with those of neighboring regions, so we use these parameters without additional correction.

5.9 Acknowledgements

This research was supported by the NASA Earth and Space Science Fellowship Program, and by NSF EAR0811772.

Chapter 5, in part, is currently being prepared for submission for publication of the material. Luttrell, K., and D. Sandwell, Constraints on 3-D stress in the crust from support of mid-ocean ridge topography. The dissertation author was the primary investigator and author of this material.

5.10 References

- Becker, J.J., D.T. Sandwell, W.H.F. Smith, J. Braud, B. Binder, J. Depner, D. Fabre, J. Factor, S. Ingalls, S.H. Kim, R. Ladner, K. Marks, S. Nelson, A. Pharaoh, R. Trimmer, J. Von Rosenberg, G. Wallace, and P. Weatherall (2009), Global Bathymetry and Elevation Data at 30 Arc Seconds Resolution: SRTM30_PLUS, *Marine Geodesy*, 32 (4), 355-371, doi: 10.1080/01490410903297766.
- Behn, M.D., J. Lin, and M.T. Zuber (2002), Evidence for weak oceanic transform faults, *Geophysical Research Letters*, 29 (24).
- Blackman, D.K., and D.W. Forsyth (1989), Axial Topographic Relief Associated with Ridge Transform Intersections, *Earth and Planetary Science Letters*, 95 (1-2), 115-129.
- Buck, W.R., L.L. Lavier, and A.N.B. Poliakov (2005), Modes of faulting at mid-ocean ridges, *Nature*, 434 (7034), 719-723.
- Chen, Y.J. (1992), Oceanic Crustal Thickness Versus Spreading Rate, *Geophysical Research Letters*, 19 (8), 753-756.
- Chen, Y.J. (1996), Dynamics of the mid-ocean ridge plate boundary: Recent observations and theory, *Pure and Applied Geophysics*, 146 (3-4), 621-648.
- Choi, E.S., L. Lavier, and M. Gurnis (2008), Thermomechanics of mid-ocean ridge segmentation, *Physics of the Earth and Planetary Interiors*, 171 (1-4), 374-386.
- Cochran, J.R. (1979), Analysis of Isostasy in the Worlds Oceans .2. Midocean Ridge Crests, *Journal of Geophysical Research*, 84 (NB9), 4713-4729.
- Dahlen, F.A. (1981), Isostasy and the Ambient State of Stress in the Oceanic Lithosphere, *Journal of Geophysical Research*, 86 (NB9), 7801-7807.
- DeMets, C., R.G. Gordon, and D.F. Argus (2010), Geologically current plate motions, *Geophysical Journal International*, 181 (1), 1-80.
- Dick, H.J.B., J. Lin, and H. Schouten (2003), An ultraslow-spreading class of ocean ridge, *Nature*, 426 (6965), 405-412.
- Forsyth, D.W., R.L. Ehrenbard, and S. Chapin (1987), Anomalous Upper Mantle beneath the Australian-Antarctic Discordance, *Earth and Planetary Science Letters*, 84 (4), 471-478.
- Gerya, T. (2010), Dynamical Instability Produces Transform Faults at Mid-Ocean Ridges, *Science*, 329 (5995), 1047-1050.

- Gregg, P.M., J. Lin, M.D. Behn, and L.G.J. Montesi (2007), Spreading rate dependence of gravity anomalies along oceanic transform faults, *Nature*, 448 (7150), 183-U5.
- Grindlay, N.R., and P.J. Fox (1993), Lithospheric Stresses Associated with Nontransform Offsets of the Mid-Atlantic Ridge - Implications from a Finite-Element Analysis, *Tectonics*, 12 (4), 982-1003.
- Gudmundsson, A. (1995), Stress fields associated with oceanic transform faults, *Earth and Planetary Science Letters*, 136 (3-4), 603-614.
- Heidbach, O., M. Tingay, A. Barth, J. Reinecker, D. Kurfeß, and B. Müller (2008), The World Stress Map database release 2008, doi:10.1594/GFZ.WSM.Rel2008.
- Holmes, R.C., M. Tolstoy, A.J. Harding, J.A. Orcutt, and J.P. Morgan (2010), Australian Antarctic Discordance as a simple mantle boundary, *Geophys. Res. Lett.*, 37 (L09309), doi:10.1029/2010GL042621.
- Laske, G., G. Masters, and C. Reif (2001), CRUST 2.0: A New Global Crustal Model at 2x2 Degrees, <http://igppweb.ucsd.edu/~gabi/rem.html>.
- Love, A.E.H. (1929), The stress produced in a semi-infinite solid by pressure on part of the boundary, *Proc. Roy. Soc. Lond. A*, 228, 377-420.
- Luttrell, K., X. Tong, D. Sandwell, and B. Brooks (2010), Estimates of stress drop and crustal tectonic stress from the February 27, 2010 Maule, Chile earthquake: implications for fault strength, *manuscript in preparation*.
- Macdonald, K.C. (1982), Mid-Ocean Ridges - Fine Scale Tectonic, Volcanic and Hydrothermal Processes within the Plate Boundary Zone, *Annual Review of Earth and Planetary Sciences*, 10, 155-190.
- Macdonald, K.C., P.J. Fox, R.T. Alexander, R. Pockalny, and P. Gente (1996), Volcanic growth faults and the origin of Pacific abyssal hills, *Nature*, 380 (6570), 125-129.
- Macdonald, K.C., P.J. Fox, L.J. Perram, M.F. Eisen, R.M. Haymon, S.P. Miller, S.M. Carbotte, M.H. Cormier, and A.N. Shor (1988), A New View of the Mid-Ocean Ridge from the Behavior of Ridge-Axis Discontinuities, *Nature*, 335 (6187), 217-225.
- Menard, H.W. (1984), Evolution of Ridges by Asymmetrical Spreading, *Geology*, 12 (3), 177-180.
- Neves, M.C., M.H.P. Bott, and R.C. Searle (2004), Patterns of stress at midocean ridges and their offsets due to seafloor subsidence, *Tectonophysics*, 386 (3-4), 223-242.

Oldenburg, D.W., and J.N. Brune (1972), Ridge Transform Fault Spreading Pattern in Freezing Wax, *Science*, 178 (4058), 301-304.

Pan, J.F., M. Antolik, and A.M. Dziewonski (2002), Locations of mid-oceanic earthquakes constrained by seafloor bathymetry, *Journal of Geophysical Research-Solid Earth*, 107 (B11).

Parker, R.L. (1972), Rapid Calculation of Potential Anomalies, *Geophys. J. R. astr. Soc.*, 31 (4), 447-455.

Phipps-Morgan, J., and E.M. Parmentier (1984), Lithospheric Stress near a Ridge-Transform Intersection, *Geophysical Research Letters*, 11 (2), 113-116.

Pockalny, R.A., P. Gente, and R. Buck (1996), Oceanic transverse ridges: A flexural response to fracture-zone-normal extension, *Geology*, 24 (1), 71-74.

Purdy, G.M., L.S.L. Kong, G.L. Christeson, and S.C. Solomon (1992), Relationship between Spreading Rate and the Seismic Structure of Midocean Ridges, *Nature*, 355 (6363), 815-817.

Sandwell, D.T. (1986), Thermal-Stress and the Spacings of Transform Faults, *Journal of Geophysical Research-Solid Earth and Planets*, 91 (B6), 6405-6417.

Sandwell, D.T., and W.H.F. Smith (2009), Global marine gravity from retracked Geosat and ERS-1 altimetry: Ridge segmentation versus spreading rate, *Journal of Geophysical Research-Solid Earth*, 114.

Small, C., and D.T. Sandwell (1994), Imaging Midocean Ridge Transitions with Satellite Gravity, *Geology*, 22 (2), 123-126.

Watts, A.B. (2001), *Isostasy and Flexure of the Lithosphere*, Cambridge University Press, Cambridge, United Kingdom.

Zoback, M.L. (1992), 1st-Order and 2nd-Order Patterns of Stress in the Lithosphere - the World Stress Map Project, *Journal of Geophysical Research-Solid Earth*, 97 (B8), 11703-11728.

Chapter 6

Strength of the Lithosphere of the Galilean Satellites

Abstract

Several approaches have been used to estimate the ice shell thickness on Callisto, Ganymede, and Europa. Here we develop a method for placing a strict lower bound on the thickness of the strong part of the shell (lithosphere) using measurements of topography. The minimal assumptions are that the strength of faults in the brittle lithosphere is controlled by lithostatic pressure according to Byerlee's law and the shell has relatively uniform density and thickness. Under these conditions, the topography of the ice provides a direct measure of the bending moment in the lithosphere. This topographic bending moment must be less than the saturation bending moment of the yield strength envelope derived from Byerlee's law. The model predicts that the topographic amplitude spectrum decreases as the square of the topographic wavelength. This explains why Europa is rugged at shorter wavelengths (~ 10 km) but extremely smooth, and perhaps conforming to an equipotential surface, at longer wavelengths (> 100 km). Previously compiled data on impact crater depth and diameter [Schenk, 2002] on Europa show good agreement with the spectral decrease predicted by the model and require a lithosphere thicker than 2.5 km. A more realistic model, including a ductile lower lithosphere, requires a thickness greater

than 3.5 km. Future measurements of topography in the 10 to 100 km wavelength band will provide tight constraints on lithospheric strength.

6.1 Introduction

Three of the four Galilean Satellites of Jupiter have significant quantities of water and are referred to as icy satellites [*Pappalardo et al.*, 1999; *Showman and Malhotra*, 1999]. Galileo spacecraft magnetometer data from Europa indicate a near-surface conductive layer [*Kivelson et al.*, 2000] suggesting that a liquid ocean lies beneath an ice shell. The thickness of the ice shell is of chief importance for the understanding of geologic processes on the Galilean satellites, the search for astrobiological activity on Europa, and the planning of future spacecraft missions. The ice shell is believed to be rheologically layered (Figure 6.1a) consisting of a strong upper layer, or lithosphere, and possibly a convecting lower layer [*Goldsby and Kohlstedt*, 2001; *McKinnon*, 1999; *Nimmo et al.*, 2003b]. Here we investigate a new method for estimating the integrated strength of the lithosphere by measuring topographic moment. The new strength estimates provide a strict lower bound on the thickness of the lithospheres of Callisto, Ganymede, and Europa although they do not provide an estimate of the total shell thickness of these satellites.

Ice shell thickness is usually estimated in one of three ways [*Billings and Kattenhorn*, 2005]. The first approach uses models of heat transport along with estimates of internal heat generation to determine the thickness of the ice shell. Thermal studies on Europa yield total shell thicknesses ranging from 2-5 km [*Thomson and Delaney*, 2001] to 4 km [*Ruiz*, 1997] to 10-20 km [*McKinnon*, 1999] to

30 km [Wang and Stevenson, 2000]. The second approach compares observed topography with the flexural response of a thin elastic plate to an assumed initial load to determine the thickness of the plate [Watts, 2001]. For the terrestrial planets, the thickness of the elastic plate is about half of the total lithospheric thickness. Europa's elastic plate thickness has been estimated at 100-500 m [Williams and Greeley, 1998] to 4 km and 6 km [Figueredo *et al.*, 2002; Nimmo *et al.*, 2003a] yielding total shell thickness of 15 km [Nimmo *et al.*, 2003a]. Effective elastic plate thickness estimates on Ganymede are 0.15-1.7 km [Nimmo and Pappalardo, 2004; Nimmo *et al.*, 2002]. A third approach to estimating shell thickness involves examining the morphologic transitions of impact craters and relating these to rheologic transitions at depth. Estimates of Europa's total shell thickness range from greater than 3-4 km [Turtle and Pierazzo, 2001] to 19-25 km [Schenk, 2002].

Here we develop a fourth approach to estimating the strength and minimum thickness of just the lithosphere. This involves comparing the bending moment needed to support topography with the maximum bending moment that the lithosphere is capable of supporting. Topography of satellites or planets having thin lithospheres can be supported either by a local compensation mechanism (e.g., Airy or Pratt) or by the strength of the lithosphere. On the terrestrial planets, compositional stratification enables a mix of compensation mechanisms so other information such as gravity and reflection seismology is needed to establish the dominant mechanism [Watts, 2001]. However, since the lithospheres of the Galilean satellites are largely homogeneous, lithospheric strength may be the dominant support mechanism. On Earth, studies of plate bending at subduction zones show that the critical measure of lithospheric

strength is the topographic bending moment which can be calculated from the topography of the trench and outer rise [Goetze and Evans, 1979]. The trench/outer rise topography would collapse if the overall strength of the lithosphere, or *saturation bending moment*, is less than the topographic bending moment [McAdoo et al., 1978]. Thus measurements of topography provide a strict lower bound on lithospheric strength.

We use a similar approach to estimate the saturation bending moment of the lithosphere on the Galilean satellites. We assume that topography initially caused by large impact craters or tectonic processes induces stresses that exceed the strength of the lithosphere and have a bending moment greater than the long-term, saturation bending moment of the lithosphere. The lithosphere relaxes under the load to achieve stable topography in a state of moment saturation. We compare estimates of topographic bending moment derived from studies of impact craters [Schenk, 2002] to end-member models of lithospheric strength to determine a lower bound for the lithospheric thickness. These bounds are in agreement with flexural studies of Europa [e.g., Figueredo et al., 2002] and also provide insights into the lithospheric properties of Ganymede and Callisto.

An interesting feature of moment saturation analysis is that it predicts a particular form for the topographic spectrum. At wavelengths greater than the lithospheric thickness, the amplitude of the topography decreases as the square of the wavelength; this simple model explains why Europa appears smooth at large horizontal scales yet rough at small scales. At wavelengths less than the lithospheric thickness, the slope of the topography is limited by the angle of repose of the ice. The

combined spectrum has a shape that depends only on the saturation bending moment. Using this spectrum we simulate the topography of Europa and compare artificial profiles with actual topographic profiles derived from stereo topography [Schenk and Pappalardo, 2004]. We also convolve the synthetic topography with a series of averaging filters to investigate the practical sampling characteristics an altimeter mission would need in order to detect tidal fluctuations or variations in the equipotential surface (geoid) height.

6.2 Saturation bending moment and yield strength envelope models

When the lithosphere is subjected to a small bending moment it flexes with a curvature that is linearly related to the applied moment [Turcotte and Schubert, 2002]. The thin elastic plate flexure model is only valid in this linear regime. As the applied moment is increased, stresses on the top and bottom of the lithosphere exceed the strength of the material and a plastic hinge develops [McAdoo *et al.*, 1978]. Eventually the lithosphere becomes *moment-saturated* so that the curvature of the *hinge* continues to increase without an increase in applied moment. At this point the thickness of the elastic core of the plate goes to zero [McNutt and Menard, 1982]. The magnitude of the saturation moment is a measure of the overall strength of the lithosphere. Moment saturation commonly occurs at ocean trenches on the Earth where lithosphere is permanently bent prior to subduction into the mantle [Levitt and Sandwell, 1995; McNutt and Menard, 1982]. The nearly complete failure of the plate is evident as deeply penetrating normal faults that develop in the outer trench wall [Masson, 1991]. Topographic profiles across the trench and outer rise provide a direct

measure of the applied bending moment that can be compared with the rheological saturation bending moment [*Brace and Kohlstedt*, 1980; *Goetze and Evans*, 1979].

The strength of the lithospheric versus depth, or yield strength envelope, depends on pressure, temperature, and strain rate. In the upper lithosphere, strength is controlled primarily by the increase in lithostatic pressure with depth which inhibits sliding along preexisting fault planes according to Byerlee's law [*Byerlee*, 1978]. As temperature increases in the lower part of the lithosphere, yielding occurs by ductile flow and strength decreases with depth [*Goetze and Evans*, 1979]. While laboratory experiments have been partially successful in constraining the ductile rheology of the lower lithosphere [*Kirby*, 1983] the ultimate test for tenability of a rheologic model is whether the integrated yield strength is capable of supporting the observed trench/outer rise topography.

Here we apply the same concepts to the lithospheres of the icy Galilean satellites. Cold dry ice undergoes brittle yielding similar to that of the terrestrial lithosphere. Beeman [1988] has conducted frictional sliding experiments on very cold (77-115 K) saw-cut ice cores and established a frictional sliding relationship that is specific to ice with a coefficient of friction value of 0.69 (i.e., Byerlee's Law for ice). The strength of the lower ductile portion of the lithosphere is highly uncertain [*Goldsby and Kohlstedt*, 2001] and depends on unknown parameters such as grain size, thermal gradient, strain rate, and activation energy. Given this uncertainty, we consider two cases. In the first case (*mirrored model*), the strength of the lower ductile layer decreases linearly with depth and mirrors the strength of upper brittle

layer (Figure 6.1b). The yield stress envelope for this case is [Brace and Kohlstedt, 1980; Watts, 2001]

$$\begin{aligned}\Delta\sigma_{\text{comp}} &= \begin{cases} -C\rho gz & z < h/2 \\ -C\rho g(h-z) & z > h/2 \end{cases} \\ \Delta\sigma_{\text{ten}} &= \begin{cases} \alpha C\rho gz & z < h/2 \\ \alpha C\rho g(h-z) & z > h/2 \end{cases}\end{aligned}\quad (6.1)$$

where ρ is the density of the ice ($980 \text{ kg}\cdot\text{m}^{-3}$), g is gravity ($1.3 \text{ m}\cdot\text{s}^{-2}$), h is the thickness of the lithosphere, and the dimensionless factors $C = 2.6$ and $\alpha = 0.3$ are constants resulting from our use of Byerlee's law for ice (compare with $C = 4$ and $\alpha = 0.2$ for most types of rock [e.g., Watts, 2001]). In the second case (*ice sheet model*), strength increases with depth in the brittle layer and abruptly goes to zero as one would find for a brittle ice sheet floating on a liquid ocean. This case has a yield strength envelope given by

$$\begin{aligned}\Delta\sigma_{\text{comp}} &= -C\rho gz \\ \Delta\sigma_{\text{ten}} &= \alpha C\rho gz\end{aligned}\quad (6.2)$$

For a prescribed lithospheric thickness h , the ice sheet model will support the maximum topographic moment. Thus given a topographic moment, this model provides an absolute lower bound on lithospheric thickness.

In addition to the shape of the yield strength envelope, the saturation bending moment also depends on the sign of the curvature - whether the lithosphere is flexed

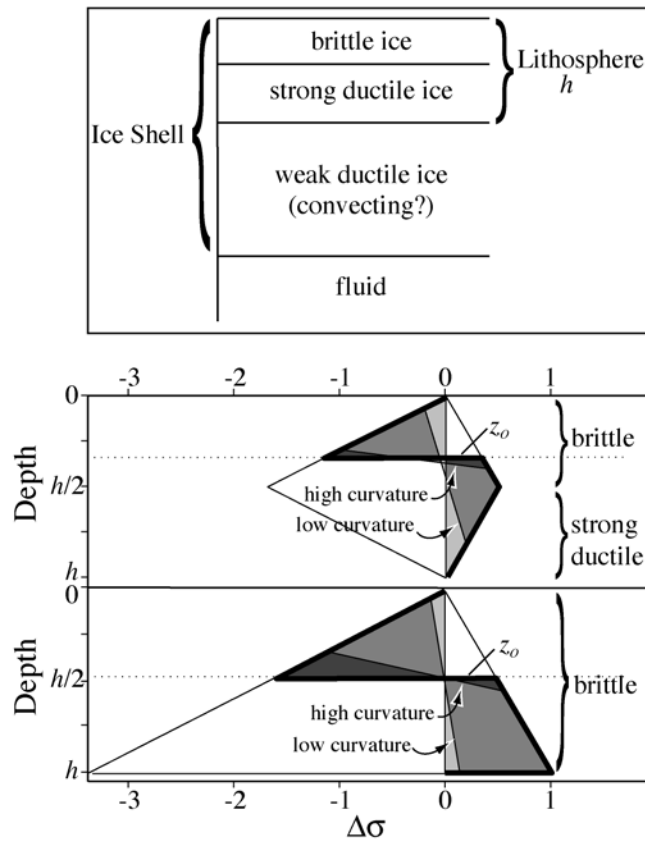


Figure 6.1 (a) Ice shell consists of a strong lithosphere overlying a possibly-convecting weak ice layer. The lithosphere has a brittle upper layer and a strong ductile lower layer. (b) Yield strength envelope models for concave up bending. Mirrored model (above) represents a plausible lithosphere (Eq. 6.1). Ice sheet model (below) represents the strongest possible lithosphere (Eq. 6.2). Compressional deviatoric stress is negative, extensional stress is positive. Dotted line shows nodal plane depth z_0 for a moment-saturated plate, heavy black line shows stress state of a moment-saturated plate, and shaded sections indicate stress state for a plate with low and high curvatures.

concave up or concave down. When the lithosphere is flexed concave down, such as at a subduction zone, the top portion of the lithosphere undergoes tension (weaker) while the bottom part undergoes compression. In concave up flexure, such as under a seamount, the top portion of the lithosphere is in compression (stronger); this usually results in a larger saturation bending moment due to the shape of the strength

envelope. Saturation moment is found by integrating yield strength times moment arm over depth (Eq. 6.3).

$$M_s = \int_0^h \Delta\sigma_{\text{yield}} (z - z_0) dz. \quad (6.3)$$

For concave up bending, $\Delta\sigma_{\text{yield}} = \Delta\sigma_{\text{comp}}$ above the nodal plane, or neutral unstrained surface, and $\Delta\sigma_{\text{yield}} = \Delta\sigma_{\text{ten}}$ below the nodal plane. For concave down bending the roles of tensile yield stress and compressive yield stress are reversed. The moment arm $(z - z_0)$ is the distance above or below the nodal plane. We assume there is no net horizontal force on the lithosphere so the nodal depth, z_0 , is found by requiring the integral of stress over depth equal zero (Eq. 6.4).

$$\int_0^{z_0} \Delta\sigma_{\text{yield}} dz + \int_{z_0}^h \Delta\sigma_{\text{yield}} dz = 0. \quad (6.4)$$

The nodal depth will depend on both the sign and magnitude of the lithosphere curvature. At low curvature, z_0 will be close to $h/2$. As curvature increases, z_0 will drift away from $h/2$ to reach an extreme value when the lithosphere reaches moment saturation. The relation between saturation nodal depth and h , given in Table 6.1, depends on both the geometry of the yield strength envelope and the sign of the curvature. For a moment-saturated lithosphere with ice sheet yield strength envelope, the location of z_0 is highly asymmetric with respect to bending direction, located near the center of the concave up lithosphere and near the bottom of the concave down

Table 6.1 Depth to nodal plane z_0 in moment-saturated plate as a function of plate thickness h for four different cases.

	Concave up	Concave down
Mirrored model (brittle and strong ductile)	$z_0 = \sqrt{\frac{\alpha}{2(1+\alpha)}}h = .34h$	$z_0 = \left[1 - \sqrt{\frac{\alpha}{2(1+\alpha)}}\right]h = .66h$
Ice sheet model (brittle only)	$z_0 = \sqrt{\frac{\alpha}{1+\alpha}}h = .48h$	$z_0 = \sqrt{\frac{1}{1+\alpha}}h = .88h$

lithosphere. A moment-saturated lithosphere with mirrored yield strength envelope has a z_0 location that is symmetric with regard to the direction of bending located significantly away from the center of the lithosphere.

Having identified two yield strength envelopes of interest and their four possible saturation nodal depths, we calculate the saturation bending moment using equation 6.3. For all cases above the saturation moment is proportional to the lithostatic pressure ρgh times lithosphere thickness squared times a dimensionless factor γ that depends on the shape of the yield strength envelope and the sign of lithosphere curvature (Eq. 6.5).

$$M_s = \gamma \rho gh^3. \quad (6.5)$$

Table 6.2 Dimensionless geometric factor γ , depending only on the 5.8 constants $C = 2.6$ and $\alpha = 0.3$ from Byerlee's Law for ice.

	Concave up	Concave down
Mirrored	$\gamma = C \left[\frac{1}{8}\alpha - \frac{1}{6\sqrt{2}} \frac{\alpha^{3/2}}{(1+\alpha)^{1/2}} \right] = 0.053$	$\gamma = -C \left[\frac{1}{8}\alpha - \frac{1}{6\sqrt{2}} \frac{\alpha^{3/2}}{(1+\alpha)^{1/2}} \right] = -0.053$
Ice Sheet	$\gamma = C \left[\frac{1}{3}\alpha - \frac{1}{3} \frac{\alpha^{3/2}}{(1+\alpha)^{1/2}} \right] = 0.135$	$\gamma = -C \left[\frac{1}{3} - \frac{1}{3} \frac{1}{(1+\alpha)^{1/2}} \right] = -0.107$

The geometric factor γ for the four cases is given in Table 6.2. For an ice sheet model of thickness h , the magnitude of the saturation bending moment is greater for concave up bending than for concave down bending because the lithosphere is stronger in compression than in tension and brittle strength increases dramatically with depth. For a mirrored model of the same thickness, the magnitude of the saturation moment is independent of bending direction and is about half the value of the concave down ice sheet model.

6.3 Maximum observed topographic bending moment

A unique feature of the Galilean satellites, and in particular Europa, is that the density of the icy shell is nearly uniform ($< 5\%$ density variation) [*Schenk and Pappalardo*, 2004]. On the Earth and other terrestrial planets, the lithosphere is comprised of a lower density crust underlain by a higher density mantle. Since both layers are imbedded within the relatively strong elastic layer, long-wavelength topography can be supported by Airy compensation. On Europa, topography at wavelengths greater than about 1000 km could be maintained over long timescales by significant shell-thickness variations if the rheology of the shell is non-Newtonian [*Nimmo*, 2004]. At wavelengths shorter than about 100 km, however, the horizontal pressure gradients between the weak ductile ice layer at the base of the shell and the liquid water below will cause the base of the shell to flatten on relatively short timescales [*Nimmo*, 2004; *O'Brien et al.*, 2002; *Stevenson*, 2000]. These properties have important consequences for how topography is physically supported. Because

Airy compensation is unlikely on the Galilean satellites, especially over horizontal length scales less than 100 km [Nimmo, 2004], topography must be supported by an alternative mechanism. It is possible to support a few hundred meters of topography through Pratt compensation if the shell thickness is > 15 km [Schenk and Pappalardo, 2004]. For this analysis, however, we consider the integrated strength of the lithosphere as the primary support mechanism so that we may explore the possibility of thinner (< 10 km) shells and put an absolute lower bound on shell thickness.

As shown in many investigations on Earth, the appropriate parameter to characterize strength of a plate is the saturation bending moment which is the integral of the yield strength over depth times the distance to the flexural nodal plane [Goetze and Evans, 1979] (see previous section). Bending moment can also be measured from the observed topography without knowledge of the plate material or yield strength profile. In the case of trench flexure, the bending moment depends on the integral of the vertical topographic load $g\rho w(x)$ times the moment arm $(x - x_0)$

$$M_s = \gamma \rho g h^3 \quad (6.6)$$

where x_0 is the first zero crossing outboard of the trench axis. This is a simple integration of topography with no unknown model parameters; the results depend only on the location of the zero crossing.

We show next that the topographic spectrum of the Galilean satellites can be used to estimate the bending moment of the lithosphere. Conversely, given the saturation bending moment of the lithosphere (previous section), one can derive an

upper bound on the topographic spectrum. In the case of real Galilean topography there may not be a dominant flexural wavelength as in the case of trench flexure so we first consider the case of arbitrary topography to develop a general expression for the moment. We then consider the case of cylindrically symmetric topography to calculate an approximate moment associated with impact craters of a given depth and diameter [Schenk, 2002].

Consider an event such as a meteorite impact or other tectonic process that instantaneously creates topography $a(\mathbf{x})$ with a bending moment greater than the saturation bending moment of the lithosphere (Figure 6.2a). Over geologic timescales the lithosphere will relax by an amount $w(\mathbf{x})$ to support this initial topographic load. The final topography, which can be observed, will be the sum of the initial topography and the plate deflection $t(\mathbf{x}) = a(\mathbf{x}) + w(\mathbf{x})$ (Figure 6.2b). The standard thin-plate moment balance equation is used to calculate the plate deflection from the applied topographic load [e.g., Turcotte and Schubert, 2002]:

$$-\nabla^2 M(\mathbf{x}) + \rho g w(\mathbf{x}) = -\rho g a(\mathbf{x}) \quad (6.7)$$

where M is the bending moment and ρ is the density of the ice. Note that this analysis does not assume a linear relationship between moment and curvature as in the case of elastic plate flexure. Because the base of the ice shell is flat on long timescales there is no contribution to the restoring from the ice/water interface. The solution to Equation (6.7) in the Fourier domain is

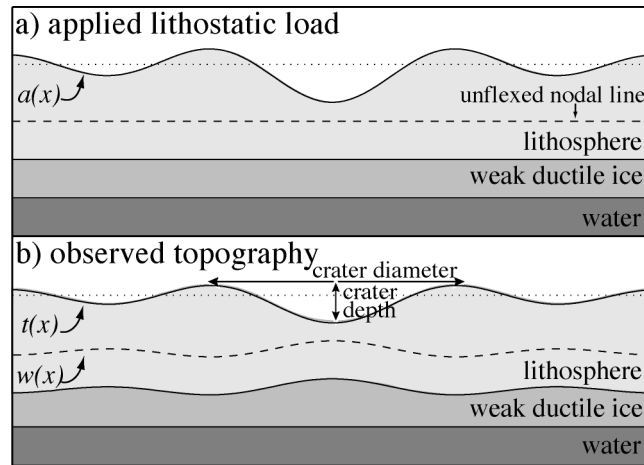


Figure 6.2 Response of the lithosphere to an initial topographic load. (a) Topographic load $a(x)$ applied to an initially unbent plate (dashed line represents nodal plane). (b) Observed topography $t(x)$ following relaxation is the sum of the applied topography $a(x)$ and the bending response $w(x)$.

$$M(\mathbf{k}) = -\frac{\rho g}{(2\pi|\mathbf{k}|)^2} T(\mathbf{k}) \quad (6.8)$$

where $T(\mathbf{k})$ is topography in the wavenumber domain, $k_x = 1/\lambda_x$, $k_y = 1/\lambda_y$, and $|\mathbf{k}| = \sqrt{k_x^2 + k_y^2}$. This relationship between bending moment and observed topography is independent of rheology and only depends on the gravitational restoring force. This is directly analogous to equation 6.6 where the trench/outer rise topography is used to estimate bending moment.

Equation 6.8 has some exciting implications. First, if one had complete topographic measurements of the icy satellites, then the bending moment could be calculated directly without having to assume values for unknown parameters. Moreover, if the lithosphere has a spectrally uniform saturation bending moment, then

the topographic spectrum must decrease as the wavelength squared. This could explain why Europa appears smooth on global scales yet quite rugged on local scales (~ 10 km). Second, at intermediate and perhaps long wavelengths, the topography of Europa may conform to an equipotential surface of gravity so topographic measurements could provide direct measurements of geoid height. These could be used to search for the gravitational signatures of volcanoes at the bottom of Europa's ocean, for example.

We test the saturation moment prediction of Equation (6.8) through a comparison of impact crater topography on the icy Galilean satellites [Schenk, 2002]. Craters shapes are highly variable so we approximate their topography $t(r)$ (Eq. 6.9) using a radially symmetric Bessel function of the first kind (Figure 6.2)

$$t(r) = A_0 J_0(2\pi k_0 r) \quad (6.9)$$

where r is radial distance, k_0 is a characteristic radial wavenumber and A_0 is the central amplitude. Taking the Hankel transform of equation 6.9, substituting into equation 6.8, and then taking the inverse Hankel transform we obtain the topographic bending moment as a function of radius (Eq. 6.10).

$$M(r) = -\frac{\rho g}{(2\pi k_0)^2} A_0 J_0(2\pi k_0 r) \quad (6.10)$$

The maximum bending moment magnitude occurs at the center of the crater where $J_0(0) = 1$, and has a value given by

$$M_{\max} = \frac{\rho g}{(2\pi k_0)^2} A_0 \quad (6.11)$$

We follow the convention of *Schenk* [2002] to define crater depth as the vertical distance between the central minimum and the first maximum and crater diameter as the horizontal distance between the two maxima (Eq. 6.12).

$$\begin{aligned} \text{depth} &= 1.4028 A_0 \\ \text{diameter} &= \frac{3.8317}{\pi k_0} \end{aligned} \quad (6.12)$$

Combining equation 6.11 and equation 6.12, provides a relationship between crater depth, crater diameter, and maximum bending moment

$$\text{depth} = 20.5958 \left(\frac{4M_{\max}}{\rho g} \right) \frac{1}{\text{diameter}^2}. \quad (6.13)$$

Although a single wavenumber Bessel function may seem like a crude approximation to the shape of the topography of an impact crater, we have found through simulations that the topographic moment is dominated by the amplitude of the longest wavelength

component. In other words, adding complicated short wavelength topographic structure will have negligible effect on maximum moment.

6.4 An upper bound on the topographic spectrum from the yield strength envelope

Before applying these concepts to the icy Galilean satellites it is instructive to test the approach using subduction zone data on the Earth. *Levitt and Sandwell* [1995] estimated topographic moment across 37 trench and outer rise flexures. Rather than numerically integrate the noisy topographic data, they first fit the topographic profiles with a thin elastic plate flexure model and then integrated the best-fit model to estimate the moment (Eq. 6.6). Their results (Figure 6.3a) show that the topographic moment increases nearly linearly with lithospheric age, which is explained by a combination of thickening and strengthening of the lithosphere as it cools. The measured moments are then compared to the saturation bending moment computed from a yield strength envelope consisting of a brittle layer following Byerlee's law and a power law ductile flow using a half-space cooling model [*Goetze and Evans*, 1979]. In all but three of the cases, the topographic moment of the trench is less than the model saturation bending moment suggesting that the cooling model and rheology are in accordance with the data.

Figure 6.3b shows the trench measurements of outer rise height (analogous to crater depth) versus flexural wavelength (analogous to crater diameter), $\lambda = \sqrt{2\pi\alpha} = 1/k$ where α is the flexural parameter [*Watts*, 2001]. The model curves

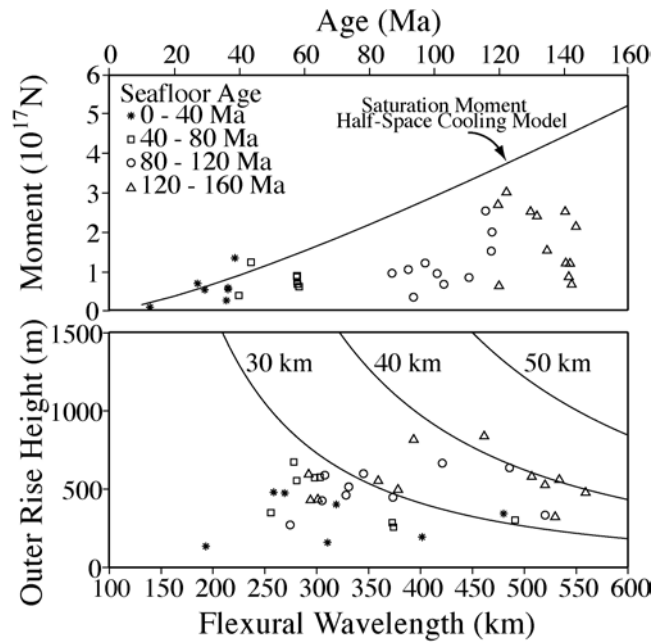


Figure 6.3 (a) Topographic moment (symbols) across 37 trench and outer rise profiles on the Earth [Levitt and Sandwell, 1995]. Saturation moment (solid curve), based on a yield strength envelope model, increases with age as the lithosphere cools and thickens. All but three of the observed moments fall below the saturation moment curve. (b) Outer rise height and flexural wavelength of the same 37 profiles. Saturation moment contours (solid curves) for a lithosphere with mirrored yield strength envelope (Figure 6.1b). Saturation moment and lithospheric thickness increase with age, as expected for Earth.

are calculated by combining Equations (6.5) and (6.8) to relate lithosphere thickness h to wavelength $1/k$ using the γ value of a mirrored yield strength envelope. While the mirrored model is a crude approximation to the actual Earth, it provides an informative check on a well-understood data set. The comparisons show that older lithosphere (triangles and circles) generally require a thicker plate than younger lithosphere (asterisks and squares). The thicknesses are in good agreement with the flexural modeling estimates [Levitt and Sandwell, 1995]. The success of this simple

formulation on Earth data suggests it can be applied to the icy satellites where topographic information is far more limited.

To apply these concepts to the icy Galilean satellites we need to examine topographic features that are moment-saturated and have a dominant characteristic wavelength. The best published data set for this purpose is impact crater depth (rim to floor) versus diameter (rim to rim) [Schenk, 2002]. For small craters (< 5 km in diameter) there is a nearly linear relationship between crater depth and diameter that is consistent with a maximum ice slope of 17° . Schenk [2002] interpreted all of these small craters as having a *simple* morphology suggesting that they did not penetrate the lithosphere. Larger craters (> 10 km) have more complex morphology suggesting they penetrated partially (*complex crater*) or entirely through the lithosphere (*central pit or dome crater*) [Schenk, 2002].

We propose that crater depth is limited by the minimum of two competing mechanisms - the 17° maximum slope and the saturation bending moment. Figure 6.4 compares impact crater data from Callisto, Ganymede, and Europa with contours of lithosphere thickness calculated by combining equations (6.5) and (6.13) using $\gamma = 0.135$, the value of an ice sheet yield strength envelope with concave up bending. For Callisto and Ganymede (Figure 6.4a, 6.4b), there is no clear upper bound on the crater data; rather a range of thickness 2-10 km fits the data. The lack of a single thickness for the upper bound can be explained in three ways: i) the true thickness is greater than 10 km and the crater topographies do not represent moment saturation; ii) the thickness varies with location; iii) the thickness has changed with time so some craters formed while the lithosphere was thick while others formed while the

lithosphere was thin. Note that the Earth data show a similar dispersion that is due to thickening of the lithosphere with age.

The relationship between crater depth and diameter is notably different on Europa (Figure 6.4c). Crater depth peaks at a diameter of about 8 km and then falls roughly following the 2-km thick lithosphere. The peak in the observed crater depth (~800 m) is not as large as the model peak (~1500 m) possibly because the thin plate approximation breaks down in this wavelength band. Nevertheless there is good

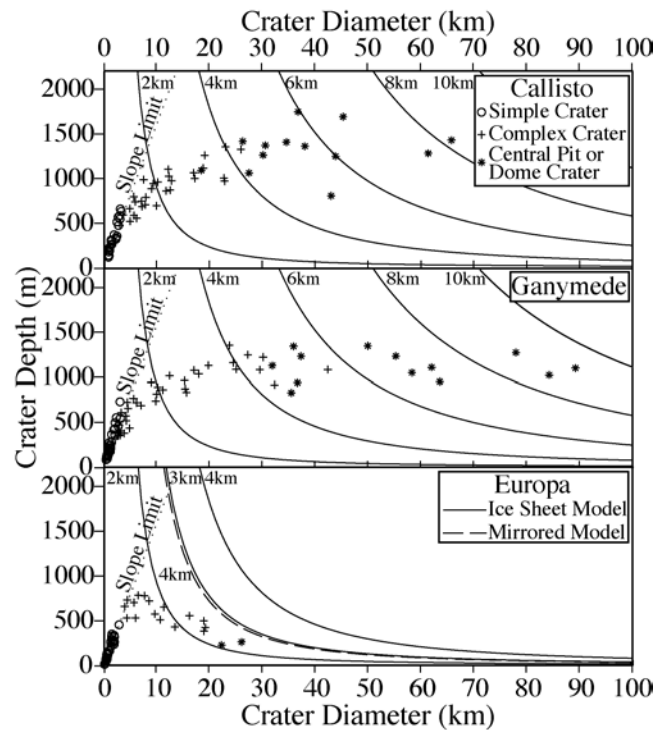


Figure 6.4 Impact crater depth versus crater diameter (after *Schenk* [2002]). Dotted line shows 17° slope limit for small diameter craters. Solid curves are crater depth predicted by a moment-saturated lithosphere having the ice sheet yield-strength envelope. Large diameter craters on (a) Callisto and (b) Ganymede are supported by a lithosphere thickness ranging from 2-10 km. Large diameter craters on (c) Europa are supported by a minimum 2.5 km thick lithosphere. The more realistic mirrored model requires a minimum 3.5 km thick lithosphere.

agreement between these simple models and the available data suggesting Europa's lithosphere is no thinner than 2.5 km. The more realistic mirrored model requires a thickness greater than 3.5 km. The most important feature of this comparison is the decreasing crater depth with increasing diameter, especially for diameters > 20 km. This spectral decrease is consistent with the apparent blue topographic spectrum of Europa; it appears smooth at intermediate wavelengths (100 km - 1000 km) but quite rough at smaller scales (2 - 20 km). In contrast, most rocky planets, e.g. Venus, Earth, and Mars have a red topographic spectrum [*Bills and Lemoine, 1995*].

6.5 Discussion

One of the interesting predictions of this method is that it places an upper bound on the topographic spectrum of Europa. This has important tectonic and practical consequences. From a tectonics perspective, any long wavelength topography that exceeds this bound [e.g., Murias Chaos "Mitten", *Figueredo et al., 2002*] must be supported either by local compensation, due to nonuniform tidal heating [*Ojakangas and Stevenson, 1989*], or by convective activity in the weak ductile ice beneath the lithosphere. From a practical perspective, the upper bound on the amplitude spectrum can be used to design topographic sampling strategies for measuring tides, long-wavelength topography due to shell thickness variations, and geoid height in regions not dominated by Airy-compensated topography.

Existing topographic grids are not large enough for accurate spectral analysis and also have long-wavelength errors due to the inaccuracies in the stereo-DEM generation process. Moreover, spectra produced from a 1-D profile do not accurately

represent the true 2-D spectrum, especially when the spectrum is blue. Therefore we explore the tectonic and practical consequences of the predicted topographic spectrum by generating synthetic topography that has bending moment less than or equal to the saturation moment observed in Figure 6.4c and surface slopes less than or equal to 17° . This is accomplished using a statistical approach by first generating random topography uniformly distributed in wavenumber domain, and then forcing it to conform to the model spectrum of Figure 6.4c.

An important issue on Europa is whether or not density variations within the shell are required to explain the observed topography in the 20 - 100 km wavelength band. *Schenk and Pappalardo* [2004] have proposed that intermediate-scale topography (~20-100 km) must be supported by Pratt isostasy since the bottom surface of the ice shell will become flat, erasing any perturbations, over a relatively short timescale (10^5 years) [*Nimmo*, 2004; *Stevenson*, 2000] making Airy isostasy impossible. They in turn use this argument to rule out the possibility of a thin-shelled Europa. Here we show that Pratt isostasy is not required, although still possible, because the 20km-scale topography could be supported by the strength of the shell. Figure 6.5a shows a 200 km long profile of topography on Europa taken from the Conamara Chaos region of relatively large amplitude topography. The topography data comes from a stereo-controlled photogrammetry Digital Elevation Model produced by *Schenk and Pappalardo* [2004] and has a standard deviation of 77 m and a maximum slope of 16° . Figure 6.5b shows a profile taken from our synthetically derived topography, bounded by a 17° slope and the saturation moment corresponding to a 3 km thick ice sheet model lithosphere. The two profiles have similar peak to

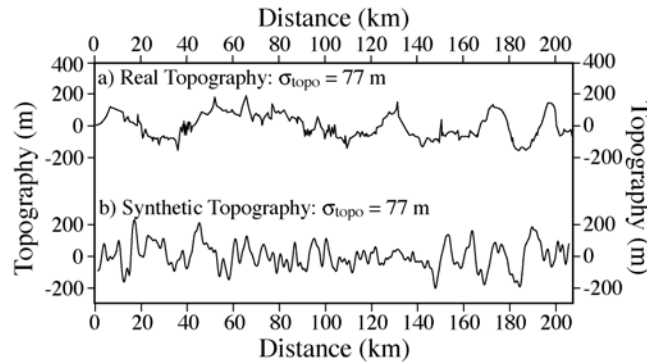


Figure 6.5 (a) Topographic profile from Conamara Chaos region of Europa with standard deviation 77 m and maximum slope 16° [Schenk and Pappalardo, 2004]. (b) Synthetically derived topography with standard deviation 77 m and maximum slope 17° . Maximum moment along this profile corresponds to a 3-km thick plate.

trough amplitude and visually similar spectrum. This analysis suggests that Pratt isostasy is not required to explain the 20 km-scale topography since it can also be supported by the strength of the lithosphere. However, if one were to observe topography outside the saturation moment limit, then another mechanism of support such as local isostasy or convection would be needed.

A second important issue on Europa is how best to measure the long-wavelength topographic variations due to tides, shell thickness variations, and geoid height. Proposed instruments include a laser altimeter profiler, which has excellent absolute height accuracy but poor spatial sampling, and a synthetic aperture radar interferometer that can measure a wide swath but has inferior height accuracy. Tidal fluctuations are estimated to be as large as 30 m [Greenberg *et al.*, 2002; Moore and Schubert, 2000] on a global scale ($\sim 10,000$ km wavelength). To learn something new about generation of heat by tidal dissipation will require understanding the phase lag

of the tide relative to the gravitational forcing functions so perhaps a 1-m accuracy will be needed. Another possible feature of interest is the shape of the planet's equipotential surface, or "geoid", caused by mass variations at the floor of Europa's ocean. If the ocean and ice shell are in isostatic equilibrium at long wavelengths (> 200 km), it may be possible to measure the height of the geoid with an altimeter. Altimeters have been used to measure the geoid over areas of permanent ice cover on the Earth [*Laxon and McAdoo*, 1994]. The expected geoid signal can be crudely estimated by placing a large uncompensated volcano at the base of a 100 km deep ocean. A volcano having mass comparable to Mauna Loa (Hawaii) or Haemus Montes or Euboea Montes (Io) [*Schenk and Bulmer*, 1998] produces a geoid bump 1 - 10 m tall and 400 km across. Thus both the tidal signal and the geoid signal are about 100 times smaller than the RMS of the topography of Europa so the question is - what is the best way to sample and average the topography to extract the small-amplitude long-wavelength signals from the shorter-wavelength topographic "noise"?

To assess the possibility of measuring topography to a 1 m vertical accuracy at long wavelengths, we investigate the end member strategies for sampling and averaging of a synthetic topography grid with the model spectrum of Figure 6.4c. (Note the tidal fluctuations can also be detected at crossover points of altimeter profiles and our analysis does not consider this type of sampling.) The laser altimeter has 200 m diameter footprint and 200 m along-track sampling. The swath altimeter has the same 200-m by 200-m resolution but samples a swath 10 km wide (i.e., 50 pixels wide). Of course, the swath data can be averaged across-track to reduce the topographic noise by a factor of ~ 5 but this still does not achieve the desired accuracy

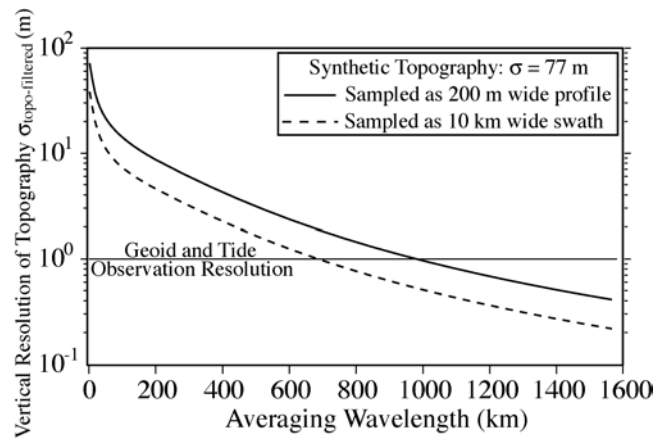


Figure 6.6 Vertical accuracy of sampled topography versus wavelength of averaging. Solid and dashed lines are for profile instrument (200 m width) and swath instrument (10 km width) respectively. A 1 m vertical resolution is required to study geoid and tide variations.

of 1 m. Additional noise reduction is gained by Gaussian-averaging the profiles along the satellite track. Figure 6.6 shows the level of vertical accuracy achieved by the two instruments by along-track averaging. The laser-altimeter achieves the 1-m threshold at an averaging wavelength of 1000 km. This sampling is adequate for resolving the 10,000-km wavelength tides but inadequate for detecting the geoid expression of a large ocean floor volcano. The swath altimeter achieves the 1-m threshold at a wavelength of 700 km. In this case the tidal signal is resolved but only the longer-wavelength components of the ocean floor volcano could be resolved. It must be emphasized that these results rely on the assumption that all topography is supported by the strength of the lithosphere. This assumption is likely to be invalid at some points on Europa's surface. Any long-wavelength topography having amplitude > 1 m that is supported by an Airy, Pratt, or convective mechanism will mask the tidal and

geoid signals. In this case a crossover analysis will be needed to extract the tidal signal and the geoid signal will be immeasurable.

6.6 Conclusions

Saturation moment analysis is a useful companion to existing methods of estimating lithosphere thickness. Rather than relying on estimates of specific material properties that are poorly constrained, it instead makes a more fundamental estimation of the first-order behavior of the general material by selecting the shape of the lithosphere's yield strength envelope. By using the strongest possible yield strength envelope, an absolute lower bound on lithospheric thickness can be established. Moment analysis also gives a more robust estimate of lithosphere thickness since it simultaneously incorporates multiple features of multiple length scales to constrain its estimates rather than a single feature of a single scale.

Craters of large diameter ($> \sim 10$ km) on Callisto and Ganymede exhibit multiple topographic moments, as do trenches at subduction zones on Earth, indicating a range of lithosphere thicknesses. We conclude that lithosphere thickness on these satellites in the vicinity of these impact craters either i) varies in the range of a few km to ~ 10 km or ii) is everywhere thicker than 10 km (or some combination of the two). These estimates are significantly larger than previous estimates of effective elastic plate thickness. Craters on Europa coincide with a single observed topographic moment for large craters (diameter $> \sim 6$ km) suggesting a lithosphere thickness greater than 2.5 km in the vicinity of the craters. This estimate lies between the

thinner effective elastic thickness estimates of *Williams and Greeley* [1998] and thicker estimates of *Figueredo et al.* [2002] and *Nimmo et al.* [2003a].

The impact crater depth/diameter relationship on Europa is consistent with a moment saturation model having a blue spectrum. This model explains why Europa appears smoother at long wavelengths than it does at short wavelengths. This spectrum can be used to statistically create synthetic topography grids much larger than the DEMs available from current data. Simulation of topography with this spectrum reveals that observed chaos topography can be supported by the strength of the lithosphere and do not require Pratt isostasy as a mechanism of support as has been suggested. Large synthetic topography grids allow us to examine intermediate wavelength characteristics and consider possible sampling strategies for an altimeter at Europa. Observation of geoid height and new understanding of tides requires 1 m of vertical resolution unobscured by small-scale topography. A 10 km swath instrument would require along track averaging of 700 km to achieve this resolution and a 200 m spot profiling instrument would require along track averaging on the order of 1000 km.

6.7 Acknowledgements

The authors thank F. Nimmo and an anonymous reviewer for their helpful comments, and thank J. Bassis, K. Lawrence, D. Agnew, and C. Johnson for in-house reviews. This research was supported by NASA Solid Earth Science Program (NAG5-13673) and NASA Earth Systems Science Fellowship Program (NGT5-30514).

Chapter 6, in full, is a reprint of the material as it appears in Luttrell, K., and D. Sandwell (2006), Strength of the lithosphere of the Galilean satellites, *Icarus*, 183 (1), 159-167, doi:10.1016/j.icarus.2006.01.015. The dissertation author was the primary investigator and author of this paper.

6.8 References

- Beeman, M., W.B. Durham, and S.H. Kirby (1988), Friction of Ice, *J. Geophys. Res.*, **93** (B7), 7625-7633.
- Billings, S.E., and S.A. Kattenhorn (2005), The great thickness debate: Ice shell thickness models for Europa and comparisons with estimates based on flexure at ridges, *Icarus*, **177**, 397-412.
- Bills, B.G., and F.G. Lemoine (1995), Gravitational and topographic isotropy of the Earth, Moon, Mars, and Venus, *J. Geophys. Res.*, **100** (E12), 26275-26295.
- Brace, W.F., and D.L. Kohlstedt (1980), Limits on Lithospheric Stress Imposed by Laboratory Experiments, *J. Geophys. Res.*, **85** (NB11), 6248-6252.
- Byerlee, J. (1978), Friction of Rocks, *Pure Appl. Geophys.*, **116** (4-5), 615-626.
- Figueredo, P.H., F.C. Chuang, J. Rathbun, R.L. Kirk, and R. Greeley (2002), Geology and origin of Europa's "Mitten" feature (Murias Chaos), *J. Geophys. Res.*, **107** (E5).
- Goetze, C., and B. Evans (1979), Stress and Temperature in the Bending Lithosphere as Constrained by Experimental Rock Mechanics, *Geophys. J. R. Astr. Soc.*, **59** (3), 463-478.
- Goldsby, D.L., and D.L. Kohlstedt (2001), Superplastic deformation of ice: Experimental observations, *J. Geophys. Res.*, **106** (B6), 11017-11030.
- Greenberg, R., P. Geissler, G. Hoppa, and B.R. Tufts (2002), Tidal-tectonic processes and their implications for the character of Europa's icy crust, *Rev. Geophys.*, **40** (2).
- Kirby, S.H. (1983), Rheology of the Lithosphere, *Rev. Geophys.*, **21** (6), 1458-1487.
- Kivelson, M.G., K.K. Khurana, C.T. Russell, M. Volwerk, R.J. Walker, and C. Zimmer (2000), Galileo magnetometer measurements: A stronger case for a subsurface ocean at Europa, *Science*, **289** (5483), 1340-1343.
- Laxon, S., and D. McAdoo (1994), Arctic-Ocean Gravity-Field Derived from Ers-1 Satellite Altimetry, *Science*, **265** (5172), 621-624.
- Levitt, D.A., and D.T. Sandwell (1995), Lithospheric Bending at Subduction Zones Based on Depth Soundings and Satellite Gravity, *J. Geophys. Res.*, **100** (B1), 379-400.
- Masson, D.G. (1991), Fault Patterns at Outer Trench Walls, *Mar. Geophys. Res.*, **13** (3), 209-225.

- McAdoo, D.C., J.G. Caldwell, and D.L. Turcotte (1978), Elastic-Perfectly Plastic Bending of Lithosphere under Generalized Loading with Application to Kuril Trench, *Geophys. J. R. Astr. Soc.*, *54* (1), 11-26.
- McKinnon, W.B. (1999), Convective instability in Europa's floating ice shell, *Geophys. Res. Lett.*, *26* (7), 951-954.
- McNutt, M.K., and H.W. Menard (1982), Constraints on Yield Strength in the Oceanic Lithosphere Derived from Observations of Flexure, *Geophys. J. R. Astr. Soc.*, *71* (2), 363-394.
- Moore, W.B., and G. Schubert (2000), The tidal response of Europa, *Icarus*, *147* (1), 317-319.
- Nimmo, F. (2004), Non-Newtonian topographic relaxation on Europa, *Icarus*, *168* (1), 205-208.
- Nimmo, F., B. Giese, and R.T. Pappalardo (2003a), Estimates of Europa's ice shell thickness from elastically-supported topography, *Geophys. Res. Lett.*, *30* (5).
- Nimmo, F., and R.T. Pappalardo (2004), Furrow flexure and ancient heat flux on Ganymede, *Geophys. Res. Lett.*, *31* (19).
- Nimmo, F., R.T. Pappalardo, and B. Giese (2002), Effective elastic thickness and heat flux estimates on Ganymede, *Geophys. Res. Lett.*, *29* (7).
- Nimmo, F., R.T. Pappalardo, and B. Giese (2003b), On the origins of band topography, Europa, *Icarus*, *166* (1), 21-32.
- O'Brien, D.P., P. Geissler, and R. Greenberg (2002), A melt-through model for chaos formation on Europa, *Icarus*, *156* (1), 152-161.
- Ojakangas, G.W., and D.J. Stevenson (1989), Thermal State of an Ice Shell on Europa, *Icarus*, *81* (2), 220-241.
- Pappalardo, R.T., M.J.S. Belton, H.H. Breneman, M.H. Carr, C.R. Chapman, G.C. Collins, T. Denk, S. Fagents, P.E. Geissler, B. Giese, R. Greeley, R. Greenberg, J.W. Head, P. Helfenstein, G. Hoppa, S.D. Kadel, K.P. Klaasen, J.E. Klemaszewski, K. Magee, A.S. McEwen, J.M. Moore, W.B. Moore, G. Neukum, C.B. Phillips, L.M. Prockter, G. Schubert, D.A. Senske, R.J. Sullivan, B.R. Tufts, E.P. Turtle, R. Wagner, and K.K. Williams (1999), Does Europa have a subsurface ocean? Evaluation of the geological evidence, *J. Geophys. Res.*, *104* (E10), 24015-24055.
- Ruiz, J. (1997), Onset of Convection, Heat Flow and Thickness of the Europa's ice Shell, *Earth, Moon, and Planets*, *77* (2), 99-104.

Schenk, P.M. (2002), Thickness constraints on the icy shells of the galilean satellites from a comparison of crater shapes, *Nature*, 417 (6887), 419-421.

Schenk, P.M., and M.H. Bulmer (1998), Origin of mountains on Io by thrust faulting and large-scale mass movements, *Science*, 279 (5356), 1514-1517.

Schenk, P.M., and R.T. Pappalardo (2004), Topographic variations in chaos on Europa: Implications for diapiric formation, *Geophys. Res. Lett.*, 31 (16).

Showman, A.P., and R. Malhotra (1999), The Galilean satellites, *Science*, 286 (5437), 77-84.

Stevenson, D.J. (2000), Limits on the variation of thickness of Europa's ice shell, *Lunar Planet. Sci.* 31, 1506 (abstract).

Thomson, R.E., and J.R. Delaney (2001), Evidence for a weakly stratified European ocean sustained by seafloor heat flux, *J. Geophys. Res. - Planets*, 106 (E6), 12355-12365.

Turcotte, D.L., and G. Schubert (2002), *Geodynamics*, 456 pp., Cambridge Univ. Press, New York.

Turtle, E.P., and E. Pierazzo (2001), Thickness of a European ice shell from impact crater simulations, *Science*, 294 (5545), 1326-1328.

Wang, H., and D.J. Stevenson (2000), Convection and internal melting of Europa's ice shell, *Lunar Planet. Sci.* 31, 1293 (abstract).

Watts, A.B. (2001), *Isostasy and Flexure of the Lithosphere*, Cambridge Univ. Press, New York.

Williams, K.K., and R. Greeley (1998), Estimates of ice thickness in the Conamara Chaos region of Europa, *Geophys. Res. Lett.*, 25 (23), 4273-4276.